

STRUCTURE-PROPERTY CORRELATIONS IN HETEROJUNCTION ORGANIC SOLAR
CELLS ACROSS MATERIAL SYSTEMS VIA SYNCHROTRON X-RAY TECHNIQUES

By

OBAID ALQAHTANI

A dissertation submitted in partial fulfillment of
the requirements for the degree of

DOCTORAL OF PHILOSOPHY

WASHINGTON STATE UNIVERSITY
School of Mechanical and Materials Engineering

JULY 2023

© Copyright by OBAID ALQAHTANI, 2023
All Rights Reserved

To the Faculty of Washington State University:

The members of the Committee appointed to examine the dissertation of OBAID ALQAHTANI find it satisfactory and recommend that it be accepted.

Brian A. Collins, Ph.D., Chair

W. H. Katie Zhong, Ph.D.

Matthew D. McCluskey, Ph.D.

ACKNOWLEDGMENT

I would like to thank everyone that has supported and assisted me throughout this Ph.D. journey. Special thanks to my advisor Dr. Brian Collins and the rest of my committee members: Dr. Katie Zhong and Dr. Matthew McCluskey. Thanks to all my (current and former) group members and my worldwide collaborators. Thanks to my whole family—special thanks to my wife (Nouf Alqahtani).

STRUCTURE-PROPERTY CORRELATIONS IN HETEROJUNCTION ORGANIC SOLAR CELLS ACROSS MATERIAL SYSTEMS VIA SYNCHROTRON X-RAY TECHNIQUES

Abstract

by Obaid Alqahtani, Ph.D.
Washington State University
July 2023

Chair: Brian A. Collins

The power conversion efficiency (PCE) of organic solar cells (OSCs) is rising, surpassing 18%. The low cost, flexibility, and uniquely tunable properties of organic materials set OSCs as a promising integrable and competitive renewable technologies. However, transferring high-performing ink-printed OSCs from the lab-scale to industrial scale remains challenging. For example, the optimal device thicknesses that are not easily achievable via large-scale printing methods like roll-to-roll printing and are rather prone to pin-hole defects. Another issue facing most of the record high-performing systems with non-fullerene acceptors (NFAs) is the need for optimization with solvent additives. Processing additives invoke many obstacles when transferring to an industrial scale, such as solvent residuals often leading to undesirable film structures and mechanical properties incompatible with printing methods. Although wide varieties of organic materials have been synthesized and tested for OSCs applications, the pool of candidates of efficient and scalable materials is very low. Understanding and control of OSC device nanostructure, which is responsible for their photo-electrical properties are essential criteria of selection regarding their industrial viability. Multimodal characterization and holistic

analysis of device performance and nanostructure of bulk heterojunction (BHJ) OSCs as functions of device fabrication variables, however, are required for judging the scalability of a material or processing condition.

This work aims to thoroughly investigate structures of a selected variety of OSCs systems with unique attributes or novel materials. Soft X-ray scattering and spectro-microscopy are excellent characterization tools due to their proven sensitivity to material contrast. Those tools are used with X-ray diffraction and other electron-based techniques for more accurate multimodal analyses of the studied OSC nanostructures. By correlating nanomorphology with device functionalities, conclusions can be drawn pertaining to the viability of material types and fabrication procedures. One of the investigated OSCs systems (polymer:fullerene) maintains relatively high PCE even with an active-layer thickness of 1 μm critical for commercial scale-up. We have discovered that sharp donor-acceptor (D-A) interfacial widths significantly reduces charge recombination. This finding might be key to successfully commercializing printed thick OSCs. Another focus of this work is investigating impacts of solvent additives on device performance and morphology in NFA OSCs. Results of studying two polymer:NFA systems show high device performance and morphology sensitivity to the most prevalent solvent additive chloronaphthalene (CN). The findings suggest that additive-free methods and carefully designed NFA molecules will be essential to industrial-scale fabrication of stable NFA OSCs. Interestingly, CN is commonly used to optimize device performance in most of the state-of-the-art NFA systems, namely PM6:Y6 (NFA) OSCs. Our results and previous literature show that PM6:Y6 system is also susceptible to typical concentration of CN as the optimizing solvent additive. In the last study of this dissertation, an alternative of CN, known as phenylnaphthalene (PN), was used to optimize device performance in PM6:Y6 OSCs. A thorough examination of

device performance and nanostructure of PM6:Y6 devices as a function of PN concentration shows that: PN is a potential eco-friendly (non-halogen) candidate to replace CN as a processing solvent additive with less concerns regarding sensitivity to the additive concentration. Also, we find that the optoelectrical charge generation processes in PM6:Y6 OSCs can be fine-tuned using the PN solvent additive.

The findings of OSC structure-property relationships in this dissertation give insights into some key aspects to be considered during material synthesis and device fabrication for successful printing of efficient OSCs. Finally, combinations of characterizing OSC device performance via holistic methods and probing their morphology via multimodal synchrotron X-ray techniques seem essential to realize the potential of emerging binary NFA OSCs and ternary systems.

TABLE OF CONTENTS

	Page
ACKNOWLEDGMENT.....	iii
ABSTRACT.....	iv
LIST OF TABLES	x
LIST OF FIGURES	xiii
CHAPTER 1: INTRODUCTION.....	1
CHAPTER 2: METHODOLOGY	5
Device performance and optoelectronic testing methods	5
Nanostructure probing techniques.....	10
Grazing incidence wide-angle X-ray scattering (GIWAXS).....	10
Near-Edge X-Ray Absorption Fine-Structure (NEXAFS) Spectroscopy	13
Scanning transmission X-ray microscopy (STXM) and NEXAFS	14
Resonant Soft X-Ray Scattering (RSoXS) and NEXAFS.....	17
CHAPTER 3: EVIDENCE THAT SHARP INTERFACES SUPPRESS RECOMBINATION IN THICK ORGANIC SOLAR CELLS.....	21
Abstract	22
Introduction	22
Results	26
Discussion	37

Conclusion.....	40
Experimental Section	41
Acknowledgments.....	44
CHAPTER 4: HIGH SENSITIVITY OF NON-FULLERENE ORGANIC SOLAR CELLS MORPHOLOGY AND PERFORMANCE TO A PROCESSING ADDITIVE	45
Abstract	46
Introduction.....	46
Results.....	50
Device Performance	50
Morphology: GIWAXS	51
Morphology: Microscopy	55
Morphology: RSoXS	59
Discussion	64
Conclusion.....	70
Experimental Section	71
Acknowledgements	75
CHAPTER 5: FIELD-INDEPENDENT GEMINATE RECOMBINATION LIMITS CHARGE SEPARATION IN PM6:Y6 ORGANIC SOLAR CELLS: DRIVEN BY MOLECULAR ORDERING OF Y6.....	76
Abstract	77
Introduction.....	77

Results	80
Discussion	87
Conclusion.....	88
Experimental Section	89
Acknowledgements	91
CHAPTER 6: CONCLUSIONS	92
REFERENCES	95
APPENDIX.....	107
APPENDIX A: SUPPORTING INFORMATION FOR CHAPTER 3: EVIDENCE THAT SHARP INTERFACES SUPPRESS RECOMBINATION IN THICK ORGANIC SOLAR CELLS	108
APPENDIX B: SUPPORTING INFORMATION FOR CHAPTER 4: HIGH SENSITIVITY OF NON-FULLERENE ORGANIC SOLAR CELLS MORPHOLOGY AND PERFORMANCE TO A PROCESSING ADDITIVE	137
APPENDIX C: SUPPORTING INFORMATION FOR CHAPTER 5: FIELD-INDEPENDENT GEMINATE RECOMBINATION LIMITS CHARGE SEPARATION IN PM6:Y6 ORGANIC SOLAR CELLS: DRIVEN BY MOLECULAR ORDERING OF Y6.....	166

LIST OF TABLES

	Page
Table 2- 1: Summary of device performance, reduction factors of bimolecular recombination and charge carrier mobilities in NT812:PC71BM films with different blend ratios, processed with and without solvent additive. The device performance parameters are an average of 6 devices. The bimolecular recombination reduction factors ($\gamma = k_L / k_{rec}$) are calculated based on steady-state bias-assisted charge extraction measurements and the mobilities (fast and slow carriers) are calculated based on resistance-dependent photovoltage measurements (see Figure S1- 2 and Figure S1- 3, SI). The listed γ values are at about 1 sun intensity ^(a)	27
Table S1- 1: Device performance summary for 1:1.5 blends with CN, at different thickness. Thick blend ~ 200 nm and thin blend ~ 100 nm.	109
Table S1- 2: Molecular packing details extracted from GIWAXS data. Scattering peak positions and d-spacing ($d = 2\pi Q$) for pi stacking (010) peaks and their corresponding lamellar (100) peaks of NT812 in pure polymer films and in blends with and without solvent additive CN. Also, the orientation of pi stacking with respect to substrate was indicated in parentheses. Note: those peak positions and d-spacing values do not change in all samples (both in neat polymer and blend films) which indicates that similar packing and ordering in neat polymer exist in blends.	114
Table S1- 3: Summary of the calculated variables via the donor-acceptor interfacial width calculation. The volume fraction values and characteristic length LC are from RSoXS analysis.....	135
Table S2- 1: summary of device performance parameters for PBDB-T:CPDT-4F blends. The device performance parameters are the mean of 10 cells \pm standard deviation.	139
Table S2- 2: summary of device performance parameters for PBDB-T:CPDT-4Cl blends. The device performance parameters are the mean of 10 cells \pm standard deviation.	139
Table S2- 3: Peak position and d-spacing results extracted from multi-peak fitting of the GIWAXS 1D scattering profiles for in-plane lamellar and out-of-plane pi stacking. Where $d = 2\pi / (\text{peak position})$. In parenthesis meaning: (polymer) means values for polymer peaks in blends and (SM) means values for small molecule peaks in blends.....	146
Table S3- 1: Summary of the J-V parameters for PM6:Y6 OSCs with different concentrations of the solvent additive (PN). Uncertainties are the standard errors.....	167

Table S3- 2: A summary of the current densities as calculated and extracted for PM6:Y6 blends with 0, 0.5, and 2 % PN solvent additive. J_{\max} is calculated from the photon irradiance. J_{abs} is calculated from the transfer matrix modeling. J_{sat} is the current density of each blend at voltage of -3 V. J_{gen} is the current density that was generated via TDCF at maximum power point voltage (V_{mpp}). J_{mpp} is the current density at maximum power point.... 174

Table S3- 3: A summary of charge losses at each step of the charge generation process in relation to the maximum current density J_{\max} in PM6:Y6 devices with 0, 0.5, and 2% PN. The first column shows how each loss is calculated. FI stands for field-independent, and FD stands for field-dependent..... 174

Table S3- 4: Quantum efficiencies of light absorption, charge separation, and charge extraction in PM6:Y6 devices with 0, 0.5, and 2 % PN. 174

Table S3- 5: A summary of peak position, d-spacing, and CCL values as extracted from MPF for the OoP pi-pi stackings in pure PM6, pure Y6 and PM6:Y6 blend films with different amounts of PN. (d-spacing= $2 \cdot \pi / \text{peak position}$)..... 182

Table S3- 6: A summary of peak position, d-spacing, and CCL values as extracted from MPF for the IP lamellar stackings in pure PM6 and pure Y6 films with different amounts of PN 182

LIST OF FIGURES

	Page
Figure 1- 1: a) Global tilt corrected for as AM 1.5 as the standard solar irradiance for testing solar cells. b) I-V experiment setup. c) depiction of a BHJ architecture. d) A J-V curve example for an OSC showing the important parameters (J_{sc} , V_{oc} , J_m , V_m , and M_{pp}).....	6
Figure 1- 2: A schematic of the charge generation processes in an OSC device.....	7
Figure 1- 3:a) A schematic of the TDCF experimental setup. b) a schematic of the TDCF timeline.c) J-V curve with a photocurrent (J_{ph}) trace of a device under 1 Sun (red) and a generated current via TDCF (blue) scaled to J_{ph} at -3 V.....	9
Figure 1- 4: Depiction of GIWAXS geometry and setup. X-ray with grazing incidence angle (θ_i) and scattering angle (θ_{scat}). A two-dimensional charge-coupled device (CCD) detector is used to record the scattering x-ray, with sample-to-detector distance about 27 cm. On the left side, an example of 2D GIWAXS images with IP and OoP lineouts examples (red). Bottom shows an example of peak fitting with the fitting parameters results of peak '0' in the orange box. Cartoons on the right-side show two examples of molecular packing and orientations with respect to the substrate.....	11
Figure 1- 5: a). A transmission setup of NEXAFS spectroscopy. b) Spectra examples of a polymer (NT812) and a fullerene (PC71BM) calculated via Beer-Lambert equation and scaled to the bare atom absorbance.....	13
Figure 1- 6: a) STXM setup. b) NEXAFS spectra examples. STXM OD maps at 284.4 eV (c) and 320 eV (f) of a polymer:fullerene BHJ OSC film. Thickness and composition maps (d) and (e) as well as 1D profile examples (g).....	16
Figure 1- 7: a) Experimental setup of RSoXS. b) 1D reduced lineouts from 2D RSoXS images showing scattering intensity vs. q for a polymer:fullerene blend, at X-ray energy of 270eV (black) and 283.5 eV (orange). c) NEXAFS spectra of a polymer and fullerene real (δ) and imagery (β) parts of their indices for refraction. The material contrast between polymer-fullerene (black) as well as material-vacuum contrasts. Note that the polymer-fullerene contrast is maximized at around 284 eV.....	18
Figure 2- 1: a) Chemical structure for the fullerene (top) and polymer (bottom). b) J-V characteristic curves for the four different solar cells. c) UV-Vis absorbance for neat polymer with and without CN as well as for all blends. d) Reduction factor of bimolecular recombination as a function of carrier density in all four NT812: PC71BM blends. Black circles show the reduction factor data points at about 1 sun.....	24

Figure 2- 2: GIWAXS results for neat materials (NT812 and fullerene) and blends. 2D GIWAXS scattering results for NT812: PC71BM blends of (3:1) blend with CN (a) and 1:1.5 blend with CN (b). The 2D images are plotted with the same color scale of the scattering intensities [a.u.], also corrected for the missing wedge. c) 1D GIWAXS profiles extracted from the 2D images in the OoP vertical direction (qz) for all blends. Also, the graph includes the GIWAXS profile of neat PC71BM (black) to help with peak assignments. PC71BM and (010) peaks are indicated in the graph. d) Coherence length (D) for PC71BM peak at $qz=1.36 \text{ \AA}^{-1}$ (open circles) and (010) peak at $qz=1.83 \text{ \AA}^{-1}$ (solid circles) in blends as well as in neat materials were calculated via Scherrer analysis (details in the Supporting Information)..... 31

Figure 2- 3. Morphology investigation of OSC active layer in a 100 nm thin (1:1.5) blend with CN. a) NEXAFS spectra: pure NT812 (orange), PC71BM (blue), blend (Red), and a linear combination fit of spectra for NEXAFS for pure components (black). b) STXM composition scan was acquired at 284.4 eV, which is fullerene absorption peak. PC71BM (dark regions) and NT812 (white fibrils). c) Concentration profiles of NT812 across different compositional domains; (blue) raw and (grey) deconvoluted..... 33

Figure 2- 4. a) Lorentz-corrected RSoXS profiles acquired at 283.5 eV for active layers of the four investigated samples as indicated in the graph legend. b) Averaged differences in composition between different domains, based on two-domain model. The dotted lines represent the mathematically calculated ΔC_{RMS} values of composition differences as a function of the D-A interfacial width. The black circles are the extracted values of the D-A interfacial width based on STXM and RSoXS results..... 36

Figure 2- 5: Depicted representation of morphology of OSC active layer in the investigated NT812: PC71BM blends. Polymer fibrils (blue) with stacked polymer chains (black) and matrix of fullerene (Red). We note that the fast growth direction of the fibril is unknown for this polymer and may not be the pi-stacking direction as is depicted here..... 37

Figure 3- 1: a) Shows the chemical structures of the materials that were used to fabricate active layers in the investigated OSCs in this work. (Top) the polymer electron donor (PBDB-T) and (bottom) electron NFA acceptor (CPCD-4X, where X is Cl or F). The average parameters of device performance are plotted as a function of amounts of solvent additive (CN vol.%); b) J_{sc} , c) FF, d) V_{oc} , and e) PCE at 1 sun. The solid green circles indicate the F-blends (PBDB-T:CPDT-4F) with (1:1) weight ratio and open blue circles represent the Cl-films (PBDB-T:CPDT-4Cl) with (1:1.2) weight ratio. See Table S2- 1, Table S2- 2 and Figure S2- 1 in the supporting information for more about device performance, J-V curves, and external quantum efficiency (EQE) profiles. The device performance parameters are the mean of 10 cells \pm standard deviation..... 50

Figure 3- 2: (a,b,d,e,g,h) 2D GIWAXS images in as arbitrary color scale: pure materials without additive (left) and with 1% CN (middle). c) 1D GIWAXS profiles for pure polymer with and without CN extracted in the out of plane (OoP) direction to show changes in peak intensity of OoP π - π stacking. The PEDOT:PSS background is appended to the graph in green for reference. (f) and (i) present pole figures of π - π stacking in pure CPDT-4F and pure CPDT-4Cl, respectively, without additive (blue) and with 1% CN (red)..... 52

Figure 3- 3: 1D GIWAXS profiles for all the investigated blends (as indicated in the legends)—plus PEDOT:PSS background shown in green. Profiles in the IP sector (top) and OoP (bottom). Data for PBDB-T:CPDT-4F blends (a and c) and data for PBDB-T:CPCT-4Cl (b and d). More GIWAXS results and analysis can be found in the supporting information (Figure S2- 2 to Figure S2- 7, and Table S2- 3)..... 53

Figure 3- 4: GIWAXS analysis of coherence length and peak intensity for neat films and blends as indicated in the legends. Diffraction coherence length vs CN vol.% concentrations for (a) out of plane π - π stacking (010) and (b) in-plane lamellar stacking (100). (c) and (d) are analogous plots for diffraction peak intensity. The values are extracted from peaking fitting analysis of GIWAXS data, see examples methods description in Figure S2- 7. 54

Figure 3- 5: Micrographs of PBDB-T:CPDT-4Cl blends with different amounts of solvent additive using X-ray, electron, and atomic force microscopies. STXM scans for blend with 0% (a), 1% (b), and 2% CN (c) where dark regions represent NFA-rich domains (more in Figure S2- 11-Figure S2- 15). TEM scans of blend with 0% (d), 1% (e) 2% CN (more in Figure S2- 26-Figure S2- 27). AFM scans of blends with 0% (g), 1% (h), and 2% CN (i) (more in Figure S2- 20-Figure S2- 21). Scans of the Cl-blends with 2 vol.% CN: an optical microscope sane (j) (more in Figure S2- 23), a topology SEM scan (k), and cross-section SEM scan (l). More SEM scans in Figure S2- 24-Figure S2- 25). Scale bars are indicated for each scan. 56

Figure 3- 6: PBDB-T:CPDT-4Cl with 1 vol.% CN blend. a) NEXAFS spectra for the blend and neat films (as indicated in the legends). The fit (black) of the NEXAFS spectrum of the blend (red) confirms the average weight ratio (i.e., ~ 55% small molecule). b) A STXM image that was acquired at 284.85 eV, which is a small molecule resonant energy. The dark regions indicate small molecule domains, and the gray regions indicate polymer-rich domains c) Compositional line out represents variation of the small molecule concentration across different domains along the red rectangle that is indicated on the STXM image in part b (for more details, refer to Figure S2- 14). 58

Figure 3- 7: Scattering profiles and TSI for all blends. a) RSoXS 1D averaged profiles for PBDB-T:CPDT-4F blends. Their TSI and composition variation are shown in (b). TSI calculated by integrating areas under scattering profiles. Then the composition variation was calculated by normalizing TSI for all blends to TSI of the blend with 1% CN. c) 1D scattering profiles for the PBDB-T:CPDT-4Cl blends. d) TSI and composition variation values for the

Cl-blends. In b and d, the red circles represent TSI, and blue diamond shapes represent composition variation “average domain purity”. This data was acquired at X-ray energy of 285.2 eV, Lorentz corrected, and corrected for X-ray fluorescence background. Where X-ray energy of 285.2 eV is slightly below the resonant energy of the polymer material, to increase the material contrast. Additional scattering data taken at different energies can be found in Figure S2- 16 and Figure S2- 17..... 61

Figure 3- 8: A general depiction of morphology evolution with solvent additive (CN) in the investigated blends. Blue regions indicate polymer-rich domains with blue lines representing ordered polymer chains. The red regions represent NFA-rich domains with red lines indicating ordered molecules. The π - π stacking of the polymer which is mostly face-on with respect to the substrate as depicted here does not mean that the direction of the fibril growth is known in those systems..... 64

Figure 3- 9: FF and Jsc plotted as functions of normalized TSI: a) For the PBDB-T:CPDT-4F blends. b) For the Cl-blends. FF (red circles) plotted on the left y-axis and Jsc (blue circles) on the right y-axis. FF and Jsc plotted as functions of GIWAXS peak intensity of the NFA π - π stacking: c) for the F-blends and (d) for the Cl-blends. Note that the presented results here are for blends with 0, 0.5, and 1 vol.% CN. 67

Figure 4- 1: a) UV-VIS absorbance spectra of PM6:Y6 blends with different amounts of PN. b) J-V curves of the studied blends. The corresponding J-V parameters at 0, 0.5, and 2% PN are summarized in (c) Fill factor (FF) and open-circuit voltage, (d) short-circuit current density, and PCE. The plotted values in c and d are the averages of at least six independent devices, and the uncertainty bars are the standard errors..... 80

Figure 4- 2: Current densities vs. voltage for the PM6:Y6 with 0% (a), 0.5% (b) and 2% PN (c). From top to bottom: J_{mpp} (dashed black) is current density at maximum power point, J_{ph} (solid red) is the photocurrent JV curve ($J_{ph}=J_{LIGHT} - J_{DARK}$), J_{gen} (blue circles) is current density based on generated charges via TDCF, J_{sat} (dashed green) is the saturated current density that is at voltage= -3 V, J_{abs} (dashed orange) is the current density as calculated from the transfer matrix, and J_{max} (dashed cyan) is the current density of the solar simulator in wavelength range of 350-1000nm. d) Schematic of all the current densities and how they are extracted. 82

Figure 4- 3: a) Charge density at each step of the charge generation process in PM6:Y6 OSCs as a function of the concentration of solvent additive PN [vol.%]. “Abs. Loss” means absorption loss due to photons not being absorbed. “FI Gem”: field-independent geminate recombination loss. “FD Gen”: loss to field-dependent geminate recombination. “BMR” loss to bimolecular recombination. “Extracted” means extracted charges. Note that all are relative to the maximum current density (J_{max}) that can be given to an OSC by the incident photons of the solar spectrum. Since the extracted charges in (a) is relative to J_{max} , it does not directly reflect Jsc. b) Quantitative efficiencies of each of the charge generation processes in the

investigated OSCs: namely the absorption, charge speciation and charge extraction efficiencies. 83

Figure 4- 4: Microscopic scans of PM6:Y6 blends. a-c) AFM height scans of films with 0, 0.5 and 2 % PN, respectively. d-f) TEM scans of films with 0, 0.5 and 2 % PN, respectively..... 84

Figure 4- 5: a) Lorentzian corrected RSoXS profiles of the PM6:Y6 blends with different amounts of PN. Data was taken at 284.5 eV. b) Relative domain purity which is \propto *Total Scattering Intensity* and the characteristic length $L_c = 2 \cdot \pi / q$ (feature position). c) 2D GIWAXS scan of PM6:Y6 blend without PN as an example, in an arbitrary intensity color scale. Reduced 1D GIWAXS profiles of PM6:Y6 with different amounts of PN: (d) in the IP direction. (e) in the OoP direction. f) The crystal coherence length of the IP pi-pi stacking. 85

Figure 4- 6: a) Trends in charge separation and device performance parameters (FF, Jsc and PCE) as functions of PN concentration. b) A comparison of FI geminate recombination loss vs IP pi-pi stacking CCL..... 87

Figure S1- 1: UV-Vis absorbance for 1:1.5 with CN blends for comparison of 100 nm thick (solid) vs. 200 nm thick films (dashed). 109

Figure S1- 2: Coefficient of bimolecular recombination as a function of carrier intensity in all four NT812:PC71BM blends. Calculated via steady-state bias-assisted charge extraction measurements, k_{rec} shown as black squares. The predicted Langevin recombination coefficient k_L is shown as dashed red lines. a) for NT812:PC71BM (3:1) blend without CN. b) for NT812:PC71BM (3:1) blend with CN. c) for NT812:PC71BM (1:1.5) blend without CN. d) for NT812:PC71BM (1:1.5) blend with CN. 110

Figure S1- 3: Charge carrier mobilities were calculated via resistance-dependent photovoltage (RPV) transient measurements in all four blends of NT812:PC71BM with active layer thickness ~ 200 nm. a) for NT812:PC71BM (3:1) blend without CN. b) for NT812:PC71BM (3:1) blend with CN. c) for NT812:PC71BM (1:1.5) blend without CN. d) for NT812:PC71BM (1:1.5) blend with CN..... 111

Figure S1- 4: 2D GIWAXS results for all blends as the labels indicate. All blends show PC71BM ring at $q = 1.36 \text{ \AA}^{-1}$ and pi stacking (010) of the polymer at $q = 1.83 \text{ \AA}^{-1}$. The pi stacking shows stronger OoP signal meaning face-on preferential pi packing in face-on orientation with respect to the substrate. The 2D images are plotted with an arbitrary color scale of the scattering intensities, also corrected for the missing wedge a) for NT812:PC71BM (3:1) blend without CN. b) for NT812:PC71BM (3:1) blend with CN. c) for NT812:PC71BM (1:1.5) blend without CN. d) for NT812:PC71BM (1:1.5) blend with CN..... 112

Figure S1- 5: 1D GIWAXS profiles extracted from 2D GIWAXS results in Figure S1- 4. Additionally, 1D profiles for neat PC71BM are included as reference for peak assignments. a) Profiles taking in the horizontal sector, i.e. in plane (IP). (b) Profiles taking in the vertical sector, i.e. out of plane (OoP). 112

Figure S1- 6: 1D OoP GIWAXS data (red) were fitted with multi-peak fitting (blue) for PC71BM peak (at $q=1.36 \text{ \AA}^{-1}$) and pi stacking face-on peak (010) for the polymer (at $q=1.83 \text{ \AA}^{-1}$). Each peak was fitted to a Lorentzian with a linear background (green). FWHM values from the fitting results (black) were inserted in Scherrer equation [$D = 2\pi KFWHM$, $K (\text{constant}) = 0.94$] to calculate the corresponding coherence length (D) for the real-space molecular packing and ordering that causes those scattering peaks. a) for NT812:PC71BM (3:1) blend without CN. b) for NT812:PC71BM (3:1) blend with CN. c) for NT812:PC71BM (1:1.5) blend without CN. d) for NT812:PC71BM (1:1.5) blend with CN.... 113

Figure S1- 7: 1D GIWAXS profiles for neat polymer (NT812) spin casted on Na:PSS/Si substrates from solution with and without additive CN. a) 1D profiles for the IP direction. b) 1D profiles for the OoP direction. 114

Figure S1- 8: In plane GIWAXS profiles for all blends and neat films with and without CN (left) for (100) peak. Right: coherence length (D) for the in-plane lamellar peaks (100) that are presented on the left side..... 114

Figure S1- 9: a) Pole figures for NT812 (010) pi-stacking were processed for all blends from GIWAXS data. Where “Omega” defines the angle between the crystallite orientation and the surface of the substrate. b) Bar graph representation of relative degree of crystallinity (rDoC) for (010) pi-stacking in all NT812: PC71BM blends, calculate by integrating the profiles in part (a). 115

Figure S1- 10: a) NEXAFS spectra for pure NT812 and pure PC71BM scaled to their bare atom absorption coefficient. The STXM imaging energies were selected based on those NEXAFS spectra, mass absorbance, for the donor and acceptor. b) A zoomed in version of (a). At 284.4 eV, the fullerene has higher absorbance than the polymer. Another imaging energy was chosen to be 320 eV where the fullerene and polymer absorb about the same. c) NEXAFS spectra for pure polymer with and without solvent additive CN as shown in (c). The mass absorbance is relatively similar for neat polymer (NT812) with and without CN. 116

Figure S1- 11: NEXAFS for NT812: PC71BM (1:1.5) blends (red) with CN, but different thicknesses. Linear fits (black) of the NEXAFS spectra of the blend films (red) with reference NEXAFS spectra for neat materials, NT812 (orange) and PC71BM (blue). The fitting of NEXAFS spectra for blend films enables quantitative determination of average chemical composition. The film thickness also calculated from beer-lambert law. The fit

residuals shown on top (gray). Results show that the average composition of both blends ~ 60% PC71BM, which agree with the blending weight ratio (1:1.5). a) for a thin NT812:PC71BM (1:1.5) blend with CN. b) for a thick NT812:PC71BM (1:1.5) blend with CN..... 116

Figure S1- 12: Composition mapping analysis for a thin NT812: PC71BM (1:1.5) blend with CN. a) A STXM image was taking at fullerene resonant energy (284.4 eV) and the image in (b) was taken at a non-resonant energy (320 eV). By combining those STXM images with NEXAFS spectra for neat materials, a thickness map (c) as well as a composition map (d) were generated. e) Line profiles show variation in thickness (Red) and composition (blue) across a region of the blend film as presented in colored lines in c and d. From (e) the average thickness is about 85 nm. Also, the polymer concentration in the polymer-rich domain is 82 ± 3 wt. % and 27 ± 5 wt. % in the fullerene rich domain. The deconvolution of the X-ray beam tails suggests pure domains (see Figure S1- 13- Figure S1- 15 for the deconvolution analysis)..... 117

Figure S1- 13: The composition images on the left, a, c and e are the same composition image as in Figure S1- 12 d with bars that correspond to the spots where the 1D line profiles in b, d and f were extracted from. b). Shows 1D concentration profiles that were extracted from different spots as indicated with colored lines in (a). The general trends of feature size and compositional fluctuation are consistent across the film. d). The profiles were extracted from fullerene-rich spots, as indicated with white bars in (c), to show that the polymer concentration gets as low as 25% or less. f). Concentration 1D profiles extracted from (e) as indicated by white bars to show that the polymer concentration can got above 75%. The blue traces in d and f are the same as the blue one in b. In general, the polymer concentration fluctuation, high and low, can be found in several spots of the film. It was impossible to get 100% or 0% polymer concentration profiles from the raw compositional maps due to the x-ray beam convolution with the relatively small domain sizes in those NT812: PC71BM systems. Therefore, 1D and 2D deconvolution analyses were conducted to retrieve the real molecular concentration in the polymer and fullerene domains. 118

Figure S1- 14: a). This is the same image as the raw composition map in Figure S1- 12d but zoomed in on the spot where the blue line is, also in a grays color scale instead. b). A smoothed version of the image in (a), smoothed with a 2-pixel box filter to reduce the noise effects. c). A deconvoluted image that shows better representation of the real film. Where black is 100% fullerene, gray is 50% and white is 100% polymer. The gray regions, i.e., 50% concentration, indicate film spots where there are vertical overlaps between pure polymer and fullerene domains. d). A result of convolving (c) with the X-ray beam profile in Figure S1- 15. e). 1D line profiles to compare compositional variation across different domains in the 2D images, a, b, c and d (as indicated by colored lines in the images). 119

Figure S1- 15: Constructing a 3D representation of the X-ray beam profile. A scan across a TEM grid bar “a knife-edge scan” was taken as shown in (a). The dark regions show the

grid bars where the beam is totally blocked. The bright region is the direct beam through a mesh hole. b) An intensity scan across a knife edge of the TEM grid bar as indicated by a red line in (a). The total intensity changes from zero “dark”, where the beam is totally blocked, to direct beam (I_0). The intensity line scan was taken at $E = 320$ eV. c) A gaussian peak fitting of the derivative (red) of the intensity line scan in b. The FWHM is ~ 100 nm, which should be the maximum beam FWHM because the beam was not 100% focused. d) An approximate 3D representation of the X-ray beam, assuming a gaussian symmetric beam. e) A 2D representation of (d). f) A peak fitting for a line profile that was extracted from (e), as indicated with a red line. The fitting results suggest a gaussian beam profile with FWHM ~ 65 nm. 120

Figure S1- 16: STXM composition scans were taken on ~ 200 nm films at 284.4 eV, which is fullerene absorption peak, i.e., a fullerene resonant energy. PC71BM (dark regions) and NT812 (white fibrils). The images are for a 1:1.5 blend without CN% (a) and a 3:1 blend with 0.5 CN% (b). The overall shapes of PC71BM domains and polymer fibrils in the thick (1:1.5) film is similar to the thin film (see Figure 2- 3b in the main text). 121

Figure S1- 17: Scattering intensity (I) is proportional to the contrast function, $I(E) \propto |\Delta n|^2$, where (n) is index of refraction $n = 1 - \delta + i\beta$. The imaginary part (beta) is related to absorbance, calculated from NEXAFS measurements, and the real part (delta) is calculated from the Kramers Kronig transform. The graphs show the real (red) and imaginary (blue) parts of indices of refraction for neat polymer (a) and neat fullerene (b). 122

Figure S1- 18: Materials and vacuum contrast functions based on the material indices of refraction, where contrast function is $C = E^2 |\Delta n|^2$ 122

Figure S1- 19: NEXAFS measurements for all blends to determine film thickness at the same spots where RSoXS data was taken on each film. NEXAFS profiles were scaled to the mass absorbance coefficient (black fits) of the bare atoms. Film thickness calculated via Beer-lambert’s law then used to normalize RSoXS data. Where *the film hickness* = $1/\mu(E) \times \rho \ln I_0(E)/I(E)$, here $I_0(E)$ is the intensity of the direct incident beam, $I(E)$ is intensity of the transmitted beam through the film, $\mu(E)$ is the mass absorption coefficient, and ρ is the film density. 123

Figure S1- 20: Calculations based on RSoXS results in the main text (Figure 2- 4a). a) Characteristic length (L_c) of the corresponding features (black) for each film was calculated as $L_c = 2\pi/q$ where q is the peak position (green). b) The composition variation in each blend was calculated by normalizing the total scattering intensity (TSI) values for each blend to TSI for 1:1.5 with CN, which shows the highest scattering intensity. The TSI \sim integral of the RSoXS scattering profiles in Figure 2- 4a of the main text. 124

Figure S1- 21: a) Concentration variation of the polymer as a function of its volume fraction, based on two domains model. b) Composition fluctuation of the polymer between the two domains ($\Delta C_{12} = C_1 - C_2$) which indicates the lateral RMS of the polymer concentration in a film. 124

Figure S1- 22: RSoXS results at 45-degrees sample tilt plotted to explore the q_z component. Data examples shown here are for the 3:1 (200 nm) film with CN and 1:1.5 (100 nm) film with CN. 2D RSoXS data shown in Q_z vs Q_{xy} (top) and extracted average 1D profiles (bottom). The intensity decreases in direction of $-Q_z$ due to higher absorption of photons that travel longer paths through the sample as shown in the 45-degee RSoXS geometry diagram on the right side..... 125

Figure S1- 23: Model to calculate interfacial width. a) Schematic of fibril cross-sections. b & c) composition profiles extracted from the green lines in (a). 126

Figure S1- 24: a) The usual case of Fubini’s Theorem. b) The coarea formula is a deep generalization. It applies to wild sets of mappings F that are merely Lipschitz continuous. c) Our case—a common one in physics problems with symmetries—is the case in which the level sets are spheres of some dimension..... 129

Figure S1- 25: a) Example of a set E , a union of eight equilateral triangles. b) Basic equilateral formed by centers, where the center-to-center spacing d equals the characteristic length LC that was measured from RSoXS. 131

Figure S1- 26: RSoXS profiles for 1:1.5 blends with CN. The solid profile is for a 100 nm thick blend and dashed for a 200 nm thick film. The results are very similar, suggesting that the composition variation and characteristic length are almost thickness independent..... 136

Figure S1- 27: 1D GIWAXS profiles for 1:1.5 with CN blends with different thickness: 100 nm (solid) and 200 nm (dashed). In plane (left) and out of plane (right). The thinner sample shows lower peak intensities as expected. Otherwise, the results are similar, indicating similar packing and crystallinity in those blends. 136

Figure S2- 1: J-V characteristics and EQE profiles for PBDB-T:CPDT-4F blends are presented in (a) and (b), respectively. For PBDB-T:CPDT-4Cl, (d) and (e) show J-V curves and EQE, respectively. The data is for junction blends processed from CB with 0, 0.5, 1, and 2% CN solvent additive (as indicated by the different colors and legends). See the summary tables of device performance below..... 138

Figure S2- 2: GIWAXS data for pure polymer (PBDB-T) without CN (top) and with 1% CN (bottom). 2D GIWAXS images (left) and 1D GIWAXS profiles (right) with

background profiles of PEDOT:PSS. 140

Figure S2- 3: GIWAXS data for pure small molecule (CPDT-4F) without CN (top) and with 1% CN (bottom). 2D GIWAXS images (left) and 1D GIWAXS profiles (right) with background profiles of PEDOT:PSS. 141

Figure S2- 4: GIWAXS data for pure small molecule (CPDT-4Cl) without CN (top) and with 1% CN (bottom). 2D GIWAXS images (left) and 1D GIWAXS profiles (right) with background profiles of PEDOT:PSS. 142

Figure S2- 5: GIWAXS data for PBDB-T:CPDT-4F with different CN concentration as indicated in the legends. 2D GIWAXS images (left and middle). 1D GIWAXS profiles (right) for IP and OoP sectors as indicated by y-axis labels. The background profiles of PEDOT:PSS were appended to the 1D profile graphs for reference (shown in green). 143

Figure S2- 6: GIWAXS data for PBDB-T:CPDT-4Cl with different CN concentration as indicated in the legends. 2D GIWAXS images (left and middle). 1D GIWAXS profiles (right) for IP and OoP sectors as indicated by y-axis labels. The background profiles of PEDOT:PSS were appended to the 1D profile graphs for reference (shown in green). 144

Figure S2- 7: A few examples of peaking fitting of GIWAXS scattering profiles in OoP direction: a) PEDOT:PSS, b) PBDB-T 1% CN, c) CPDT-4F with 1% CN, d) CPDT-4Cl with 1% CN, e) a PBDB-T:CPDT-4F blend with 2% CN, and f) for a PBDB-T:CPDT-4Cl with 2% CN. The GIWAXS profiles are shown in (red), Lorentzian fits (black) with linear background (green). The fit residuals are shown in gray. When fitting a blend profile, only the peak positions are held at the same q values as for the pure materials until a good fit is achieved. After that, the constrains are left so peak positions can freely adjust to get an optimal fit. 145

Figure S2- 8: NEXAFS spectra for neat materials (left). Right: contrast functions of material-vacuum and material-material calculated based on the material indices of refraction $\mathbf{n}=\mathbf{1}-\delta+i\beta$, where the imaginary part is the mass absorbance, and the real part was calculated via the Kramers Kronig transform. The contrast function is $\mathbf{C}=\mathbf{E}^4\times|\Delta\mathbf{n}|^2$, where E is the X-ray energy. 147

Figure S2- 9: Quick NEXAFS absorbance spectra taking for each blend on the same spots where the X-ray scattering (RSoXS) data was taken then scaled to bare atom absorbance fits (black dotted) to extract the exact film thickness at that spot. The left graph is for fluorinated blends and the right one is for the chlorinated blends. The extracted thickness values were used to normalize RSoXS scattering profiles. (RSoXS data and results shown below)..... 147

Figure S2- 10: STXM images of neat films without (left) and with 1% CN solvent additive (right). 148

Figure S2- 11: STXM images and NEXAFS spectra of the fluorinated blends (PBDB-T: CPDT-4F). Top row shows STXM scans for blends with different CN amounts (left to right: 0, 1, and 2% CN). The second-row shows zoomed out and in scans of the blend with 2 % CN on different regions “domains” as indicated with the red squares. No features or textures were detected within those largely separates domains in 2% CN blend. NEXAFS spectra taken across those large domains in the 2% CN blends are shown in the third row. When the spectra were fitted to reference spectra of neat materials, results suggest pure polymer domains and a vertical average of 64% small molecules in the other domains. The bottom row show NEXAFS spectra taken across 0% CN blend (left) and 1% CN blend (right). Their peak fitting results confirm the weight ratio of the small molecules in those blends (i.e., ~50 wt.%) 149

Figure S2- 12: STXM compositional analysis of the fluorinated blend (PBDB-T: CPDT-4F) with 2% CN. Images were taken a polymer resonant energy (285.25 eV) and a non-resonant energy for both the small molecule and polymer (320 eV). Composition analysis was performed to extract compositional and thickness maps (shown in the middle). Then 1D profiles of thickness and composition (presented on the right side) were extracted from those maps across different domains as indicated by the red and blue lines on the maps. 150

Figure S2- 13: STXM images and NEXAFS spectra of chlorinated blends (PBDB-T: CPDT-4Cl). Top row shows a STXM scan and NEXAFS spectrum for the blend without CN. Domains are within the STXM resolution and are not big enough to conduct compositional analysis. NEXAFS fitting results confirm the weight ratio (i.e., ~ 55 wt.% small molecule). The second row shows a STXM scan and NEXAFS spectrum for the 1% CN blend. The domains were big enough to perform composition analysis on this film (see Figure 3- 6 in the main text and Figure 3- 6). The results of fitting the NEXAFS scan also confirms the weight ratio in this blend. Finally, data of the film with 2% CN is presented at the bottom of this graph. The STXM image show strong phase separation, with the dark domains being mostly small molecule and the bright regions being mostly polymer—as confirmed by fitting NEXAFS scans that were taken across those different domains (as indicated by the red arrows)..... 151

Figure S2- 14: STXM compositional analysis of the chlorinated blend (PBDB-T: CPDT-4Cl) with 1% CN. Images were taken a small molecule resonant energy (284.85 eV) and a non-resonant energy for both the small molecule and polymer (320 eV). Composition analysis was performed to extract compositional and thickness maps (shown in the middle). Then 1D profiles of thickness and composition (presented on the right side) were extracted from those maps across different domains as indicated by the red and blue lines on the maps 152

Figure S2- 15: STXM compositional analysis of the chlorinated blend

(PBDB-T: CPDT-4Cl) with 2% CN. Images were taken a small molecule resonant energy (284.8 eV) and a non-resonant energy for both the small molecule and polymer (320 eV). Composition analysis was performed to extract compositional and thickness maps (shown in the middle). Then 1D profiles of thickness and composition (presented on the right side) were extracted from those maps across different domains as indicated by the red and blue lines on the maps..... 153

Figure S2- 16: 1D Lorentz-corrected scattering profiles of the fluorinated blends (PBDB-T: CPDT-4F) where $I \cdot Q^2$ vs Q (top) and anisotropy vs Q (bottom). The anisotropy is calculated as the difference between scattering in the vertical direction and horizontal direction over their sum. RSoXS was conducted at different X-ray energies as indicated in the graph legends. 154

Figure S2- 17: 1D Lorentz-corrected scattering profiles of the chlorinated blends (PBDB-T: CPDT-4Cl), where $I \cdot Q^2$ vs Q (top) and anisotropy vs Q (bottom). The anisotropy is calculated as the difference between scattering in the vertical direction and horizontal direction over their sum. RSoXS was conducted at different X-ray energies as indicated in the graph legends. 155

Figure S2- 18: Shown (top) are peak fitting of the scattering profiles of the chlorinated blends (PBDB-T: CPDT-4Cl) to calculate the component scattering intensity (CSI) of the primary peaks and secondary peaks (the secondary peaks emerge with solvent additive CN). Where data (red), fits (black), and fit residuals (gray). The results suggest that the dominate scattering feature that contribute to the total scattering intensity (TSI) is the one at high Q , i.e., CSI of the primary feature. Thus, CSI of the primary feature follows a similar trend as TSI of the entire scattering profiles (see red and blue traces in the bottom right graph). Whereas the CSI of the secondary features is negligible. This RSoXS data was taken at X-ray energy of 285.2 eV. 156

Figure S2- 19: Summary of the 1D Lorentz-corrected scattering data and peak fitting analysis of the fluorinated blends (left) and chlorinated blends (right): where $I \cdot Q^2$ vs Q (top), anisotropy vs Q (middle), and peak fitting results of peak positions and characteristic lengths (bottom). The anisotropy is calculated as the difference between scattering intensities in the vertical direction and horizontal direction over their sum. RSoXS was acquired at an X-ray energy of 285.2 eV. The onset L_c values are for the best performing devices, those are the blends with 1% CN. 157

Figure S2- 20: AFM height scans of the fluorinated blends (PBDB-T: CPDT-4F) with different amount of solvent additive (0, 0.5, 1, and 2 % CN from left to right, respectively). Scale bars of 2 μm 158

Figure S2- 21: AFM height scans of the Chlorinated blends (PBDB-T: CPDT-4Cl) with

different amount of solvent additive (0, 0.5, 1, and 2 % CN from left to right, respectively).... 158

Figure S2- 22: AFM height scans for pure materials; processed from CB without solvent additive (left) and with 1% CN (right). Scale bars of 500 nm. 159

Figure S2- 23: Visible optical microscope images were obtained via IA Nikon Eclipse LV100 at 10X magnification. The small molecule domains are so large due to the dramatic phase segregation in both fluorinated and chlorinated blends with 2% CN additive. 160

Figure S2- 24: SEM scans of the fluorinated blend (PBDB-T: CPDT-4F) with 2% CN additive. SEM surface scans (left and center) and a SEM cross-section (right)..... 161

Figure S2- 25: SEM scans of the chlorinated blend (PBDB-T: CPDT-4Cl) with 2% CN additive. SEM surface scans (top). The bottom left is a zoomed in SEM surface scan on a bright mountain-like region as indicated with the red square. A SEM cross-section scan shown on the bottom right. 161

Figure S2- 26: TEM bright-field scans of the fluorinated blends (PBDB-T: CPDT-4F) with different amount of solvent additive. Top from left to right: 0, 0.5, 1, and 2 % CN, respectively. The bottom images are zoomed out and in scans of the blend with 2 % CN on different regions “domains” as indicated with the red squares. 162

Figure S2- 27: TEM bright-field scans of the chlorinated blends (PBDB-T: CPDT-4Cl) with different amount of solvent additive. Top from left to right: 0, 0.5, 1, and 2 % CN, respectively. The bottom images are zoomed out and in scans of the blend with 2 % CN on different regions “domains” as indicated with the red squares. 163

Figure S2- 28: TEM bright-field scans of pure materials: without solvent additive (left) and with 1% CN (right). 164

Figure S2- 29: Visible light microscope (VLM) images of PM6:Y6 blends processed from chloroform with different concentrations of CN [vol.%]. a-e) 0, 0.5, 1, 1.5, and 2 vol. % CN, respectively. Scale bar of 10 μm 165

Figure S3- 1: J-V results to compare 145 nm (~ 45 ohms/sq) vs. 185 nm (~15 ohms/sq). Also, J-V curves of PM6:Y6 active layers on the different ITO substrates are plotted here for comparing. 167

Figure S3- 2: UV-VIS Spectra of films processed with different concentrations of solvent additive PN. a) Pure PM6 films. b) PM6:Y6 blends. c) Pure Y6 films 168

Figure S3- 3: UV-VIS spectra of the different layers used in the examined OSCs: Glass, ITO, PEDOT: PSS, and PDINO.	169
Figure S3- 4: Optical constants (k and n) of glass, ITO, PDINO, Ag, and PEDOT:PSS.....	170
Figure S3- 5: Optical constants (n and k) of a pure PM6 film, a pure Y6 film, and blends of M6:Y6. The k profiles of the blends were converted from the UV-VIS absorbance of the blends and compared to the literature. n is measured from VASE. The film thicknesses of the blends are about 92 nm.	171
Figure S3- 6: Transfer matrix modeling results. a) Fraction of light absorbed or reflected by all device layers. b) Fraction of absorbed light of PM6:Y6 active layers with different amounts of PN.....	172
Figure S3- 7: The yellow curve is the photon irradiance of the used solar simulator to test the investigated OSCs. The blue, red and blue curves show the photon irradiance scaled to the fraction of absorbed light by the PM6:Y6 blends with 0, 0.5 and 2% PN.....	173
Figure S3- 8: Photoluminescence spectra of pure PM6, pure Y6, and blend PM6:Y6 films with different amounts of solvent additive (PN).....	175
Figure S3- 9: AFM height scans of pure films with different amounts of PN. a-c) For pure PM films with 0%, 0.5%, and 2% PN, respectively. d-f) For pureY6 films of Y6 with 0%, 0.5%, and 2% PN, respectively.....	176
Figure S3- 10: a-c) AFM height scans of PM6:Y6 blends with 0%, 0.5%, and 2% PN, respectively. d-f) Phase scans of the blends with 0%, 0.5%, and 2% PN, respectively.	176
Figure S3- 11: a) NEXAFS spectra of neat films of PM6 and Y6. The π^* resonant energy of Y6 is about 285.15 eV. The π^* resonant energy of PM6 is about 285.15 eV. b) Contrast functions of materials-vacuum and material-material. The green arrow points are X-ray energy of 284.5 eV which was used to conduct the RSoXS measurement.	177
Figure S3- 12: 2D GIWAXS scans of pure PM6 films (a-c), pure Y6 films (d-f) and PM6:Y6 blends (g-i) with different amounts of PN as indicated on each scan.	178
Figure S3- 13: In plane (IP) and out of plane (OoP) 1D GIWAXS profiles of pure PM6 films (a and b), PM6:Y6 films (c and d), and pure Y6 films (e and f). The films were processed with different amounts of PN as indicated in the figure legends. The diffraction patterns of pure PM6 and Y6 films were used to peak assign those of the blends.	179

Figure S3- 14: Pole figures of the pi-pi stacking for: a) PM6 films, (b) Y6 films, and (c) PM6:Y6 blends. The films were processed with different amounts of PN as indicated in the figure legends. d) The relative degree of crystallinity (rDoC) of pi-pi stacking in pure and blend films. 180

Figure S3- 15: A multipeak fitting (MPF) example of fitting the pi-pi stacking of PM6 and Y6 in the out of plane direction in the PM6:Y6 blend without PN. Similar fitting method was used to extract peak positions and areas which then used to calculate d-spacings and crystal coherence length (CCL) values of peaks of interest. CCL were calculated using Scherrer analysis. Where $CCL \sim 2 \cdot \pi / FWHM$ 181

Figure S3- 16: a) 1D GIWAXS profiles of PM6:Y6 blends with 0, 0.2, 0.5, 2, and 5 % PN additive. a) GIWAXS intensity profiles in the OoP direction. b) Profiles in the IP direction. c) CCL values of the IP pi-pi (010) stacking. 183

CHAPTER 1: INTRODUCTION

Since the 2000 Nobel Prize in Chemistry was awarded to Heeger, MacDiarmid and Shirakawa for their work that started in 1970s with the discovery of semiconducting polymers, organic semiconductors have rapidly developed.¹ The tunable properties of organic semiconductors have opened the door for ongoing developments of materials for many applications of organic electronics and photonics. That includes organic light emitting diodes (OLEDs),² organic thin film transistors (OTFTs),³ organic bioelectronics,⁴ and organic solar cells (OSCs).⁵

In the last three decades, semiconducting organic materials (polymers and small molecules) have been targeted for photoelectronic applications such as OSCs due to their tunable properties, mechanical flexibility and low cost.⁶⁻⁸ Vast varieties of organic polymers and small molecules have been synthesized and devolved for OSC applications.⁹⁻¹¹ Power conversion efficiency (PCE) of OSCs is continuously rising, with a record at 20%.^{12,13} Ink-printed OSCs with bulk-heterojunction (BHJ) active layers, unlike p-n bilayer architecture, allows for more D-A interfaces which are beneficial for photo-electric processes such as charge separation. The 3D BHJ morphologies are known for governing the overall OSC device performance. In general, there are no absolute guidelines for optimal morphologies due to their 3D complexity, so they are instead system type-dependent.^{14,15}

OSCs utilize semiconducting organic polymers and molecules to convert sun light into electricity by means of the photovoltaic effect.⁷ First successful effort of fabricating a two-layer “bilayer” OSC by Tang (in 1986) resulted in about 1% PCE.¹⁶ Rapid development of conjugated polymers and small molecules in the last three decades has continuously increased PCE.

Significantly, the device efficiency of OSCs with BHJ architecture (Figure 1- 1 c) is approaching 20%.^{12,13,17,18} The official PCE record is > 18% for BHJ ink-printed OSCs.¹⁹ However, there are significant barriers facing lab-to-fab transition of novel organic systems. For example, film dimensions (e.g. too thin layers) and processing strategies (e.g. additives) are standard practices to optimize device performance, but are incompatible with large-scale productions.^{14,20-22} Ongoing research endeavors of exploring organic material candidates and their compatibility with scalable film-deposition methods often consider film nanostructures and their impacts on device property as a selection criteria.²¹⁻²³ Although that filters out many of the novel OSC systems that are industrially viable, the feedback often is insightful. It can guide research in the fields of material engineering, molecular design, and device processing. Hopefully, those collective research efforts will overcome such challenges to fully realize the commercialization of OSCs then soon after, the world would reap the benefits of these promising renewable energy technologies.

Printed mixture ink of donor and acceptor (D-A) into a single layer “BHJ” results in more D-A interfaces than a bilayer, which is beneficial for charge photogeneration processes. However, bi-continuous 3D structures are required for efficient charge extraction (Figure 1- 1c). Although BHJ morphologies often govern and correlate with device performance, optimum nanostructures are rather system dependent.^{14,21,24-26} The 3D morphological aspects, such as domain size, are important for charge separation. Domain purity and continuity are critical aspects for reducing charge recombination and aiding extraction. Domain crystallinity and orientation often impact charge transport. D-A interfacial morphologies, however, are often difficult to probe in BHJ blends and hard to correlate to device properties directly.^{27,28} In this work, we thoroughly investigate device performance and nanostructures for a variety of OSC

systems and then correlate their structures and properties in an effort of exploring their industrial viability. The examined systems were selectively chosen either for the uniqueness of their device properties,^{29–31} or novelty of the materials,^{32–35}. Details are provided in the research studies below.

There are a few remaining challenges facing the full potential of transferring efficient OSCs from lab-scale fabrication to industrial-scale often related to achieving optimal and stable active-layer morphologies.^{20,36} One of the challenges facing the industrialization of OSCs at a large scale is the difficulty of controlling and processing thin active layers.²⁰ Most large-scale fabrication methods, e.g., roll-to-roll printing, can only reproducibly deposit pin-hole-free films greater than 400 nm.³⁷ Additionally, most of the state-of-the-art OSCs with non-fullerene acceptors (NFAs) require processing additives to optimize active-layer morphological aspects such as crystallinity and phase separation. That often leads to better charge generation, recombination, and extraction processes.^{14,24,38,25,39} However, the amount of additives has to very precise to avoid undesired formation of morphologies making this process more complex and challenging when processing on industrial scale. Also, the overall stability of devices processed with additives remains questionable.¹⁴ Overall, the strong phase separation effect occurring in high performance polymer-NFA OSCs has not been studied in detail.

This dissertation aims to explore property-structure relationships in selective OSC systems as an effort of exploring or addressing the challenges mentioned above facing full-potential of OSC indoctrination. To probe nanostructures of the investigated OSCs in this work, a suite of X-ray techniques (spectroscopy, microscopy, scattering, and diffraction) was utilized in conjunction with electron-based scanning techniques (details provided in the experimental section). Device physics is either conducted by collaborators who synthesized and fabricated the

investigated OSCs, or commercial materials were obtained, processed, and tested via testing capabilities at our laboratory, Washington State University.

One investigated system, polymer:fullerene OSCs, has a unique nanostructure. It was of interest to examine and understand why it was possible for this system to maintain relatively high efficiency even with a BHJ active-layer thickness of 1 μm . The discovery pertaining to the impacts of D-A interfacial morphologies on device performance is detailed in Chapter 3. The findings showcase a model system that can be targeted to achieve efficient OSCs with film thickness suitable for large-scale fabrication.

The second study examines the impacts of a solvent processing additive on morphology and device performance of two NFA OSCs systems, detailed in chapter 4. The findings show extreme sensitivity to the additive concentration and suggest that solvent-additive processing of similar NFA OSCs may not be feasible on a large-scale. Therefore, alternative approaches, whether on the molecular design side or fabrication side, might be necessary for successfully industrial fabrication of efficient NFA OSCs.

In the third study, we substitute the commonly used solvent additive—which has been used in our second study—with a non-halogen (green) solvent phenyl naphthalene (PN) to optimize device performance in one of the records OSC systems. We utilized a holistic analysis of charge generation losses and a thorough morphology characterization to probe and examine structure-property relationships in this system as a function of the additive concentration, as detailed in chapter 5.

CHAPTER 2: METHODOLOGY

In this work, we leverage a unique device testing method, known as time-delayed collection field (TDCF),^{27,40} to explore the quantum efficiencies and charge losses of each step of the charge generation process in OSCs. Additional device-physics testing techniques, such as UV-VIS and photoluminescence spectroscopies, are utilized as mentioned throughout the dissertation chapters with details provided in the experimental sections or later in the appendices.

On the morphology side, a wide variety of techniques—e.g., neutron, optical, X-ray, or electron-based methods—have been employed to characterize nanostructures of OSC films.^{21,41–43} In this work, standard electron and optical-based microscopies are utilized with advanced synchrotron X-ray based techniques to achieve multimodal analysis of the investigated systems. We specifically utilize advanced synchrotron X-ray techniques such as resonant soft X-ray scattering and spectro-microscopy due to their unique sensitivity to molecular composition, bonding, and orientation in organic materials.^{44–48} Additional techniques such as transmission electron microscopy (TEM) are used to probe the lateral nanostructures, such domain shape and size. Scanning electron microscopy (SEM) is also utilized to probe the film topology and cross-sections. Also, atomic force microscopy (AFM) is used to examine topology and film roughness.

Device performance and optoelectronic testing methods

Device performance of OSCs is characterized via an I-V measurement (Figure 1- 1) under solar simulated sunlight with air mass of (AM 1.5) global spectrum, and incidental power of $P_{in} = 1000 \left[\frac{W}{m^2} \right]$, calibrated using a photodiode. As shown in the I-V experiment setup in Figure 1- 1b, a solar simulated irradiance is shed onto an OSC device then an I-V curve is collected via a source meter. Next, the current (I) is converted into a current density (J) by

dividing by the device area (4 mm^2), see Figure 1- 1d. J_{sc} denotes the short-circuit current density, i.e., when no voltage is applied across a cell. V_{oc} indicates open-circuit voltage, which is the voltage output of a cell when there is no current going through it. The maximum power point (M_{pp}) is defined as a point on the J-V curve where the product of J and V at the point results in the highest power output ($M_{pp} = J_m \times V_m$). Another device parameter is fill factor (FF), which is calculated as $FF = (J_m \times V_m)/(J_{sc} \times V_{oc})$. In other words, it is the ratio of the blue area in Figure 1- 1b to the red area. Now, the power conversion efficiency (PCE) of a solar

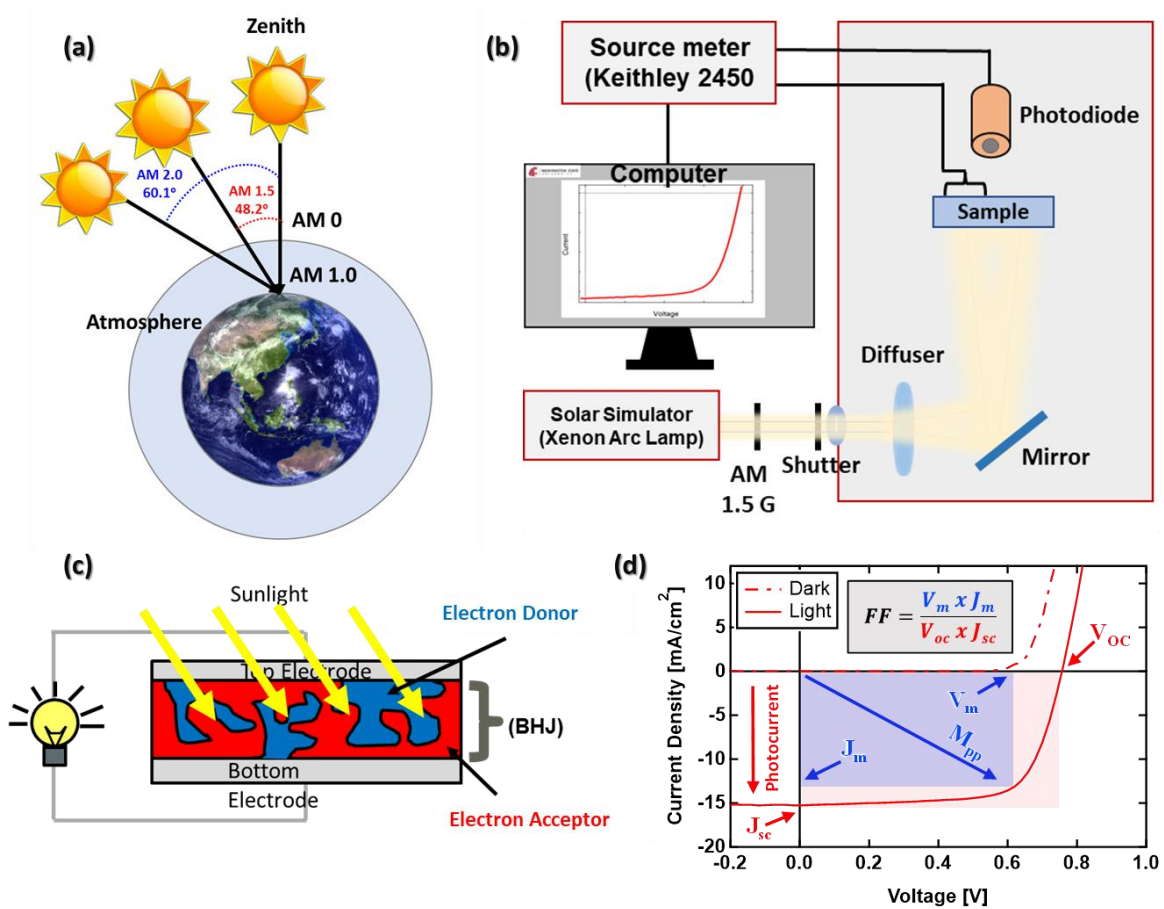


Figure 1- 1: a) Global tilt corrected for as AM 1.5 as the standard solar irradiance for testing solar cells. b) I-V experiment setup. c) depiction of a BHJ architecture. d) A J-V curve example for an OSC showing the important parameters (J_{sc} , V_{oc} , J_m , V_m , and M_{pp}).

cell—also known as η_{power} —is determined as the ratio of power output to power input and calculated as $\eta_{power}[\%] = \frac{P_{out}}{P_{in}} = \frac{J_m \times V_m}{P_{in}} = \frac{FF \times J_{sc} \times V_{OC}}{P_{in}}$. This is the overall device efficiency of converting sunlight into power. However, as detailed below, absorbed photons can be efficiently converted and extracted as electrons or lost at any step through the photocurrent process.

Figure 1- 2 is a scheme presenting the photoelectric charge generation processes in OSCs. First, when a photon is absorbed by electron-donating materials, a photogenerated exciton—a strongly bonded electron-hole pair—is created. OSC absorption can be measured via UV-VIS spectroscopy combined with transfer matrix calculation to simulate reflection and transmission.⁴⁹ Next, the exciton can make it to a donor-acceptor interface and transfer the electrons to an acceptor molecule while still strongly coulombically bonding to it. This is known as the charge transfer (CT) state. Otherwise, the exciton can be lost due to exciton recombination, which can

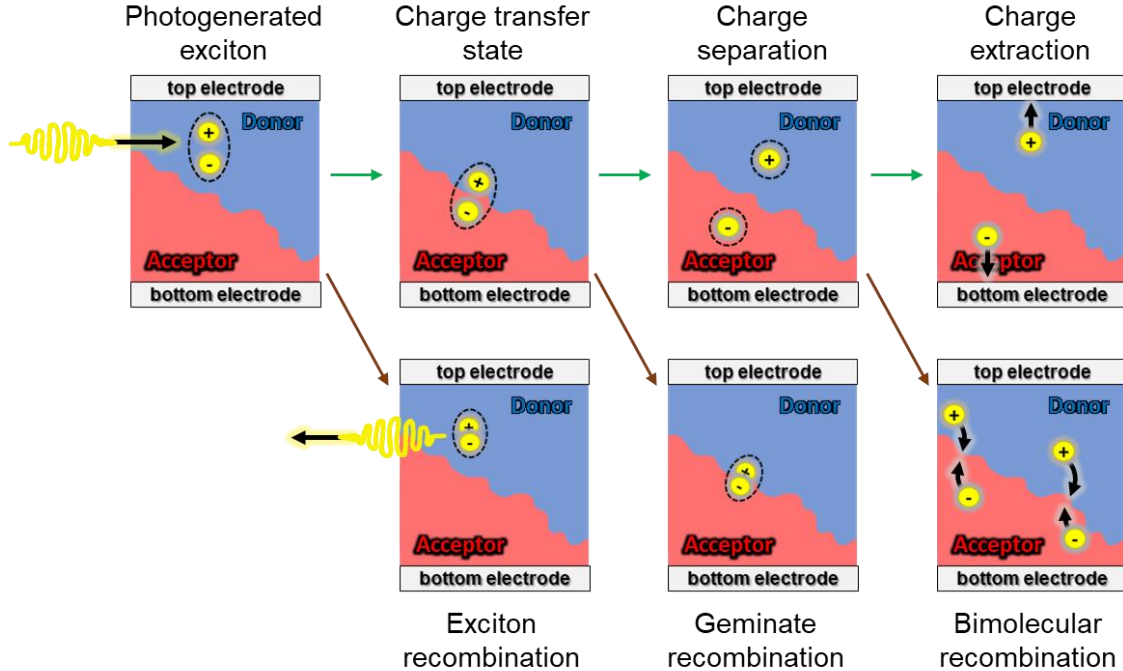


Figure 1- 2: A schematic of the charge generation processes in an OSC device.

be measured via photoluminescence quenching (PLQ) spectroscopy. The PLQ experiment measures relative reduction in photoluminescence (PL) in a blended film compared to a pure film. At the CT state, the pair of charges could split into free charges, known as the charge separation (CS) state or could recombine through a process called geminate recombination, where the same pair of charges decay. After charge separation, free charges could successfully make out of the device “extracted charges” or encounter free opposite charges then recombine via bimolecular recombination (BMR). The geminate and bimolecular recombination usually takes place on a fast timescale and can be challenging to untangle. However, the time delayed collection field (TDCF) technique is a unique electrical probe that is helpful in separating and quantifying those types of recombination losses.^{27,40}

The efficiencies for each of the charge generation processes can be quantified as follows. The absorption efficiency (η_{abs}) = J_{abs}/J_{max} , where J_{abs} is the current density of absorbed photons by an OSC sample and J_{max} is current density of the total incident photons within the sample’s absorbance spectrum range. The CT state efficiency can be quantified via PLQ. For a system with 100% CT state efficiency, the charge separation efficiency (η_{sep}) = J_{gen}/J_{abs} , where J_{gen} is the current density of extracted charges via TDCF (as described below). Finally, charge extraction efficiency (η_{ext}) = J_{ph}/J_{gen} , where J_{ph} is the photocurrent density.

A TDCF measurement is conducted by illuminating a device with a laser pulse (see Figure 1- 3 for the experimental setup) while holding the device at a pre-bias voltage (V_{pre}) to simulate operation conditions (e.g., V_{mpp}), see Figure 1- 3b. After a delay time (5 ns) to make sure only CS states left, an over pulse voltage is applied for a very short time to bring the actual voltage across the device up to the collecting voltage ($V_{coll} = -3$ V) to sweep out and count the

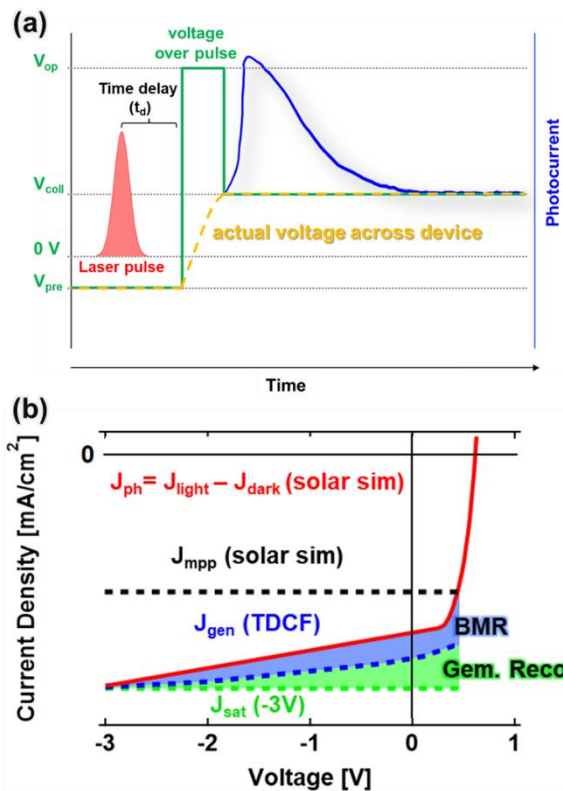
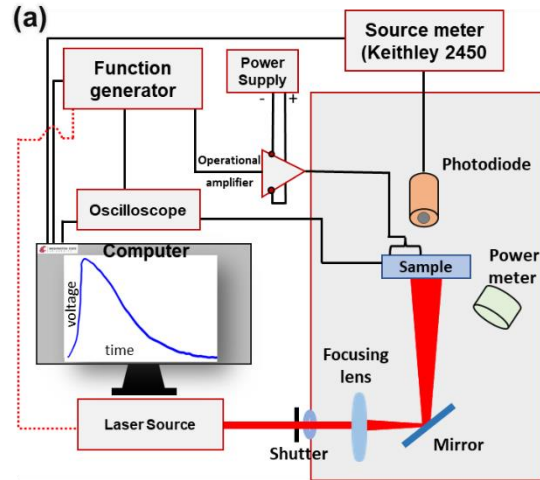


Figure 1- 3:a) A schematic of the TDCF experimental setup. b) a schematic of the TDCF timeline.c) J-V curve with a photocurrent (J_{ph}) trace of a device under 1 Sun (red) and a generated current via TDCF (blue) scaled to J_{ph} at -3 V.

generated charges. It is worth noting that the purpose of the over pulse voltage is applied only to overcome any delay due to the circuit RC constant. The actual voltage across the OSC active layer is not higher than V_{coll} . Next, generated charges by the laser pulse are measured via an

oscilloscope by integrating the photocurrent transient. Another important aspect of TDCF is that V_{pre} can be varied to examine field dependence of charge recombination on the operating field in the cell.

Next, the TDCF collected charges can be scaled to photocurrent at a saturation bias (-3 V) which is high enough bias to aid in sweeping out all generated charges, see Figure 1- 3c. The photocurrent density (J_{ph}) at -3 V is known as saturation photocurrent density (J_{sat}) because J_{ph} does not increase at high reverse bias. The generated photocurrent via TDCF is referred to as J_{gen} in Figure 1- 3c. At this point, charge recombination losses can be quantified. The differences between J_{sat} and J_{gen} (the green area) are due to geminate recombination losses that depend on the operation field. On the other hand, the differences between J_{gen} and J_{ph} (the blue area) are due to BMR losses. Most important V_{pre} is V_{mpp} where device is expected to operate. Other advanced techniques such as transient absorption spectroscopy (TAS) cannot probe recombination under these operational conditions.⁴⁰

Nanostructure probing techniques

Grazing incidence wide-angle X-ray scattering (GIWAXS)

GIWAXS, also known as X-ray diffraction (XRD), has been utilized to probe molecular ordering, crystallinity, and aggregation in organic thin films.^{21,41,50} Figure 1- 4 shows a GIWAXS setup with x-ray hitting a thin sample at an incidental grazing angle to probe thin-film structures. This incident angle, often between 0.1-0.2 for organic thin films, ensures that the scattering is coming from the whole film rather than the surface, which gives a better signal to noise ratio. Also, the experiment is usually conducted in an inert environment (helium or vacuum) to reduce scattering from air. As X-ray photons travel along the sample, scattering occurs depending on molecular structure and packing in the film. A two-dimensional detector is placed nearby the

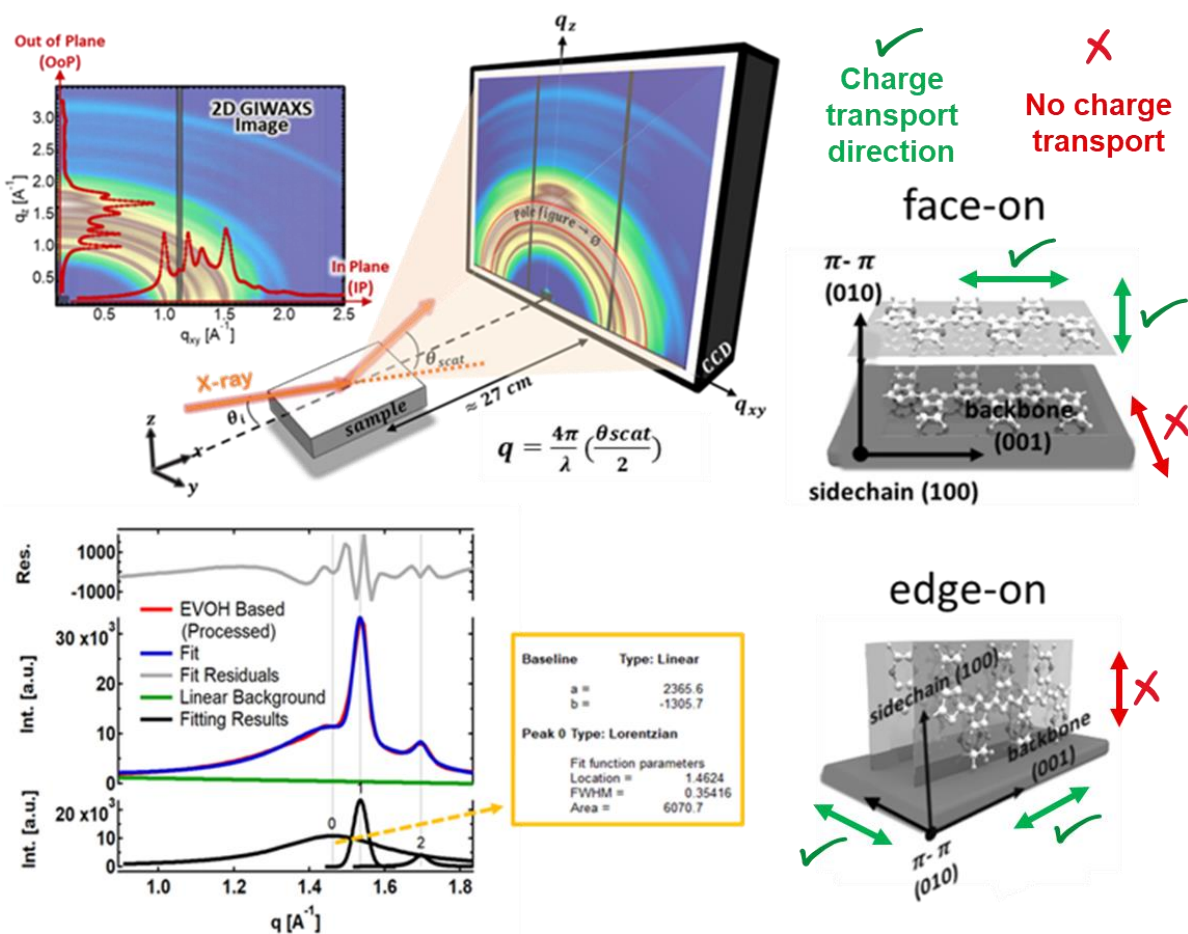


Figure 1- 4: Depiction of GIWAXS geometry and setup. X-ray with grazing incidence angle (θ_i) and scattering angle (θ_{scat}). A two-dimensional charge-coupled device (CCD) detector is used to record the scattering x-ray, with sample-to-detector distance about 27 cm. On the left side, an example of 2D GIWAXS images with IP and OoP lineouts examples (red). Bottom shows an example of peak fitting with the fitting parameters results of peak '0' in the orange box. Cartoons on the right-side show two examples of molecular packing and orientations with respect to the substrate.

sample to allow for capturing scattered photons even at a high scattering angle (θ_{scat}) or scattering vector q . The scattering vector is proportional to the scattering angle, $q = (4\pi/\lambda) \sin(\theta_{scat}/2)$ where λ is the x-ray wavelength. Note that Bragg's diffraction angle equals half the scattering angle in this geometry. Subsequently, acquired 2D GIWAXS data by the detector can be reduced into 1D profiles or lineouts at any desirable azimuthal angle or sector. For example, the 2D GIWAXS image on the top-left side of Figure 1- 4 was used to extract 1D profiles

horizontally, known as in-plane (IP) sector, and vertically, known as out of plane (OoP). Those 1D profiles are then plotted on top of the 2D GIWAXS image in red color to visually guide the eye on how the intensity changes in each sector as q increases.

Further analysis can be done to examine the structure of interest. For example, the spacing between scatterers in real space, known as d-spacing, can be calculated as $d = \frac{2\pi}{q^*}$, where q^* is defined as the peak position. To accurately extract peak positions, peak fitting is used as in the example in Figure 1- 4. Other fitting parameters such as peak intensity, can be used to examine the population of a scattering group/structure. Peak intensity can also be plotted vs the angle of detector, known as pole figure analysis (see Figure 1- 4), to examine the orientation distribution of crystal populations with respect to substrate. That can give insights into material texture and the relative degree of crystallinity across a set of samples. Additionally, FWHM can be inserted into Scherrer's equation to quantify the stacking coherence "quality or size" of specific diffracting layers, called crystal coherence length (CCL) or ($D_{\text{coh}} \sim 2\pi K / \text{FWHM}$) where K is a constant—typically ~ 0.9 for semicrystalline materials.⁵¹ The orientation of molecular packing in OSC films is crucial to device properties such as charge transport. One important packing type of organic molecules is π - π staking (shown in Figure 1- 4) where molecular charge hopping (transport) occurs. The orientation of the packing, face-on vs. edge-on with respect to the substrate, is important because charges transport this way. For example, in many OSC systems, face-on π - π orientation is favorable to charge transport and D-A interfacial morphologies. Primary orientation can be ascertained by comparing the IP vs. OoP scattering profiles.

Near-Edge X-Ray Absorption Fine-Structure (NEXAFS) Spectroscopy

NEXAFS spectroscopy near the carbon K-edge absorption is suitable for characterizing organic materials due to its sensitivity to different chemical bonds and moieties.⁴⁵ It is extremely powerful technique, especially when combined with soft X-ray microscopy or scattering at C K-edge. The multimodality of those techniques enables spaciochemical analysis or organic films and makes the complex 3D BHJ structures more accessible,⁵⁻⁹ more details will follow later in the X-ray microscopy and scattering sections. Now, different chemical bonds and moieties usually have unique spectral fingerprints manifested in their NEXAFS spectra near the carbon 1s K-edge. Those fingerprints—known as resonant absorption features—are due to electronic transitions from 1s state to unoccupied molecular states/orbitals, which are unique to specific molecular bonds (example shown in Figure 1- 5b). This allows for chemical mapping of different materials when mixed in a BHJ manner. Additionally, the absorption intensity is sensitive to the orientation of the transition of dipole moment (TDM) relative to the electric field (\vec{E}) of the

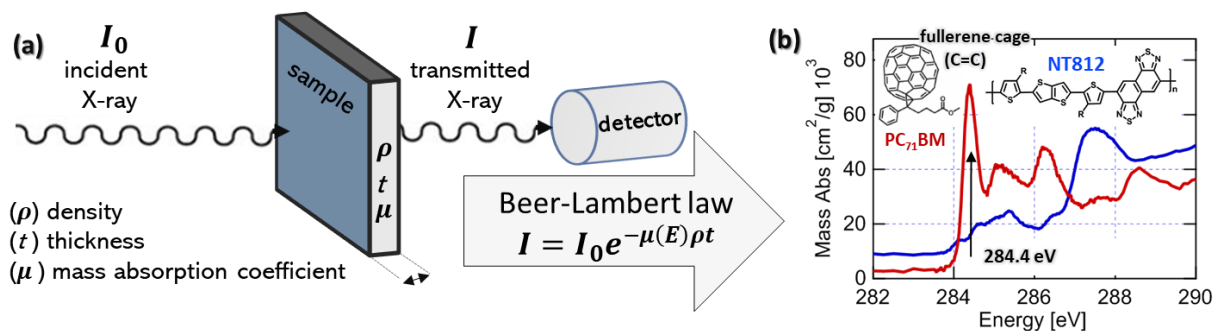


Figure 1- 5: a). A transmission setup of NEXAFS spectroscopy. b) Spectra examples of a polymer (NT812) and a fullerene (PC71BM) calculated via Beer-Lambert equation and scaled to the bare atom absorbance.

incident X-ray.⁴⁵ The absorption intensity depends on the TDM- \vec{E} alignment (i.e. Malus' Law), with most absorption at perfect alignment and zero absorption if not aligned. This phenomenon has been exploited to probe orientations and alignments in organic thin films. Additionally, a

NEXAFS spectrum of an organic BHJ blend is usually a linear combination of NEXAFS spectra of its pure components because of van der Waals interactions rather than chemical bonds in blends. That allows for composition analysis of blends.⁴⁵

NEXAFS can be conducted in a transmission mode (Figure 1- 5a) where X-ray transmits through a sample and then the transmitted signal recorded by a photodiode detector. From Beer-Lambert law, a sample's mass absorption coefficient $\mu(E)$ can be calculated from $I = I_0 e^{-\mu\rho t}$. I_0 is the intensity of the direct X-ray beam, I or I_t is the intensity of the transmitted X-ray, ρ and t are film density and thickness, respectively. μ can be easily converted to another physical parameter, optical density (OD), as follows $OD = \mu\rho t = \ln(I_0/I)$. More details will be provided in the following section.

Scanning transmission X-ray microscopy (STXM) and NEXAFS

STXM, as a technique has a similar operating concept as TEM but using X-rays instead electrons, with tunable photon energy.^{43,52} The soft X-ray energy range (~ 100 - 2500 eV) makes it suitable for probing organic materials since they compose mostly of elements such C, N, and O. Absorbance edges of those materials fall in this wide energy range. Therefore, X-ray spectro-microscopy—a combinatory of STXM and NEXAFS—has been successfully utilized to probe OSCs due to their sensitivity to different elements and chemical bonds.^{43,45,46} With spatial resolution around 30 nm,^{43,53} quantitative analyses of domain composition, purity, and size of D-A nanodomains with BHJ OSCs have been developed.^{45,46}

Figure 1- 6a shows a STXM setup where synchrotron X-ray is focused on a thin film of interest then transmitted photons are collected by a detector. Raster scanning of the sample is implemented to acquire 2D lateral images as shown in Figure 1- 6c and f. A compositional analysis of an OSC blend can be achieved by acquiring a 'stack' of STXM images at carefully

selected energies based on the NEXAFS spectra of its pure D and A components. For the example shown in Figure 1- 6, E_1 matches the resonant energy of the fullerene component, meaning it absorbs more than the other component (NT812 polymer in this example), i.e., the fullerene will have higher OD than the polymer. E_2 , on the other hand, is chosen to be at a non-resonant energy for simplicity where both components have similar mass absorbance coefficients $\mu(E)$. Knowing the I_0 at each energy, enables converting the STXM scans from photon counts to OD which is energy dependent.⁴⁶

$$OD(E) = \ln\left(\frac{I_0}{I_t}\right) = \sum_i \mu_i(E) \rho_i t_i = \frac{1}{A} \sum_i \mu_i(E) m_i$$

Where ρ_i , t_i , and m_i are the mass density, thickness, and mass of each component in every STXM scanned pixel. E is the X-ray energy and A is the illuminated area, which is constant. For the two-component BHJ OSC film in this example, the OD (E) becomes.

$$OD(E) = \frac{1}{A} (\mu_a(E) m_a + \mu_b(E) m_b)$$

Now, $\mu_b(E)$ and $\mu_a(E)$ are known from the NEXAFS spectra in Figure 1- 6b. Also, $OD(E_1)$ and $OD(E_2)$ are acquired from STXM on the same spot of the investigated film (Figure 1- 6c and f). Thus, the mass of component a can be calculated in each pixel as follows.

$$m_a = A \frac{\mu_b(E_2) OD(E_1) - \mu_b(E_1) OD(E_2)}{\mu_a(E_1)\mu_b(E_2) - \mu_a(E_2)\mu_b(E_1)}$$

Similarly, m_b can be calculated from all the knowns at those two energies. Finally, the mass concentration of component a, for example, at each pixel is calculated as

$$m_a[\%] = \frac{m_a}{m_a + m_b} \times 100$$

Next, compositional maps (concentration maps) as well as thickness maps can be generated by following this procedure,⁴⁶ examples shown in Figure 1- 6d and e. Out of those maps 1D profiles can be extracted vs. the lateral distance at any region of interest of the investigated film (example shown in Figure 1- 6g).

Quantitative analysis beyond nominal resolution of microscope can be conducted to achieve absolute compositional mapping of OSC by deconvoluting the point spread function (PSF) of the X-ray beam from acquired STXM scans.^{24,53,54} This is extremely useful when

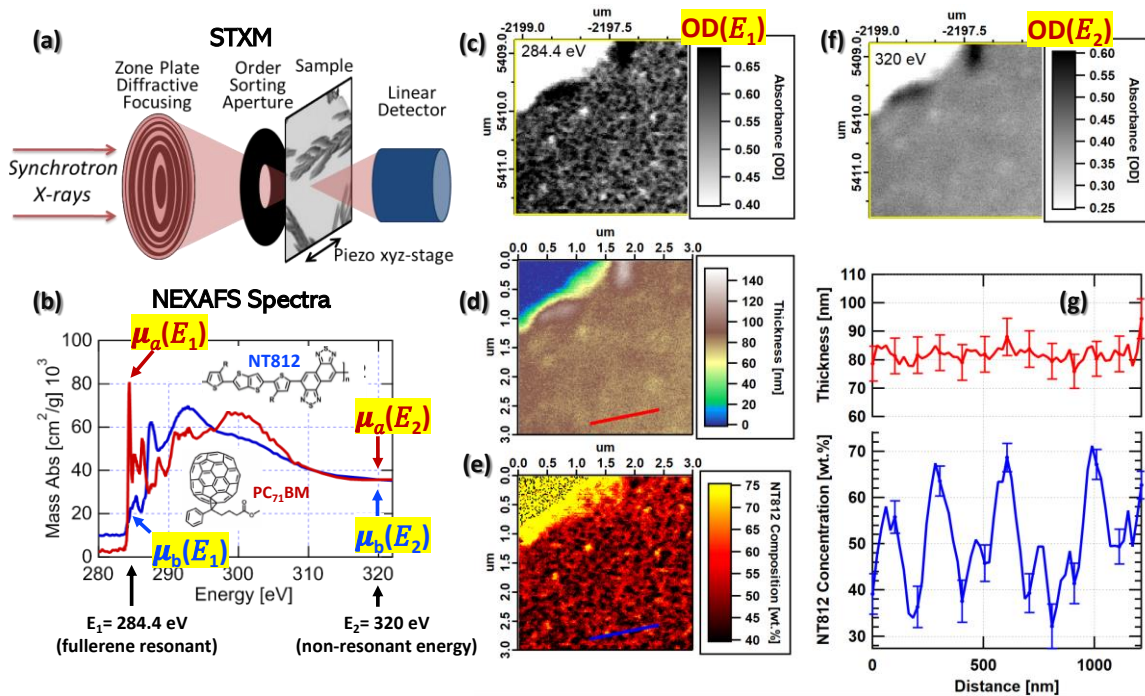


Figure 1- 6: a) STXM setup. b) NEXAFS spectra examples. STXM OD maps at 284.4 eV (c) and 320 eV (f) of a polymer:fullerene BHJ OSC film. Thickness and composition maps (d) and (e) as well as 1D profile examples (g).

features “domains” of a film are not big enough in size thus the PSF effect is significant (≤ 50 nm).

Resonant Soft X-Ray Scattering (RSoXS) and NEXAFS

RSoXS is a powerful techniques that combines small-angle scattering with NEXAFS spectroscopy.⁴⁴ This enables probing nano-to-meso structures in thin organic materials due its unique sensitivity chemical bonds and molecular orientation.^{21,41,44} Figure 1- 7a shows that incident X-rays pass through the sample and a CCD detector records scattered photons in all scattering angles (θ_{scat}) simultaneously. Like GIWAXS, scattering intensities are reduced into 1D profiles that are often plotted as a function of the scattering vector q (as shown in Figure 1- 7b). Although L_c (known as characteristic length) is calculated similarly to d-spacing in GIWAXS ($L_c = \frac{2\pi}{q^*}$), it rather defines domain spacing here if the scattering peak is well-defined as in the examples shown in Figure 1- 7b. The origin of domains in a BHJ blend (e.g. roughness vs. molecular domains) can be deduced from the energy dependence of scattering data by comparing to energy-dependency of differences in the index of refraction between materials (material contrast). The index of refraction for absorbing materials is complex and defined as $\tilde{n}(E) = 1 - \delta(E) + i\beta(E)$, where E is the X-ray energy, the imaginary part (beta) of the index of refraction is related to absorbance and can be calculated from NEXAFS measurements $\beta(E) = \frac{\lambda\rho m}{4\pi} \mu(E)$, and the real part (delta) can be calculated from (beta) via the Kramers-Kronig relations.⁵⁵

Because scattering comes from spatial fluctuations in n , the scattering intensity originates from the difference in the index between any two lateral regions or domains in a sample. Thus, the scattering intensity for a given pair of domains is proportional to $|\Delta\tilde{n}(E)|^2$ between the domains—known as contrast function (as polymer-fullerene example is shown as a black trace in Figure 1- 7c). In the red and blue traces, material-vacuum contrast is shown. Here, the contrast is

rather between materials and vacuum ($n=1$), therefore the observed contrast originates from film roughness or porosity. As the contrast function transitions into X-ray energies closer to the absorbance edge, above 280eV, the material contrast is enhanced relative to vacuum contrast and the scattering intensity begins to probe differences in the molecular composition of the domains in the sample. If dealing with a pure sample (i.e., only one component), then nonzero values of $|\Delta\tilde{n}(E)|^2$ originates from density or orientation fluctuations. However, at a material resonance, for example ~ 284 eV in Figure 1- 7c, the differences in index between the two molecules become much larger than the density fluctuations. That means of contrast in RSoXS originates

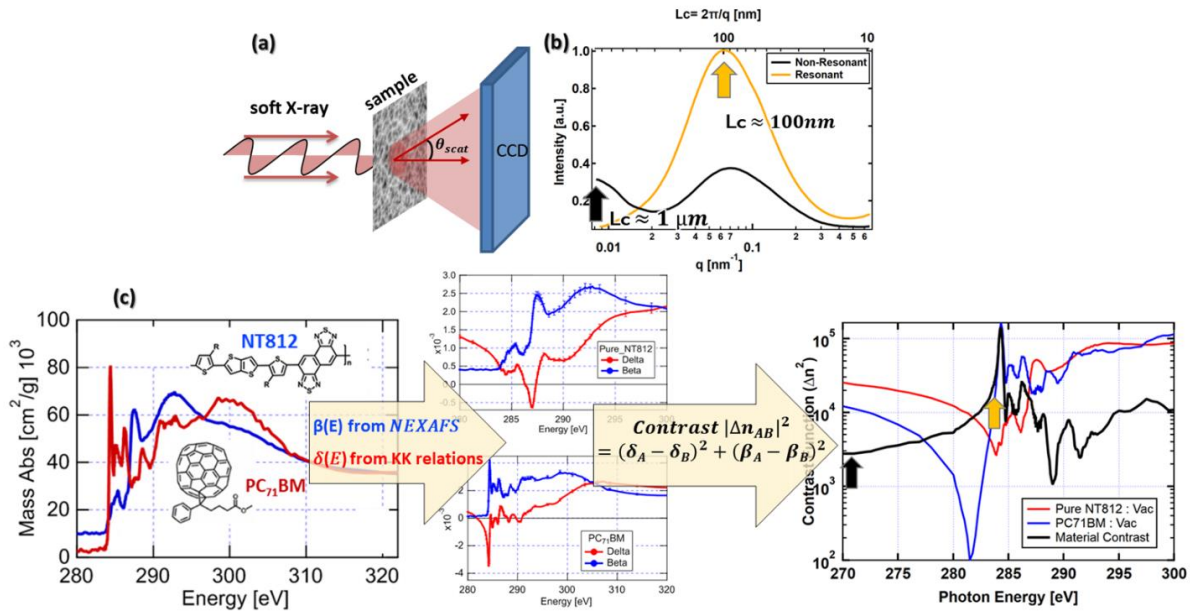


Figure 1- 7: a) Experimental setup of RSoXS. b) 1D reduced lineouts from 2D RSoXS images showing scattering intensity vs. q for a polymer:fullerene blend, at X-ray energy of 270eV (black) and 283.5 eV (orange). c) NEXAFS spectra of a polymer and fullerene \rightarrow real (delta) and imagery (beta) parts of their indices for refraction \rightarrow The material contrast between polymer-fullerene (black) as well as material-vacuum contrasts. Note that the polymer-fullerene contrast is maximized at around 284 eV.

from a large difference in the energy and orientation-dependent complex index of refraction.

Therefore, contrast functions can aid in interpreting the patterns in RSoXS 1D profiles. For the polymer:fullerene example in Figure 1- 7b, the 1 μm features scatter about twice as much at the

non-resonant energy than the resonant energy indicating that the pure material domains are responsible for this feature. On the other hand, the feature with $L_c \approx 30$ nm domain scatters several orders of magnitude stronger at resonant than non-resonant energy. Therefore, the non-resonant profile is probing primarily the roughness and porosity of the film, while the resonant lineout is probing the molecular domains.

Now—knowing that contrast functions determine scattering intensities—the process via which RSoXS probes orientation and composition can be described. The measured total scattering intensity (TSI) is a measure of the scattering power of a sample over all angles (reciprocal space) and allows quantification of the composition of a domain within the sample via its relation to the theoretical Porod Invariant Q under the assumption of two phases. The TSI can be calculated as⁵⁶:

$$TSI = \int I(q)q^2 dq = Q = V\Delta x_{12}\Delta n_{AB}^2\phi_1\phi_2$$

where $I(q)$ is the scattering intensity at a given q -value, V is the scattering volume, Δn_{AB} is the contrast between molecules A and B, and ϕ_i is the volume fraction of domain $i=1,2$. We now have a way to determine the relative domain purity through Δx_{12} in organic/polymeric films and have applied it in several recent studies.^{24,44} In addition to domain size and purity, polarized RSoXS enable investigation of molecular orientation and D-A interfacial morphologies.^{28,31} Prior knowledge of sample prep conditions (ϕ_1 and ϕ_2) and domain purity (Δx_{12}) and TSI via RSoXS have also allowed for quantifying BHJ D-A interfacial width and morphologies.^{24,27,31}

Now, all the above structural probes can be combined for multimodal characterization of OSC samples over different size scales. GIWAXS and UV-VIS absorbance spectroscopy can probe molecular ordering and crystallinity. STXM and RSoXS can probe domain size and purity.

Some common and general hypotheses to start with regarding how morphology governs power generation in OSCs are: 1) domain sizes should be reasonable (10s nm) for excitons to make it to donor-acceptor interfaces in order for CT state to happen. 2) crystalline and ordered domains can aid absorption as well as charge transport. 3) continuous 3D network of pure domains is required for free (separated) charges to travel to the electrodes. 4) high domain purity can aid charge extraction by reducing BMR losses. 5) Thick OSC active layers can have more complex 3D morphologies and thus charges have to travel for long distances to make to the electrodes. That increases the chances for BMR losses to happen thus additional structural properties might be required for successful charge generation in thick OSCs, e.g., bigger and purer domains compared to those of thin OSCs.

CHAPTER 3: EVIDENCE THAT SHARP INTERFACES SUPPRESS RECOMBINATION IN THICK ORGANIC SOLAR CELLS

Alqahtani, O.; Hosseini, S. M.; Ferron, T.; Murcia, V.; McAfee, T.; Vixie, K.; Huang, F.; Armin, A.; Shoaee, S.; Collins, B. A. “Evidence That Sharp Interfaces Suppress Recombination in Thick Organic Solar Cells.” *ACS Appl. Mater. Interfaces* **2021**, *13* (47), 56394–56403. <https://doi.org/10.1021/acsami.1c15570>.

Attributions:

O. Alqahtani conducted the nano-structure characterization, data analysis and wrote the first draft of the manuscript. S. M. Hosseini, S. Shoaee and A. Armin conducted the device fabrication and characterization of the examined solar cells. T. Ferron, V. Murcia, and T. McAfee helped with the data acquisition at the Advanced Light Source, Lawrence Berkeley National Laboratory. K. Vixie derived the co-area formula. F. Huang synthesized the polymer material used in this study as the electron donor. B. A. Collins provided funds and supervised this study.

Note: the supporting information of this manuscript is provided in APPENDIX A.

Abstract

Commercialization and scale-up of organic solar cells (OSCs) using industrial solution printing requires maintaining maximum performance at active-layer thicknesses >400 nm – a characteristic still not generally achieved in non-fullerene acceptor OSCs. NT812:PC71BM is a rare system whose performance increases up to these thicknesses due to highly suppressed charge recombination relative to the classic Langevin model. The suppression in this system, however, uniquely depends on device processing, pointing towards the role of nano-morphology. We investigate the morphological origins of this suppressed recombination by combining results from a suite of X-ray techniques. We are surprised to find that while all investigated devices are composed of pure, similarly aggregated nanodomains, Langevin reduction factors can still be tuned from ~ 2 to >1000 . This indicates that pure aggregated phases are insufficient for non-Langevin (reduced) recombination. Instead, we find that large well-ordered conduits and, in particular, sharp interfaces between domains appear to help to keep opposite charges separated and percolation pathways clear for enhanced charge collection in thick active layers. To our knowledge, this is the first quantitative study to isolate donor:acceptor interfacial width correlated to non-Langevin charge recombination. This new structure-property relationship will be key to successful commercialization of printed OSCs at scale.

Introduction

Organic solar cells (OSCs) with solution-printed active layers have attracted a great deal of attention due to their tunable properties, mechanical flexibility, and continuously rising power conversion efficiency (PCE) in the last two decades.^{12,13} The current PCE record for OSCs is about 18%.^{57,58} In bulk heterojunction (BHJ) OSCs, where electron donating and accepting materials are blended together in a common ink, PCE usually maximizes when the thickness of

the active layer is around 100 nm. As the BHJ thickness increases, light absorbance increases following an interference-induced oscillatory pattern, potentially resulting in higher current densities in the thicker junctions. However, charge recombination increases faster with increasing thickness scaling inversely with the square of the film thickness.⁵⁹ Consequently, in most polymer-based OSCs, the device performance rapidly decreases as the BHJ thickness increases beyond the first absorbance interference peak.^{30,60-62} One of the existing challenges facing the industrialization of OSCs at a large scale is the difficulty of controlling and processing thin active layers.²⁰ This is because most large-scale fabrication methods, e.g. roll-to-roll printing, can only reproducibly deposit pin-hole-free films greater than 400 nm.³⁷

The investigated system is amongst relatively few systems that maintain high efficiencies in the thick junction regime.^{20,63} The recently synthesized electron donating co-polymer, Naphtho[1,2-c:5,6-c']bis([1,2,5]-thiadiazole) based copolymer (NT812, Figure 2- 1a bottom), exhibits PCE>10% when fabricated into OSCs with phenyl-C71-butyric acid methyl ester (PC71BM) fullerene as the electron acceptor (Figure 2- 1a top).²⁹ The novelty of NT812 appeared when this system maintained high PCE even with thick BHJ active layers ~ 1µm. It was found that at optimal fabrication conditions, bimolecular recombination is significantly suppressed up to 800x below what is expected for the diffusive Langevin model (where charges' trajectories are random and depend on the charge carrier mobilities—for more details we refer the reader to our previous work,³⁰ or to original work of Langevin classical model⁶⁴). This non-Langevin behaviour leads to OSCs with less recombination losses, i.e. Shockley-type solar cells.³⁰ In fact, recombination is suppressed so much in this system that its performance increases rather than decreases with thickness up to 300 nm, making it one of the highest performing systems to exhibit such favourable behaviour.⁶⁵ Although non-fullerene acceptor (NFA) systems

dominate performance with thin active layers, work to reduce recombination in these systems has only just begun,⁶⁶ and to our knowledge no NFA systems have demonstrated such increased performance beyond the first interference maximum.

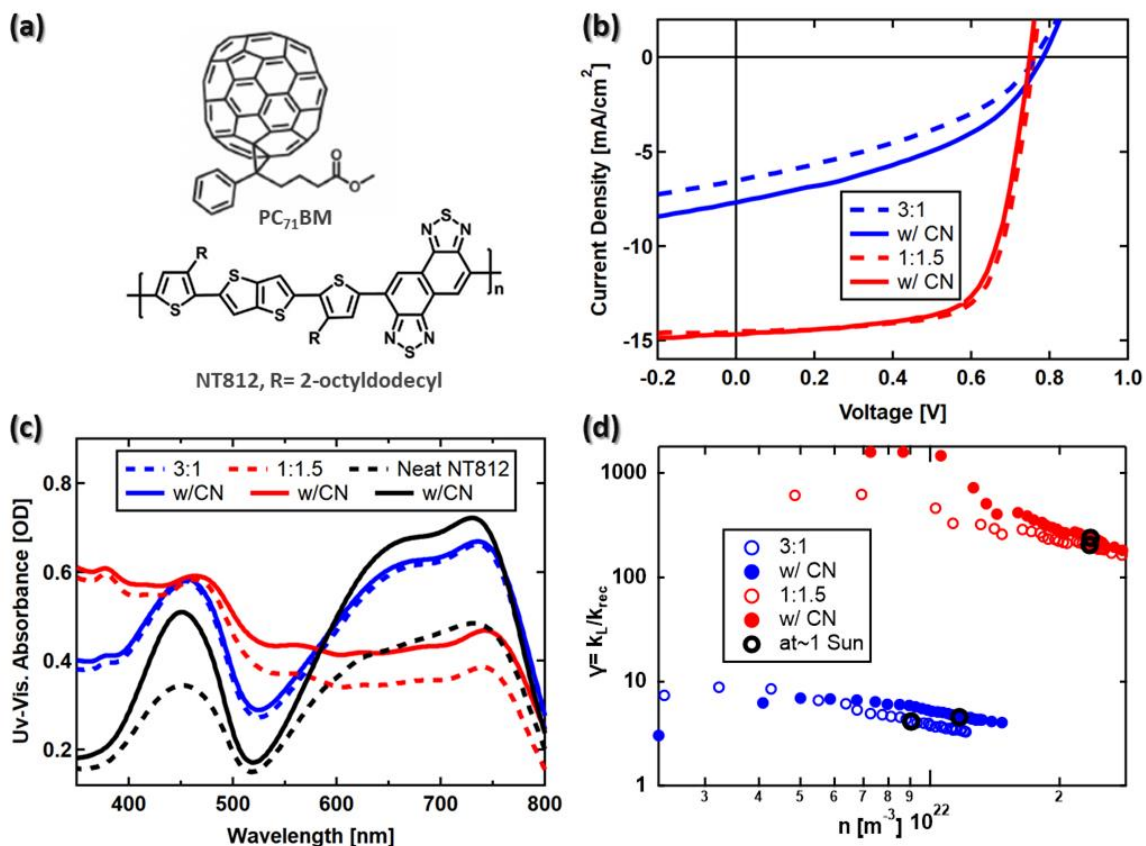


Figure 2- 1: a) Chemical structure for the fullerene (top) and polymer (bottom). b) J-V characteristic curves for the four different solar cells. c) UV-Vis absorbance for neat polymer with and without CN as well as for all blends. d) Reduction factor of bimolecular recombination as a function of carrier density in all four NT812: PC71BM blends. Black circles show the reduction factor data points at about 1 sun.

Investigation into the origin of this phenomenon demonstrated that the charge mobilities of the NT812:PC71BM system are rather mundane and cannot explain the very efficient charge collection. A proposed scenario is either a unique interfacial charge transfer (CT) state with fast dissociation dynamics relative to the decay rate or a special morphology that allows thick non-Langevin BHJ OSCs.^{30,67} A combinatory scenario can be possible as well where improved nano-

morphology enhances CT state dynamics. Importantly, one study found that nearly classical Langevin recombination could be exhibited in this system by changing the donor-acceptor ratio³⁰, which indicates a morphological origin to the non-Langevin behaviour. Only a handful of other D:A combinations show similar behaviour.^{62,68,69}

General work on the topic has suggested that high crystallinity of the donor is important,^{70,71} or in the case of amorphous polymers, that relatively pure phases help by reducing charge recombination.⁷² Unfortunately, early experimental and computational work investigating interfacial sharpness on recombination have resulted in conflicting conclusions. While some reports suggest that sharp interfaces reduce recombination,^{73,74} others conclude that disordered or mixed interfaces are best.^{75,76} However, none of these studies directly measured bulk heterojunction interfacial properties such as interfacial sharpness. Clarke et al. compared two polymer:fullerene systems with similar nanostructure but distinct charge recombination behaviours to probe morphological origins of non-Langevin dynamics. Their transmission electron microscopy (TEM) investigation could not reveal any significant morphological difference, however, and they were not able to compare Langevin and non-Langevin recombination in the same material system.⁷⁷ The NT812:PC71BM system, with its ability to switch between the two behaviours, represents an opportunity to reveal the critical nanostructure leading to non-Langevin recombination but will require an advanced quantitative characterization of the nanostructure.

We have shown in our previous work that the critical morphological parameters of crystallinity, domain purity, and domain size can be measured by a strategic application of a suite of synchrotron X-ray techniques.^{24,27,46} Our recent work has demonstrated the capability of these techniques to additionally probe interfacial sharpness.^{27,38} The work highlighted the

importance of interfaces on charge generation but wasn't conclusive with respect to recombination. Venkatesan et al. noted reduced recombination with enhanced Kelvin probe surface potential differences between domains in blends cast from solvent additives.⁷⁸ This correlated with increased domain purity, but they didn't investigate interface morphology. Another study reported evidence that rough D:A bulk heterointerfaces correlated with good exciton dissociation but did not monitor recombination.⁷⁹ Thus to date, no work has directly measured morphology including interfaces, while at the same time isolating and suppressing recombination.

In this work we apply our suite of X-ray nanoprobe to directly reveal the critical morphology behind the activation of highly suppressed non-Langevin recombination. We uniquely combine our measurements to quantify the donor-acceptor (D-A) interfacial sharpness in BHJ blends. Varying the active layer blend ratio and solvent additive content effectively switches the charge recombination dynamics between Langevin and non-Langevin in the same system, suggesting that reduced recombination is morphology driven. We are surprised to find that even our active layers exhibiting Langevin recombination are composed of pure, well-aggregated phases. Instead, we find that large domains with sharp D-A interfaces correlate with suppressed, non-Langevin recombination with reduction factors >1000 , indicating these are the morphological mechanisms that enable thick and efficient active layers. Such findings can guide future research to achieve high-performing systems suitable for large-scale production of OSCs.

Results

OSC active layers were spin coated with a (D:A) blend *wt.* ratios of (1:1.5) and (3:1) both with and without 0.5 vol % chloronaphthalene (CN) as a solvent additive, since these conditions exhibited both Langevin and Non-Langevin recombination dynamics previously.³⁰ Rather than

1 μm thick active layers, ~200 nm active layers were investigated to enable both device physics and X-ray nanoprobe analyses on the same set of samples by the participating groups. 100 nm and 200 nm active layers revealed identical morphologies and performance scaled only by absorption (see Figure S1- 1, Figure S1- 26, and Figure S1- 27, SI). It is worth noting that our previous device physics investigation of thin (100 nm) and thick (800 nm) films show similar carrier mobilities in both junctions.³⁰ Thus, thicker films are likely to have similar morphologies. Figure 2- 1b displays the JV curves under AM1.5G solar illumination, and Table 1 summarizes device performance metrics, which are similar to previous reports.^{29,30} In particular, the (1:1.5) devices show about four times more efficiency than (3:1) blends with all of the improvement from the short circuit current (J_{sc}) and fill factor (FF).⁸⁰ Although UV-Vis spectra on pure films show some differences when adding the CN additive, no significant difference in aggregation due to CN can be detected in the blends investigated, suggesting that the polymer in all blends is well aggregated.

Figure 2- 1d shows the reduction factor of the bimolecular recombination γ , which is the ratio of the classical Langevin recombination coefficient k_L ,⁶⁴ to the coefficient k_{rec} in a given photoactive layer, $\gamma = k_L / k_{rec}$. The bimolecular recombination in the limit of a homogeneous

Blend (NT812:PC71BM)	Additive CN [vol %]	V_{oc} [V]	J_{sc} [mA.cm ⁻²]	FF [%]	Avg. PCE [%]	$\gamma =$ k_L/k_{rec} (a)	μ_s [cm ² V ⁻¹ s ⁻¹]	μ_f [cm ² V ⁻¹ s ⁻¹]
(3:1)	0	0.77	6.42	39	1.88(0.08)	2	2.5×10^{-4}	2.5×10^{-4}
(3:1)	0.5	0.78	7.49	41	2.43(0.06)	5	3.0×10^{-4}	3.0×10^{-4}
(1:1.5)	0	0.75	14.69	70	7.85(0.25)	200	2.2×10^{-4}	8.1×10^{-3}
(1:1.5)	0.5	0.74	14.79	69	7.67(0.13)	250	2.9×10^{-4}	9.0×10^{-3}

Table 2- 1: Summary of device performance, reduction factors of bimolecular recombination and charge carrier mobilities in NT812:PC71BM films with different blend ratios, processed with and without solvent additive. The device performance parameters are an average of 6 devices. The bimolecular recombination reduction factors ($\gamma = k_L / k_{rec}$) are calculated based on steady-state bias-assisted charge extraction measurements and the mobilities (fast and slow carriers) are calculated based on resistance-dependent photovoltage measurements (see Figure S1- 2 and Figure S1- 3, SI). The listed γ values are at about 1 sun intensity^(a).

medium can be approximated by the Langevin recombination rate constant, which is proportional to the mean carrier mobility. This was calculated in a similar manner to our previous work (see Figure S1- 2, SI).³⁰ As expected, the (3:1) blend without the CN additive exhibits nearly classical diffusive Langevin recombination. In contrast, the (1:1.5) devices show about two orders of magnitude lower recombination coefficients with $\gamma_{max} > 1000$. The (1:1.5) devices are, therefore, considered to exhibit non-Langevin recombination dynamics. The solvent additive also improves the reduction factor (more significantly for the 3:1 blends) with all trends holding true at the operational conditions (~ 1 sun), see Table 1 and the black circles in Figure 2-1d.

Resistance-dependent photovoltage (RPV) transient measurements were used to separately determine faster and slower carrier mobilities in each blend. All mobilities, are unremarkable and rather typical of values in other high performing polymer:fullerene OSCs— in agreement with previous work.³⁰ We were not able to separate the slower and faster carrier mobilities in the (3:1) blends, likely due to them being too similar. Importantly, there are no significant changes in mobilities due to processing conditions other than the fast carriers (typically identified as electrons in the fullerene phase)^{81,82} have increasing mobilities in the films with the better blend ratio as shown in Table 1 (also see Figure S1- 3, SI). However, increasing electron mobilities only serves to unbalance the charge transport, and even these mobilities are still typical of polymer:fullerene blends. These results suggest that the charge extraction rate is not extraordinary, but rather the bimolecular recombination rate is low. This allows for efficient charge collection even when the film thickness increases.³⁰ Contrary to mobility, γ improves by about 100 times with the blend ratio. In many other OSCs with either polymer or small molecule donors, the non-Langevin behavior has been shown to be key for

maintaining high FF even at active layer thickness ~ 300 nm.^{62,67,68,83,84} Thus, the lower FF values in (3:1) blends can be attributed to their higher biomolecular recombination in comparison to their (1:1.5) counterparts.

We now turn to morphological characterization to understand how the additive and D-A ratios can turn on and off the Langevin recombination property. We first investigate the crystallinity of the electron donor (NT812) and fullerene (acceptor) aggregates using grazing-incidence wide-angle X-ray scattering (GIWAXS) measurements. The results of the experiments on both neat and blend films are presented in Figure 2- 2 with additional results and analysis provided in the supporting information. Figure 2- 2a and b show 2D GIWAXS images for (3:1) and (1:1.5) blends, respectively, both with CN. The strong scattering ring at $q=1.36 \text{ \AA}^{-1}$ indicates the presence of pure PC71BM aggregates as evidenced by the similar ring for a pure PC71BM film. The scattering peaks at $q=0.29 \text{ \AA}^{-1}$ indicate polymer lamellar (100) stacking with only a weak second order (200) detectable. The primarily out-of-plane (OoP) peaks at $q_z=1.83 \text{ \AA}^{-1}$ represents π -stacking (010) with a face-on orientated population with respect to the substrate in addition to a randomly oriented crystal population. We focus on these face-on π -stacking peaks because this packing is favourable for charge transport. Figure 2- 2c shows 1D GIWAXS profiles extracted from the 2D images in the OoP direction, i.e. a line cut in the vertical direction (q_z). Figure S1- 5 and Figure S1- 7, in SI, show vertical and horizontal 1D profiles and peak assignments. The intensities of both peaks closely follow the blend ratio, suggesting the degree of crystallinity or aggregation is similar in all blends. Pole figures analysis of (010) supports the claim of similarity in degree of crystallinity in all blends (see Figure S1- 9, SI). The polymer and PC71BM diffraction characteristics in all blends are consistent with their pure film counterparts and suggests the existence of both pure polymer and pure PC71BM domains in all active layers.

Results of peak width Scherrer analysis (Figure S1- 6, SI) of the coherence length (D) are displayed in Figure 2- 2d and Figure S1- 7, SI—where D is a measure of length-scale ordering within a crystal or crystal size.⁸⁵ In each case, the solvent additive enhances ordering in the blends by increasing D for the OoP π -stacking (Figure 2- 2d). While there is little change in π -stacking for the (3:1) blend film, π -stacking is significantly enhanced for the (1:1.5) blends. A similar improvement occurs for electronically insulating lamellar stacking (Figure S1- 7, SI). All blends cast with the CN additive, however, have similar π -stacking coherence lengths to the pure polymer film. The enhancement of coherence length with CN is consistent with its role as a plasticizer and the effect of the fullerene to increasingly disrupt polymer packing.²¹ In contrast to the polymer packing, D of the main fullerene peaks are invariant with CN, and D in (1:1.5) blends are equal to those in pure fullerene. (3:1) blends show similar, but smaller values of fullerene D . This suggests slightly more disordered PC71BM aggregates in (3:1) films, which is consistent with lower electron mobilities in these blends as interpreted from our RPV experiments. Coherence length also sets a lower limit to the size of pure phases in the blends. We cannot say much about the size of pure fullerene domains as even pure films only exhibit diffraction with $D \sim 2nm$ (Figure 2- 2d). However, the polymer lamellar diffraction demonstrates $D \sim 14 nm$ for all samples (Figure S1- 7, SI), making this the lower limit of pure polymer domains in the blends. From Figure S1- 7, it is noticeable that D of the lamellar peak in neat polymer films is lower than in the blends. Although that might seem counterintuitive, there is precedent in the literature for other systems that show similar behavior.⁸⁶ We observe that as the amount of fullerene increases, the in plane lamellar peaks narrow and thus result in higher coherence length (Figure S1- 7). Such an effect could arise from a strong drive to phase separate early during film formation, enabling more time to order.

To more accurately probe domain size, composition, and connectivity, we used scanning transmission X-ray microscopy (STXM)⁵² combined with near-edge X-ray absorbance fine structure (NEXAFS).⁴⁵ Figure 2- 3 presents NEXAFS and STXM results for a (1:1.5) with CN blend with film thickness ≈ 100 nm for better clarity in the transmission mode image. The similarity of the results on this film were confirmed by identical scattering profiles between the

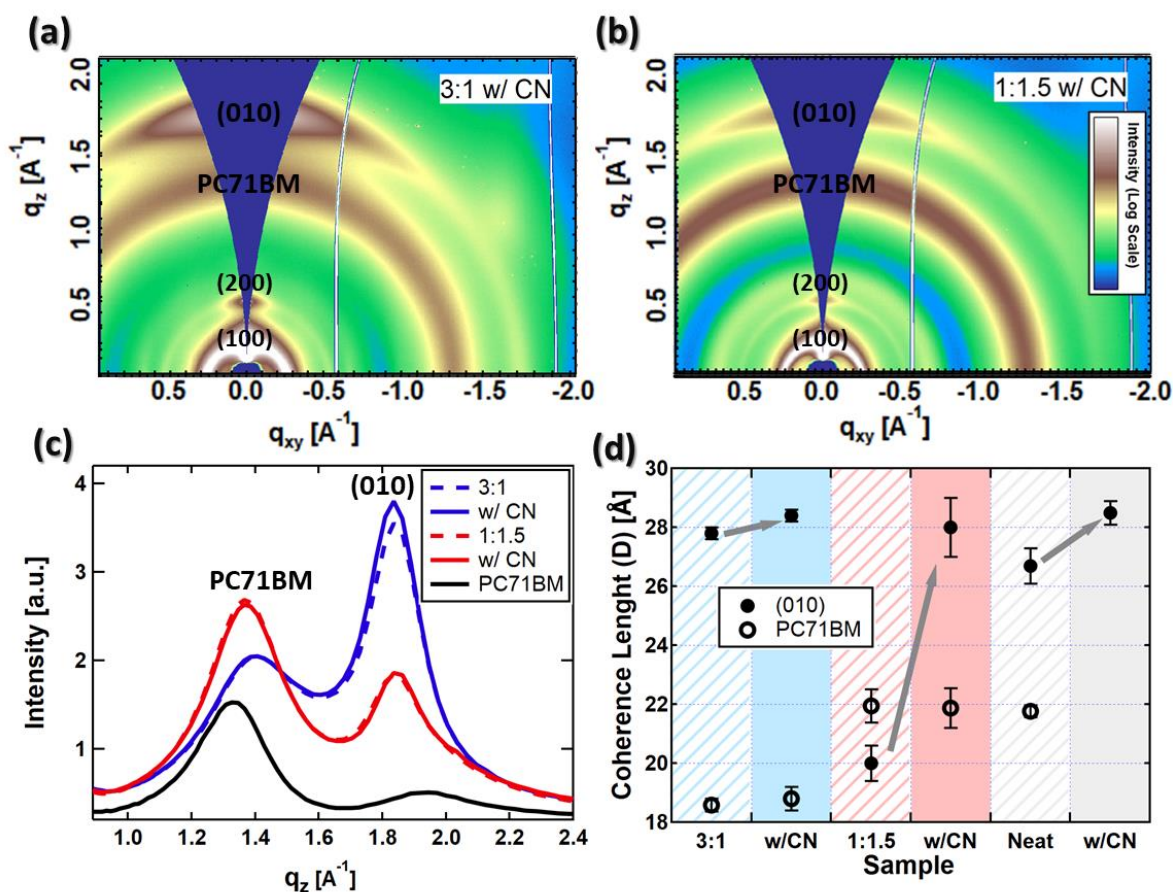


Figure 2- 2: GIWAXS results for neat materials (NT812 and fullerene) and blends. 2D GIWAXS scattering results for NT812: PC71BM blends of (3:1) blend with CN (a) and 1:1.5 blend with CN (b). The 2D images are plotted with the same color scale of the scattering intensities [a.u.], also corrected for the missing wedge. c) 1D GIWAXS profiles extracted from the 2D images in the OoP vertical direction (q_z) for all blends. Also, the graph includes the GIWAXS profile of neat PC71BM (black) to help with peak assignments. PC71BM and (010) peaks are indicated in the graph. d) Coherence length (D) for PC71BM peak at $q_z=1.36 \text{ \AA}^{-1}$ (open circles) and (010) peak at $q_z= 1.83 \text{ \AA}^{-1}$ (solid circles) in blends as well as in neat materials were calculated via Scherrer analysis (details in the Supporting Information).

thinner and thicker active layers (see Figure S1- 26, SI) as well as qualitative STXM images of thicker films (Figure S1- 16, SI). The linear fitting of NEXAFS spectra for the blend, shown in Figure 2- 3a, confirms the average weight ratio, 40% polymer, across the film. Figure 2- 3b presents a STXM image where dark regions represent a matrix of (50-100 nm sized) PC71BM rich domains, and the white fibrils indicate polymer rich domains that are 30-50 nm in width. These measurements are consistent with the lower limits of domain size determined from the GIWAXS analysis. The fibrillar nature of the polymer domains indicates well-connected pure crystalline polymer conduits for hole transport that are larger than the classical P3HT-based OSC fibril network. The PC71BM domains are large enough to easily connect to the electrodes—we anticipate that to hold true even in thick films. A qualitative comparison between the two blend ratios with active layers at thicknesses >200 nm (see Figure S1- 16, SI) shows a similar fibril network with the (3:1) film exhibiting polymer fibrils with a smaller spacing due to less PC71BM loading.

The spectroscopic nature of STXM imaging enables chemical mapping of the domains. Our quantitative analysis (details in Figure S1- 12 and Figure S1- 13, SI) is carried out on the thinner 100 nm film, near regions likely to be mostly one domain throughout the film thickness (e.g. nodes of polymer fibrils) with an example composition line profile shown in Figure 2- 3c (many more in Figure S1- 13, SI). The peaked nature of the composition profiles originates from the STXM beam size (~50 nm). After correcting for the X-ray beam convolution in a similar fashion to our previous work (details in Figure S1- 14 and Figure S1- 15, SI),²⁴ the deconvoluted results indicate pure polymer and pure fullerene domains, agreeing with the GIWAXS analysis.

We were not able to conduct compositional analysis on thick films due to vertically overlapping domains.

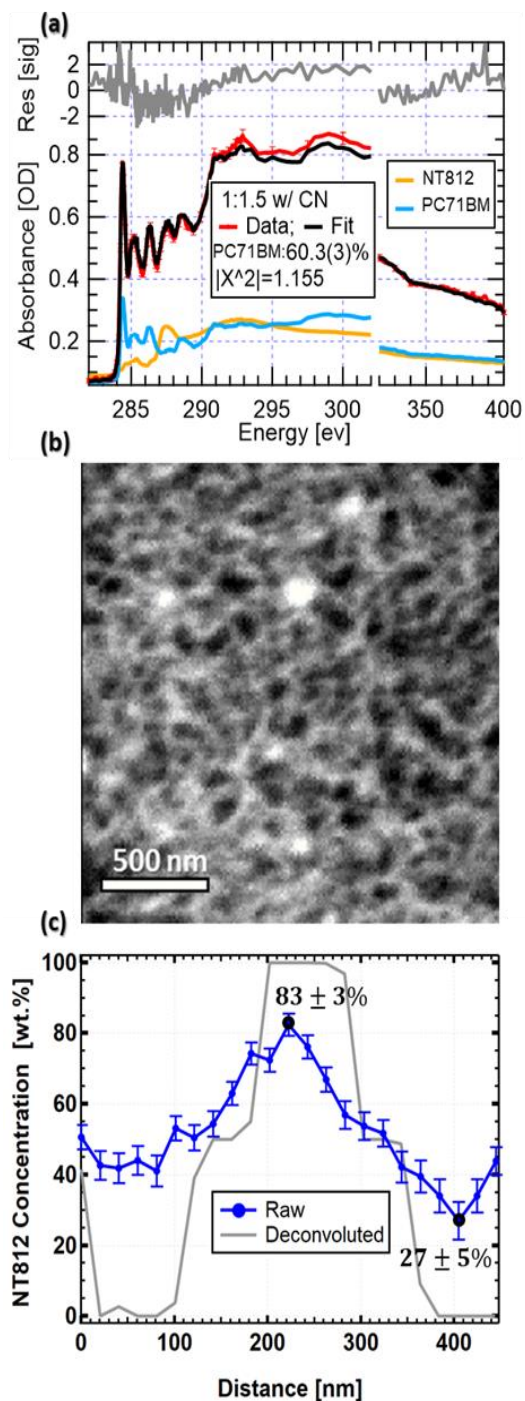


Figure 2- 3. Morphology investigation of OSC active layer in a 100 nm thin (1:1.5) blend with CN. a) NEXAFS spectra: pure NT812 (orange), PC71BM (blue), blend (Red), and a linear combination fit of spectra for NEXAFS for pure components (black). b) STXM composition scan was acquired at 284.4 eV, which is fullerene absorption peak. PC71BM (dark regions) and NT812 (white fibrils). c) Concentration profiles of NT812 across different compositional domains; (blue) raw and (grey) deconvoluted.

We now turn to resonant soft X-ray scattering (RSoXS) as a complementary measurement of domain size and purity with the unique opportunity to also investigate D-A interfaces.⁴⁴ The Lorentz-corrected RSoXS scattering profiles in Figure 2- 4a were strategically acquired just below the absorption edge to enhance phase contrast, limit damage, reduce orientation contrast, and eliminate X-ray fluorescence backgrounds. They show that the (3:1) blends have scattering peaks at $q=0.10 \text{ nm}^{-1}$ which corresponds to a characteristic length (which determines the average center-to-center distance between scatterers and defined as $L_C = 2\pi/q^*$ where q^* is the peak position) of 62 nm. On the other hand, the (1:1.5) films show scattering peaks at $q=0.064 \text{ nm}^{-1}$ and $L_C \approx 98 \text{ nm}$. Although without modeling these values are only approximate, however, they are consistent with the domain spacing from STXM analyses. Given that the (3:1) blends are 75% polymer, it is likely that the polymer domains in this blend are the same size as in the (1:1.5) blend. This is due to the self-limiting nature of polymer fibrils seen in most semicrystalline polymer films. Thus, a smaller characteristic length is likely due to a reduction in fullerene domain size to below 30 nm as estimated from L_C as detailed in the supporting information, part S10. CN does not affect the peak position and therefore has no impact on the characteristic length (Figure S1- 20, SI) but does increase the scattering intensity. The insensitivity of L_C to the plasticizing CN indicates that the nanostructure is driven by crystallinity rather than liquid-liquid phase separation. Furthermore, anisotropic scattering at the X-ray energy of 285.4 eV was measured and has been interpreted as indicating a preferential molecular orientation at D-A interfaces, similar to other systems.²⁸ Here the scattering anisotropy is the same sign for all blends, suggesting that the in D-A interfacial orientation does not change with the investigated processing conditions and is thus not a significant factor determining performance in this case. Additional tilted-film RSoXS measurements, conducted to express the

qz component (see Figure S1- 22)⁸⁷ were consistent with no vertical stratification and in agreement with pure domains measured in STXM that integrates the vertical film direction.

The increase in RSoXS intensity with CN suggests that the solvent additive enhances the average composition variation between the polymer and fullerene domains. The total scattering intensity (TSI) calculated by integrating the scattering profiles over all of reciprocal space (area under the profiles in Figure 2- 4a) is proportional to the mean-squared composition difference between domains ($\Delta C_{RMS} \propto \sqrt{TSI}$, RMS is root-mean-squared).²⁴ ΔC_{RMS} was calculated on an absolute scale by combining this measurement with the STXM domain composition analysis and prior knowledge of the donor/acceptor ratio as we have done in our previous work²⁴ with details shown in Figure S1- 17-Figure S1- 21, SI. Figure 2- 4b displays the result of this analysis (y-axis) with uncertainties primarily from convolution of domain composition with volume fraction (Figure S1- 21, SI). The ΔC_{RMS} analysis tracks the RSoXS profile intensities seen in Figure 2- 4a with the average domain composition fluctuation greatest for the (1:1.5) blends and with the CN additive.

There is significant evidence (from GIWAXS and STXM) that both polymer and fullerene domains are pure. However, $\Delta C_{RMS} < 100\%$ means that mixed regions of the active layer must exist somewhere. There is no clear evidence of a separate third phase in our STXM images, so the mixed region must actually be manifest as interfacial mixing in a narrow region below the resolution limit of the microscope. Such an interpretation follows from other systems like this one where evidence of mixing with fullerenes only occurs at polymer fibril interfaces.^{27,88-90} Previously we determined interfacial width in a block copolymer using absolute scattering intensity.⁸⁷ The required measurements for such analysis were not conducted here, but we can instead combine ΔC_{RMS} with measurements of domain spacing and volume fraction to

extract an interfacial width. In this calculation (detailed in Figure S1- 23-Figure S1- 25, SI) we assume circular fibril cross-sections and a linear interfacial composition profile. This results in a simple analytic solution for the interfacial width between pure domains, which notably makes no assumption of the packing arrangement of the fibrils and is also robust to a wide distribution of fibril sizes. The results of calculating the interfacial width are shown as the x-position of the black dots in Figure 2- 4b. Thus, we attribute the increase of ΔC_{RMS} with CN additive to the D-A interfaces becoming sharper, with the widest interfaces at 12 nm sharpening to less than 5 nm in width. In short, the CN plasticizing solvent additive enables cleaner crystallinity-driven phase separation, sharpening the D-A interfaces.

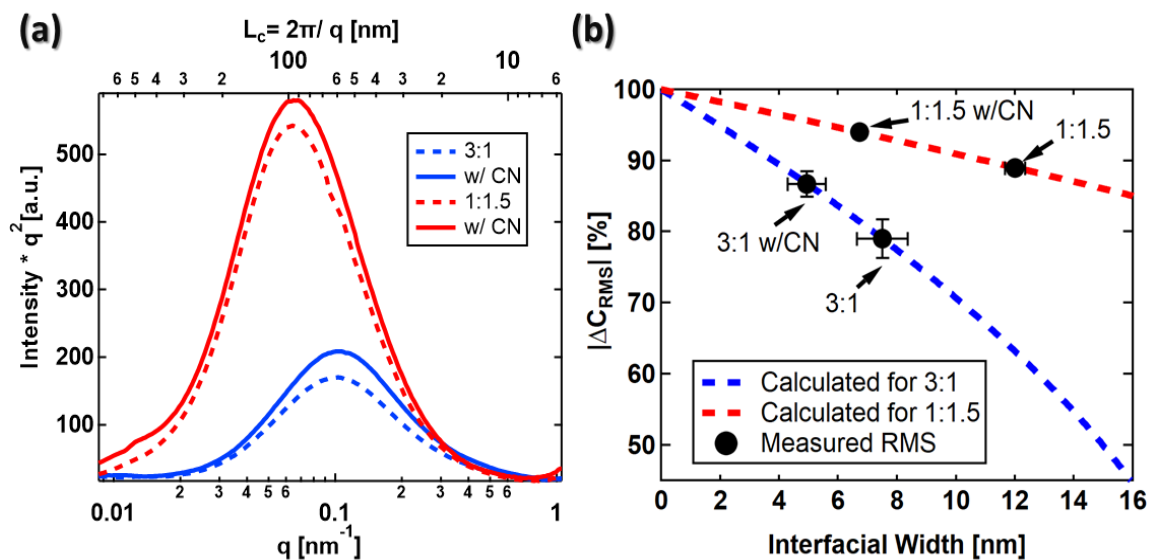


Figure 2- 4. a) Lorentz-corrected RSoXS profiles acquired at 283.5 eV for active layers of the four investigated samples as indicated in the graph legend. b) Averaged differences in composition between different domains, based on two-domain model. The dotted lines represent the mathematically calculated ΔC_{RMS} values of composition differences as a function of the D-A interfacial width. The black circles are the extracted values of the D-A interfacial width based on STXM and RSoXS results.

Discussion

Figure 2- 5 depicts the morphology of the investigated NT812:PC71BM active layers that is consistent with all measurement results and analysis presented above. Blue represents pure polymer fibrils in a red matrix of pure fullerene. The black bars symbolize polymer chains inside the fibrils whose packing slightly improves with the solvent additive (see coherence length measurements). Notably there is only evidence of improvement in 1:1.5 blends, but not in 3:1 blends (see also the UV-Vis spectra for 3:1 blends). The color gradient at fibril edges depicts interfacial mixing, which decrease with the CN additive, thus making the domain interfaces sharper (and increasing ΔC_{RMS}). Finally, more fibrils closer together are depicted for the (3:1)

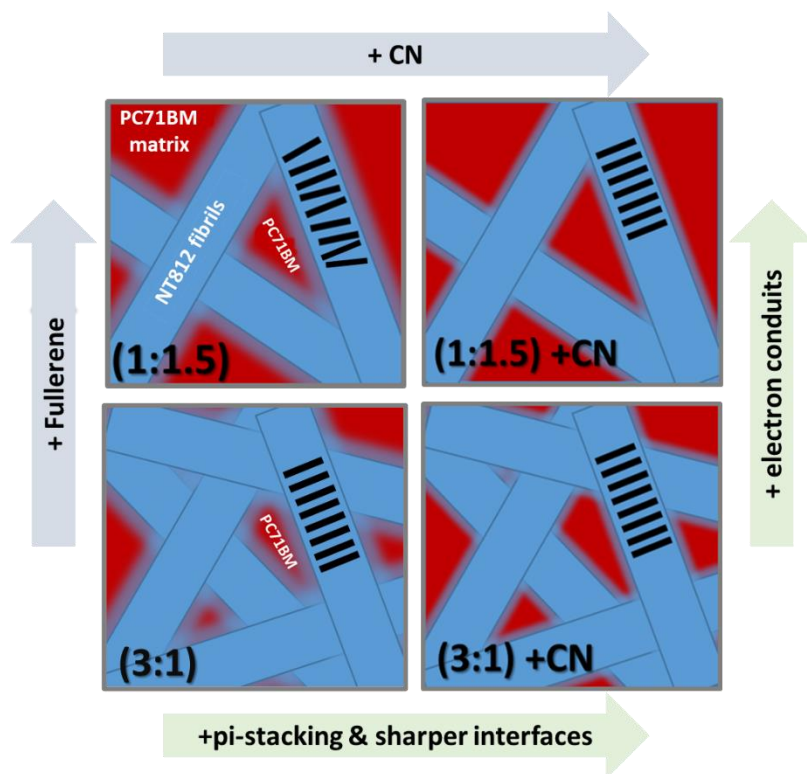


Figure 2- 5: Depicted representation of morphology of OSC active layer in the investigated NT812: PC71BM blends. Polymer fibrils (blue) with stacked polymer chains (black) and matrix of fullerene (Red). We note that the fast growth direction of the fibril is unknown for this polymer and may not be the pi-stacking direction as is depicted here.

blend ratio making the fullerene domains smaller and reducing the characteristic length as evidenced by the RSoXS analysis.

The question to be answered is what aspects of morphology are important to realize highly suppressed, non-Langevin recombination. In general, it has been found that domain purity in polymer based OSCs is important for device performance by aiding charge extraction and hindering recombination.^{25,72,74,91} This is likely an important prerequisite here, but the presence of pure domains in blends exhibiting both Langevin and non-Langevin recombination suggest this situation alone is insufficient. Venkatesan et al. have shown that charge recombination is high in low-performing polymer:fullerene systems with narrow domains despite good domain purity and conductivity.⁹² Our results go further to show that large and clean conduits to the electrodes keep charges from interacting with their counterparts in neighbouring domains, whereas narrow pure domains increase the likelihood that charges will encounter each other or trap states at the interfaces. This is the most prevalent morphological change between the cells with Langevin versus non-Langevin recombination dynamics. Note that 25% PC71BM loading in the (3:1) blends, aggregating into pure phases, is well above the 3D percolation threshold, so although isolated-domain traps are possible,^{93,94} general fullerene domain connectivity should be no issue here.

A further clue to the importance of interfacial interaction comes from the correlation of sharpening interfaces rather than crystalline coherence with decreased recombination for both blend films. In particular, in (3:1) blends the recombination reduction factor γ more than doubles when interfacial mixing is reduced through the CN additive while there is no detectible change in crystallinity (GIWAXS) or aggregation (UV-Vis spectroscopy). The improvement in γ is not nearly as significant for the corresponding (1:1.5) blend devices, even though pi-stacking

improves dramatically for them. We interpret this situation to mean that highly mixed or wide D-A interfaces can encroach on the charge pathways – especially when they are narrow – and enable holes and electrons to mingle and recombine in a way well-described by the Langevin model. Devices with large pure percolation pathways are more immune to interfacial details such that sharper interfaces are less critical for non-Langevin recombination.⁹⁵ The crystallinity improving with CN might also help in keeping holes toward the middle of transport conduits because the energy states in a well-delocalized crystal are lower than a defective crystal,⁹⁶ thus, resulting in even higher γ . Domain size must not be allowed to increase too far, however, due to the limitations of the exciton diffusion length (~20 nm). On top of suppressing recombination, there is increasing evidence that sharp interfaces are important for charge generation as well in semicrystalline systems.^{27,38} Thus, the highest efficiency devices will likely still depend on sharp interfaces and smaller domains to simultaneously harvest all excitons and transport charges.

Although we cannot conclusively say that perfectly discrete (zero width) interfaces are best, we have been able to uniquely remove the effects of domain purity and crystallinity/aggregation from the equation. Furthermore, our direct correlation to the Langevin reduction factor rather than short-circuit current enables us to eliminate possible influences of changing charge generation rates. Combined, these results reveal a definitive influence of interfacial sharpness on suppressing recombination.

To put our findings about the NT812 system into perspective, we compare it to the classical electron donor, poly3-hexylthiophene (P3HT), which exhibits non-Langevin recombination as well in fullerene based BHJ OSCs with thermal post-treatment.^{84,97,98} Both systems phase segregate in BHJ layers and result in pure fibrils at optimal fabrication conditions and both have similar charge carrier mobilities. In fact, fibrillar structures are good at purifying,

sharpening, and limiting how large the domains get, so they do not get so big as to lower exciton dissociation efficiencies. However, the best NT812 OSCs' γ are higher than for P3HT devices (>1000 vs 100s). We attribute this to the fact that NT812, like many other polymers,^{99–101} has a stiffer and longer monomer than P3HT, which causes the NT812 fibrils to be wider resulting in larger charge conduits. On the other hand, there is significant room for improvement in NFAs, which now top OSC performance in thin layers but lose significant efficiency as thickness increases, even when processed to optimize aggregation.⁶⁶ Therefore, more systems with NT812 type morphology are needed, namely with larger fibrils that strongly phase separate from the acceptor phase to result in sharp interfaces. Such a strategy will enable high efficiency devices with thicknesses >400 nm.

Conclusion

We have investigated the morphological mechanisms behind a novel high-performing polymer:fullerene OSC system known to exhibit both highly suppressed non-Langevin recombination and classical diffusive Langevin recombination dependent on the blend ratio. Our suite of synchrotron-based X-ray techniques were combined to reveal pure phases in all preparation conditions, suggesting pure phases alone are not sufficient to realize non-Langevin recombination. Instead, we found that larger (>30 nm), pure, and well-aggregated domains with sharp D-A interfaces likely act as charge conduits across the active layers to effectively segregate charges and suppress bimolecular recombination via fast dissociation of charge transfer states for near-ideal charge generation and collection. Such morphological features are possible explanations to how efficient devices can be achieved with printable active layers up to $1\mu\text{m}$ in thickness. Thus, large, pure percolation pathways with sharp heterointerfaces may be required to achieve efficient OSCs suitable for large-scale industrial production.

Experimental Section

Device Fabrication

The polymer (NT812) was supplied by Fei Huang in Institute of Polymer Optoelectronic Materials and Devices, South China University of Technology. The fullerene acceptor, PC71BM was purchased from Solenne. The solvents Chlorobenzene (CB) and 1,2-Dichlorobenzene (DCB), and the additive chloronaphthalene (CN) were purchased from Carl Roth and Alfa Aesar, respectively. The devices were fabricated with a conventional structure. First, the patterned indium tin oxide (ITO) glass substrates were cleaned in an ultrasonic bath with detergent, acetone, deionized water, and isopropyl alcohol and dried by nitrogen. The dried substrates were treated by oxygen plasma at room temperature for 4 min. Then PEDOT:PSS (purchased from Heraeus Deutschland (Clevios P AI4083)) was spin coated on top of the substrates (3000 rpm for 30 s, thickness of ≈ 30 nm) and the substrates were annealed at 150 °C for 15 min in air. For deposition of active layers, blend solution of NT812 and PC71BM at a weight ratio of 1:1.5 and 3:1 dissolved in CB:DCB = 3:1 (with/without 0.5 vol % of CN) with total concentration of (20 mg ml⁻¹) were spin coated on top of PEDOT:PSS layer in a nitrogen filled glovebox. The blend films were annealed at 100 °C for 15 min on a hot plate. After cooling down, a 5 nm poly 9,9-bis6-(N,N,N-trimethylammonium) hexylfluorene-alt-co-phenylenebromide (PFN-Br) layer was spin coated from methanol solution onto the active layers. Finally, the films were transferred into a vacuum evaporator connected to the glovebox, and 100 nm silver was deposited sequentially through a shadow mask under ($\approx 1 \times 10^{-7}$ mbar), with an active area of the cells of ($A = 0.06$ cm²).

In order to prepare the films for morphology study, silicon wafers were cleaned as the ITO substrates cleaning process and then Na:PSS was spin coated (3000 rpm for 30 s) on top of

it simulate the device PEDOT:PSS surface roughness and surface energy. The substrates were annealed at (150 °C) for (15 min) in air. The active layers were spin coated and then thermally annealed as described above.

Resistance-Dependent Photovoltage (RPV)

The devices were illuminated by a pulsed second harmonic Nd:YAG laser (NT242, EKSPLA) at 532 nm with 6 ns pulse duration. The laser intensity was attenuated with a normal optical density (OD) filter and set to the low intensity in order to prevent a redistribution (screening) of the internal electric field and maintaining quasi-short-circuit conditions regardless of the load resistance. Then the photocurrent and photovoltage transients were recorded by a digital storage oscilloscope (DSO9104H) via a LabVIEW code. Refer to previous work for more details about those techniques.³⁰

Bias-assisted Charge Extraction (BACE)

To establish steady-state conditions, we used a high power (1 W, 638 nm) laser diode (insaneware) with a switch-off time of (10 ns). The laser diode was operated at (500 Hz) with a duty cycle of 50%, such that illumination lasted 1 ms and the diode was switched off for also 1 ms. A pulse generator (Agilent 81150A) was used to apply the prebias (V_{OC}) and collection bias which are amplified by a home-built amplifier, allowing a fast extraction time of (10-20 ns). The current transients were measured via a (10 Ω) resistor in series with the sample and recorded with an oscilloscope (Agilent DSO9104H).

Morphology Measurements

To probe the active-layer nanomorphology in the investigated OSC systems, we utilized synchrotron-based X-ray microscopy, spectroscopy, and scattering techniques. GIWAXS, RSoXS and Spectroscopy/STXM were conducted at the Advanced Light Source, Berkeley, CA

at beamlines 7.3.3,⁵⁰ 11.0.1.2,⁴⁷ and 5.3.2,⁵² respectively. The morphologically examined active layers were prepared from the same batch as the examined OSC devices. GIWAXS data were taken at X-ray energy (10 KeV) and incident angle of (0.2 deg) (above the substrate critical angle) enabling intensities linear to the illuminated sample volume. Samples were spin coated on Na:PSS/Si. In addition to grazing incident angle (0.2 deg), a rocking scan was acquired around an incident angle of 10.55, which is the specular angle of the pi-pi scattering peak of the polymer. Additional angles of incidence were explored as well (e.g. 5.18, 7.72, 9.94 degrees). The data at 7.72 degree was used to patch up the missing wedge in the 0.2 degree data and to analyze for pole figures in a similar fashion to previous literature done Michael F. Toney et al.¹⁰² RSoXS data were taken at X-ray energy below the C-edge at (283.5 eV). Samples were spin coated on Na:PSS/Si substrates then floated off in deionized water onto Si₃N₄ windows, low stress Si₃N₄ membrane with a size of (2 mm²) and thickness of (100 nm). RSoXS data were normalized to film thickness, which was measured via NEXAFS absorbance spectra acquired at the same position as where RSoXS was acquired and with the same X-ray beam. The RSoXS measurements were conducted in transmission mode at normal incidence, also at 45 degrees of sample tilt (see Figure S1- 22).

STXM images, quantify chemical composition, were acquired at a fullerene resonant energy (284.4 eV) and non- resonant energy (320 eV). These energies were selected from NEXAFS spectra for neat materials. All STXM and NEXAFS samples were spin coated on Na:PSS/Si substrates then floated off in deionized water onto TEM grids.

Acknowledgments

Major funding for this work was provided by the US National Science Foundation DMR Electronic and Photonics Program under Grant #1905790 which also provided funding support for O.A. and T.M. The authors also acknowledge the Alexander von Humboldt Foundation (Sofja Kovalevskaja prize) for funding and Dieter Neher (PWM) for access to labs. Funding support for T.F. and V.M. was provided by the US Department of Energy Early Career Research Program under Grant DE-SC0017923. This research used resources of the Advanced Light Source, which is a DOE Office of Science User facility under contract no. DE-AC02-05CH11231.

CHAPTER 4: HIGH SENSITIVITY OF NON-FULLERENE ORGANIC SOLAR CELLS

MORPHOLOGY AND PERFORMANCE TO A PROCESSING ADDITIVE

Alqahtani, O.; Lv, J.; Xu, T.; Murcia, V.; Ferron, T.; McAfee, T.; Grabner, D.; Duan, T.; Collins, B. A. "High Sensitivity of Non-Fullerene Organic Solar Cells Morphology and Performance to a Processing Additive." *Small*, 2202411. <https://doi.org/10.1002/sml.202202411>

Attributions:

O. Alqahtani conducted the nano-structure characterization, data analysis, and wrote the first draft of the manuscript. J. Lv, T. Xu and T. Duan synthesized the small-molecule materials, fabricated device, and tested device performance. of the examined solar cells. V. Murcia, T. Ferron, T. McAfee and D. Grabner helped with the data acquisition at the Advanced Light Source, Lawrence Berkeley National Laboratory. B. A. Collins provided funds supervised this study.

Note: the supporting information of this manuscript is provided in APPENDEX B.

Abstract

Although solvent additives are used to optimize device performance in many novel non-fullerene acceptor (NFA) organic solar cells (OSCs), the effect of processing additives on OSC structures and functionalities can be difficult to predict. Here, we present two polymer-NFA OSCs with highly sensitive device performance and morphology to the most prevalent solvent additive chloronaphthalene (CN). Devices with 1% CN additive are found to nearly double device efficiencies to 10%. However, additive concentrations even slightly above optimum significantly hinder device performance due to formation of undesirable morphologies. A comprehensive analysis of device nanostructure shows that CN is critical to increasing crystallinity and optimizing phase separation up to the optimal concentration for suppressing charge recombination and maximizing performance. Here domain purity and crystallinity are highly correlated with photocurrent and fill factors. However, this effect is in competition with uncontrolled crystallization of NFAs that occur at CN concentrations slightly above optimal. This study highlights how slight variations of solvent additives could impart detrimental effects to morphology and device performance of NFA OSCs. Therefore, successful scale-up processing of NFA based OSCs will require extreme formulation control, a tuned NFA structure that resists runaway crystallization, or alternative methods such as additive-free fabrication.

Introduction

Power conversion efficiency (PCE) in organic solar cells (OSCs) is rising now with a record surpassing 18%.^{58,103} In solution-processed bulk heterojunction (BHJ) OSCs, non-fullerene acceptors (NFAs) —such as Y6³² and Y6-derivatives¹⁰³—show higher performance than their fullerene-based counterparts.^{104–106} In contrast to fullerenes, development in synthesis and designing for NFAs has allowed for achieving new molecules with more efficient visible to

near infra-red (NIR) absorption, faster electron mobility and lower band gaps.^{107,108} Chemical modification of NFAs and elemental substitution, such as halogenation, are strategies of molecular design to manipulate material properties.¹⁰⁹ For example, fluorination of electron-accepting molecules often tends to affect device performance by improving energy levels, suppressing recombination and increasing the electron-withdrawal.¹¹⁰ However, there have been relatively little investigation of the effects of different NFA halogen type on morphology.^{111–113}

On the processing and fabrication side, methods like thermal annealing and solvent additives are commonly implemented to improve the morphology of BHJ active layers in OSCs.^{14,18,114–116} Solvent additives have been found to not only better dissolve donor and acceptor materials, but also increase film formation time to enhance the donor-acceptor phase separation.¹⁴ However, the effectiveness and compatibility of solvent additives varies and depends on the solvent-solute materials.^{14,114,117} In small-molecule:fullerene OSCs, in general, additives improve crystallinity which is considered as an additional factor that leads to phase separation. This favorably influences charge generation, recombination and extraction processes in many systems.^{14,24,25,38,39} For example, 1,8-diiodooctane (DIO) and 1-chloronaphthalene (CN) are commonly used as plasticizing solvent additives to allow for phase separation and ordering in small-molecule OSCs.¹¹⁸ By and large, there is a required balance between increasing phase separation to achieve an optimal length scale and domain composition/ordering for efficient exciton dissociation and oversized “strong” phase separation in small-molecule based OSCs.^{14,39} The additive-sensitivity in device performance, in some small-molecule:fullerene cases, has been attributed to the additive amount controlling the film morphology.³⁹ Polymer fullerene OSCs generally are less sensitive to over crystallization or excessive phase separation. Despite the

relative popularity, however, to our knowledge the strong phase separation effect occurring in high performance polymer-NFA OSCs have not been studied in detail.

Recently, we have developed synthetically simple, NIR, CPDT-based NFAs for OSC applications (Figure 3- 1a).³⁵ Those NFAs were paired in binary BHJ OSCs with the electron-donating polymer—poly[[4,8-bis[5-(2-ethylhexyl)-2-thienyl]benzo[1,2-b:4,5-b']dithiophene-2,6-diyl]-2,5-thiophenediyl[5,7-bis(2-ethylhexyl)-4,8-dioxo-4H,8H-benzo[1,2-c:4,5-c']dithiophene-1,3-diyl]], (PBDB-T)— Figure 3- 1a (top). The impacts of fluorination (F) and chlorination (Cl) of the NFA on the device performance were previously investigated revealing an extended absorption to the NIR region. Both NFAs show optical bandgap about 1.3 eV which is near ideal to achieve the maximum Shockley–Queisser limit,¹¹⁹ and comparable to that of Y6 (1.33 eV).³² Device performance noticeably was found to be very sensitive to the amount of additive where the efficiency almost doubles to about 10% at the optimal additive concentration. Beyond that, any extra amount, even 0.1 %, of solvent additive results in drastic drops in device performance. The overall trends of device performance are comparable in OSCs with either F- or Cl-NFA variants.³⁵ The overall comparability in device performance of fluorinated vs chlorinated NFAs is common among many of the high-performing systems. For example, PM6:BTP-4F (Y6) and PM6:BTP-4Cl yield ~16.5% PCE, PM7:TPIC-4F/4Cl give ~15%, PM6:IT-4F/4Cl (~13.4%),¹¹¹ and PBDB-T:FDICTF(2F)/(2Cl) yield about 16.5 % PCE.¹⁰⁹ However, that cannot be generalized because other chlorinated NFAs slightly outperform their fluorinated analogs, e.g. PBDB-T:IPIC-4F gives 10.7% while its chlorinated derivative yields 13.0% PCE.¹¹²

In this work, we present a case study of these two CPDT-based NFAs to investigate the morphological origins of extreme performance sensitivity to the CN processing additive. Many CPDT-based NFAs have been synthesized and investigated for OSC applications.^{120–122}

However, this is the first study to investigate the morphological evolution and sensitivity of this type of materials to the concentration of CN solvent additive. Findings of this work underscore the importance of continuing to explore scale-up processing strategies for industrialization of NFA OSCs. Our investigation of the F- and Cl-active layers reveals the high sensitivity of their performance and morphology to the concentration of the solvent additive. The morphological characterization indicates that domain purity and molecular packing are enhanced with the additive amount up to the optimal concentration of 1 vol.%. Both morphological aspects, crystallinity and domain purity, are highly correlating with device fill factor (FF) and short-circuit current density (J_{sc}) in the investigated systems. Thus, optimal concentration of CN (1 %) almost doubled the device PCE compared to the BHJ devices without the additive. However, amounts of CN beyond the optimum concentration results in over-crystallization and strong phase separation as manifested in micron-scale pure NFA crystallites, as in the case of blends with 2% CN. As a result, the device performance is significantly hindered due to inefficient exciton dissociation and increased charge recombination. This result indicates that NFAs in general face a similar challenge to scale up as in comparison to their all small-molecule counterparts. Morphologies in F-blends versus Cl-blends are found to be similar except for a stronger tendency of Cl-based NFA to aggregate into crystallites, which may be due to enhanced interaction with the CN additive.

Results

Device Performance

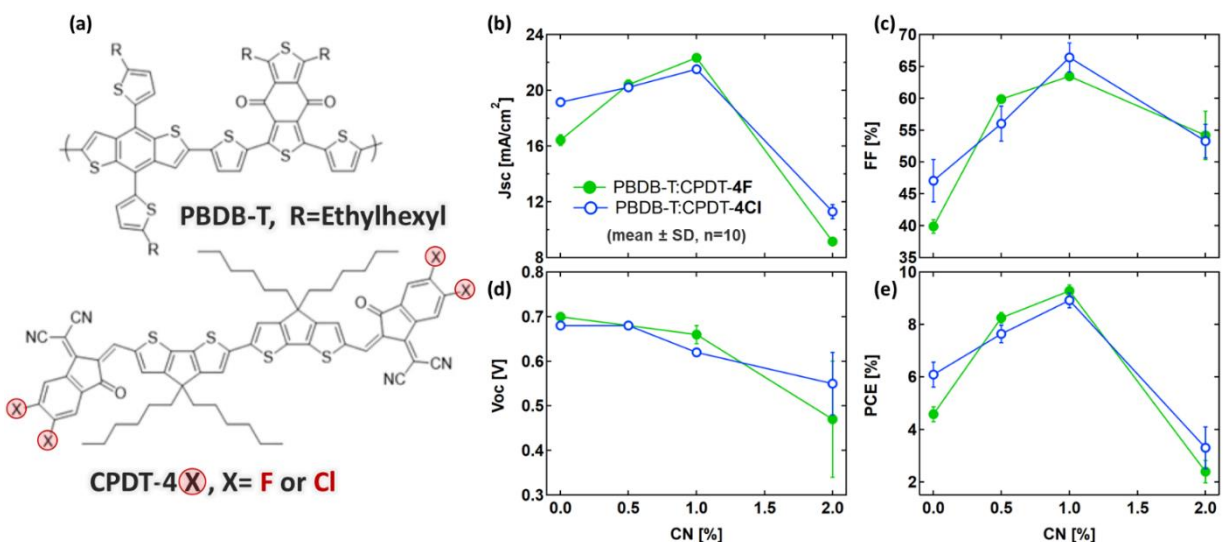


Figure 3- 1: a) Shows the chemical structures of the materials that were used to fabricate active layers in the investigated OSCs in this work. (Top) the polymer electron donor (PBDB-T) and (bottom) electron NFA acceptor (CPDT-4X, where X is Cl or F). The average parameters of device performance are plotted as a function of amounts of solvent additive (CN vol.%); b) J_{sc} , c) FF, d) V_{oc} , and e) PCE at 1 sun. The solid green circles indicate the F-blends (PBDB-T:CPDT-4F) with (1:1) weight ratio and open blue circles represent the Cl-films (PBDB-T:CPDT-4Cl) with (1:1.2) weight ratio. See Table S2-1, Table S2- 2 and Figure S2- 1 in the supporting information for more about device performance, J-V curves, and external quantum efficiency (EQE) profiles. The device performance parameters are the mean of 10 cells \pm standard deviation.

Figure 3- 1(b-e) presents the device performance parameters of the investigated OSCs, processed from chlorobenzene (CB) with different CN additive concentrations. More performance details can be found in Figure S2- 1, Table S2- 1 and Table S2- 2. The J_{sc} increases with the additive up to 1% (vol%) CN, where maximum J_{sc} values are about 22 mA/cm² for both systems, then significantly drops down in the blends with 2% CN. The FF follows a similar trend as J_{sc} in both the F- and Cl-systems, with maximum FF values about 63% and 66%, respectively. On the other hand, the V_{oc} steadily decreases with of solvent additive, with the highest V_{oc} \sim 0.7 V for the blends without additives. At 1% CN, V_{oc} drops to 0.66 and 0.62 V for the F- and Cl-systems, respectively. The lower V_{oc} relative to record systems such as

PM6:Y6 likely originates from a less favorable energy level alignment. The performance of the devices as represented by PCE in Figure 3- 1e follows closely the trends in the Jsc and FF, with maximum PCE of 9.51% for the F-systems and 9.20% for the Cl-devices. Overall, the fluorinated and chlorinated cells exhibit similar device behaviors with the solvent additive (CN). The overall performance trends are very similar to those of our original work.³⁵ In that work, even an increment of 0.1 % CN beyond the optimal concentration resulted in a considerable reduction (~ 20%) in PCE.³⁵

Previous measurements of Jsc and Voc dependency on intensity of incident light suggest that both systems with 1% CN have bimolecular recombination that limits performance to some extent, which were attributed to unbalanced charge mobilities.³⁵ Overall, the Cl-blends show similar trends in device performance to the F-blends in this work and the previous work indicating good reproducibility. In the current work, the EQE spectra of the blends without and with 1% CN (Figure S2- 1) are similar to the published work in terms of their overall peak intensity, shape, and range, with the optimum devices having ~70% EQE between ~ 455 nm and the CPDT absorption edge at ~850 nm. Generally, EQE follows the trends of device performance with solvent additive. However, the F-system exhibited higher trap-assisted recombination in the previous work, which was thought to originate from the morphology of active layer.³⁵

Morphology: GIWAXS

Now, we examine the morphological evolution of the active layers beginning with molecular ordering and packing via grazing-incidence wide-angle X-ray scattering (GIWAXS) measurements.⁵⁰ First, we examined pure films to determine how CN affects individual crystallization habits. The GIWAXS patterns of the PBDB-T donor polymer, presented in Figure 3- 2 (a-c) and Figure S2- 2, show that the polymer has a face-on orientation with respect to the

substrate surface. The solvent additive slightly enhances packing quality for both (100) and (010) by increasing the coherence length (D_{coh}) of both (Figure 3- 4a and b, see red squares). Also, 1% of CN additive increases the (010) face-on population which can be seen as an increase in the peak intensity (Figure 3- 2c).

For pure NFA films, the scattering results (Figure 3- 2 and SI), show that both small molecules have π - π stacking at $q \sim 1.8 \text{ \AA}^{-1}$ and lamellar at $q \sim 0.33 \text{ \AA}^{-1}$ corresponding to d-spacings of ~ 3.5 and 19 \AA , respectively. For both small molecules, π - π stacking populations are

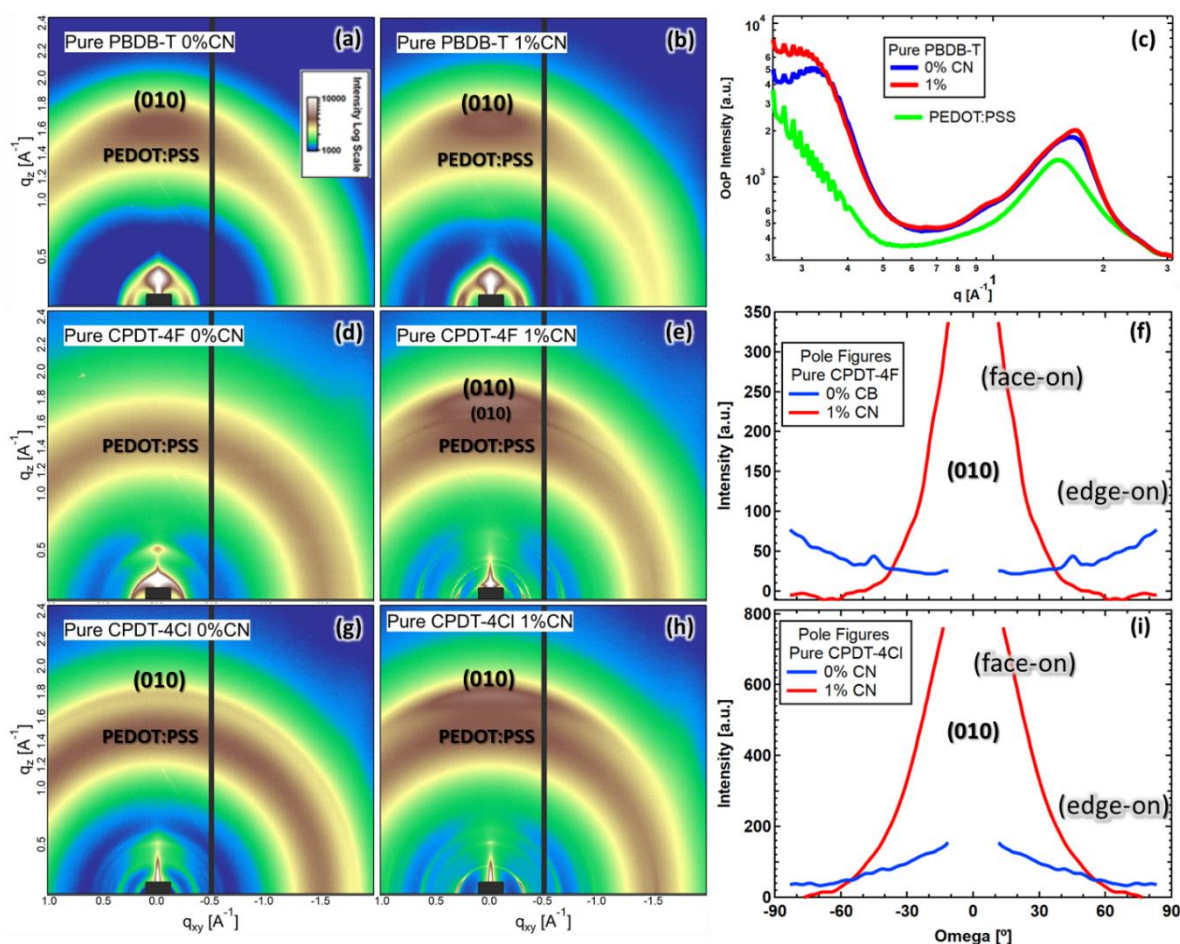


Figure 3- 2: (a,b,d,e,g,h) 2D GIWAXS images in as arbitrary color scale: pure materials without additive (left) and with 1% CN (middle). c) 1D GIWAXS profiles for pure polymer with and without CN extracted in the out of plane (OoP) direction to show changes in peak intensity of OoP π - π stacking. The PEDOT:PSS background is appended to the graph in green for reference. (f) and (i) present pole figures of π - π stacking in pure CPDT-4F and pure CPDT-4Cl, respectively, without additive (blue) and with 1% CN (red).

randomly oriented when processed without additive and orient mostly face-on to the substrate with 1% CN, as shown in the GIWAXS 2D images and pole figures in Figure 3- 2. The OoP (010) peak intensity increases with the additive, suggesting an increase in the small molecule crystal population. Additionally, new packing structures appear in both small molecules with 1% CN—especially in CPDT-4F where a second face-on (010) population forms with a very narrow reflection at $q \sim 1.7 \text{ \AA}^{-1}$ (d-spacing of $\sim 3.7 \text{ \AA}$, Figure 3- 2e and Figure S2- 3). Due to the very different peak width, we interpret this to be a different polymorph as has been seen in other OSC small molecules.³⁹ The coherence length of the primary polymorph, on the other hand, does not improve with CN for π - π stacking in both pure small molecules (blue and green squares in Figure 3- 4a).

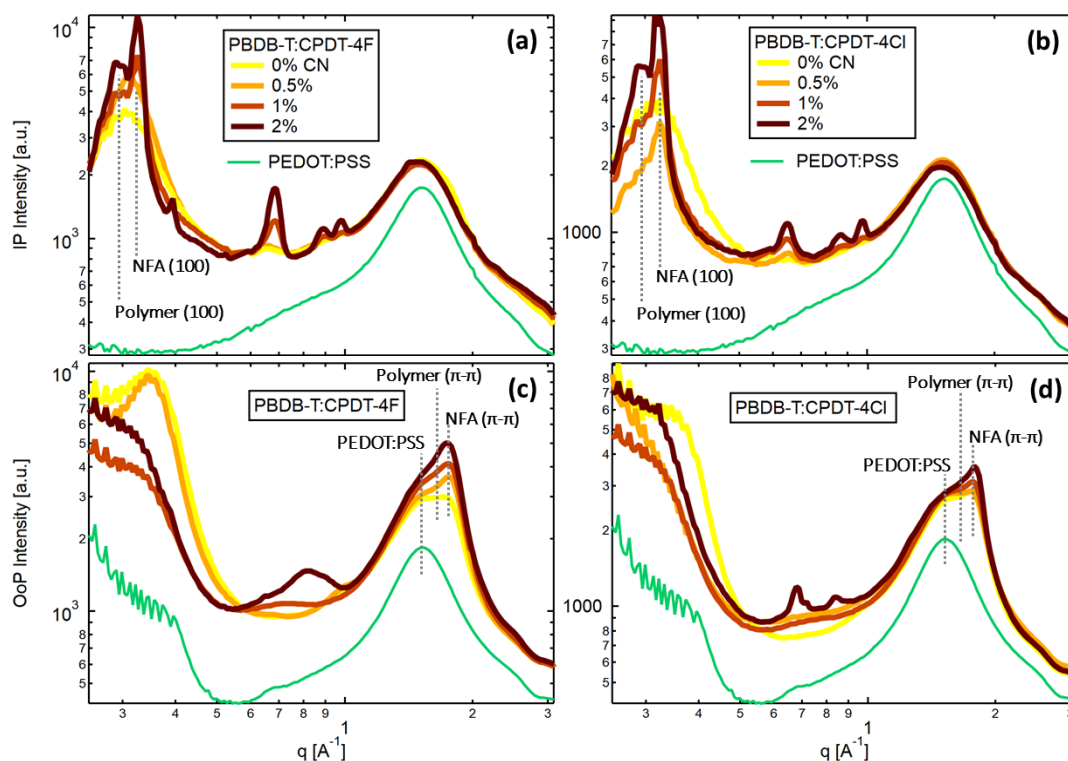


Figure 3- 3: 1D GIWAXS profiles for all the investigated blends (as indicated in the legends)—plus PEDOT:PSS background shown in green. Profiles in the IP sector (top) and OoP (bottom). Data for PBDB-T:CPDT-4F blends (a and c) and data for PBDB-T:CPCT-4Cl (b and d). More GIWAXS results and analysis can be found in the supporting information(Figure S2- 2 to Figure S2- 7, and Table S2- 3).

For the blends, the GIWAXS patterns are similar to the neat materials without any new formed packing structures (e.g. the second NFA polymorph) upon blending into BHJ films. The 1D scattering profiles are shown in Figure 3- 3 (more data and analysis in the SI). The peak positions and d-spacing of lamellar and π - π stacking are summarized in Table S2- 3. The focus here is on the in plane (IP) scattering peaks of (100) “lamellar”, and OoP (010) “ π - π ” stackings, because of their dominant effects on charge transport. In Figure 3- 4a, surprisingly, D_{coh} for π - π stacking of both the NFA and polymer materials is constant within uncertainties and remains relatively short in all blends (≤ 4 nm) with no obvious trends with solvent additive. On the other

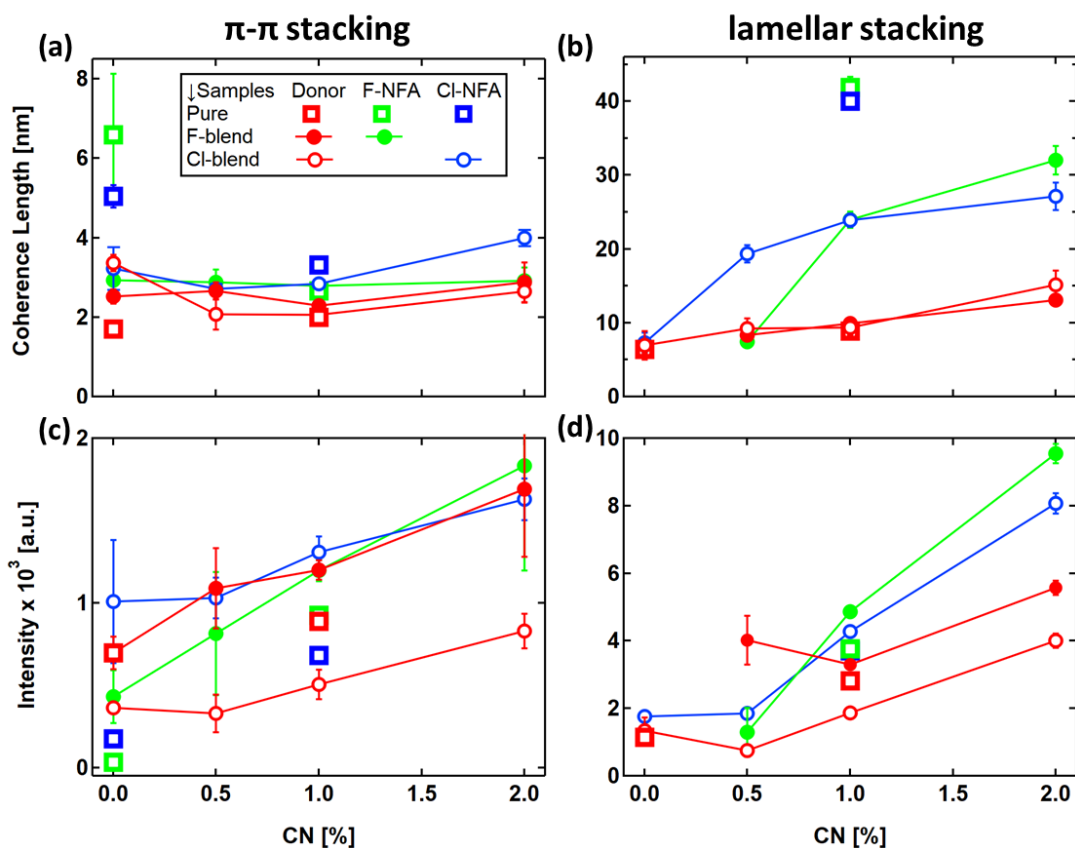


Figure 3- 4: GIWAXS analysis of coherence length and peak intensity for neat films and blends as indicated in the legends. Diffraction coherence length vs CN vol.% concentrations for (a) out of plane π - π stacking (010) and (b) in-plane lamellar stacking (100). (c) and (d) are analogous plots for diffraction peak intensity. The values are extracted from peaking fitting analysis of GIWAXS data, see examples methods description in Figure S2- 7.

hand, D_{coh} for lamellar of the polymer stacking increases with CN, in pure materials and blends, from 4 nm to 18 nm as shown in Figure 3- 4b. D_{coh} for lamellar of NFA stacking for in neat films with 1% CN was found to be ~40 nm. In blend films, Figure 3- 4b, D_{coh} of the NFAs monotonically increases with CN from 5 nm to 30 nm. Additionally, the intensities of both diffraction peaks (Figure 3- 4 c and d) of polymer and NFA materials in blends generally increase with CN. That suggests that rather than π - π coherence, the crystal population is the main beneficiary of the additive in both F- and Cl-blends. The increase in lamellar coherence lengths, seen for all materials, suggests a straightening of the polymer backbone and alignment of NFAs leading to the increases π - π stacking population. High crystalline domains are often considered beneficial in aiding charge transport.⁴¹ Positive correlations between FF and molecular ordering of NFAs has been reported in many non-fullerene systems.¹²³

Morphology: Microscopy

Figure 3- 5 presents key results from a multimodal microscopy study of the Cl-blends. That includes using: carbon edge scanning transmission X-ray microscopy (STXM), transmission electron microscopy (TEM), atomic force microscopy (AFM), (cross-sectional) secondary electron microscopy (SEM), and optical microscopy. STXM (Figure 3- 5 a-b, Figure S2- 11 and Figure S2- 13) and TEM (Figure 3- 5 d-e, Figure S2- 26, and Figure S2- 27) show that domains gradually coarsen and purify with the additive up to 1% CN, more noticeable in the Cl-blends. AFM scans (Figure 3- 5g-h and Figure S2- 20-Figure S2- 21) support and complement the STXM findings by showing that the film roughness increases with the concentration of solvent additive. The micron scale crystallization of Cl-NFA in the 1% CN blend film as measured by AFM is at odds with TEM and STXM because AFM was conducted

on separate films. This sample-to-sample discrepancy shows just how sensitive the CI-NFA is to

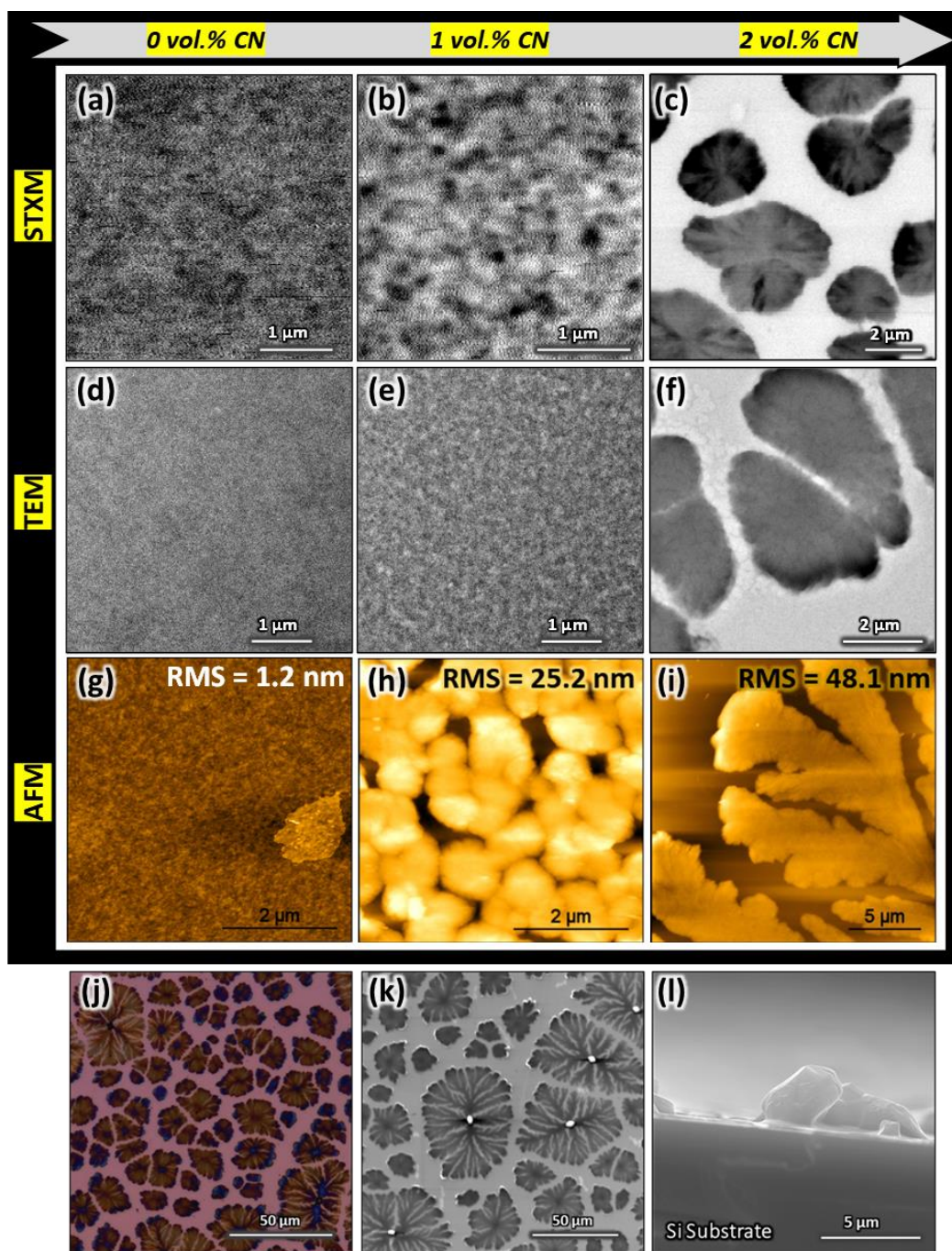


Figure 3- 5: Micrographs of PBDB-T:CPDT-4Cl blends with different amounts of solvent additive using X-ray, electron, and atomic force microscopies. STXM scans for blend with 0% (a), 1% (b), and 2% CN (c) where dark regions represent NFA-rich domains (more in Figure S2- 11-Figure S2- 15). TEM scans of blend with 0% (d), 1% (e) 2% CN (more in Figure S2- 26-Figure S2- 27). AFM scans of blends with 0% (g), 1% (h), and 2% CN (i) (more in Figure S2- 20-Figure S2- 21). Scans of the CI-blends with 2 vol.% CN: an optical microscope sane (j) (more in Figure S2- 23), a topology SEM scan (k), and cross-section SEM scan (l). More SEM scans in Figure S2- 24-Figure S2- 25). Scale bars are indicated for each scan.

the precise concentration of the additive. Notably, the F-blends were consistent across all measurements, possibly suggesting slightly less sensitivity.

In the F- and Cl-blends with 2% CN, strong phase separation and drastic domain growth take place, with domain size at the micron scale. The micron-size features are confirmed with STXM spectroscopic scans of pure films (Figure S2- 8) to be NFA domains, likely large crystals. The NFA domains in the 2% blends were easily observed under TEM, SEM of topology and cross-sections (Figure 3- 5k-l, Figure S2- 24Figure S2- 25), and even under the optical microscope (Figure 3- 5j and Figure S2- 23). In addition to the SEM images, AFM scans

indicate that the NFA crystals bulge out of the film. Within those large domains, neither TEM nor STXM were able to resolve obvious features or textures that originate from D/A domains (Figure S2- 11, Figure S2- 26 and Figure S2- 27). The polymer and NFA sensitivity to the processing additive in the blends are similar to the pure films. The pure polymer films remain smooth and uniform with no significant changes with CN (Figure S2- 28, Figure S2- 10, and Figure S2- 22). On the other hand, STXM and TEM scans of neat films of F- and Cl-small molecules show some textures that can be orientational domains or thickness variations (Figure S2- 10 and Figure S2- 28). Crystals of small molecules coarsen with CN—again more pronounced in the Cl-film than the F-film—leading to rougher film surfaces. TEM alone is not enough to conduct compositional analysis of the blends due to similarities in electron densities of the investigated NFA and polymer materials. STXM, on the other hand, is a more suitable tool to conduct this type of analysis because of its sensitivity of chemical bonds.

To quantitatively measure nanodomain composition in blends, we followed our previous methods of combining X-ray microscopy with spectroscopy.^{45,46} Spatially averaged spectra of F-

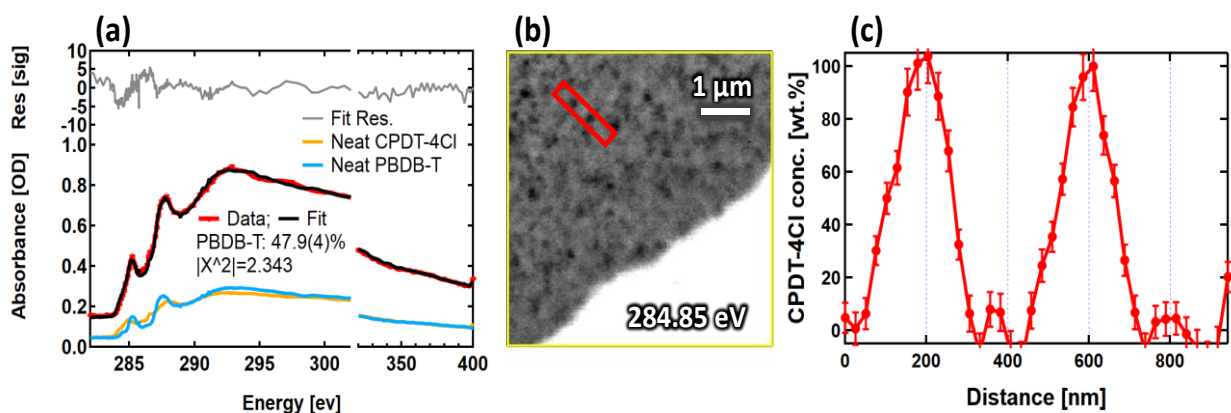


Figure 3- 6: PBDB-T:CPDT-4Cl with 1 vol.% CN blend. a) NEXAFS spectra for the blend and neat films (as indicated in the legends). The fit (black) of the NEXAFS spectrum of the blend (red) confirms the average weight ratio (i.e., ~ 55% small molecule). b) A STXM image that was acquired at 284.85 eV, which is a small molecule resonant energy. The dark regions indicate small molecule domains, and the gray regions indicate polymer-rich domains c) Compositional line out represents variation of the small molecule concentration across different domains along the red rectangle that is indicated on the STXM image in part b (for more details, refer to Figure S2- 14).

and Cl-blends—without and with 1% CN—confirm the average film composition, i.e.

donor:acceptor weight ratios (Figure 3- 6a, others in the SI). The results of composition mapping of the chlorinated blend with 1% CN, shown in Figure 3- 6b, show that pure small-molecule and pure polymer domains exist in this blend, which is with optimal concentration of CN. The extracted composition profile (Figure 3- 6c), reveals ~ 200 nm NFA domains surrounded by polymer. Having pure domains in polymer-small molecule OSCs has been proven to be beneficial for device performance by reducing charge recombination,²⁶ but 200 nm domains may be too large for efficient exciton capture. Such quantitative compositional mapping was not viable for the F-blends up to 1% CN due to the domain size in those films being below the STXM resolution.^{31,53} We attribute this to both the slightly higher NFA loading in Cl-blends (55% vs 50%) and the apparently increased propensity of the Cl-NFA to aggregate at lower CN concentrations than the F-NFA. The latter has been observed in blends (Figure 3- 5h, Figure S2- 20 and Figure S2- 21) and pure films (Figure S2- 22 and Figure S2- 28).

For 2% CN blends (both F & Cl), the composition analysis (Figure S2- 11-Figure S2- 15) shows NFA-rich domains (~ 65-70 wt.%) surrounded by polymer-rich domains (~60-90 wt.% for Cl-blends, but pure for F-blends). Impure domains here are not at odds with the conclusion of pure NFA crystals because these compositional analyses average over the vertical direction of a film. Therefore, it is likely that a vertical stratification of pure domains takes place. If that is accurate, then the topology AFM and SEM scans of the 2% CN blends would suggest that NFA crystals form on top of the (NFA-depleted) film. In particular, the cross-sectional imaging shows that those large NFA crystals tower (10s of microns) over the film, which is taller than thicknesses of films in their wet stage of processing (wet films usually are a few microns thick).^{39,124} We hypothesize that NFA runaway crystallization to be promoted by mobile NFA molecules that join from underneath then push large crystals upward with respect to the substrate surface. However, further work to understand what appears to be an interesting mechanism of film formation is required.

In short, both domain size and purity increase with solvent additive. Pure domains were detected in the Cl-blend with 1% CN, where domain purity is usually beneficial for device performance by reducing charge recombination.²⁶ Additional amount of additive beyond 1% CN results in strong phase separation leading to micron-scale NFA crystallites, which hinder exciton dissociation. The Cl-based films show increased sensitivity to the CN additive, aggregating and crystallizing at lower concentrations, even potentially being unstable to slight variations at the optimized concentration.

Morphology: RSoXS

To further examine how domain size and purity evolve as the amount of CN increases, especially in the blends with domains that were not well-resolved by microscopy, we turn to resonant soft X-ray scattering (RSoXS).⁴⁷ In addition to domain size and purity, RSoXS as a technique is very helpful in gaining insights into phase volume fraction and molecular orientation.^{41,44} Figure 3- 7a and c show the Lorentz corrected¹²⁵ scattering profiles for the F- and Cl-blends, respectively, versus the scattering vector (Q). For RSoXS, the donor-acceptor contrast is dependent on the index of refraction (Figure S2- 8). The Q-position of a scattering feature (Q*) approximately indicates the structure factor or spacing of scatterers called the characteristic length ($L_c = 2\pi/Q^*$).⁴⁴

For the F-blends, scattering data shown in Figure 3- 7a shows a feature that shifts to a lower Q with solvent additive, suggesting gradually growing domains with L_c increasing from about 30 nm to ~ 60 nm. Data of the F-blend with 2% CN shows that a secondary feature emerges at very low Q indicating morphological domains with size > 0.5 μm . We assign that to the NFA crystallites that were observed via microscopy. For all the Cl-blends, on the other hand, the scattering profiles show a primary feature ranging between $L_c \sim 25\text{-}50$ nm with additive with a secondary feature appearing and shifting to lower Q with increasing CN. Like the F-system, the secondary peak in Cl-blend with 2% CN points toward formation of large NFA domains with sizes >0.5 μm (summarized in Figure S2- 19). For the Cl blend with 1 vol.% CN, the secondary feature gives $L_c \sim 200$ nm which is in good agreement with the STXM results (Figure 3- 6c). Our results of examining anisotropic scattering patterns (Figure S2- 16, Figure S2- 17 and Figure S2- 19) show that there is no drastic change of molecular orientation with solvent additive or type of

halogenation. Although orientational scattering might still present, we believe that is negligible compared to material scattering.

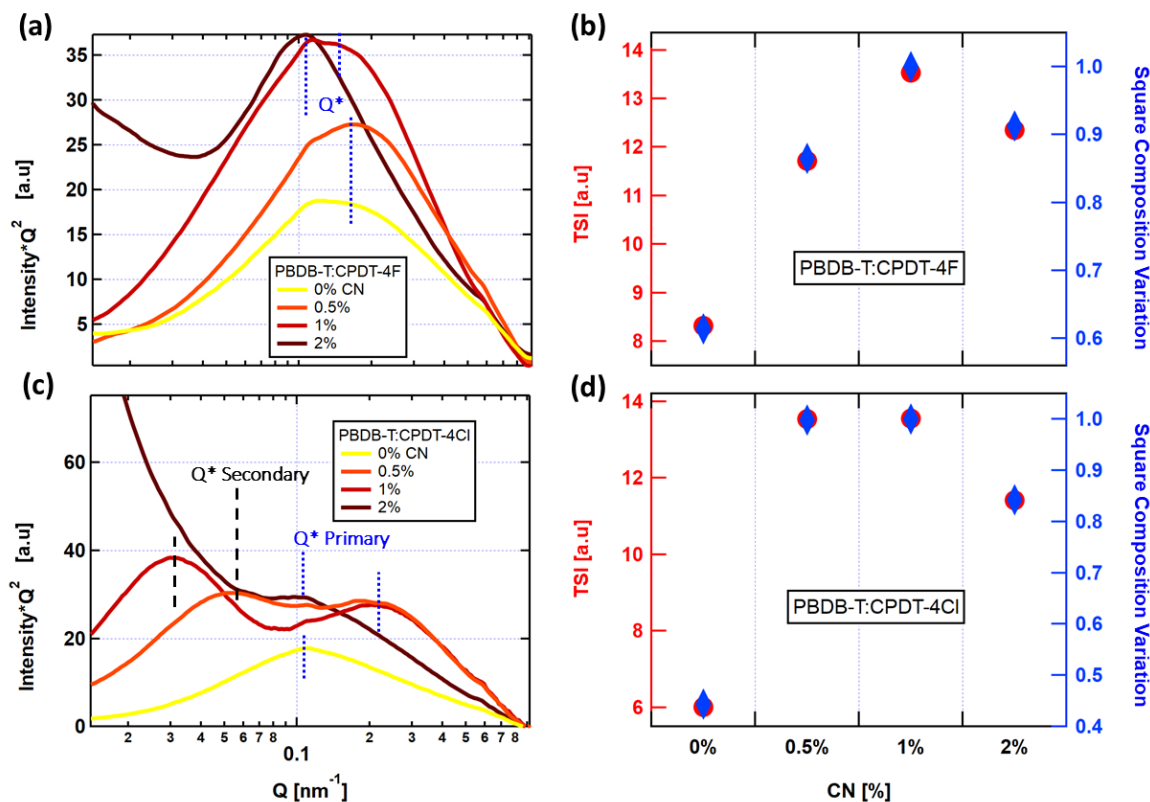


Figure 3- 7: Scattering profiles and TSI for all blends. a) RSoXS 1D averaged profiles for PBDB-T:CPDT-4F blends. Their TSI and composition variation are shown in (b). TSI calculated by integrating areas under scattering profiles. Then the composition variation was calculated by normalizing TSI for all blends to TSI of the blend with 1% CN. c) 1D scattering profiles for the PBDB-T:CPDT-4Cl blends. d) TSI and composition variation values for the Cl-blends. In b and d, the red circles represent TSI, and blue diamond shapes represent composition variation “average domain purity”. This data was acquired at X-ray energy of 285.2 eV, Lorentz corrected, and corrected for X-ray fluorescence background. Where X-ray energy of 285.2 eV is slightly below the resonant energy of the polymer material, to increase the material contrast. Additional scattering data taken at different energies can be found in Figure S2- 16 and Figure S2- 17.

Thus far, the RSoXS results in agreement with STXM and GIWAXS in terms of domain-size growth with solvent additive. The scattering data also shows that multi-length scale features appear with solvent additive, that happens sooner in the Cl-blends than the F-films. Multi-length scale domains, often manifested as two peaks in the scattering profiles, have been observed in

other binary and ternary BHJ blends.^{126–128} Usually, the scattering features at high Q are associated with a domain size that is crucial for device performance, that includes aspects such as exciton diffusion length and J_{sc} . In this work, therefore, we refer to those high-Q scattering features as the primary features. To examine how average domain purity changes with solvent additive, the total “or integrated” scattering intensity (TSI) of the RSoXS profiles is commonly used.^{26,41,44} Figure 3- 7b and d present the TSI, where the composition difference between domains (and therefore domain purity) is proportional to square root of TSI. That also can be used to investigate morphological details at the donor-acceptor interfaces.^{28,31} The results show that the average domain purity in the examined blends increases with the amount of solvent additive up to 1% CN. Compared to the F-blends, the CI-samples seem to purify faster with solvent additive. TSI results of the CI-blends suggest that domain purity in the film with 0.5% CN is almost as high as in the 1% CN sample, where the latter consists of STXM-measured pure domains.

The presence of multi-length scale morphology, however, demands careful analysis of the RSoXS TSI to arrive to more reliable conclusions. The goal is to determine the significance of the component scattering intensity (CSI) of both the primary and secondary features. To examine that, we apply two-peak fitting and extracted the CSI values by following previous procedures that have been implemented to analyze multi-feature RSoXS data of OSCs systems.^{127,129} That analysis assumes multi-feature scattering data comes from distinct uncorrelated structures. The multi-peak fitting results and comparison (see examples in Figure S2- 18) show that CSI of primary peaks is the main contributor to TSI, and the CSI of secondary features is negligible. Thus, we base our interpretations of domain purity being enhanced with CN on the observed increases in CSI of the primary peaks, which corresponds to morphological

features with crucial size to affect performance. It is worth noting that TSI drops significantly for blends with 2% CN, which we attribute to reduction in phase volume fraction as many NFA molecules migrate into much larger domains.

Based on RSoXS and STXM results, the main finding is that domain purity in both halogenated systems increases with amount of solvent additive and reaches complete domain purity around 1 vol.% CN. In general, domain purity has been viewed as a critical aspect of morphology that can be correlated to many device performance parameters in OSCs such as bimolecular recombination, FF, and Jsc.²⁶

Discussion

Based on the combined morphological results, Figure 3- 8 depicts the general trend of morphology evolution with CN additive in both halogenated systems. Red and blue colors represent NFA and polymer domains, respectively. The lines represent ordered NFA molecules (red) and ordered polymer chains (blue). With higher concentration of solvent additive, the length of the lines increases indicating improvement in the lamellar stacking, but not in the π - π

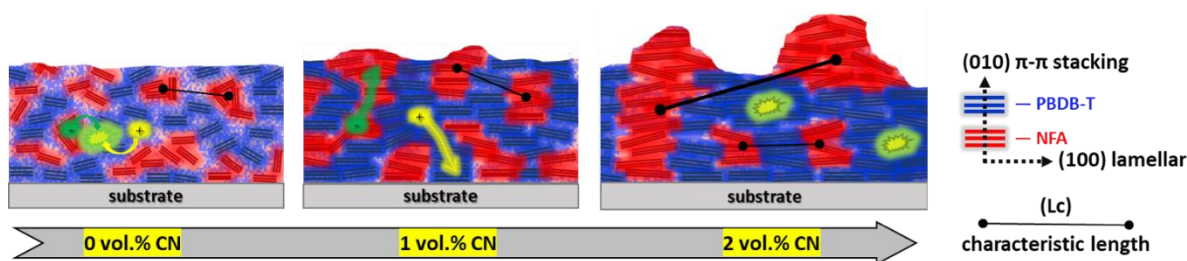


Figure 3- 8: A general depiction of morphology evolution with solvent additive (CN) in the investigated blends. Blue regions indicate polymer-rich domains with blue lines representing ordered polymer chains. The red regions represent NFA-rich domains with red lines indicating ordered molecules. The π - π stacking of the polymer which is mostly face-on with respect to the substrate as depicted here does not mean that the direction of the fibril growth is known in those systems.

stacking (refer to the coherence length results). It is noticeable as depicted that NFAs start with random crystal orientations (direction of the red lines) but prefer to orient face-on with respect to the substrate when CN is added. Additionally, the solvent additive increases populations of face-on π - π stacking which was measured via GIWAXS as an increase in peak diffraction intensities of both NFA and polymer materials. For domain size, films processed from CB consist of small domains that slightly grow with solvent additive, in addition to large-scale domains that evolve with CN. Finally, domain purity increases with CN and is depicted as pure blue and pure red colors.

Since the F- and Cl-active layers show mostly similar trends in terms of their device performance with solvent additive (CN), they were expected to have similar morphologies. Our

findings in general confirm that where solvent additive enhances domain purity, increases crystallinity and packing, and eventually leads to multi-length scale domains in both systems. However, we find the main difference between the two systems is the higher sensitivity to the amount of CN in the Cl-films. Their sensitivity is manifested as secondary features in RSoXS profiles that emerge immediately even with 0.5% CN. Then domains continue to grow from ~ 100 nm (0.5% CB) to ~ 200 nm (with 1% CN) before the NFA crystals eventually grow into 10s-of-microns domains with 2% CN. In the F-systems, on the other hand, the secondary features form with relatively higher concentration of CN >1%, where micron-scale domains suddenly appear in the 2% CN film. This seems to be dependent on the type of halogenation where CN enables stronger aggregation, phase separation, or intermolecular interaction in the CPDT-4Cl molecules than CPDT-4F. Such a difference could originate from a stronger interaction of the Cl-NFA with CN due to the matched halogens as compared with the unmatched F-NFA. Further investigation remains required to examine the thermodynamic effects of CN on the different types of halogenations.

At the optimal processing conditions of this study, 1% CN, the F-blend have domains with size ~ 50 nm whereas Cl-blends compose of multi-length domains ~ 25 nm and ~200 nm. Although the primary small domains are beneficial for exciton dissociation, having relatively large features in the Cl-blends may aid as continuous pathways that facilitate charge transport to the electrodes. In comparison, the F-blend with 1% CN consists of only small domains which may increase the possibility of having isolated domains that act as traps. If that scenario is true, then it might be the explanation to why trap-assisted charge recombination was higher in the F-blend than Cl-blend. The charge recombination was examined previously via measurements of V_{oc} as a function of incident light intensity.³⁵ We cannot rule out the possibility of co-existence

of impure domains in the F-blend with 1% CN for two reasons. First, quantitative examination of domain purity in that BHJ sample via STXM was limited due to domain size being below the resolution limits of the technique.⁵³ Secondly, although the CI-blend with 1% CN contains 100% pure domains via RSoXS and STXM, also the RSoXS TSI of the 1% CN F-blend point towards domains with high purity, none of that is enough to quantitatively measure domain purity in the F-blend without absolute scattering intensities. Thus, it is possible that the relatively higher rate of trap-assisted recombination in the F-blend with 1% CN may be due to some percolation via domain mixing.

To examine potential structure-property relations in the investigated BHJ systems, FF and J_{sc} are plotted in Figure 3- 9a-b as functions of normalized TSI.²⁶ The data of the 2% CN blends are not presented in Figure 3- 9, but the results—as mentioned above—confirm high domain purity regardless of the relatively lower normalized TSI. That drop in TSI for the 2% CN blends is attributed to reduction in volume fraction of the small domains of NFAs as they migrate into largely crystallized domains. Clear correlations can be seen in Figure 3- 9 where both device parameters, FF and J_{sc} , increase monotonically with domain purity of the primary features. Those primary features, i.e. small domains, are size-compatible with the standard exciton diffusion length (~ 10 nm) in OSCs. Linear correlation between domain purity and FF is often found in OSC,²⁶ where domain purity suppresses charge recombination. In the investigated F-blends, the device FF improved by about 60% up to the optimum CN concentration. Interestingly, the average domain purity as measured by the normalized TSI is about 60% higher over the same series. The CI-blend processed from CB has FF=47% that improves to 66% with 1% CN. We also find direct correlation between J_{sc} and domain purity, which is usually known for reducing charge recombination.²⁶

Another important morphological aspect is crystallinity, which improves with amount of the plasticizer additive in the investigated films, potentially aiding charge transport across the active layers.⁴¹ Positive correlations between FF and coherence length of small-molecules has been established in many NFA systems.¹²³ We did not see any obvious trends in the D_{coh} values of π - π stacking with solvent additive. Therefore, we plotted FF and Jsc in Figure 3- 9c-d as functions of the diffraction peak intensity of π - π stacking of the NFAs, the latter is often related to relative degree of crystallinity (rDoC).⁴¹ We similarly find a monotonic relationship between the face-on π - π stacking intensity of the NFAs and the device parameters; FF and Jsc. However,

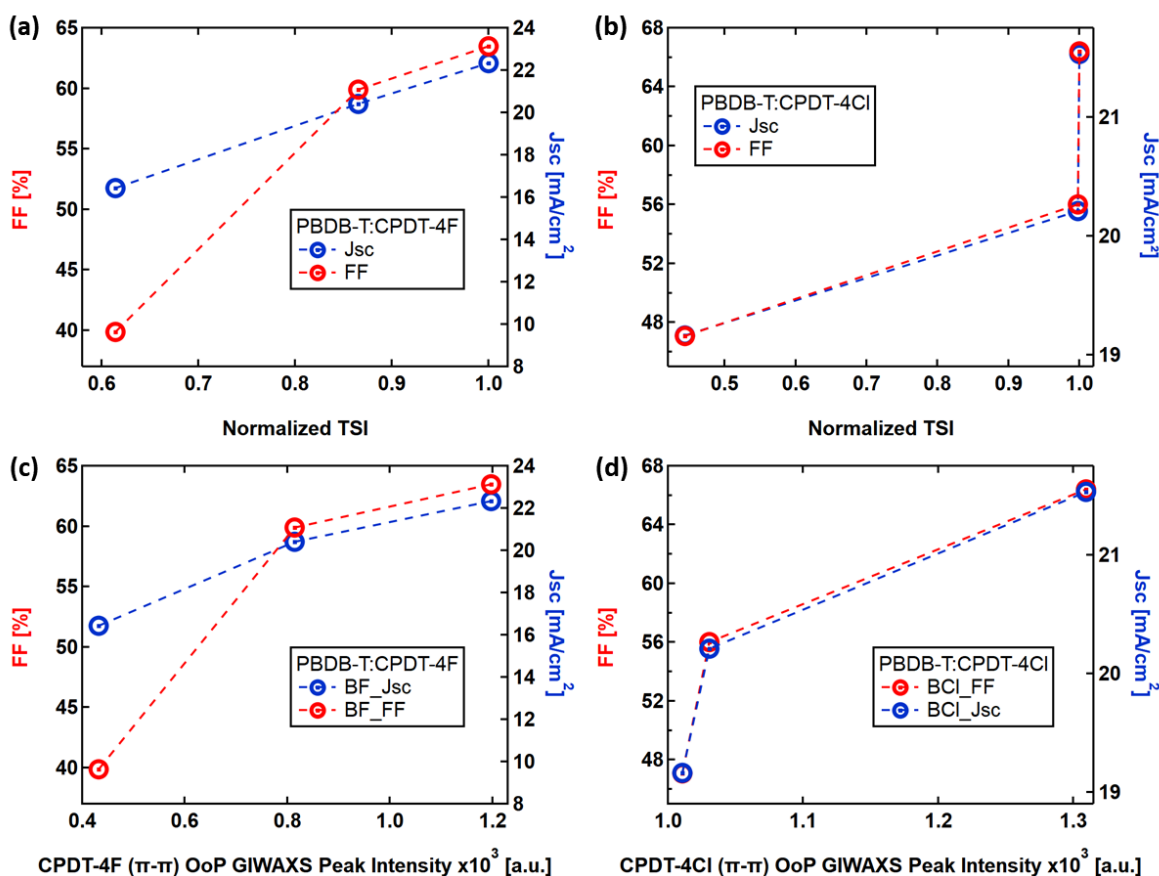


Figure 3- 9: FF and Jsc plotted as functions of normalized TSI: a) For the PBDB-T:CPDT-4F blends. b) For the Cl-blends. FF (red circles) plotted on the left y-axis and Jsc (blue circles) on the right y-axis. FF and Jsc plotted as functions of GIWAXS peak intensity of the NFA π - π stacking: c) for the F-blends and (d) for the Cl-blends. Note that the presented results here are for blends with 0, 0.5, and 1 vol.% CN.

2% CN leads to over-crystallization, high domain purity, and oversized domains that likely result in poor efficiency of exciton dissociation and thus low J_{sc} .¹⁴ On the other hand, V_{oc} constantly decreases as the concentration of solvent additive increases which can be attributed to the improved crystallinity.¹³⁰ Increased electron delocalization due to crystallinity is known for lowering the acceptor's lowest unoccupied molecular orbital (LUMO) energy level which reduces V_{oc} . At the same time, crystallinity decreases charge recombination which increases V_{oc} . It appears that the former effect dominates the latter in the investigated NFA systems. This behavior is commonly observed in many OSCs systems with processing additives.^{131–133}

Importantly, the oversensitivity of device performance and morphology of NFA systems to the amount of processing additive is similar to the detrimental behavior seen in small-molecule:fullerene systems.²⁴ The findings of this work would suggest the significant reduction in device performance of those CPDT-based OSCs that we have observed previously,³⁵ even with 0.1% CN above optimum, can be attributed to potentially undesirable crystallization and strong phase separation. This suggests that CN probably is not a compatible solvent additive for large scale fabrication of NFA OSCs as extreme precision is required to avoid any excess amount of additive that could result nucleation of large-scale crystallization that ruins the panel. It is worth mentioning that the solvent additive used here, CN, is a commonly used plasticizer to optimize device performance in many of the state-of-the-art NFA systems such as PM6:Y6.^{32,33} Although device performance and perhaps morphology of PM6:Y6 system seem less sensitive to amount of processing additive around optimal conditions,^{18,32} extra residuals of solvent additive result in drastic evolution in molecular packing, leading to significant reduction in device performance.^{66,134} The extreme device-performance sensitivity of PM6:Y6 OSCs to concentrations of CN was found in films with thickness (400 nm) that is better suitable for

industrial-scale production. Specifically, the optimal amount of CN (1.5%) yields PCE = 14.4%, while 1.8 % of CN gives only 8.6%.⁶⁶ Initial microscopic results of ongoing work, provided in Figure S2- 29, manifest the morphological sensitivity of PM6:Y6 blends to excessive amounts of CN. However, thorough morphological investigations of the sensitivity of this novel system to concentrations of processing additive needs further exploration.

Routes to overcome such an issue include introducing alternative additives,¹³⁵ binary solvent additives,¹⁷ non-volatile solid additives, and third components as in ternary OSCs.^{14,136} For example, we have previously substituted the halogen element Cl in the CN molecule with F or Br to mitigate phase separation in PM6:Y6 OSCs and achieved 17.5% PCE.¹⁸ Thus, modifying molecular structure to resist runaway crystallization may be one route to make OSCs more robust. Other work focuses on substituting CN with a halogen-free additive that actually shows comparable effects on optimizing efficiencies in PM6:Y6 OSCs.¹³⁷ It is noticeable in the latter study that the device performance is quite tolerant to the amount of additive beyond optimum. This result is consistent with ours that similar halogens on the additive and NFA may increase the propensity to crystallize. Despite the successful lab endeavors to optimize device performance in NFA OSCs, scaling up device fabrication with processing additives imposes many challenges. For example, optimization of the rheological properties of BHJ inks and extreme precision to avoid undesirable solvent residuals are required when processing large-area devices with plasticizers.¹³⁸ Additionally, any excessive residuals of solvent additives that lead to undesirable morphologies such as strong aggregation result in film hardness that is incompatible with roll-to-roll fabrication.¹³⁹ Overall, the long-term stability of devices processed with additives like CN remains questionable.¹⁴

There are some possible alternative strategies for industrial printing of NFA OSCs. That includes manipulating BHJ ink concentrations to optimize device performance,¹³⁹ exploring eco-friendly single solvent compatibilities with BHJ materials,¹⁴⁰ and re-engineering of NFA molecular structures for better morphological outcomes.¹⁴¹ Successful approaches to avoid issues related to solvent additives are even encouraging to target additive-free fabrication methods. For example, Jeong et al. have successfully blade-cast PTB7-th:EH-IDTBR OSCs with device area of 85 cm² and PCE > 8% by simply controlling the ink concentrations. That showcases an additive-free and temperature-independent printing method that can be potentially implemented in large scale to prevent undesirable effects of those processing treatments on film structures.¹³⁹ Other exciting work by Dong et al. of synthesizing a Y6 derivative (named DTY6) with longer alkyl chains resulted in a good solubility in non-halogen (o-xylene) solvent and suppressed excessive aggregations compared to Y6. They found that PM6:DTY6 OSCs, processed from a single non-halogen solvent, outperform the record-efficiency PM6:Y6 devices. That also allowed for fabrication of blade-cast devices with active areas of 18 cm² and certified PCE of 13.98 %.¹⁴¹ Although we have only focused on CN in this study, the findings encourage devoting more attention to explore alternative additive-free strategies of large-scale production of NFA OSCs to control the sensitivity to processing additives.

Conclusion

In this study, a characterization of device performance and morphology of PBDB-T: non-fullerene OSCs was conducted to examine their sensitivity to the processing additive. CN was used as a plasticizer additive to optimize device performance. We find the device performance to be very sensitive to the amount of additive where PCE was almost doubled up to the optimum concentration, 1% CN. Here, domain purity and crystallinity strongly correlate with device FF

and Jsc up to optimal conditions. However, any additional increments in the concentration of the additive, beyond optimum, lead to a drastic fall off in device performance. Excessive phase separation and over-crystallization occur in the blends with 2% CN, leading to large NFA crystals which we interpret as the main cause to poor performance. The over sensitivity of device performance and morphology to the processing additive in the examined NFA OSCs is remarkable. This seemingly common issue among many small-molecule systems stresses the importance of careful selections of solvent additive or even additive-free methods to achieve successful fabrication of NFA OSCs. We also examined the impacts of the type of halogenation of NFAs (fluorination vs. chlorination) on meso-structures and found that the Cl-molecules show a higher rate of aggregation. Results of this work give insights onto the effects of halogenation and solvent additive on morphology and device performance of synthetically simple, near infra-red CPDT-NFA based OSCs.

Experimental Section

Device fabrication

The device structures were ITO/PEDOT:PSS/ active layer/Phen-NaDPO/Ag. Organic solar cell devices were fabricated using ITO-coated glass substrates ($15 \Omega \text{ sq}^{-1}$), which were cleaned with detergent water, deionized water, acetone and isopropyl alcohol in an ultrasonic bath sequentially for 20 min, and further treated with UV exposure for 30 min in a UV-ozone chamber. A thin layer (ca. 30 nm) of PEDOT:PSS (Bayer Baytron 4083) was first spin-coated on the pre-cleaned ITO-coated glass substrates at 4000 rpm and baked at 160°C for 15 min under ambient conditions. The substrates were then transferred into a nitrogen-filled glovebox. Subsequently, the precursors of the photoactive layer were stirred overnight at 80°C before spinning. The optimized overall concentration were 22 mg/ml and 20mg/ml chlorobenzene

solution with feed ratio of 1:1.2 (w/w) and 1:1 (w/w) for PBDB-T: acceptors, respectively. Solvent additive, 1-CN, was used to improve the intermixing of the electron donor and acceptor phases. The spin speed was 2000 rpm, and the corresponding thickness was around ~100 nm. Then Phen-NaDPO as the electron transporting layer was spin-coated on the active layer by 2000 rpm from isopropyl alcohol solution. At the final stage, the substrates were pumped down in high vacuum at a pressure of 3×10^{-4} Pa, and Ag layer (100 nm) was thermally evaporated onto the active layer. Shadow masks were used to define the OSC active area (0.11 cm^2) of the devices.

Device testing: J-V curves and external quantum efficiency (EQE)

The current density–voltage (J–V) characteristics of unencapsulated photovoltaic devices were measured under N₂ using a Keithley 2400 source meter. A 300 W xenon arc solar simulator with an AM 1.5 global filter operated at 100 mW/cm^2 was used to simulate the AM 1.5G solar irradiation. The illumination intensity was corrected by using a silicon photodiode with a protective KG5 filter calibrated by the National Renewable Energy Laboratory (NREL). The external quantum efficiency (EQE) was performed using certified IPCE equipment (Zolix Instruments, Inc, Solar Cell Scan 100). The average parameters were calculated from 10 independent cells.

X-ray measurements

We used synchrotron X-ray diffraction, microscopy, spectroscopy, and scattering to investigate the nanomorphology of the active layers in those NFA OSCs. The X-ray measurements (NEXAFS/STXM, RSoXS, GIWAXS) were conducted at the Advanced Light Source (ALS) at Berkeley National Lab in CA at 5.3.2,⁵² 11.0.1.2,⁴⁷ and 7.3.3⁵⁰ beamlines, respectively. The fabrication of the examined films was the same as the J-V devices which is similar to the previously published batch of OSC devices.³⁵ GIWAXS data was conducted with

hard X-ray (energy=10 keV) at an angle of incidence= 0.2° , which is higher than the critical angle of the Si substrate. Samples were cast on PEDOT:PSS layer on Si substrates. RSoXS data was conducted at X-ray energies 270 and 285.2 eV. Thin films—from the same substrates as the GIWAXS films—were floated off in deionized water onto low stress Si_3N_4 membrane with size= 2 mm^2 and thickness= 100 nm. NEXAFS absorbance spectra were collected at the same spot of each film as where the RSoXS data was taken to determine the exact thickness of the scattering part of each film. Then RSoXS data was normalized to thickness film. STXM images were acquired at resonant energies of the polymer and small molecule materials as indicated in graph captions and legends in main text and supporting information. The imaging energies were selected based on the NEXAFS spectra of the neat materials (see Figure S2- 8). STXM and NEXAFS were combined to extract quantitative, chemical maps of composition. The STXM and NEXAFS samples were floated off in deionized water onto TEM grids from the same substrates used for GIWAXS and RSoXS.

Atomic force microscopy (AFM) and scanning electron microscopy (SEM)

The AFM and SEM samples were cleaved from the same substrates that were prepped for the X-ray measurements. The film roughness was probed via AFM (Dimension Icon, Bruker) with SCANASYST-AIR silicon tip on nitride lever (70 kHz, 0.4 N/m). The film topology and cross-section of the 2% CN blend films were acquired via SEM (QUANTA FEG250, FEI) with the electron gun at 30 kV or SEM Tescan Vega3. The samples were sputter coated with gold for better surface conductivity.

Transmission electron microscopy (TEM)

Samples were cast on PEDOT:PSS/Si substrates then floated in deionized water onto TEM grids for TEM measurements. TEM images were acquired in bright-field mode via FEI

Technai G2 20 Twin (Thermo Fisher, Waltham MA, USA) with a 200 kV LaB6 electron source and FEI Eagle 4k CCD camera detector or via a Talos F200S.

Statistical analysis

The sample size of J-V measurements is ten independent devices ($n=10$ cells). The presented parameters are the mean \pm standard deviation. The AFM data was processed using Gwyddion 2.60 software, ($n=1$). The root mean square (RMS) roughness was extracted for the distribution of surface height over the probed film area of each film. The probed film areas are: ($2\ \mu\text{m} \times 2\ \mu\text{m}$) for pure materials, ($15\ \mu\text{m} \times 15\ \mu\text{m}$) for PBDB-T:CPDT-4F blend with 2% CN, ($20\ \mu\text{m} \times 20\ \mu\text{m}$) for the PBDB-T:CPDT-4Cl blend with 2% CN, and ($5\ \mu\text{m} \times 5\ \mu\text{m}$) the rest of the blend films. Custom software based in Igor Pro are used to process and analyze all X-ray data for RSoXS, STXM/NEXAFS, and GIWAXS. Sample size for all those X-ray measurements is ($n=1$). For the GIWAXS measurements, ($n=1$), 2D scans collected via CCD camera are reduced into 1D profiles via custom and Nika software.¹⁴² The reduced 1D profiles are then normalized to film thickness, sample length, and X-ray exposure time. Peaks of interest were Gaussian fitted, with fit parameters [peak position, peak height (intensity), and full width at half maximum (FWHM)]. Fitting results of peak intensity are presented with error bars that were extracted from peak fitting. Other fitting results such as FWHM of specific GIWAXS peaks are used in Scherrer analysis to calculate coherence lengths. RSoXS data was processed like GIWAXS, but with a custom software based on Igor Pro. That takes into account other important experimental parameters such as background readings of the CCD camera and X-ray intensity of direct beam at a given scattering energy. NEXAFS spectra analysis for composition and optical constants calculations was conducted using custom Igor Pro based codes. Details of spectra peak fitting, residuals, chi-squared value, and origin of uncertainties can be found in our previously published

procedure.⁴⁵ Also, a custom software was used to convert STXM data into quantitative composition maps, details of the analysis of composition maps can be found in our previous procedure.⁴⁶

Acknowledgements

This work is funded mainly by the US National Science Foundation DMR Electronic and Photonics Program under Grant #1905790. This grant supported O.A. V.M., and D.G. were supported by the US Department of Energy Early Career Research Program under Grant DE-SC0017923. This research used resources of the Advanced Light Source, which is a DOE Office of Science User facility under contract no. DE-AC02-05CH11231. Also, this research used the resources of the Franceschi Microscopy & Imaging Center at Washington State University.

CHAPTER 5: FIELD-INDEPENDENT GEMINATE RECOMBINATION LIMITS CHARGE
SEPARATION IN PM6:Y6 ORGANIC SOLAR CELLS: DRIVEN BY MOLECULAR
ORDERING OF Y6

Alqahtani, O.; Alotaibi, A.; Collins, B. A. “FIELD-INDEPENDENT GEMINATE RECOMBINATION LIMITS CHARGE SEPARATION IN PM6:Y6 ORGANIC SOLAR CELLS: DRIVEN BY MOLECULAR ORDERING OF Y6”, 2023.

Written for submission to the Journal of Physical Chemistry Letters and reproduced here in its original format.

Attributions:

O. Alqahtani fabricated the devices, conducted device performance testing, and nanostructure characterization, and wrote the first draft of the manuscript. A. Alotaibi helped with the TDCF experiment. B. A. Collins provided funds and supervised this study.

Note: the supporting information of this manuscript is provided in APPENDEX C.

Abstract

This study focuses on investigating the impacts of utilizing a green solvent processing additive, phenylanthracene (PN), on device performance and nanostructure of the state-of-the-art binary PM6:Y6 organic solar cells (OSCs). A holistic analysis of charge generation losses, along with a suite of synchrotron X-ray techniques are leveraged to explore potential structure-property relationships in PM6:Y6 OSCs as a function of PN additive concentration. We find that PN increases Y6 aggregation and domain purity, leading to more efficient light absorption and charge extraction. PN also reduces bimolecular (BMR) and field-dependent (FD) geminate recombination types. However, as the amount of the PN additive passes optimum, 0.5 vol %, we observed an increase in field-independent (FI) geminate recombination. That leads to a reduction in the charge separation efficiency. The charge separation behavior as a function of PN concentration follows the trends of device performance. Our morphological investigation suggests that the FD geminate recombination loss can be a result of the increasing molecular order of Y6 at PN concentrations ≥ 2 vol%. These findings highlight the importance of detecting structure-property correlations when optimizing the device performance of non-fullerene OSCs using green solvent additives, which have the potential as low-cost, printable technology for renewable energy.

Introduction

Organic solar cells (OSCs) are attractive due to the tunability of their optoelectrical properties, mechanical flexibility, and abundance of materials. The record of power conversion efficiency (PCE) of OSCs is approaching 20%, with non-fullerene acceptors (NFA) leading the way.^{10,103,143,144} Thorough understanding of structure-property relationships and quantification of charge losses are essential to realizing the potential of NFA OSCs.

The family of Y-NFA^{32,103,143} can yield efficient bulk heterojunction (BHJ) OSCs, e.g. PM6:Y6 OSCs can give PCE > 17%,^{18,145} are usually processed from chloroform (CF) as a main solvent with halogenated additives such as Br-N Cl-N.¹⁸ 1-chloronaphthalene (CN) is commonly used as a plasticizing solvent additive and found to optimize film nanostructure and hence device performance.^{18,32} However, we have seen previously that CN requires extreme precision to avoid excessive amount of solvent additive, which can lead to runaway crystallinity of NFA molecules^{146,147}. Crystallinity of NFA molecules is an essential aspect of active-layer morphology. It is important knowing the balance when optimized NFA molecular packing through film processing with solvent additives.

Ye et al. have proposed a hydrocarbon solvent additive, namely phenyl-naphthalene (PN), to replace CN. Their work demonstrates that PN can effectively replace CN to optimize device performance in multiple NFA OSC systems while relatively maintaining efficient device performance even with excessive amounts of the PN additive.¹³⁷ However, the impacts of PN on PM6:Y6 device performance and nanostructure have yet to be examined in detail. Additionally, it has been shown that the PM6:Y6 system has some field-independent (FI) geminate recombination losses, but the morphological origins of that have yet to be specified.¹⁴⁸

Here, we substitute CN with the halogen-free additive, PN, to optimize device performance of PM6:Y6 OSCs. Motivated by our previous work of quantifying loss mechanisms in polymer:fullerene OSCs through a holistic analysis,^{27,149} we exploit the potential of this analytical method to examine charge losses in PM6:Y6 systems as a function of PN concentration. The evolution of film morphology with PN additive is probed via a suite of synchrotron-based X-ray techniques combined with complementary electron-based methods. We also examined whether excessive amounts of PN lead to runaway crystallinity similar to CN.

In this work, we examined in detail the loss mechanisms and nanostructure evolutions of PM6:Y6 OSCs processed from CF with different concentrations of PN as a solvent additive. The device performance maximizes at 0.5 vol % PN yielding PCE of ~ 14.5 %, then decreases as the amount of PN increases. Despite the decline in the overall device performance, PN reduces the absorption and FD geminate recombination and improves charge extraction by means of lowering BMR. X-ray scattering results show that domain purity increases with solvent additive. Also, X-ray diffraction measurements show that Y6 molecules become more ordered at PN \geq 2 vol % as manifested by the pronounced appearance of its backbone (001) diffraction peak. We conclude that this 3D order in Y6 molecules at PN \geq 2% causes the observed increase in FI geminate recombination, which leads to less charge separation. Finally, we find that even at elevated concentrations of PN (\geq 2 vol %), there are no signs of runaway crystallinity in the NFA molecules compared to using CN additive, as observed in previous studies.^{146,147} Those findings present the potential for using eco-friendly solvent additives to optimize device performance in NFA OSCs. It is worth mentioning that both the main (host) solvent (CF) and the additive (guest) solvent (PN) evaporate and totally leave the films shortly after casting, leaving behind solid thin film of the PM6:Y6 active layers.

Results

Device performance and optoelectronic testing

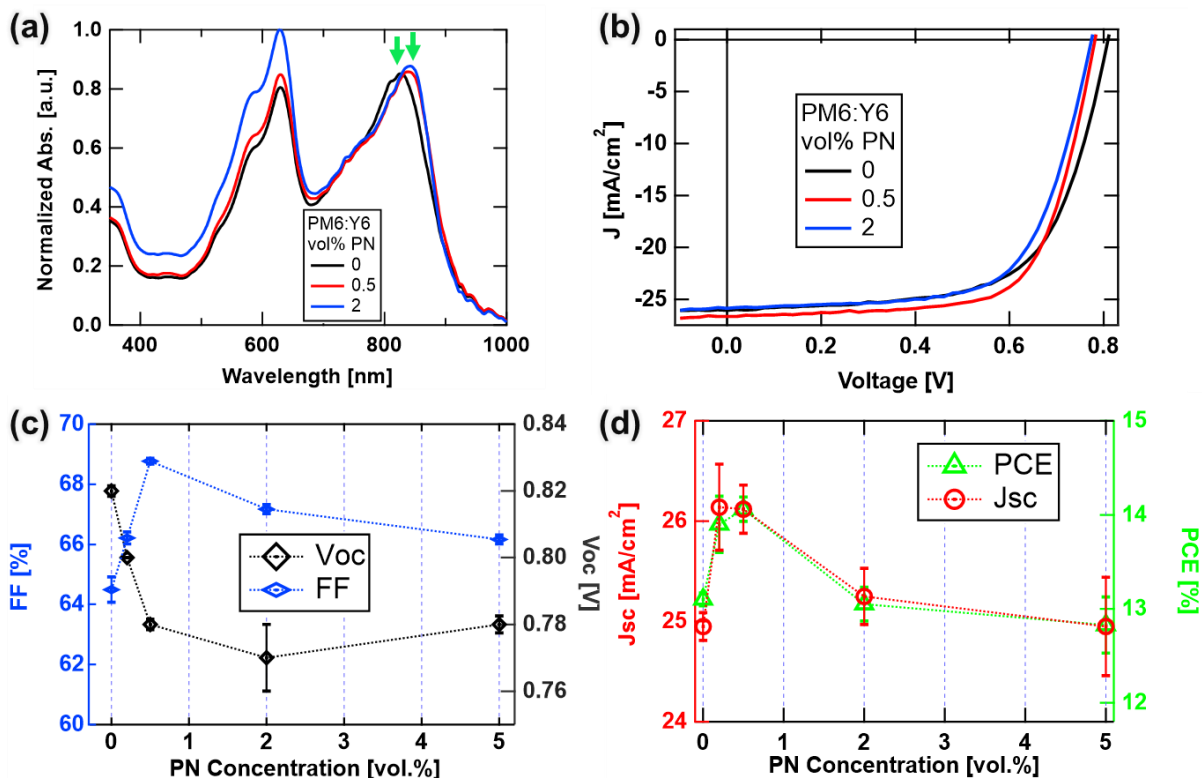


Figure 4- 1: a) UV-VIS absorbance spectra of PM6:Y6 blends with different amounts of PN. b) J-V curves of the studied blends. The corresponding J-V parameters at 0, 0.5, and 2% PN are summarized in (c) Fill factor (FF) and open-circuit voltage, (d) short-circuit current density, and PCE. The plotted values in c and d are the averages of at least six independent devices, and the uncertainty bars are the standard errors.

Figure 4- 1a presents the UV-VIS absorbance spectra of PM6:Y6 active layers with 0, 0.5, and 2 vol % PN solvent additive. The PN additive gradually increases the intensities of PM6 peaks at 580 and 630 nm. The film thickness is similar for all blends (~ 90 nm) as measured by variable angle spectroscopic ellipsometry (VASE), Figure S3- 5. That could mean PN increases polymer aggregations. The additive also causes a red-shift in the Y6 absorbance peak from 830 nm, without PN, to about 840 nm with 0.5% PN then increases peak intensity gradually as the amount of PN increases. That indicates changes in Y6 molecular aggregations with solvent

additive. The PN additive impacts the UV-VIS absorbance of the PM6 and Y6 pure films in the exact manner as in blends, Figure S3- 2. The J-V characteristics are summarized of all JV in Table S3- 1. The device performance maximizes at 0.5 vol % PN with Jsc and FF determining the trends in device performance which Voc steadily decreasing. The overall behavior of J-V characteristics as functions of PN are similar to previous work.¹³⁷ To understand the trend of device performance with the PN additive, a thorough investigation of the charge generation processes to quantify efficiencies of each step is required. That includes the absorption, generation, and extraction efficiencies.

To examine the exciton dissociation efficiency, photoluminescence quenching was performed on pure and blended films. The results, shown in Figure S3- 8, indicate that the PM6:Y6 active layers have efficient exciton dissociation, in agreement with previous work.¹⁵⁰ Thus, the exciton recombination is negligible. In this series, we turn to time-delayed collection field (TDCF) experiment to measure generation current density (J_{gen}) and then compare that to the photocurrent density (J_{ph}) from the J-V characterization, Figure 4- 2. To quantify charge recombination losses and calculate the quantum efficiencies in the investigated PM6:Y6 OSCs, analyses from our previous work are followed.^{27,149} The calculations and results of losses as effective photocurrent densities [mA/cm^2], charge losses [%], and device quantum efficiencies [%] are detailed in Table S3- 2, Table S3- 3 , and Table S3- 4; and displayed in Figure 4- 3.

The bimolecular recombination in the examined PM6:Y6 devices is about 8-11 % of all lost charges. Field-dependent geminate recombination is responsible for about 1-2% of lost photons which is very low and has been seen in other systems.^{151,152} The PN additive slightly reduces both BMR and FD geminate recombination losses. Importantly, Field-independent (**FI**) geminate recombination loss is ~ 3 % without PN, decreases slightly with 0.5 % PN, then

increases up to ~ 7 % lost photons with 2% PN. Unlike PCPDTBT:PCBM OSCs,¹⁴⁹ the investigated PM6:Y6 devices here suffer to some degree of FI geminate recombination losses, in agreement previous work.¹⁴⁸

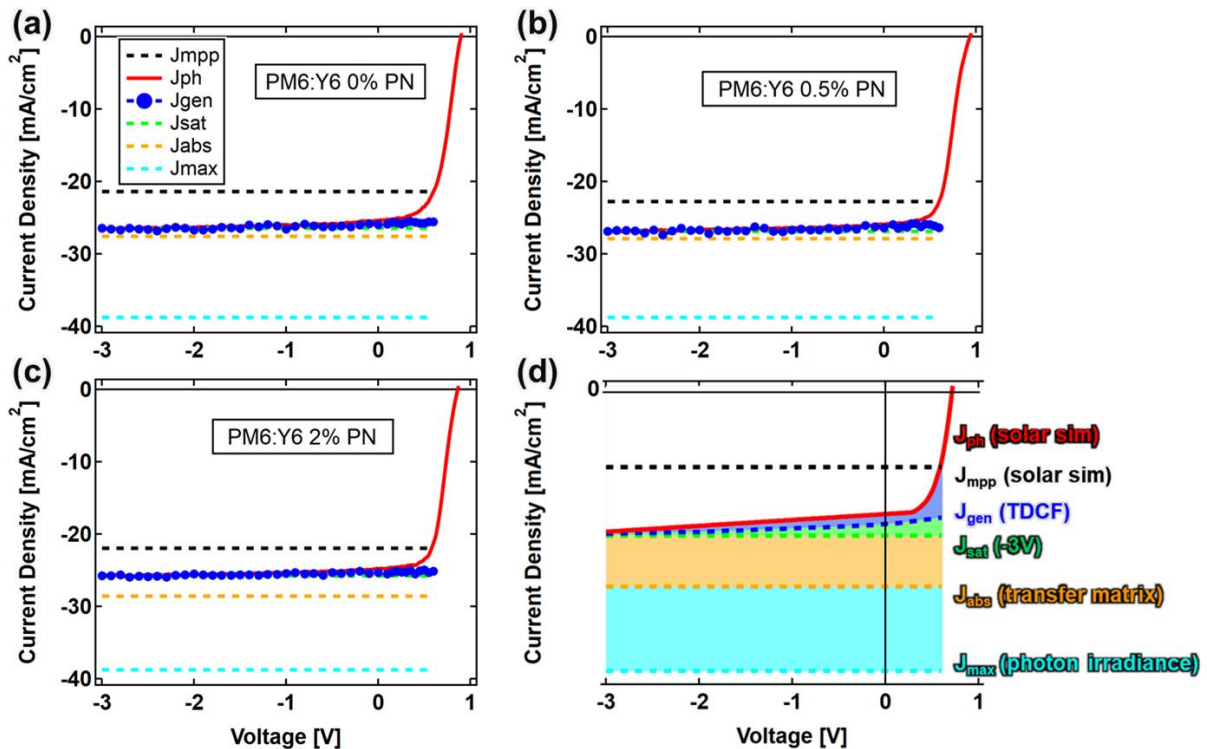


Figure 4- 2: Current densities vs. voltage for the PM6:Y6 with 0% (a), 0.5% (b) and 2% PN (c). From top to bottom: J_{mpp} (dashed black) is current density at maximum power point, J_{ph} (solid red) is the photocurrent JV curve ($J_{ph}=J_{LIGHT}-J_{DARK}$), J_{gen} (blue circles) is current density based on generated charges via TDCF, J_{sat} (dashed green) is the saturated current density that is at voltage= -3 V, J_{abs} (dashed orange) is the current density as calculated from the transfer matrix, and J_{max} (dashed cyan) is the current density of the solar simulator in wavelength range of 350-1000nm. d) Schematic of all the current densities and how they are extracted.

The absorbance current density (J_{abs}) was calculated from transfer matrix modeling of the PM6:Y6 active layers.⁴⁹ more in the supporting information, Figure S3- 6 and Figure S3- 7. The total of incidental photons that were not absorbed—i.e. absorbance loss—is about 26-29 % of. The PN additive slightly reduces the absorption losses. Next, efficiencies of each step of the charge generation processes in the PM6:Y6 active layers are quantified and summarized in Table

S3- 4 and Figure 4- 3b. We find that both absorption and extraction efficiencies benefit from the PN additive. On the other hand, charge separation benefits slightly from 0 % PN then declines with 2 % PN additive. Here, the charge separation efficiency is inversely related to FI geminate recombination. To examine what potentially can be the morphological origin of why the device performance peaks at 0.5% PN and why PN reduces all the loss mechanisms except the FI geminate recombination, we utilized a suite of multimodal nanostructure probes.

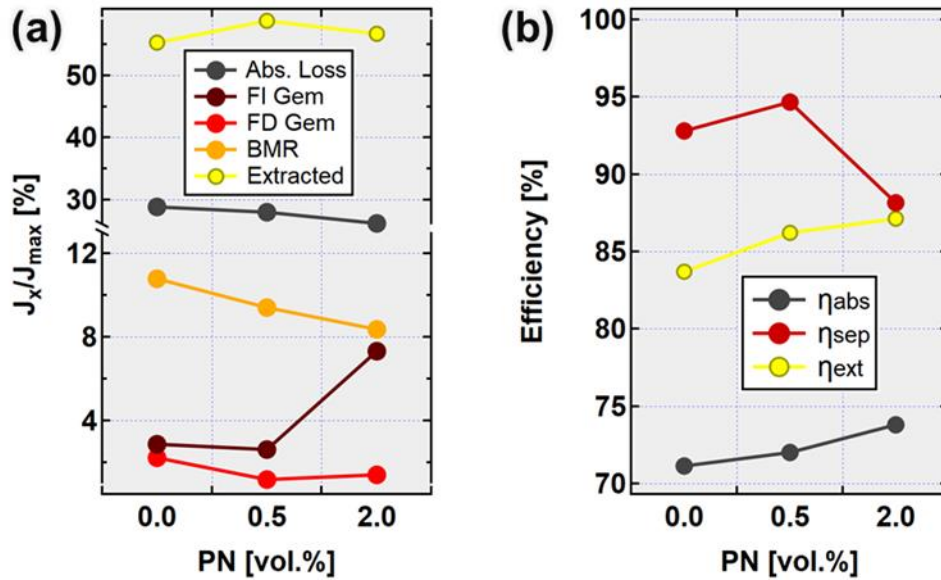


Figure 4- 3: a) Charge density at each step of the charge generation process in PM6:Y6 OSCs as a function of the concentration of solvent additive PN [vol.%]. “Abs. Loss” means absorption loss due to photons not being absorbed. “FI Gem”: field-independent geminate recombination loss. “FD Gem”: loss to field-dependent geminate recombination. “BMR” loss to bimolecular recombination. “Extracted” means extracted charges. Note that all are relative to the maximum current density (J_{max}) that can be given to an OSC by the incident photons of the solar spectrum. Since the extracted charges in (a) is relative to J_{max} , it does not directly reflect J_{sc} . b) Quantitative efficiencies of each of the charge generation processes in the investigated OSCs: namely the absorption, charge separation and charge extraction efficiencies.

Morphology

Atomic force microscopy (AFM) was used to probe the surface roughness and change in phase as function of the PN additive. Figure 4- 4a-c present AFM height scans of the PM6:Y6

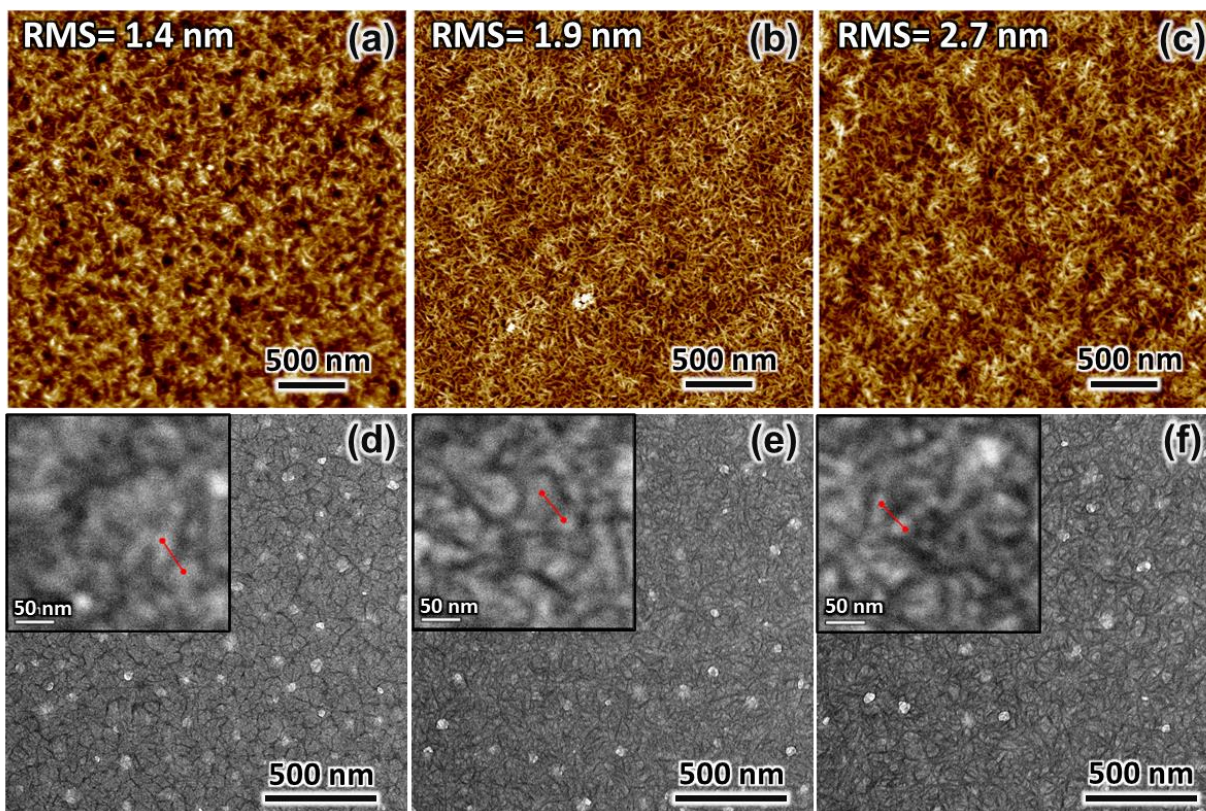


Figure 4- 4: Microscopic scans of PM6:Y6 blends. a-c) AFM height scans of films with 0, 0.5 and 2 % PN, respectively. d-f) TEM scans of films with 0, 0.5 and 2 % PN, respectively.

active layers with different amounts of PN. The root mean square (RMS) values of surface roughness suggest slight increase of surface roughness with PN. Surface roughness of pure PM6 films almost remains the same with different amounts of PN, see Figure S3- 9. Pure Y6 films are in general rougher than PM6 films. In blends, it seems the polymer slightly disrupts aggregations of Y6 molecules. AFM phase scans of the blends, in Figure S3- 10, also indicate some increase in phase as the amount PN increases which can be viewed as change in phase separation. Transmission electron microscopy (TEM) scans of the blends are presented in Figure 4- 4d-f. Based on the AFM and TEM scans, the film texture of blends with different amounts of PN qualitatively does not change and comparable across the different imaging techniques. Zooming in on the blends with TEM suggests that there are features/domains in a length scale of 10s of

nanometers. To gain more insights into the domain size and purity, we utilized resonant soft X-ray scattering (RSoXS).

Figure 4- 5a presents the RSoXS profiles of the PM6:Y6 blends with 0, 0.5 and 2 % PN additive. The data was collected at X-ray energy of 284.5 eV which is slightly below the resonant energies of both PM6 and Y6 molecules. This X-ray energy was chosen to minimize absorption while having decent contrast between the two molecular species, refer to Figure S3-11. Relative domain purity and characteristic length (L_c) of the examined PM6:Y6 blends are extracted from the RSoXS profiles and presented in Figure 4- 5b.⁴⁴ The domain purity,

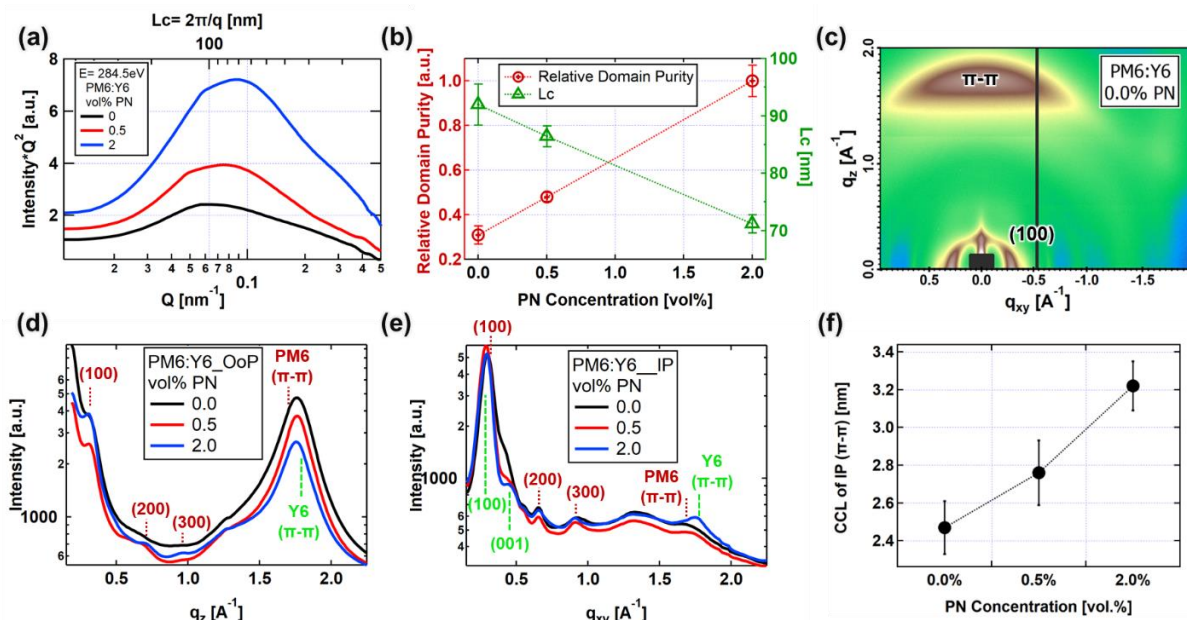


Figure 4- 5: a) Lorentzian corrected RSoXS profiles of the PM6:Y6 blends with different amounts of PN. Data was taken at 284.5 eV. b) Relative domain purity which is $\propto \sqrt{\text{Total Scattering Intensity}}$ and the characteristic length $L_c = 2 \cdot \pi / q$ (feature position). c) 2D GIWAXS scan of PM6:Y6 blend without PN as an example, in an arbitrary intensity color scale. Reduced 1D GIWAXS profiles of PM6:Y6 with different amounts of PN: (d) in the IP direction. (e) in the OoP direction. f) The crystal coherence length of the IP π - π stacking.

calculated from the TSI equation (refer to the RSoXS section, Chapter 2), increases with the PN

solvent additive—similar to the trend in the AFM phase scans. On the other hand, L_c , acquired from peak position, values are in the range of 70-90 nm and slightly decreases with PN.

Next, we utilized grazing incidence wide angle x-ray scattering (GIWAXS) to probe crystallinity and packing quality in neat and blend films of PM6 and Y6 with different amounts of PN additive. GIWAXS data and results are presented in Figure 4- 5c-f and in the supporting information. At 0 % PN concentration, both PM6 and Y6 molecules in pure and blend films show pi-pi stacking with preferential face-on orientation with respect to the substrate. As the amount of PN increases, noticeably at 2% PN, the PM6 pi-pi population prefers to migrate into face-on orientation. On the other hand, the Y6 pi-pi stacking population becomes less face-on orientated as the amount of additive increases, refer to Figure S3- 14. It is worth noting that the relative degree of crystallinity for pi-pi stacking (010) remains comparable in films with different amounts of PN. GIWAXS patterns of the neat films are used as references for peak assignment of the blends Figure S3- 13, and fitting for peak position and d-spacing, and calculating the crystal coherence length (CCL) values of pi-pi stacking and lamellar packing (see Figure S3- 15, Table S3- 5, and Table S3- 6). The CCL values of the face-on pi-pi stacking does not undergo significant changes with PN. However, the CCL of edge-on pi-pi stacking increases gradually with amount of solvent additive, see Figure S3- 16c. This increase in CCL is specifically attributed to the increasing order in between Y6 molecules. Another indicator of the increasing order in Y6 is the change in the shape of its in-plane (IP) backbone (001) diffraction peak. The Y6 IP backbone peak starts as shoulder (see Figure S3- 16d) then at PN concentration ≥ 2 % it becomes distinguishable suggesting that Y6 starts to increase 3-dimensional order.

Discussion

Combining the holistic analysis of charge losses with probing the nanostructures enabled having deep insights into the trends of device performance. We find that the solvent additive PN changes the Y6 molecular aggregation and enhances the absorption of PM6 and hence leads to monotonic improvement in absorption efficiency of the studied PM6:Y6 OSCs. The steady increase in domain purity as a function of PN concentration is correlated with reduction in BMR and FD geminate recombination. The reduction in those two types of charge recombination can be the cause behind the improvement in the charge extraction efficiency. Despite the positive

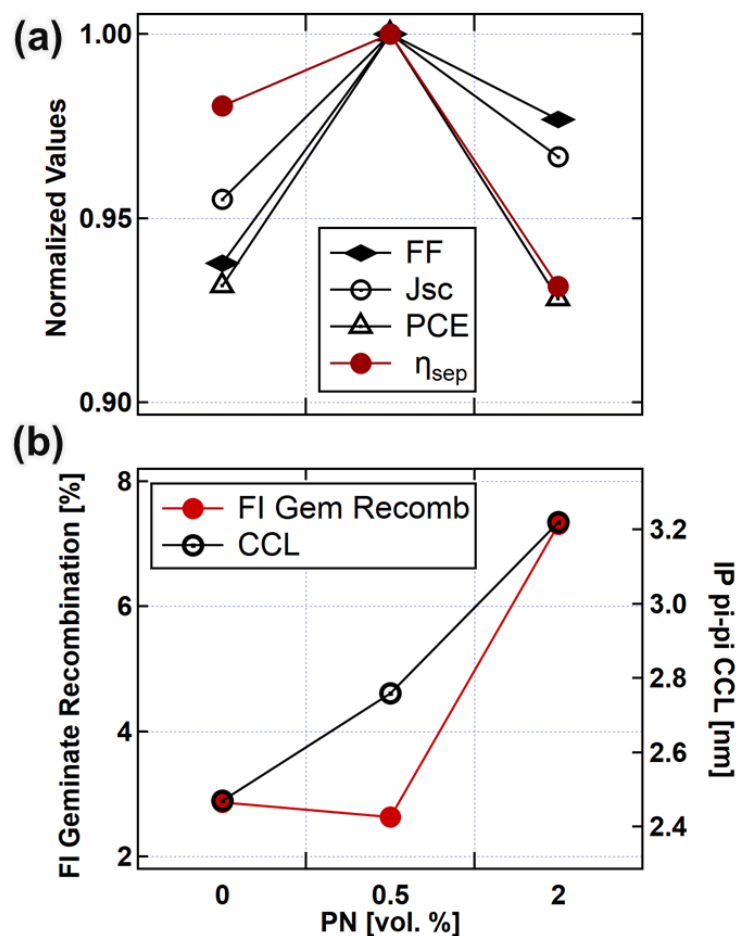


Figure 4- 6: a) Trends in charge separation and device performance parameters (FF, J_{sc} and PCE) as functions of PN concentration. b) A comparison of FI geminate recombination loss vs IP pi-pi stacking CCL.

impacts of PN on reducing BMR and FD geminate recombination and improving absorption and charge extraction, 2% PN increases FI geminate recombination and hence reduces the charge separation efficiency. We find the later to follow similar trend as the device performance as presented in Figure 4- 6a. The most FI geminate recombination takes place in the blend with 2% PN. In the same blend, we observed an increase in the IP pi-pi CCL of Y6 as well as an emergence of the Y6 backbone differentiation peak. This increase in the order of Y6 is also observed in the blend with 5% PN. Therefore, our morphology results points toward a relationship between crystalline ordering of Y6 and the increase in FI geminate recombination. It has been suggested that highly ordered active layers¹⁵³—ordered Y6 molecules¹⁵⁴—lead to low driving force which is considered as key for efficient charge generation. Our findings, however, seem to be in line with the previously proposed scenario that charge generation benefits from disordered interfaces.¹⁵⁵

Conclusion

In conclusion, we have quantified all losses at each step of charge generation in PM6:Y6 OSCs processed from CF with PN as optimizing solvent additive. Increasing the concentration of PN generally enhances absorption and charge extraction efficiencies and reduces FD geminate recombination and BMR. Those enhanced efficiencies can be related to changes in Y6 aggregations and increases in domain purity. However, we find that the main loss mechanism is FI geminate recombination which limits charge generation when exceeding an optimum amount of PN additive (> 0.5 vol%). It appears that the increased losses due FI geminate is driven by the emergence of 3D ordered Y6 crystallites. These results show that eco-friendly solvent additive can be potentially used to optimize device performance in NFA OSCs, also shed some light onto key structure-property aspects.

Experimental Section

Device fabrication of solar cells with structure of Glass/ITO/PEDOT:PSS/PM6:Y6/PDINO/Ag. Organic powders purchased from 1-Material are: the electron-donating polymer PM6 (poly[(2,6-(4,8-bis(5-(2-ethylhexyl-3-fluoro)thiophen-2-yl)-benzo[1,2-b:4,5-b']dithiophene))-alt-(5,5-(1',3'-di-2-thienyl-5',7'-bis(2-ethylhexyl)benzo[1',2'-c:4',5'-c']dithiophene-4,8-dione)]); electron-accepting non-fullerene Y6 ((2,20-((2Z,20Z)-((12,13-bis(2ethylhexyl)-3,9-diundecyl-12,13-dihydro-[1,2,5]thiadiazolo[3,4-e]thieno[2,"30':4',50]thieno[20,30:4,5]pyrrolo[3,2-g]thieno[20,30:4,5]thieno[3,2-b]indole-2,10-diyl)bis(methanylylidene))bis(5,6-difluoro-3-oxo-2,3-dihydro-1H-indene-2,1-diylidene))dimalononitrile)); and the electron-transporting material PDINO (2,9-Bis[3-(dimethyloxidoamino)propyl]anthra[2,1,9-def:6,5,10-d'e'f']diisoquinoline-1,3,8,10(2H,9H)-tetrone). The solvents, CF and PN, were purchased from Sigma-Aldrich. The PEDOT:PSS solution was purchased from Heraeus (Clevios P VP AI 4083). ITO patterns have a resistivity of about 45 ohms/sq. The Glass/ITO were cleaned sequentially in detergent, deionized water, acetone, then isopropyl alcohol for 10 min each. Next, the substrates were puffed with N₂ gas and placed in UV-Ozone cleaner for 4 min. A layer of PEDOT:PSS was spin-cast at 5000 rpm of spin speed for 30 s, then left on a hot plate (150°C) for 20 min. Next, the substrates were moved into a nitrogen glovebox with O₂ and H₂O levels at about 0.1 ppm. Solutions of the active layers were prepared and left stirring on a hot plate (50°C) the night before casting. PM6:Y6 weight ratio is 1:1.2 and was dissolved in CF at 11 g/L concentration. The PN additive was added 30 min before casting at concentrations of 0, 0.2, 0.5, 2, and 5 vol.%. The active layers were cast with spin speeds between 1100-2000 rpm for 50 s. The films are then placed on a hot plate (100°C) for 10 min, then let cool for another 10 min before casting a layer of PDINO (1 g/L in

methanol). The PDINO layer was cast at 3000 rpm spin speed for 30 s. Lastly, a 100 nm top electrode of Ag was thermally deposited in a vacuum at pressure $\sim 5 \times 10^{-7}$ Torr. The active device area is 4 mm².

Device performance was characterized by conducting current density–voltage (J–V) measurements using Keithley 2450 and AAA solar simulator (AM1.5 global filter) with a Xenon arc lamp (Oriel 300W Newport) at irradiance power of 1000 W/m². The J-V characterization was done in a nitrogen glovebox.

Time-delayed collection field (TDCF) measurements were conducted immediately after the J-V characterization on the same devices in the same testing station inside the nitrogen glovebox. Excitation was achieved with 600 nm laser light (ND-YAG pumped OPO Espla NT232 with a pulse width of 3 ns and frequency of 100 Hz). The laser fluence was about 150 nJ/cm². A time delay of 5 ns was given to a device then a collection voltage was applied via a customized overpulse method to overcome the device RC time constant. The customized amplification circuit is synchronized with the laser pulse through a function generator (240 MHz bandwidth, Tektronix AFG 3251). A 1 GHz bandwidth oscilloscope (Teledyne LeCory, HDO 4104) was then used to measure the transient photocurrents.

Atomic force microscopy (AFM) was performed on films cast on Si substrates. Height and phase scans were acquired via AFM (Dimension Icon, Bruker) with TESPA-V2 SAMPLE tip.

Transmission electron microscopy (TEM) scans were taken on films mounted onto TEM grids. The measurements were done in bright-field mode via FEI Technai G2 20 Twin (Thermo Fisher, Waltham MA, USA). The electron source is 200 kV LaB6 and the CCD detector is FEI Eagle 4k.

X-ray measurements were conducted at Berkeley National lab, the advanced light source (ALS), at 7.3.3,⁵⁰ 5.3.2,⁵² and 11.0.1.2⁴⁷ beamlines. GIWAXS measurements are done at ALS BL 7.3.3 with 10 keV X-ray and at an incident angle of 0.2°. The GIWAXS samples were cast on Si substrates. GIWAXS data was processed using custom and Nika software.¹⁴² Near-edge X-ray absorption fine structure (NEXAFS) spectroscopy and RSoXS measurements were conducted at ALS 5.3.2 and 11.0.1.2 beamlines, respectively. Samples were cast on Na:PSS/Si substrates floated off in deionized water and picked up with TEM grids for NEXAFS spectroscopy or silicon nitride windows for RSoXS. X-ray data was processed via custom codes based on Igor Pro software.

Acknowledgements

This work is funded mainly by the US National Science Foundation DMR Electronic and Photonics Program under Grant #1905790. This grant supported O. A. and A. A. were supported by the US Department of Energy Early Career Research Program under Grant DE-SC0017923. This research used resources of the Advanced Light Source, which is a DOE Office of Science User facility under contract no. DE-AC02-05CH11231.

CHAPTER 6: CONCLUSIONS

This dissertation comprises three studies that aim to examine structure-property correlations in multiple polymer:fullerene/non-fullerene binary OSC systems by utilizing a suite of synchrotron X-ray techniques and holistic methods of testing device performance and photo-electric current losses.

The first study investigated the morphological mechanisms behind a novel high-performing thick polymer:fullerene OSC. This system was found to exhibit highly suppressed charge recombination that is dependent on the donor:acceptor blending ratio. The multimodal characterization of its nanomorphology reveals that pure donor and acceptor phases are important but not sufficient to realize extremely low recombination. Instead, it was found that larger, pure, and well-aggregated domains, and critically with sharp D-A interfaces are likely to act as charge conduits across the active layers to effectively segregate charges and suppress recombination even in active layers with film thickness up to one micrometer.

In the second study, the characterization of device performance and morphology of polymer:NFA OSCs was conducted to examine their sensitivity to the processing additive. CN was used as a plasticizer additive to optimize device performance by tuning domain purity and crystallinity. We found there is a strong correlation between phase purity and molecular ordering with device performance. Also, we found that any additional amounts of the CN additive, beyond optimum lead to a drastic decrease in device performance due to excessive phase separation and over-crystallization. This runaway crystallinity of NFA at high concentrations of CN led to poor charge generation and is a new issue not experienced by previous fullerene-based (albeit lower-performing OSCs). We also showed that even the record performance NFA

(PM6:Y6) OPVs, if not processed with extreme precision of CN additive concentrations, can suffer from this runaway crystallinity.

In the third study, we substituted CN as solvent additive with a non-halogen (green) solvent PN to optimize device performance in PM6:Y6 OSCs. We utilized a holistic analysis of charge generation losses and a thorough morphology characterization to examine potential structure-property relationships in this system as a function of PN additive concentration. We find PN increases domain purity and NFA aggregations, increasing absorption efficiency and reducing the bimolecular field-dependent geminate recombination types. However, we find that as the Y6 ordering increases with PN, the field-independent geminate recombination in this system increases, leading to a reduction in charge separation. Another important finding is that excessive amounts of PN, unlike CN, do not lead to the previously observed runaway crystallinity in PM6:Y6 OSCs. Thus, extreme precision of the concentration of PN is not very critical compared to CN.

Although it is well-established that the morphology of OSC active layers governs their device performance, there are no universal processing guidelines across different material systems. That rather depends on the material classes, and often some conclusions are system dependent and cannot be generalized. Regardless, some of the findings of this dissertation have significant implications on understanding key processing-structure-property relationships that can contribute to the successful printing of OSCs at a commercial scale. In the polymer:fullerene study here, the morphological features present some explanations for how efficient devices can be achieved with printable active layers up to $1\mu\text{m}$ in thickness. Thus, large, pure percolation pathways with sharp heterointerfaces may be required to achieve efficient polymer:fullerene OSCs suitable for large-scale industrial production. Based on the examined polymer:non-

fullerene OSC systems in this dissertation, the oversensitivity of device performance and morphology to the processing additive is remarkable. Thus, careful selection of solvent additive or even additive-free methods is vital to achieve successful fabrication of NFA OSCs.

Finally, leveraging a combination of holistic analytical methods of device-physics characterization along with advanced synchrotron X-ray probes of nano-morphology is key to understanding processing-structure-property relationships in OSCs. Such thorough approaches of multimodal characterization might be essential for emerging NFA binary and ternary OSCs to realize their potential for efficient, printable, low-cost technologies of solar energy.

REFERENCES

- (1) Bredas, J.-L.; Durrant, J. R. Organic Photovoltaics. *Acc. Chem. Res.* **2009**, *42* (11), 1689–1690. <https://doi.org/10.1021/ar900238j>.
- (2) *A survey of the structure, fabrication, and characterization of advanced organic light emitting diodes | Elsevier Enhanced Reader.* <https://doi.org/10.1016/j.microrel.2023.114959>.
- (3) Cao, L.; Ren, C.; Wu, T. Recent Advances in Doped Organic Field-Effect Transistors: Mechanism, Influencing Factors, Materials, and Development Directions. *J. Mater. Chem. C* **2023**, *11* (10), 3428–3447. <https://doi.org/10.1039/D2TC05035H>.
- (4) *Organic microelectrode arrays for bioelectronic applications | Elsevier Enhanced Reader.* <https://doi.org/10.1016/j.mser.2023.100726>.
- (5) Bi, P.; Zhang, S.; Wang, J.; Ren, J.; Hou, J. Progress in Organic Solar Cells: Materials, Physics and Device Engineering. *Chin. J. Chem.* **2021**, *39* (9), 2607–2625. <https://doi.org/10.1002/cjoc.202000666>.
- (6) Hoppe, H.; Sariciftci, N. S. Organic Solar Cells: An Overview. *J. Mater. Res.* **2004**, *19* (7), 1924–1945. <https://doi.org/10.1557/JMR.2004.0252>.
- (7) Clarke, T. M.; Durrant, J. R. Charge Photogeneration in Organic Solar Cells. *Chem. Rev.* **2010**, *110* (11), 6736–6767. <https://doi.org/10.1021/cr900271s>.
- (8) Zhao, F.; Zhou, J.; He, D.; Wang, C.; Lin, Y. Low-Cost Materials for Organic Solar Cells. *J. Mater. Chem. C* **2021**, *9* (43), 15395–15406. <https://doi.org/10.1039/D1TC04097A>.
- (9) Luo, D.; Jang, W.; Babu, D. D.; Kim, M. S.; Wang, D. H.; Kyaw, A. K. K. Recent Progress in Organic Solar Cells Based on Non-Fullerene Acceptors: Materials to Devices. *J. Mater. Chem. A* **2022**, *10*.1039.D1TA10707K. <https://doi.org/10.1039/D1TA10707K>.
- (10) Liang, X.; Wang, J.; Miao, R.; Zhao, Q.; Huang, L.; Wen, S.; Tang, J. The Evolution of Small Molecular Acceptors for Organic Solar Cells: Advances, Challenges and Prospects. *Dyes Pigments* **2022**, *198*, 109963. <https://doi.org/10.1016/j.dyepig.2021.109963>.
- (11) R. Murad, A.; Iraqi, A.; Aziz, S. B.; N. Abdullah, S.; Brza, M. A. Conducting Polymers for Optoelectronic Devices and Organic Solar Cells: A Review. *Polymers* **2020**, *12* (11), 2627. <https://doi.org/10.3390/polym12112627>.
- (12) Scharber, M. C.; Sariciftci, N. S. Efficiency of Bulk-Heterojunction Organic Solar Cells. *Prog. Polym. Sci.* **2013**, *38* (12), 1929–1940. <https://doi.org/10.1016/j.progpolymsci.2013.05.001>.
- (13) Liang, Y.; Feng, D.; Wu, Y.; Tsai, S.-T.; Li, G.; Ray, C.; Yu, L. Highly Efficient Solar Cell Polymers Developed via Fine-Tuning of Structural and Electronic Properties. *J. Am. Chem. Soc.* **2009**, *131* (22), 7792–7799. <https://doi.org/10.1021/ja901545q>.
- (14) McDowell, C.; Abdelsamie, M.; Toney, M. F.; Bazan, G. C. Solvent Additives: Key Morphology-Directing Agents for Solution-Processed Organic Solar Cells. *Adv. Mater.* **2018**, *30* (33), 1707114. <https://doi.org/10.1002/adma.201707114>.
- (15) Cui, C.; Li, Y. Morphology Optimization of Photoactive Layers in Organic Solar Cells. *Aggregate* **2021**, *2* (2), e31. <https://doi.org/10.1002/agt2.31>.
- (16) Tang, C. W. Two-layer Organic Photovoltaic Cell. *Appl. Phys. Lett.* **1986**, *48* (2), 183–185. <https://doi.org/10.1063/1.96937>.
- (17) Fo, W.-Z.; Xu, G. Y.; Dong, H.-J.; Liu, L.-N.; Li, Y. W.; Ding, L. Highly Efficient Binary Solvent Additive-Processed Organic Solar Cells by the Blade-Coating Method. *Macromol. Chem. Phys.* **2021**, *222* (17), 2100062. <https://doi.org/10.1002/macp.202100062>.

- (18) Lv, J.; Tang, H.; Huang, J.; Yan, C.; Liu, K.; Yang, Q.; Hu, D.; Singh, R.; Lee, J.; Lu, S.; Li, G.; Kan, Z. Additive-Induced Miscibility Regulation and Hierarchical Morphology Enable 17.5% Binary Organic Solar Cells. *Energy Environ. Sci.* **2021**, *14* (5), 3044–3052. <https://doi.org/10.1039/D0EE04012F>.
- (19) Zhang, M.; Zhu, L.; Zhou, G.; Hao, T.; Qiu, C.; Zhao, Z.; Hu, Q.; Larson, B. W.; Zhu, H.; Ma, Z.; Tang, Z.; Feng, W.; Zhang, Y.; Russell, T. P.; Liu, F. Single-Layered Organic Photovoltaics with Double Cascading Charge Transport Pathways: 18% Efficiencies. *Nat. Commun.* **2021**, *12* (1), 309. <https://doi.org/10.1038/s41467-020-20580-8>.
- (20) Gao, J.; Wang, J.; Xu, C.; Hu, Z.; Ma, X.; Zhang, X.; Niu, L.; Zhang, J.; Zhang, F. A Critical Review on Efficient Thick-Film Organic Solar Cells. *Sol. RRL* **2020**, *4* (11), 2000364. <https://doi.org/10.1002/solr.202000364>.
- (21) Richter, L. J.; DeLongchamp, D. M.; Amassian, A. Morphology Development in Solution-Processed Functional Organic Blend Films: An In Situ Viewpoint. *Chem. Rev.* **2017**, *117* (9), 6332–6366. <https://doi.org/10.1021/acs.chemrev.6b00618>.
- (22) Riede, M.; Spoltore, D.; Leo, K. Organic Solar Cells—The Path to Commercial Success. *Adv. Energy Mater.* **2021**, *11* (1), 2002653. <https://doi.org/10.1002/aenm.202002653>.
- (23) Xue, R.; Zhang, J.; Li, Y.; Li, Y. Organic Solar Cell Materials toward Commercialization. *Small* **2018**, *14* (41), 1801793. <https://doi.org/10.1002/sml.201801793>.
- (24) Alqahtani, O.; Babics, M.; Gorenflot, J.; Savikhin, V.; Ferron, T.; Balawi, A. H.; Paulke, A.; Kan, Z.; Pope, M.; Clulow, A. J.; Wolf, J.; Burn, P. L.; Gentle, I. R.; Neher, D.; Toney, M. F.; Laquai, F.; Beaujuge, P. M.; Collins, B. A. Mixed Domains Enhance Charge Generation and Extraction in Bulk-Heterojunction Solar Cells with Small-Molecule Donors. *Adv. Energy Mater.* **2018**, *8* (19), 1702941. <https://doi.org/10.1002/aenm.201702941>.
- (25) Mukherjee, S.; Proctor, C. M.; Tumbleston, J. R.; Bazan, G. C.; Nguyen, T.-Q.; Ade, H. Importance of Domain Purity and Molecular Packing in Efficient Solution-Processed Small-Molecule Solar Cells. *Adv. Mater.* **2015**, *27* (6), 1105–1111. <https://doi.org/10.1002/adma.201404388>.
- (26) Jiao, X.; Ye, L.; Ade, H. Quantitative Morphology–Performance Correlations in Organic Solar Cells: Insights from Soft X-Ray Scattering. *Adv. Energy Mater.* **2017**, *7* (18), 1700084. <https://doi.org/10.1002/aenm.201700084>.
- (27) Ferron, T.; Waldrip, M.; Pope, M.; Collins, B. A. Increased Charge Transfer State Separation via Reduced Mixed Phase Interface in Polymer Solar Cells. *J. Mater. Chem. A* **2019**, *7* (9), 4536–4548. <https://doi.org/10.1039/C8TA12336E>.
- (28) Tumbleston, J. R.; Collins, B. A.; Yang, L.; Stuart, A. C.; Gann, E.; Ma, W.; You, W.; Ade, H. The Influence of Molecular Orientation on Organic Bulk Heterojunction Solar Cells. *Nat. Photonics* **2014**, *8* (5), 385–391. <https://doi.org/10.1038/nphoton.2014.55>.
- (29) Jin, Y.; Chen, Z.; Dong, S.; Zheng, N.; Ying, L.; Jiang, X.-F.; Liu, F.; Huang, F.; Cao, Y. A Novel Naphtho[1,2-*c*:5,6-*C'*]Bis([1,2,5]Thiadiazole)-Based Narrow-Bandgap π -Conjugated Polymer with Power Conversion Efficiency Over 10%. *Adv. Mater.* **2016**, *28* (44), 9811–9818. <https://doi.org/10.1002/adma.201603178>.
- (30) Armin, A.; Chen, Z.; Jin, Y.; Zhang, K.; Huang, F.; Shoaee, S. A Shockley-Type Polymer: Fullerene Solar Cell. *Adv. Energy Mater.* **2018**, *8* (7), 1701450. <https://doi.org/10.1002/aenm.201701450>.
- (31) Alqahtani, O.; Hosseini, S. M.; Ferron, T.; Murcia, V.; McAfee, T.; Vixie, K.; Huang, F.; Armin, A.; Shoaee, S.; Collins, B. A. Evidence That Sharp Interfaces Suppress Recombination in Thick Organic Solar Cells. *ACS Appl. Mater. Interfaces* **2021**, *13* (47), 56394–56403. <https://doi.org/10.1021/acsami.1c15570>.
- (32) Yuan, J.; Zhang, Y.; Zhou, L.; Zhang, G.; Yip, H.-L.; Lau, T.-K.; Lu, X.; Zhu, C.; Peng, H.; Johnson, P. A.; Leclerc, M.; Cao, Y.; Ulanski, J.; Li, Y.; Zou, Y. Single-Junction Organic Solar Cell with over 15%

- Efficiency Using Fused-Ring Acceptor with Electron-Deficient Core. *Joule* **2019**, 3 (4), 1140–1151. <https://doi.org/10.1016/j.joule.2019.01.004>.
- (33) Song, H.; Hu, D.; Lv, J.; Lu, S.; Haiyan, C.; Kan, Z. Hybrid Cathode Interlayer Enables 17.4% Efficiency Binary Organic Solar Cells. *Adv. Sci.* **2022**, 9 (8), 2105575. <https://doi.org/10.1002/advs.202105575>.
- (34) Pan, M.-A.; Lau, T.-K.; Tang, Y.; Wu, Y.-C.; Liu, T.; Li, K.; Chen, M.-C.; Lu, X.; Ma, W.; Zhan, C. 16.7%-Efficiency Ternary Blended Organic Photovoltaic Cells with PCBM as the Acceptor Additive to Increase the Open-Circuit Voltage and Phase Purity. *J. Mater. Chem. A* **2019**, 10.
- (35) Wang, K.; Lv, J.; Duan, T.; Li, Z.; Yang, Q.; Fu, J.; Meng, W.; Xu, T.; Xiao, Z.; Kan, Z.; Sun, K.; Lu, S. Simple Near-Infrared Nonfullerene Acceptors Enable Organic Solar Cells with >9% Efficiency. *ACS Appl. Mater. Interfaces* **2019**, 11 (7), 6717–6723. <https://doi.org/10.1021/acsami.8b20567>.
- (36) Wadsworth, A.; Moser, M.; Marks, A.; Little, M. S.; Gasparini, N.; Brabec, C. J.; Baran, D.; McCulloch, I. Critical Review of the Molecular Design Progress in Non-Fullerene Electron Acceptors towards Commercially Viable Organic Solar Cells. *Chem. Soc. Rev.* **2019**, 48 (6), 1596–1625. <https://doi.org/10.1039/C7CS00892A>.
- (37) Andersen, T. R.; Dam, H. F.; Hösel, M.; Helgesen, M.; Carlé, J. E.; Larsen-Olsen, T. T.; Gevorgyan, S. A.; Andreasen, J. W.; Adams, J.; Li, N.; Machui, F.; Spyropoulos, G. D.; Ameri, T.; Lemaître, N.; Legros, M.; Scheel, A.; Gaiser, D.; Kreul, K.; Berny, S.; Lozman, O. R.; Nordman, S.; Välimäki, M.; Vilkmann, M.; Søndergaard, R.; Jørgensen, M.; Brabec, C. J.; Krebs, F. C. Scalable, Ambient Atmosphere Roll-to-Roll Manufacture of Encapsulated Large Area, Flexible Organic Tandem Solar Cell Modules. *Energy Environ. Sci.* **2014**, 7 (9), 2925. <https://doi.org/10.1039/C4EE01223B>.
- (38) Dhakal, P.; Ferron, T.; Alotaibi, A.; Murcia, V.; Alqahtani, O.; Collins, B. A. Evidence for Field-Dependent Charge Separation Caused by Mixed Phases in Polymer–Fullerene Organic Solar Cells. *J. Phys. Chem. Lett.* **2021**.
- (39) Engmann, S.; Bokel, F. A.; Herzing, A. A.; Ro, H. W.; Giroto, C.; Caputo, B.; Hoven, C. V.; Schaible, E.; Hexemer, A.; DeLongchamp, D. M.; Richter, L. J. Real-Time X-Ray Scattering Studies of Film Evolution in High Performing Small-Molecule–Fullerene Organic Solar Cells. *J. Mater. Chem. A* **2015**, 3 (16), 8764–8771. <https://doi.org/10.1039/C5TA00935A>.
- (40) Kniepert, J.; Schubert, M.; Blakesley, J. C.; Neher, D. Photogeneration and Recombination in P3HT/PCBM Solar Cells Probed by Time-Delayed Collection Field Experiments. *J. Phys. Chem. Lett.* **2011**, 2 (7), 700–705. <https://doi.org/10.1021/jz200155b>.
- (41) Chaney, T. P.; Levin, A. J.; Schneider, S. A.; Toney, M. F. Scattering Techniques for Mixed Donor–Acceptor Characterization in Organic Photovoltaics. *Mater. Horiz.* **2021**, 10.1039/D1MH01219C. <https://doi.org/10.1039/D1MH01219C>.
- (42) Zhao, F.; Wang, C.; Zhan, X. Morphology Control in Organic Solar Cells. *Adv. Energy Mater.* **2018**, 8 (28), 1703147. <https://doi.org/10.1002/aenm.201703147>.
- (43) Vakhshouri, K.; Kesava, S. V.; Kozub, D. R.; Gomez, E. D. Characterization of the Mesoscopic Structure in the Photoactive Layer of Organic Solar Cells: A Focused Review. *Mater. Lett.* **2013**, 90, 97–102. <https://doi.org/10.1016/j.matlet.2012.08.146>.
- (44) Collins, B. A.; Gann, E. Resonant Soft X-Ray Scattering in Polymer Science. *J. Polym. Sci.* **1**, 1–45. <https://doi.org/10.1002/pol.20210414>.
- (45) Collins, B. A.; Ade, H. Quantitative Compositional Analysis of Organic Thin Films Using Transmission NEXAFS Spectroscopy in an X-Ray Microscope. *J. Electron Spectrosc. Relat. Phenom.* **2012**, 185 (5–7), 119–128. <https://doi.org/10.1016/j.elspec.2012.05.002>.

- (46) Collins, B. A.; Li, Z.; Tumbleston, J. R.; Gann, E.; McNeill, C. R.; Ade, H. Absolute Measurement of Domain Composition and Nanoscale Size Distribution Explains Performance in PTB7:PC71BM Solar Cells. *Adv. Energy Mater.* **2013**, *3* (1), 65–74. <https://doi.org/10.1002/aenm.201200377>.
- (47) Gann, E.; Young, A. T.; Collins, B. A.; Yan, H.; Nasiatka, J.; Padmore, H. A.; Ade, H.; Hexemer, A.; Wang, C. Soft X-Ray Scattering Facility at the Advanced Light Source with Real-Time Data Processing and Analysis. *Rev. Sci. Instrum.* **2012**, *83* (4), 045110. <https://doi.org/10.1063/1.3701831>.
- (48) Gann, E.; Crofts, T.; Holland, G.; Beaucage, P.; McAfee, T.; Kline, R. J.; Collins, B. A.; McNeill, C. R.; Fischer, D. A.; DeLongchamp, D. M. A NIST Facility for Resonant Soft X-Ray Scattering Measuring Nano-Scale Soft Matter Structure at NSLS-II. *J. Phys. Condens. Matter* **2021**, *33* (16), 164001. <https://doi.org/10.1088/1361-648X/abdffb>.
- (49) Burkhard, G. F.; Hoke, E. T.; McGehee, M. D. Accounting for Interference, Scattering, and Electrode Absorption to Make Accurate Internal Quantum Efficiency Measurements in Organic and Other Thin Solar Cells. *Adv. Mater.* **2010**, *22* (30), 3293–3297. <https://doi.org/10.1002/adma.201000883>.
- (50) Hexemer, A.; Bras, W.; Glossinger, J.; Schaible, E.; Gann, E.; Kirian, R.; MacDowell, A.; Church, M.; Rude, B.; Padmore, H. A SAXS/WAXS/GISAXS Beamline with Multilayer Monochromator. *J. Phys. Conf. Ser.* **2010**, *247*, 012007. <https://doi.org/10.1088/1742-6596/247/1/012007>.
- (51) Peng, Z.; Ye, L.; Ade, H. Understanding, Quantifying, and Controlling the Molecular Ordering of Semiconducting Polymers: From Novices to Experts and Amorphous to Perfect Crystals. *Mater. Horiz.* **2022**, *9* (2), 577–606. <https://doi.org/10.1039/D0MH00837K>.
- (52) Kilcoyne, A. L. D.; Tyliszczak, T.; Steele, W. F.; Fakra, S.; Hitchcock, P.; Franck, K.; Anderson, E.; Harteneck, B.; Rightor, E. G.; Mitchell, G. E.; Hitchcock, A. P.; Yang, L.; Warwick, T.; Ade, H. Interferometer-Controlled Scanning Transmission X-Ray Microscopes at the Advanced Light Source. *J. Synchrotron Radiat.* **2003**, *10* (2), 125–136. <https://doi.org/10.1107/S0909049502017739>.
- (53) Marcus, M. A.; Shapiro, D. A.; Yu, Y.-S. Ptychography Reduces Spectral Distortions Intrinsic to Conventional Zone-Plate-Based X-Ray Spectromicroscopy. *Microsc. Microanal.* **2021**, 1–6. <https://doi.org/10.1017/S1431927621012733>.
- (54) Burke, K. B.; Luber, E. J.; Holmes, N. P.; Murray, A. J.; Belcher, W. J.; Zhou, X.; Mitlin, D.; Dastoor, P. C. A Knife-Edge Measurement of the Beam Profile of STXM 5.3.2.2 Using a Focussed Ion Beam Milled Metallic Glass. *J. Electron Spectrosc. Relat. Phenom.* **2012**, *185* (11), 453–457. <https://doi.org/10.1016/j.elspec.2012.07.003>.
- (55) Yan, H.; Wang, C.; McCarn, A. R.; Ade, H. Accurate and Facile Determination of the Index of Refraction of Organic Thin Films Near the Carbon 1 s Absorption Edge. *Phys. Rev. Lett.* **2013**, *110* (17), 177401. <https://doi.org/10.1103/PhysRevLett.110.177401>.
- (56) Roe, R. J. *Methods of X-Ray and Neutron Scattering in Polymer Science*, 2000.
- (57) Meng, L.; Zhang, Y.; Wan, X.; Li, C.; Zhang, X.; Wang, Y.; Ke, X.; Xiao, Z.; Ding, L.; Xia, R.; Yip, H.-L.; Cao, Y.; Chen, Y. Organic and Solution-Processed Tandem Solar Cells with 17.3% Efficiency. *Science* **2018**, *361* (6407), 1094–1098. <https://doi.org/10.1126/science.aat2612>.
- (58) Liu, Q.; Jiang, Y.; Jin, K.; Qin, J.; Xu, J.; Li, W.; Xiong, J.; Liu, J.; Xiao, Z.; Sun, K.; Yang, S.; Zhang, X.; Ding, L. 18% Efficiency Organic Solar Cells. *Sci. Bull.* **2020**, *65* (4), 272–275. <https://doi.org/10.1016/j.scib.2020.01.001>.
- (59) Neher, D.; Kniepert, J.; Elimelech, A.; Koster, L. J. A. A New Figure of Merit for Organic Solar Cells with Transport-Limited Photocurrents. *Sci. Rep.* **2016**, *6* (1), 24861. <https://doi.org/10.1038/srep24861>.

- (60) Bartesaghi, D.; Pérez, I. del C.; Kniepert, J.; Roland, S.; Turbiez, M.; Neher, D.; Koster, L. J. A. Competition between Recombination and Extraction of Free Charges Determines the Fill Factor of Organic Solar Cells. *Nat. Commun.* **2015**, *6* (1), 7083. <https://doi.org/10.1038/ncomms8083>.
- (61) Duan, C.; Gao, K.; Colberts, F. J. M.; Liu, F.; Meskers, S. C. J.; Wienk, M. M.; Janssen, R. A. J. Thiophene Rings Improve the Device Performance of Conjugated Polymers in Polymer Solar Cells with Thick Active Layers. *Adv. Energy Mater.* **2017**, *7* (19), 1700519. <https://doi.org/10.1002/aenm.201700519>.
- (62) Shoaee, S.; Armin, A.; Stolterfoht, M.; Hosseini, S. M.; Kurpiers, J.; Neher, D. Decoding Charge Recombination through Charge Generation in Organic Solar Cells. *Sol. RRL* **2019**, *3* (11), 1900184. <https://doi.org/10.1002/solr.201900184>.
- (63) Chang, Y.; Zhu, X.; Lu, K.; Wei, Z. Progress and Prospects of Thick-Film Organic Solar Cells. *J. Mater. Chem. A* **2021**, *9* (6), 3125–3150. <https://doi.org/10.1039/D0TA10594E>.
- (64) Langevin, P. Recombinaison et Mobilites Des Ions Dans Les Gaz. *Ann Chim Phys* **1903**, No. 28, 433–530.
- (65) Ko, S.-J.; Walker, B.; Nguyen, T. L.; Choi, H.; Seifert, J.; Uddin, M. A.; Kim, T.; Kim, S.; Heo, J.; Kim, G.-H.; Cho, S.; Heeger, A. J.; Woo, H. Y.; Kim, J. Y. Photocurrent Extraction Efficiency near Unity in a Thick Polymer Bulk Heterojunction. *Adv. Funct. Mater.* **2016**, *26* (19), 3324–3330. <https://doi.org/10.1002/adfm.201505556>.
- (66) Hosseini, S. M.; Tokmoldin, N.; Lee, Y. W.; Zou, Y.; Woo, H. Y.; Neher, D.; Shoaee, S. Putting Order into PM6:Y6 Solar Cells to Reduce the Langevin Recombination in 400 Nm Thick Junction. *Sol. RRL* **2020**, *4* (11), 2000498. <https://doi.org/10.1002/solr.202000498>.
- (67) Hosseini, S. M.; Roland, S.; Kurpiers, J.; Chen, Z.; Zhang, K.; Huang, F.; Armin, A.; Neher, D.; Shoaee, S. Impact of Bimolecular Recombination on the Fill Factor of Fullerene and Nonfullerene-Based Solar Cells: A Comparative Study of Charge Generation and Extraction. *J. Phys. Chem. C* **2019**, *123* (11), 6823–6830. <https://doi.org/10.1021/acs.jpcc.8b11669>.
- (68) Phuong, L. Q.; Hosseini, S. M.; Koh, C. W.; Woo, H. Y.; Shoaee, S. Measuring Competing Recombination Losses in a Significantly Reduced Langevin System by Steady-State Photoinduced Absorption and Photocurrent Spectroscopy. *J. Phys. Chem. C* **2019**, *123* (45), 27417–27422. <https://doi.org/10.1021/acs.jpcc.9b08901>.
- (69) Schwarz, K. N.; Geraghty, P. B.; Mitchell, V. D.; Khan, S.-U.-Z.; Sandberg, O. J.; Zarrabi, N.; Kudisch, B.; Subbiah, J.; Smith, T. A.; Rand, B. P.; Armin, A.; Scholes, G. D.; Jones, D. J.; Ghiggino, K. P. Reduced Recombination and Capacitor-like Charge Buildup in an Organic Heterojunction. *J. Am. Chem. Soc.* **2020**, *142* (5), 2562–2571. <https://doi.org/10.1021/jacs.9b12526>.
- (70) Murthy, D. H. K.; Melianas, A.; Tang, Z.; Juška, G.; Arlauskas, K.; Zhang, F.; Siebbeles, L. D. A.; Inganäs, O.; Savenije, T. J. Origin of Reduced Bimolecular Recombination in Blends of Conjugated Polymers and Fullerenes. *Adv. Funct. Mater.* **2013**, *23* (34), 4262–4268. <https://doi.org/10.1002/adfm.201203852>.
- (71) Pivrikas, A.; Sariciftci, N. S.; Juška, G.; Österbacka, R. A Review of Charge Transport and Recombination in Polymer/Fullerene Organic Solar Cells. *Prog. Photovolt. Res. Appl.* **2007**, *15* (8), 677–696. <https://doi.org/10.1002/pip.791>.
- (72) Ye, L.; Hu, H.; Ghasemi, M.; Wang, T.; Collins, B. A.; Kim, J.-H.; Jiang, K.; Carpenter, J. H.; Li, H.; Li, Z.; McAfee, T.; Zhao, J.; Chen, X.; Lai, J. L. Y.; Ma, T.; Bredas, J.-L.; Yan, H.; Ade, H. Quantitative Relations between Interaction Parameter, Miscibility and Function in Organic Solar Cells. *Nat. Mater.* **2018**, *17* (3), 253–260. <https://doi.org/10.1038/s41563-017-0005-1>.
- (73) Yan, H.; Swaraj, S.; Wang, C.; Hwang, I.; Greenham, N. C.; Groves, C.; Ade, H.; McNeill, C. R. Influence of Annealing and Interfacial Roughness on the Performance of Bilayer Donor/Acceptor

- Polymer Photovoltaic Devices. *Adv. Funct. Mater.* **2010**, *20* (24), 4329–4337. <https://doi.org/10.1002/adfm.201001292>.
- (74) Lyons, B. P.; Clarke, N.; Groves, C. The Relative Importance of Domain Size, Domain Purity and Domain Interfaces to the Performance of Bulk-Heterojunction Organic Photovoltaics. *Energy Environ. Sci.* **2012**, *5* (6), 7657. <https://doi.org/10.1039/c2ee21327c>.
- (75) Zimmerman, J. D.; Xiao, X.; Renshaw, C. K.; Wang, S.; Diev, V. V.; Thompson, M. E.; Forrest, S. R. Independent Control of Bulk and Interfacial Morphologies of Small Molecular Weight Organic Heterojunction Solar Cells. *Nano Lett.* **2012**, *12* (8), 4366–4371. <https://doi.org/10.1021/nl302172w>.
- (76) McMahon, D. P.; Cheung, D. L.; Troisi, A. Why Holes and Electrons Separate So Well in Polymer/Fullerene Photovoltaic Cells. *J. Phys. Chem. Lett.* **2011**, *2* (21), 2737–2741. <https://doi.org/10.1021/jz201325g>.
- (77) Clarke, T. M.; Rodovsky, D. B.; Herzing, A. A.; Peet, J.; Dennler, G.; DeLongchamp, D.; Lungenschmied, C.; Mozer, A. J. Significantly Reduced Bimolecular Recombination in a Novel Silole-Based Polymer: Fullerene Blend. *Adv. Energy Mater.* **2011**, *1* (6), 1062–1067. <https://doi.org/10.1002/aenm.201100390>.
- (78) Venkatesan, S.; Chen, J.; Ngo, E. C.; Dubey, A.; Khatiwada, D.; Zhang, C.; Qiao, Q. Critical Role of Domain Crystallinity, Domain Purity and Domain Interface Sharpness for Reduced Bimolecular Recombination in Polymer Solar Cells. *Nano Energy* **2015**, *12*, 457–467. <https://doi.org/10.1016/j.nanoen.2014.12.027>.
- (79) Ye, L.; Zhang, S.; Ma, W.; Fan, B.; Guo, X.; Huang, Y.; Ade, H.; Hou, J. From Binary to Ternary Solvent: Morphology Fine-Tuning of D/A Blends in PDPP3T-Based Polymer Solar Cells. *Adv. Mater.* **2012**, *24* (47), 6335–6341. <https://doi.org/10.1002/adma.201202855>.
- (80) Vandewal, K.; Gadisa, A.; Oosterbaan, W. D.; Bertho, S.; Banishoeib, F.; Van Severen, I.; Lutsen, L.; Cleij, T. J.; Vanderzande, D.; Manca, J. V. The Relation Between Open-Circuit Voltage and the Onset of Photocurrent Generation by Charge-Transfer Absorption in Polymer : Fullerene Bulk Heterojunction Solar Cells: Photocurrent Generation by Charge-Transfer Absorption. *Adv. Funct. Mater.* **2008**, *18* (14), 2064–2070. <https://doi.org/10.1002/adfm.200800056>.
- (81) Stolterfoht, M.; Armin, A.; Shoaee, S.; Kassal, I.; Burn, P.; Meredith, P. Slower Carriers Limit Charge Generation in Organic Semiconductor Light-Harvesting Systems. *Nat. Commun.* **2016**, *7* (1), 11944. <https://doi.org/10.1038/ncomms11944>.
- (82) Armin, A.; Juska, G.; Ullah, M.; Velusamy, M.; Burn, P. L.; Meredith, P.; Pivrikas, A. Balanced Carrier Mobilities: Not a Necessary Condition for High-Efficiency Thin Organic Solar Cells as Determined by MIS-CELIV. *Adv. Energy Mater.* **2014**, *4* (4), 1300954. <https://doi.org/10.1002/aenm.201300954>.
- (83) Zhang, K.; Chen, Z.; Armin, A.; Dong, S.; Xia, R.; Yip, H.-L.; Shoaee, S.; Huang, F.; Cao, Y. Efficient Large Area Organic Solar Cells Processed by Blade-Coating With Single-Component Green Solvent. *Sol. RRL* **2018**, *2* (1), 1700169. <https://doi.org/10.1002/solr.201700169>.
- (84) Armin, A.; Subbiah, J.; Stolterfoht, M.; Shoaee, S.; Xiao, Z.; Lu, S.; Jones, D. J.; Meredith, P. Reduced Recombination in High Efficiency Molecular Nematic Liquid Crystalline: Fullerene Solar Cells. *Adv. Energy Mater.* **2016**, *6* (22), 1600939. <https://doi.org/10.1002/aenm.201600939>.
- (85) Rivnay, J.; Mannsfeld, S. C. B.; Miller, C. E.; Salleo, A.; Toney, M. F. Quantitative Determination of Organic Semiconductor Microstructure from the Molecular to Device Scale. *Chem. Rev.* **2012**, *112* (10), 5488–5519. <https://doi.org/10.1021/cr3001109>.
- (86) Li, Z.; Jiang, K.; Yang, G.; Lai, J. Y. L.; Ma, T.; Zhao, J.; Ma, W.; Yan, H. Donor Polymer Design Enables Efficient Non-Fullerene Organic Solar Cells. *Nat. Commun.* **2016**, *7* (1), 13094. <https://doi.org/10.1038/ncomms13094>.

- (87) Ferron, T.; Pope, M.; Collins, B. A. Spectral Analysis for Resonant Soft X-Ray Scattering Enables Measurement of Interfacial Width in 3D Organic Nanostructures. *Phys. Rev. Lett.* **2017**, *119* (16), 167801. <https://doi.org/10.1103/PhysRevLett.119.167801>.
- (88) Kozub, D. R.; Vakhshouri, K.; Orme, L. M.; Wang, C.; Hexemer, A.; Gomez, E. D. Polymer Crystallization of Partially Miscible Polythiophene/Fullerene Mixtures Controls Morphology. *Macromolecules* **2011**, *44* (14), 5722–5726. <https://doi.org/10.1021/ma200855r>.
- (89) Pfannmöller, M.; Flügge, H.; Benner, G.; Wacker, I.; Sommer, C.; Hanselmann, M.; Schmale, S.; Schmidt, H.; Hamprecht, F. A.; Rabe, T.; Kowalsky, W.; Schröder, R. R. Visualizing a Homogeneous Blend in Bulk Heterojunction Polymer Solar Cells by Analytical Electron Microscopy. *Nano Lett.* **2011**, *11* (8), 3099–3107. <https://doi.org/10.1021/nl201078t>.
- (90) Guo, C.; Kozub, D. R.; Vajjala Kesava, S.; Wang, C.; Hexemer, A.; Gomez, E. D. Signatures of Multiphase Formation in the Active Layer of Organic Solar Cells from Resonant Soft X-Ray Scattering. *ACS Macro Lett.* **2013**, *2* (3), 185–189. <https://doi.org/10.1021/mz300547x>.
- (91) Albrecht, S.; Schindler, W.; Kurpiers, J.; Kniepert, J.; Blakesley, J. C.; Dumsch, I.; Allard, S.; Fostiropoulos, K.; Scherf, U.; Neher, D. On the Field Dependence of Free Charge Carrier Generation and Recombination in Blends of PCPDTBT/PC₇₀BM: Influence of Solvent Additives. *J. Phys. Chem. Lett.* **2012**, *3* (5), 640–645. <https://doi.org/10.1021/jz3000849>.
- (92) Venkatesan, S.; Adhikari, N.; Chen, J.; Ngo, E. C.; Dubey, A.; Galipeau, D. W.; Qiao, Q. Interplay of Nanoscale Domain Purity and Size on Charge Transport and Recombination Dynamics in Polymer Solar Cells. *Nanoscale* **2014**, *6* (2), 1011–1019. <https://doi.org/10.1039/C3NR05177C>.
- (93) Erb, T.; Zhokhavets, U.; Gobsch, G.; Raleva, S.; Stühn, B.; Schilinsky, P.; Waldauf, C.; Brabec, C. J. Correlation Between Structural and Optical Properties of Composite Polymer/Fullerene Films for Organic Solar Cells. *Adv. Funct. Mater.* **2005**, *15* (7), 1193–1196. <https://doi.org/10.1002/adfm.200400521>.
- (94) Solanki, A.; Wu, B.; Salim, T.; Lam, Y. M.; Sum, T. C. Correlation between Blend Morphology and Recombination Dynamics in Additive-Added P3HT:PCBM Solar Cells. *Phys. Chem. Chem. Phys.* **2015**, *17* (39), 26111–26120. <https://doi.org/10.1039/C5CP03762J>.
- (95) Vohra, V.; Kawashima, K.; Kakara, T.; Koganezawa, T.; Osaka, I.; Takimiya, K.; Murata, H. Efficient Inverted Polymer Solar Cells Employing Favourable Molecular Orientation. *Nat. Photonics* **2015**, *9* (6), 403–408. <https://doi.org/10.1038/nphoton.2015.84>.
- (96) Jamieson, F. C.; Domingo, E. B.; McCarthy-Ward, T.; Heeney, M.; Stingelin, N.; Durrant, J. R. Fullerenecrystallisation as a Key Driver of Charge Separation in Polymer/Fullerene Bulk Heterojunction Solar Cells. *Chem Sci* **2012**, *3* (2), 485–492. <https://doi.org/10.1039/C1SC00674F>.
- (97) Szymtkowski, J. On the Tendency of Temperature and Electric Field Dependences of Interface Recombination in a P3HT:PCBM Organic Bulk Heterojunction Solar Cell. *Semicond. Sci. Technol.* **2011**, *26* (10), 105012. <https://doi.org/10.1088/0268-1242/26/10/105012>.
- (98) Gorenflot, J.; Heiber, M. C.; Baumann, A.; Lormann, J.; Gunz, M.; Kämpgen, A.; Dyakonov, V.; Deibel, C. Nongeminate Recombination in Neat P3HT and P3HT:PCBM Blend Films. *J. Appl. Phys.* **2014**, *115* (14), 144502. <https://doi.org/10.1063/1.4870805>.
- (99) Awartani, O.; Lemanski, B. I.; Ro, H. W.; Richter, L. J.; DeLongchamp, D. M.; O'Connor, B. T. Correlating Stiffness, Ductility, and Morphology of Polymer:Fullerene Films for Solar Cell Applications. *Adv. Energy Mater.* **2013**, *3* (3), 399–406. <https://doi.org/10.1002/aenm.201200595>.
- (100) Do, K.; Huang, D. M.; Faller, R.; Moulé, A. J. A Comparative MD Study of the Local Structure of Polymer Semiconductors P3HT and PBTBT. *Phys. Chem. Chem. Phys.* **2010**, *12* (44), 14735. <https://doi.org/10.1039/c0cp00785d>.

- (101) Feng, S.; Zhang, C.; Liu, Y.; Bi, Z.; Zhang, Z.; Xu, X.; Ma, W.; Bo, Z. Fused-Ring Acceptors with Asymmetric Side Chains for High-Performance Thick-Film Organic Solar Cells. *Adv. Mater.* **2017**, *29* (42), 1703527. <https://doi.org/10.1002/adma.201703527>.
- (102) Baker, J. L.; Jimison, L. H.; Mannsfeld, S.; Volkman, S.; Yin, S.; Subramanian, V.; Salleo, A.; Alivisatos, A. P.; Toney, M. F. Quantification of Thin Film Crystallographic Orientation Using X-Ray Diffraction with an Area Detector. *Langmuir* **2010**, *26* (11), 9146–9151. <https://doi.org/10.1021/la904840q>.
- (103) Li, C.; Zhou, J.; Song, J.; Xu, J.; Zhang, H.; Zhang, X.; Guo, J.; Zhu, L.; Wei, D.; Han, G.; Min, J.; Zhang, Y.; Xie, Z.; Yi, Y.; Yan, H.; Gao, F.; Liu, F.; Sun, Y. Non-Fullerene Acceptors with Branched Side Chains and Improved Molecular Packing to Exceed 18% Efficiency in Organic Solar Cells. *Nat. Energy* **2021**, *6* (6), 605–613. <https://doi.org/10.1038/s41560-021-00820-x>.
- (104) Li, S.; Liu, W.; Li, C.-Z.; Shi, M.; Chen, H. Efficient Organic Solar Cells with Non-Fullerene Acceptors. *Small* **2017**, *13* (37), 1701120. <https://doi.org/10.1002/smll.201701120>.
- (105) McAfee, S. M.; Topple, J. M.; Hill, I. G.; Welch, G. C. Key Components to the Recent Performance Increases of Solution Processed Non-Fullerene Small Molecule Acceptors. *J. Mater. Chem. A* **2015**, *3* (32), 16393–16408. <https://doi.org/10.1039/C5TA04310G>.
- (106) Eftaiha, A. F.; Sun, J.-P.; Hill, I. G.; Welch, G. C. Recent Advances of Non-Fullerene, Small Molecular Acceptors for Solution Processed Bulk Heterojunction Solar Cells. *J Mater Chem A* **2014**, *2* (5), 1201–1213. <https://doi.org/10.1039/C3TA14236A>.
- (107) Lin, Y.; Zhan, X. Non-Fullerene Acceptors for Organic Photovoltaics: An Emerging Horizon. *Mater. Horiz.* **2014**, *1* (5), 470. <https://doi.org/10.1039/C4MH00042K>.
- (108) Chai, G.; Chang, Y.; Peng, Z.; Jia, Y.; Zou, X.; Yu, D.; Yu, H.; Chen, Y.; Chow, P. C. Y.; Wong, K. S.; Zhang, J.; Ade, H.; Yang, L.; Zhan, C. Enhanced Hindrance from Phenyl Outer Side Chains on Nonfullerene Acceptor Enables Unprecedented Simultaneous Enhancement in Organic Solar Cell Performances with 16.7% Efficiency. *Nano Energy* **2020**, *76*, 105087. <https://doi.org/10.1016/j.nanoen.2020.105087>.
- (109) Wang, Y.; Zhang, Y.; Qiu, N.; Feng, H.; Gao, H.; Kan, B.; Ma, Y.; Li, C.; Wan, X.; Chen, Y. A Halogenation Strategy for over 12% Efficiency Nonfullerene Organic Solar Cells. *Adv. Energy Mater.* **2018**, *8* (15), 1702870. <https://doi.org/10.1002/aenm.201702870>.
- (110) Liu, Z.; Zhang, X.; Li, P.; Gao, X. Recent Development of Efficient A-D-A Type Fused-Ring Electron Acceptors for Organic Solar. *Sol. Energy* **2018**, *174*, 171–188. <https://doi.org/10.1016/j.solener.2018.09.008>.
- (111) Ma, R.; Li, G.; Li, D.; Liu, T.; Luo, Z.; Zhang, G.; Zhang, M.; Wang, Z.; Luo, S.; Yang, T.; Liu, F.; Yan, H.; Tang, B. Understanding the Effect of End Group Halogenation in Tuning Miscibility and Morphology of High-Performance Small Molecular Acceptors. *Sol. RRL* **2020**, *4* (9), 2000250. <https://doi.org/10.1002/solr.202000250>.
- (112) Geng, R.; Song, X.; Feng, H.; Yu, J.; Zhang, M.; Gasparini, N.; Zhang, Z.; Liu, F.; Baran, D.; Tang, W. Nonfullerene Acceptor for Organic Solar Cells with Chlorination on Dithieno[3,2-*b*:2',3'-*d*]Pyrrol Fused-Ring. *ACS Energy Lett.* **2019**, *4* (3), 763–770. <https://doi.org/10.1021/acsenergylett.9b00147>.
- (113) Furukawa, S.; Yasuda, T. Strategic End-Halogenation of π -Conjugated Small Molecules Enabling Fine Morphological Control and Enhanced Performance of Organic Solar Cells. *J. Mater. Chem. A* **2019**, *7* (24), 14806–14815. <https://doi.org/10.1039/C9TA03869H>.
- (114) Liao, H.-C.; Ho, C.-C.; Chang, C.-Y.; Jao, M.-H.; Darling, S. B.; Su, W.-F. Additives for Morphology Control in High-Efficiency Organic Solar Cells. *Mater. Today* **2013**, *16* (9), 326–336. <https://doi.org/10.1016/j.mattod.2013.08.013>.

- (115) Datt, R.; Suman; Bagui, A.; Siddiqui, A.; Sharma, R.; Gupta, V.; Yoo, S.; Kumar, S.; Singh, S. P. Effectiveness of Solvent Vapor Annealing over Thermal Annealing on the Photovoltaic Performance of Non-Fullerene Acceptor Based BHJ Solar Cells. *Sci. Rep.* **2019**, *9* (1), 8529. <https://doi.org/10.1038/s41598-019-44232-0>.
- (116) van Franeker, J. J.; Turbiez, M.; Li, W.; Wienk, M. M.; Janssen, R. A. J. A Real-Time Study of the Benefits of Co-Solvents in Polymer Solar Cell Processing. *Nat. Commun.* **2015**, *6* (1), 6229. <https://doi.org/10.1038/ncomms7229>.
- (117) Song, X.; Gasparini, N.; Baran, D. The Influence of Solvent Additive on Polymer Solar Cells Employing Fullerene and Non-Fullerene Acceptors. *Adv. Electron. Mater.* **2018**, *4* (10), 1700358. <https://doi.org/10.1002/aelm.201700358>.
- (118) Xie, S.; Wang, J.; Wang, R.; Zhang, D.; Zhou, H.; Zhang, Y.; Zhou, D. Effects of Processing Additives in Non-Fullerene Organic Bulk Heterojunction Solar Cells with Efficiency >11%. *Chin. Chem. Lett.* **2019**, *30* (1), 217–221. <https://doi.org/10.1016/j.ccllet.2018.04.001>.
- (119) Shockley, W.; Queisser, H. J. Detailed Balance Limit of Efficiency of P-n Junction Solar Cells. **11**.
- (120) Lee, J.; Ko, S.-J.; Seifrid, M.; Lee, H.; Luginbuhl, B. R.; Karki, A.; Ford, M.; Rosenthal, K.; Cho, K.; Nguyen, T.-Q.; Bazan, G. C. Bandgap Narrowing in Non-Fullerene Acceptors: Single Atom Substitution Leads to High Optoelectronic Response Beyond 1000 Nm. *Adv. Energy Mater.* **2018**, *8* (24), 1801212. <https://doi.org/10.1002/aenm.201801212>.
- (121) Li, S.; Zhan, L.; Zhao, W.; Zhang, S.; Ali, B.; Fu, Z.; Lau, T.-K.; Lu, X.; Shi, M.; Li, C.-Z.; Hou, J.; Chen, H. Revealing the Effects of Molecular Packing on the Performances of Polymer Solar Cells Based on A–D–C–D–A Type Non-Fullerene Acceptors. *J. Mater. Chem. A* **2018**, *6* (25), 12132–12141. <https://doi.org/10.1039/C8TA03753A>.
- (122) Li, S.; Zhan, L.; Liu, F.; Ren, J.; Shi, M.; Li, C.-Z.; Russell, T. P.; Chen, H. An Unfused-Core-Based Nonfullerene Acceptor Enables High-Efficiency Organic Solar Cells with Excellent Morphological Stability at High Temperatures. *Adv. Mater.* **2018**, *30* (6), 1705208. <https://doi.org/10.1002/adma.201705208>.
- (123) Hu, H.; Jiang, K.; Chow, P. C. Y.; Ye, L.; Zhang, G.; Li, Z.; Carpenter, J. H.; Ade, H.; Yan, H. Influence of Donor Polymer on the Molecular Ordering of Small Molecular Acceptors in Nonfullerene Polymer Solar Cells. *Adv. Energy Mater.* **2018**, *8* (5), 1701674. <https://doi.org/10.1002/aenm.201701674>.
- (124) Richter, L. J.; DeLongchamp, D. M.; Bokel, F. A.; Engmann, S.; Chou, K. W.; Amassian, A.; Schaible, E.; Hexemer, A. In Situ Morphology Studies of the Mechanism for Solution Additive Effects on the Formation of Bulk Heterojunction Films. *Adv. Energy Mater.* **2015**, *5* (3), 1400975. <https://doi.org/10.1002/aenm.201400975>.
- (125) Cser, F. About the Lorentz Correction Used in the Interpretation of Small Angle X-Ray Scattering Data of Semicrystalline Polymers. *J. Appl. Polym. Sci.* **2001**, *80* (12), 2300–2308. <https://doi.org/10.1002/app.1335>.
- (126) Qin, Y.; Xu, Y.; Peng, Z.; Hou, J.; Ade, H. Low Temperature Aggregation Transitions in N3 and Y6 Acceptors Enable Double-Annealing Method That Yields Hierarchical Morphology and Superior Efficiency in Nonfullerene Organic Solar Cells. *Adv. Funct. Mater.* **2020**, *30* (46), 2005011. <https://doi.org/10.1002/adfm.202005011>.
- (127) Angunawela, I.; Ye, L.; Bin, H.; Zhang, Z.-G.; Gadisa, A.; Li, Y.; Ade, H. Multi-Length Scale Morphology of Nonfullerene All-Small Molecule Blends and Its Relation to Device Function in Organic Solar Cells. *Mater. Chem. Front.* **2019**, *3* (1), 137–144. <https://doi.org/10.1039/C8QM00503F>.

- (128) Zhang, L.; Zhao, H.; Lin, B.; Yuan, J.; Xu, X.; Wu, J.; Zhou, K.; Guo, X.; Zhang, M.; Ma, W. A Blade-Coated Highly Efficient Thick Active Layer for Non-Fullerene Organic Solar Cells. *J. Mater. Chem. A* **2019**, *7* (39), 22265–22273. <https://doi.org/10.1039/C9TA09799F>.
- (129) Mukherjee, S.; Jiao, X.; Ade, H. Charge Creation and Recombination in Multi-Length Scale Polymer:Fullerene BHJ Solar Cell Morphologies. *Adv. Energy Mater.* **2016**, *6* (18), 1600699. <https://doi.org/10.1002/aenm.201600699>.
- (130) Vandewal, K.; Tvingstedt, K.; Gadisa, A.; Inganäs, O.; Manca, J. V. Relating the Open-Circuit Voltage to Interface Molecular Properties of Donor:Acceptor Bulk Heterojunction Solar Cells. *Phys. Rev. B* **2010**, *81* (12), 125204. <https://doi.org/10.1103/PhysRevB.81.125204>.
- (131) Zheng, Z.; He, E.; Wang, J.; Qin, Z.; Niu, T.; Guo, F.; Gao, S.; Ma, Z.; Zhao, L.; Lu, X.; Xue, Q.; Cao, Y.; Mola, G. T.; Zhang, Y. Revealing the Role of Solvent Additives in Morphology and Energy Loss in Benzodifuran Polymer-Based Non-Fullerene Organic Solar Cells. *J. Mater. Chem. A* **2021**, *9* (46), 26105–26112. <https://doi.org/10.1039/D1TA08893A>.
- (132) Zhao, Q.; Lai, H.; Chen, H.; Li, H.; He, F. H- and J-Aggregation Inspiring Efficient Solar Conversion. *J. Mater. Chem. A* **2021**, *9* (2), 1119–1126. <https://doi.org/10.1039/D0TA11146E>.
- (133) Fan, B.; Zhang, D.; Li, M.; Zhong, W.; Zeng, Z.; Ying, L.; Huang, F.; Cao, Y. Achieving over 16% Efficiency for Single-Junction Organic Solar Cells. *Sci. China Chem.* **2019**, *62* (6), 746–752. <https://doi.org/10.1007/s11426-019-9457-5>.
- (134) Karuthedath, S.; Firdaus, Y.; Scaccabarozzi, A. D.; Nugraha, M. I.; Alam, S.; Anthopoulos, T. D.; Laquai, F. Trace Solvent Additives Enhance Charge Generation in Layer-by-Layer Coated Organic Solar Cells. *Small Struct.* **2022**, *3* (4), 2100199. <https://doi.org/10.1002/sstr.202100199>.
- (135) Li, M.; Liu, J.; Cao, X.; Zhou, K.; Zhao, Q.; Yu, X.; Xing, R.; Han, Y. Achieving Balanced Intermixed and Pure Crystalline Phases in PDI-Based Non-Fullerene Organic Solar Cells via Selective Solvent Additives. *Phys Chem Chem Phys* **2014**, *16* (48), 26917–26928. <https://doi.org/10.1039/C4CP04161E>.
- (136) Dong, S.; Zhang, K.; Jia, T.; Zhong, W.; Wang, X.; Huang, F.; Cao, Y. Suppressing the Excessive Aggregation of Nonfullerene Acceptor in Blade-Coated Active Layer by Using n-Type Polymer Additive to Achieve Large-Area Printed Organic Solar Cells with Efficiency over 15%. *EcoMat* **2019**, *1* (1), e12006. <https://doi.org/10.1002/eom2.12006>.
- (137) Ye, L.; Xiong, Y.; Zhang, M.; Guo, X.; Guan, H.; Zou, Y.; Ade, H. Enhanced Efficiency in Nonfullerene Organic Solar Cells by Tuning Molecular Order and Domain Characteristics. *Nano Energy* **2020**, *77*, 105310. <https://doi.org/10.1016/j.nanoen.2020.105310>.
- (138) Xue, P.; Cheng, P.; Han, R. P. S.; Zhan, X. Printing Fabrication of Large-Area Non-Fullerene Organic Solar Cells. *Mater. Horiz.* **2022**, *9* (1), 194–219. <https://doi.org/10.1039/D1MH01317C>.
- (139) Jeong, S.; Park, B.; Hong, S.; Kim, S.; Kim, J.; Kwon, S.; Lee, J.-H.; Lee, M. S.; Park, J. C.; Kang, H.; Lee, K. Large-Area Nonfullerene Organic Solar Cell Modules Fabricated by a Temperature-Independent Printing Method. *ACS Appl. Mater. Interfaces* **2020**, *12* (37), 41877–41885. <https://doi.org/10.1021/acsami.0c12190>.
- (140) Ye, L.; Xiong, Y.; Zhang, Q.; Li, S.; Wang, C.; Jiang, Z.; Hou, J.; You, W.; Ade, H. Surpassing 10% Efficiency Benchmark for Nonfullerene Organic Solar Cells by Scalable Coating in Air from Single Nonhalogenated Solvent. *Adv. Mater.* **2018**, *30* (8), 1705485. <https://doi.org/10.1002/adma.201705485>.
- (141) Dong, S.; Jia, T.; Zhang, K.; Jing, J.; Huang, F. Single-Component Non-Halogen Solvent-Processed High-Performance Organic Solar Cell Module with Efficiency over 14%. *Joule* **2020**, *4* (9), 2004–2016. <https://doi.org/10.1016/j.joule.2020.07.028>.

- (142) Ilavsky, J. *Nika* : Software for Two-Dimensional Data Reduction. *J. Appl. Crystallogr.* **2012**, *45* (2), 324–328. <https://doi.org/10.1107/S0021889812004037>.
- (143) Deng, M.; Xu, X.; Duan, Y.; Yu, L.; Li, R.; Peng, Q. Y-Type Non-Fullerene Acceptors with Outer Branched Side Chains and Inner Cyclohexane Side Chains for 19.36% Efficiency Polymer Solar Cells. *Adv. Mater.* **2023**, *35* (10), 2210760. <https://doi.org/10.1002/adma.202210760>.
- (144) Zhu, L.; Zhang, M.; Zhong, W.; Leng, S.; Zhou, G.; Zou, Y.; Su, X.; Ding, H.; Gu, P.; Liu, F.; Zhang, Y. Progress and Prospects of the Morphology of Non-Fullerene Acceptor Based High-Efficiency Organic Solar Cells. *Energy Environ. Sci.* **2021**, *14* (8), 4341–4357. <https://doi.org/10.1039/D1EE01220G>.
- (145) Guo, Q.; Guo, Q.; Geng, Y.; Tang, A.; Zhang, M.; Du, M.; Sun, X.; Zhou, E. Recent Advances in PM6:Y6-Based Organic Solar Cells. *Mater. Chem. Front.* **2021**, *5* (8), 3257–3280. <https://doi.org/10.1039/D1QM00060H>.
- (146) Alqahtani, O.; Lv, J.; Xu, T.; Murcia, V.; Ferron, T.; McAfee, T.; Grabner, D.; Duan, T.; Collins, B. A. High Sensitivity of Non-Fullerene Organic Solar Cells Morphology and Performance to a Processing Additive. *Small n/a* (n/a), 2202411. <https://doi.org/10.1002/smll.202202411>.
- (147) Zhou, X.; Zhao, C.; Alotaibi, A. N.; Wu, H.; Naveed, H. B.; Lin, B.; Zhou, K.; Ma, Z.; Collins, B. A.; Ma, W. Electrical Edge Effect Induced Photocurrent Overestimation in Low-Light Organic Photovoltaics. *Joule* **2022**, *6* (8), 1904–1917. <https://doi.org/10.1016/j.joule.2022.06.008>.
- (148) Perdigón-Toro, L.; Zhang, H.; Markina, A.; Yuan, J.; Hosseini, S. M.; Wolff, C. M.; Zuo, G.; Stolterfoht, M.; Zou, Y.; Gao, F.; Andrienko, D.; Shoaee, S.; Neher, D. Barrierless Free Charge Generation in the High-Performance PM6:Y6 Bulk Heterojunction Non-Fullerene Solar Cell. *Adv. Mater.* **2020**, *32* (9), 1906763. <https://doi.org/10.1002/adma.201906763>.
- (149) Dhakal, P.; Ferron, T.; Alotaibi, A.; Murcia, V.; Alqahtani, O.; Collins, B. A. Evidence for Field-Dependent Charge Separation Caused by Mixed Phases in Polymer–Fullerene Organic Solar Cells. *J. Phys. Chem. Lett.* **2021**, *12* (7), 1847–1853. <https://doi.org/10.1021/acs.jpcclett.0c03863>.
- (150) Perdigón-Toro, L.; Phuong, L. Q.; Zeiske, S.; Vandewal, K.; Armin, A.; Shoaee, S.; Neher, D. Excitons Dominate the Emission from PM6:Y6 Solar Cells, but This Does Not Help the Open-Circuit Voltage of the Device. *ACS Energy Lett.* **2021**, *6* (2), 557–564. <https://doi.org/10.1021/acsenergylett.0c02572>.
- (151) Vandewal, K.; Albrecht, S.; Hoke, E. T.; Graham, K. R.; Widmer, J.; Douglas, J. D.; Schubert, M.; Mateker, W. R.; Bloking, J. T.; Burkhard, G. F.; Sellinger, A.; Fréchet, J. M. J.; Amassian, A.; Riede, M. K.; McGehee, M. D.; Neher, D.; Salleo, A. Efficient Charge Generation by Relaxed Charge-Transfer States at Organic Interfaces. *Nat. Mater.* **2014**, *13* (1), 63–68. <https://doi.org/10.1038/nmat3807>.
- (152) Zusan, A.; Vandewal, K.; Allendorf, B.; Hansen, N. H.; Pflaum, J.; Salleo, A.; Dyakonov, V.; Deibel, C. The Crucial Influence of Fullerene Phases on Photogeneration in Organic Bulk Heterojunction Solar Cells. *Adv. Energy Mater.* **2014**, *4* (17), 1400922. <https://doi.org/10.1002/aenm.201400922>.
- (153) Karki, A.; Gillett, A. J.; Friend, R. H.; Nguyen, T.-Q. The Path to 20% Power Conversion Efficiencies in Nonfullerene Acceptor Organic Solar Cells. *Adv. Energy Mater.* *n/a* (n/a), 2003441. <https://doi.org/10.1002/aenm.202003441>.
- (154) Zhang, G.; Chen, X.-K.; Xiao, J.; Chow, P. C. Y.; Ren, M.; Kupgan, G.; Jiao, X.; Chan, C. C. S.; Du, X.; Xia, R.; Chen, Z.; Yuan, J.; Zhang, Y.; Zhang, S.; Liu, Y.; Zou, Y.; Yan, H.; Wong, K. S.; Coropceanu, V.; Li, N.; Brabec, C. J.; Bredas, J.-L.; Yip, H.-L.; Cao, Y. Delocalization of Exciton and Electron Wavefunction in Non-Fullerene Acceptor Molecules Enables Efficient Organic Solar Cells. *Nat. Commun.* **2020**, *11* (1), 3943. <https://doi.org/10.1038/s41467-020-17867-1>.
- (155) Hood, S. N.; Kassal, I. Entropy and Disorder Enable Charge Separation in Organic Solar Cells. *J. Phys. Chem. Lett.* **2016**, *7* (22), 4495–4500. <https://doi.org/10.1021/acs.jpcclett.6b02178>.

(156) Morgan, F. *Geometric Measure Theory: A Beginner's Guide*, 4th ed.; Academic Press/Elsevier: Amsterdam ; Burlington, MA, 2009.

APPENDIX

APPENDIX A: SUPPORTING INFORMATION FOR CHAPTER 3: EVIDENCE THAT
SHARP INTERFACES SUPPRESS RECOMBINATION IN THICK ORGANIC SOLAR
CELLS

Absorbance and J-V Characteristic Curves: Thickness Comparison

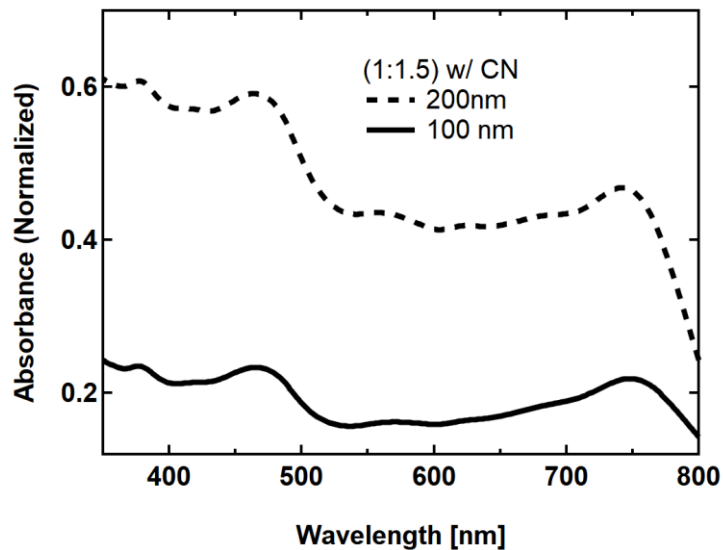


Figure S1- 1: UV-Vis absorbance for 1:1.5 with CN blends for comparison of 100 nm thick (solid) vs. 200 nm thick films (dashed).

Blend (NT812:PC71BM)	Additive CN [%]	V _{OC} [V]	J _{SC} [mA.cm ⁻²]	FF [%]	PCE (avg) [%]
(1:1.5)	0.5	0.75	14.8	70.4	7.9
(1:1.5)(thin)	0.5	0.76	13.7	73.2	7.5

Table S1- 1: Device performance summary for 1:1.5 blends with CN, at different thickness. Thick blend ~ 200 nm and thin blend ~ 100 nm.

Reduction Factors of Bimolecular Recombination

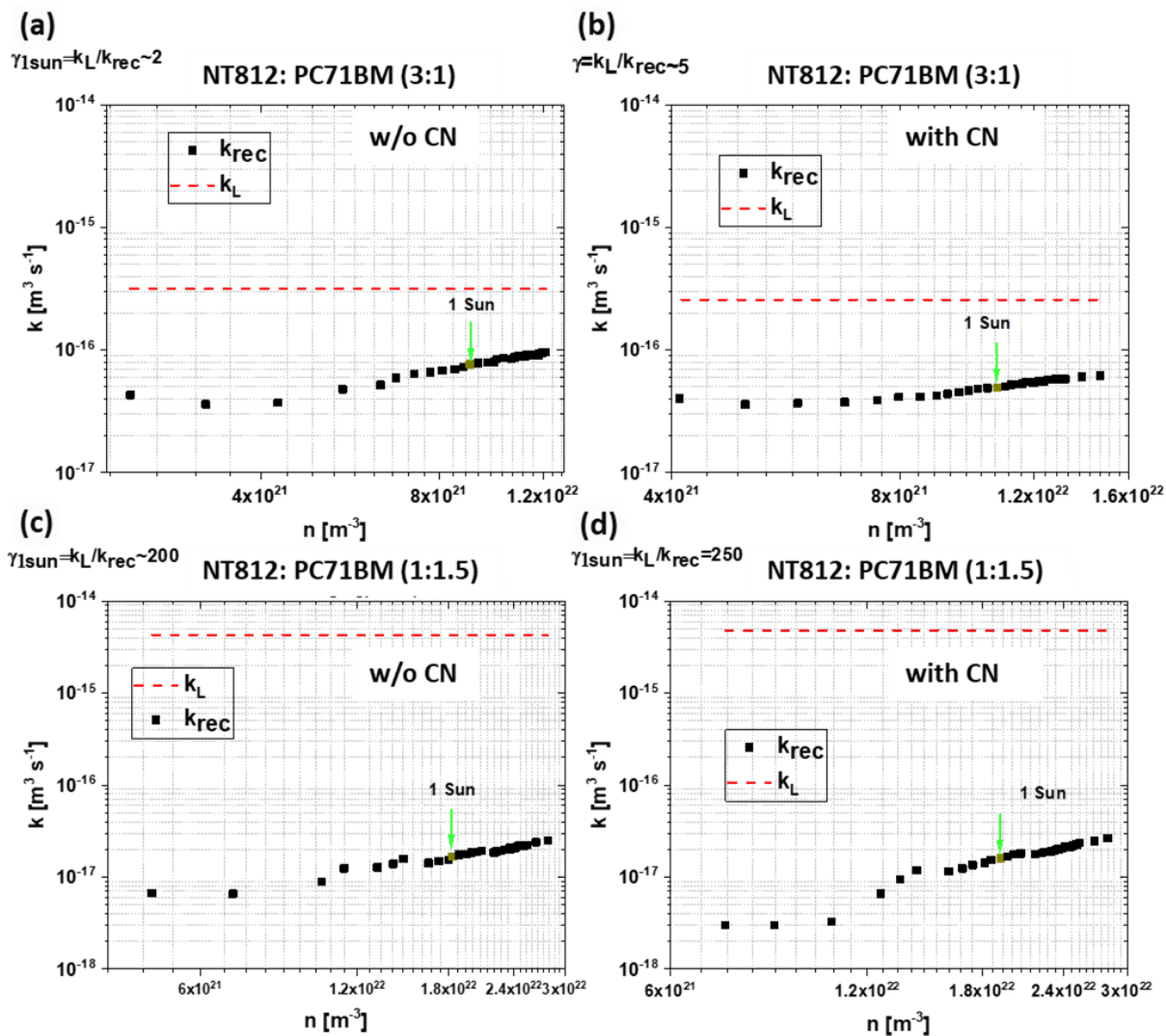


Figure S1- 2: Coefficient of bimolecular recombination as a function of carrier intensity in all four NT812:PC71BM blends. Calculated via steady-state bias-assisted charge extraction measurements, k_{rec} shown as black squares. The predicted Langevin recombination coefficient k_L is shown as dashed red lines. a) for NT812:PC71BM (3:1) blend without CN. b) for NT812:PC71BM (3:1) blend with CN. c) for NT812:PC71BM (1:1.5) blend without CN. d) for NT812:PC71BM (1:1.5) blend with CN.

See previous work for more experimental details and calculations about the coefficients of bimolecular recombination and charge carrier mobility.^{30,67} Also, refer to the experimental section in the main text.

Charge Carrier Mobilities

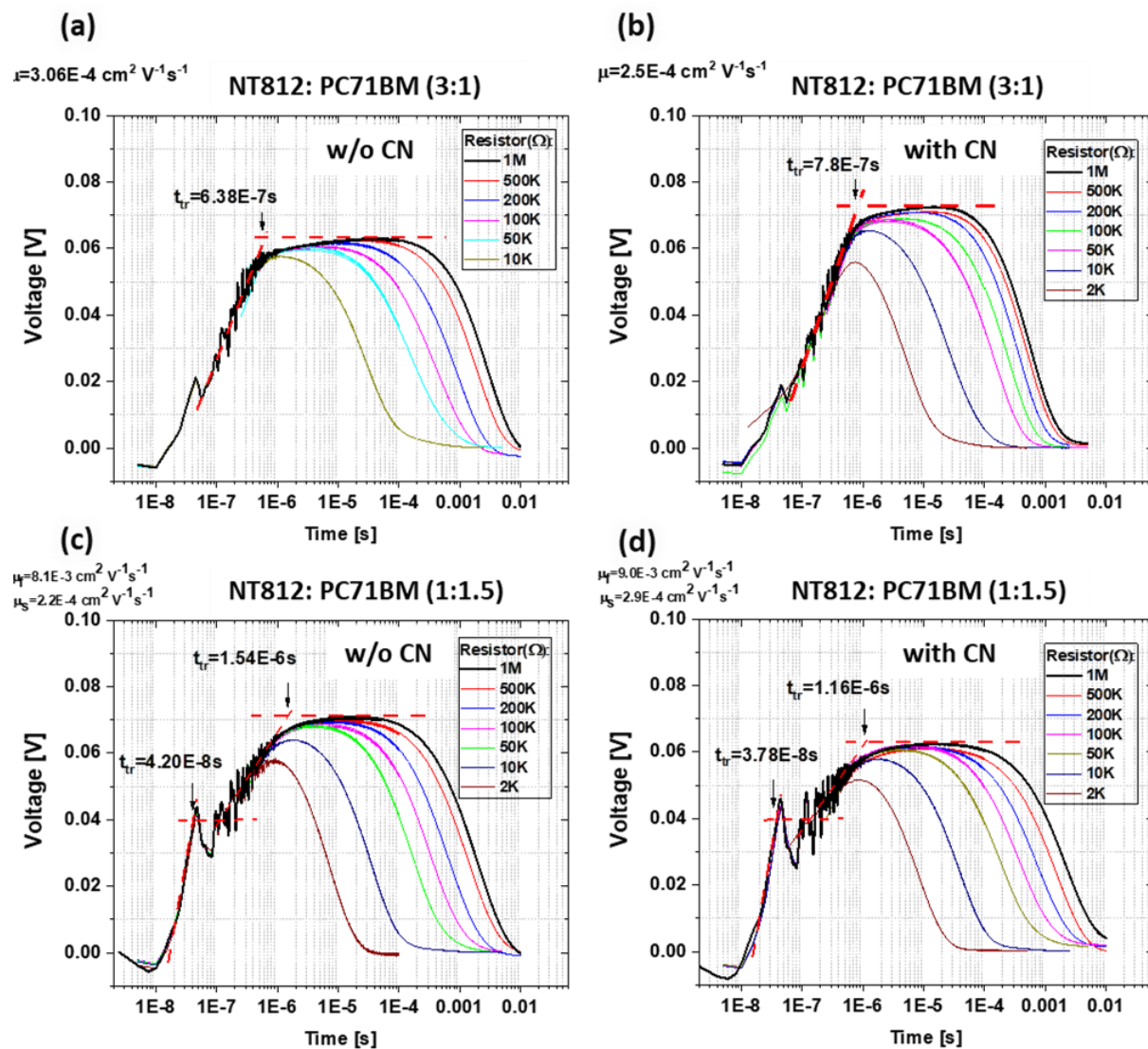


Figure S1- 3: Charge carrier mobilities were calculated via resistance-dependent photovoltage (RPV) transient measurements in all four blends of NT812:PC71BM with active layer thickness~ 200 nm. a) for NT812:PC71BM (3:1) blend without CN. b) for NT812:PC71BM (3:1) blend with CN. c) for NT812:PC71BM (1:1.5) blend without CN. d) for NT812:PC71BM (1:1.5) blend with CN.

GIWAXS Results and Analysis

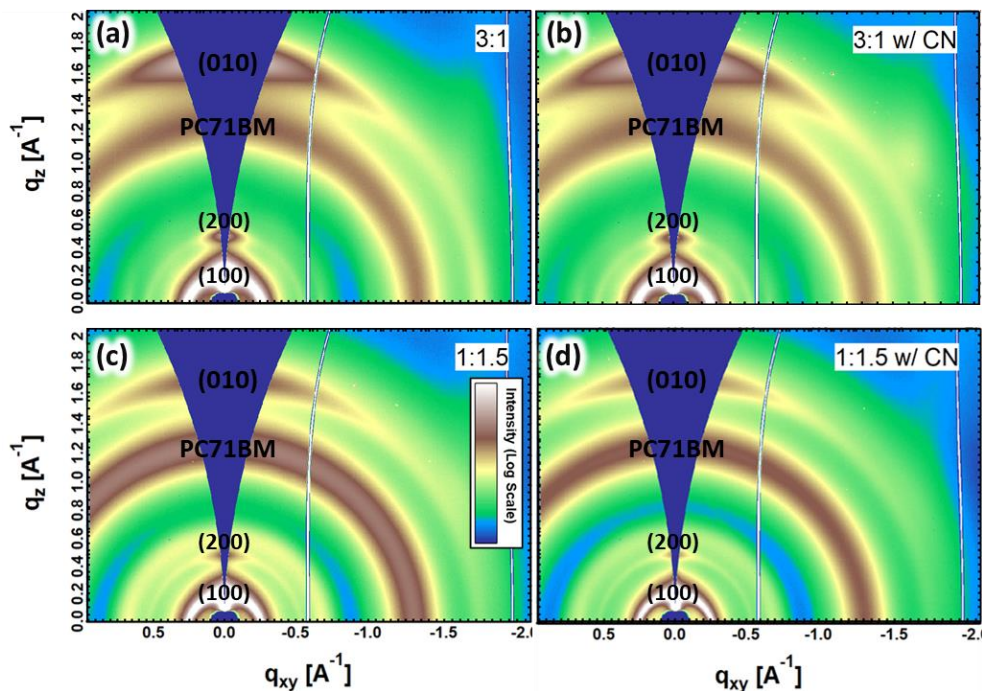


Figure S1- 4: 2D GIWAXS results for all blends as the labels indicate. All blends show PC71BM ring at $q = 1.36 \text{ \AA}^{-1}$ and pi stacking (010) of the polymer at $q = 1.83 \text{ \AA}^{-1}$. The pi stacking shows stronger OoP signal meaning face-on preferential pi packing in face-on orientation with respect to the substrate. The 2D images are plotted with an arbitrary color scale of the scattering intensities, also corrected for the missing wedge a) for NT812:PC71BM (3:1) blend without CN. b) for NT812:PC71BM (3:1) blend with CN. c) for NT812:PC71BM (1:1.5) blend without CN. d) for NT812:PC71BM (1:1.5) blend with CN.

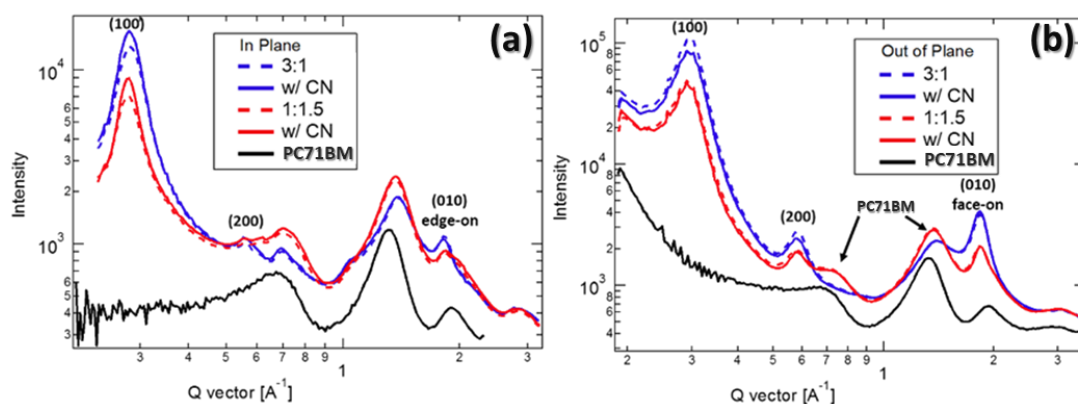


Figure S1- 5: 1D GIWAXS profiles extracted from 2D GIWAXS results in Figure S1- 4. Additionally, 1D profiles for neat PC71BM are included as reference for peak assignments. a) Profiles taking in the horizontal sector, i.e. in plane (IP). (b) Profiles taking in the vertical sector, i.e. out of plane (OoP).

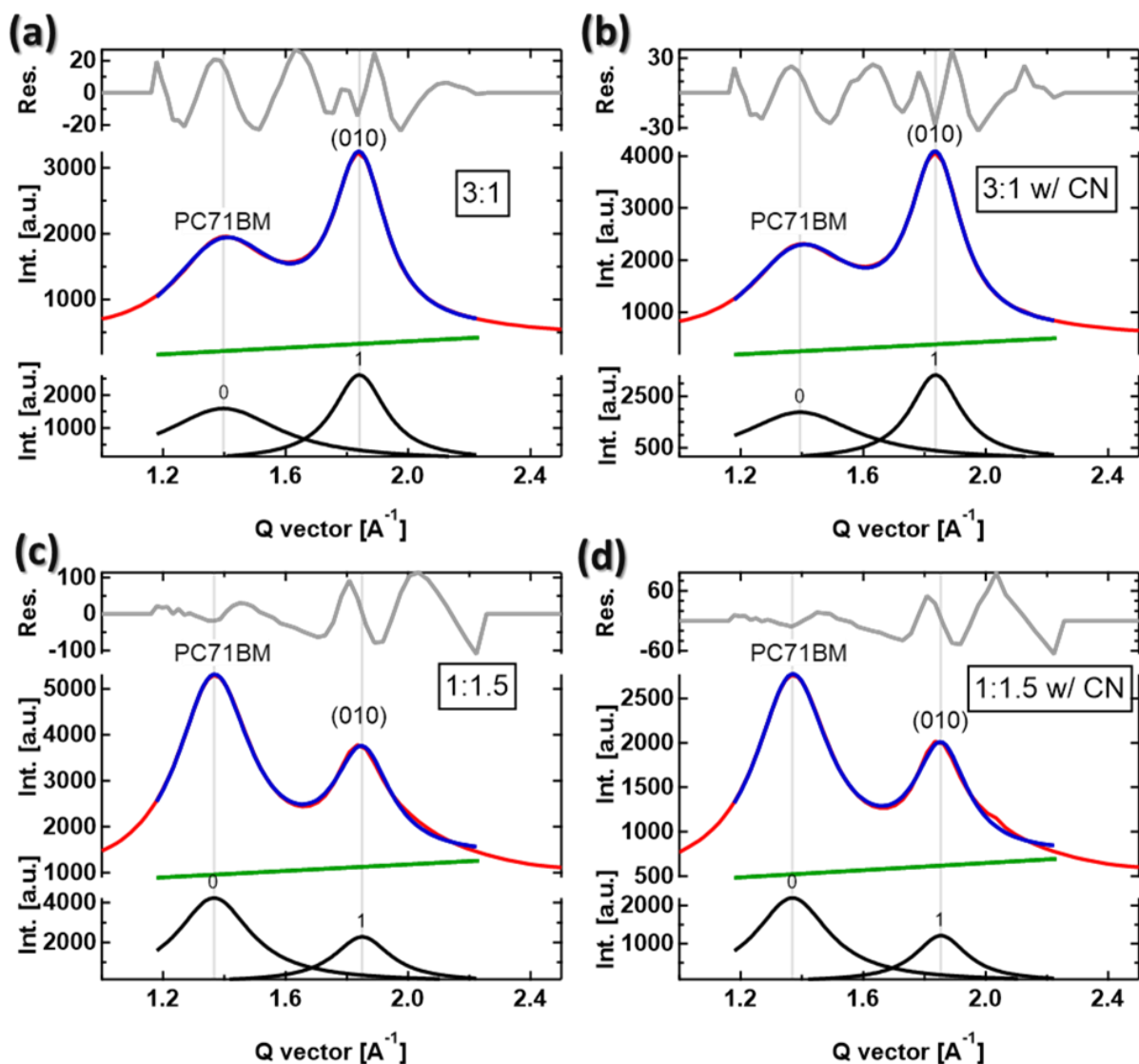


Figure S1- 6: 1D OoP GIWAXS data (red) were fitted with multi-peak fitting (blue) for PC71BM peak (at $q=1.36 \text{ \AA}^{-1}$) and pi stacking face-on peak (010) for the polymer (at $q=1.83 \text{ \AA}^{-1}$). Each peak was fitted to a Lorentzian with a linear background (green). FWHM values from the fitting results (black) were inserted in Scherrer equation [$D = \frac{2\pi K}{FWHM}$, K (constant) = 0.94] to calculate the corresponding coherence length (D) for the real-space molecular packing and ordering that causes those scattering peaks. a) for NT812:PC71BM (3:1) blend without CN. b) for NT812:PC71BM (3:1) blend with CN. c) for NT812:PC71BM (1:1.5) blend without CN. d) for NT812:PC71BM (1:1.5) blend with CN.

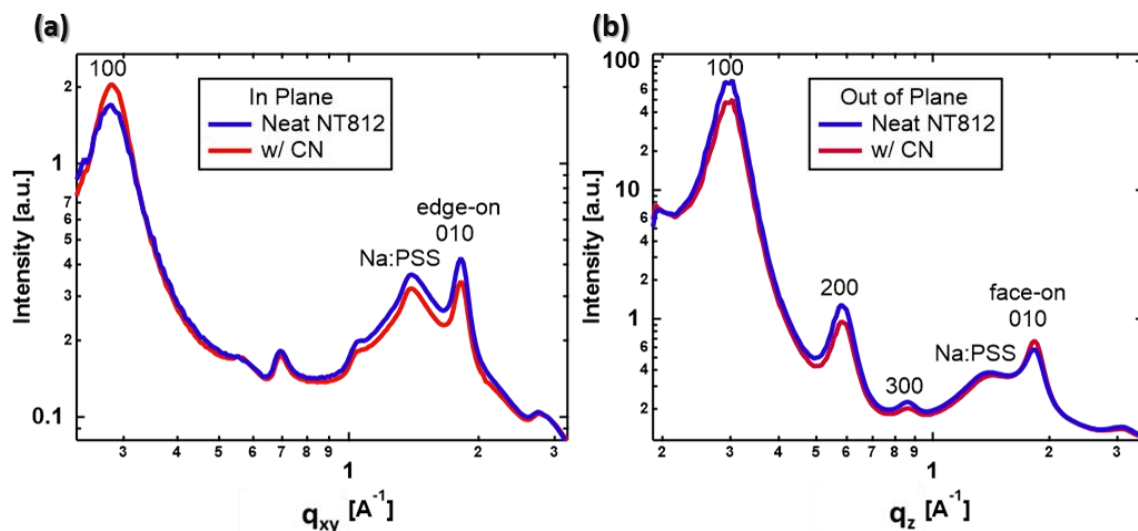


Figure S1- 7: 1D GIWAXS profiles for neat polymer (NT812) spin casted on Na:PSS/Si substrates from solution with and without additive CN. a) 1D profiles for the IP direction. b) 1D profiles for the OoP direction.

Parameter	Peak position		d-spacing	
	In Plane [\AA^{-1}]	Out of Plane [\AA^{-1}]	In Plane [\AA^{-1}]	Out of Plane [\AA^{-1}]
Lamellar (100)	0.28	0.29	22.44	21.67
Pi Stacking (010)	1.83 (edge-one)	1.83 (face-on)	3.43	3.43

Table S1- 2: Molecular packing details extracted from GIWAXS data. Scattering peak positions and d-spacing ($d = \frac{2\pi}{Q}$) for pi stacking (010) peaks and their corresponding lamellar (100) peaks of NT812 in pure polymer films and in blends with and without solvent additive CN. Also, the orientation of pi stacking with respect to substrate was indicated in parentheses. Note: those peck positions and d-spacing values do not change in all samples (both in neat polymer and blend films) which indicates that similar packing and ordering in neat polymer exist in blends.

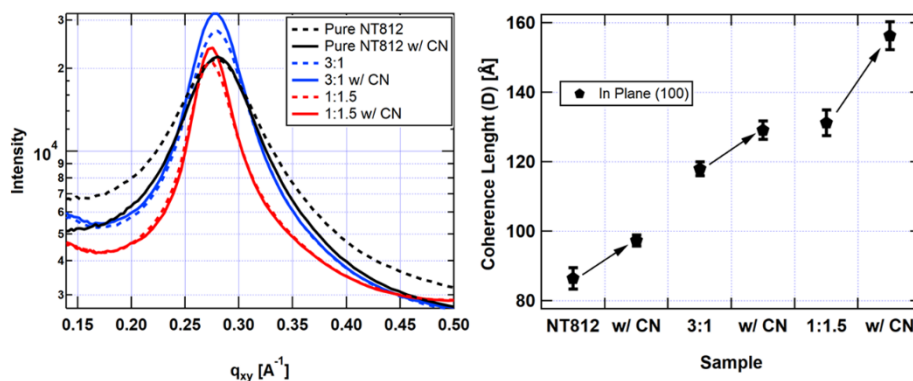


Figure S1- 8: In plane GIWAXS profiles for all blends and neat films with and without CN (left) for (100) peak. Right: coherence length (D) for the in-plane lamellar peaks (100) that are presented on the left side.

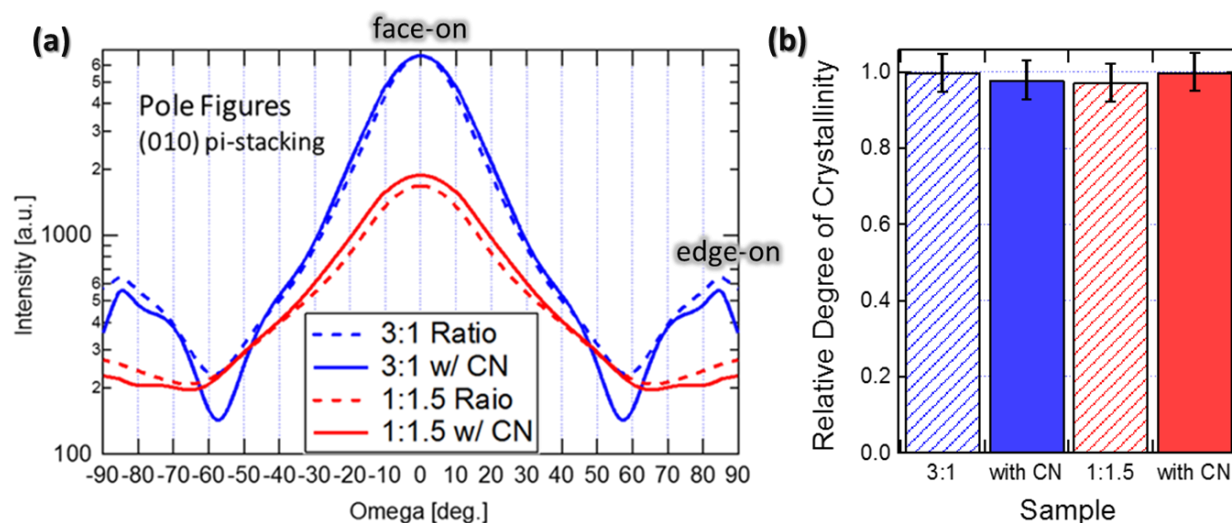


Figure S1- 9: a) Pole figures for NT812 (010) pi-stacking were processed for all blends from GIWAXS data. Where “Omega” defines the angle between the crystallite orientation and the surface of the substrate. b) Bar graph representation of relative degree of crystallinity (rDoC) for (010) pi-stacking in all NT812: PC71BM blends, calculate by integrating the profiles in part (a).

Pole figures,¹⁰² here, describe orientation distribution of the polymer π - π stacking (010). Thus, the results suggest that all blends show that NT812 prefer (face-on) orientation with respect to the substrate. Relative degree of crystallinity (rDoC) analysis for (010) pi-stacking shows that all blends have similar rDoC for the π - π stacking (010) peak in the polymer domains.

$$\text{rDoC} = \frac{\text{Volume of Polymer Crystal (all orientations)}}{\text{Total Volume of Polymer}}$$

Near-Edge X-Ray Absorption Fine-Structure (NEXAFS) Spectroscopy

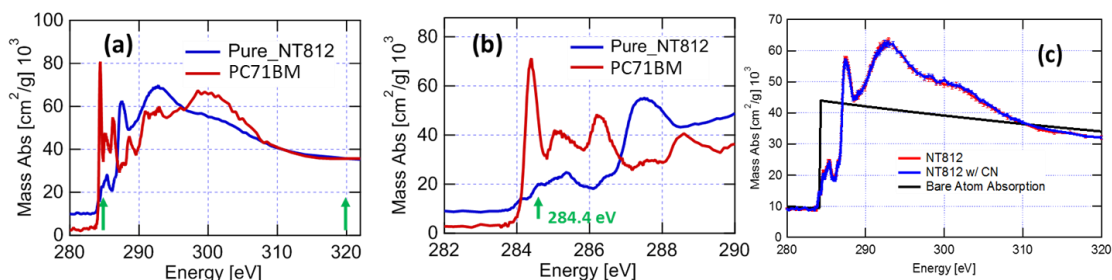


Figure S1- 10: a) NEXAFS spectra for pure NT812 and pure PC71BM scaled to their bare atom absorption coefficient. The STXM imaging energies were selected based on those NEXAFS spectra, mass absorbance, for the donor and acceptor. b) A zoomed in version of (a). At 284.4 eV, the fullerene has higher absorbance than the polymer. Another imaging energy was chosen to be 320 eV where the fullerene and polymer absorb about the same. c) NEXAFS spectra for pure polymer with and without solvent additive CN as shown in (c). The mass absorbance is relatively similar for neat polymer (NT812) with and without CN.

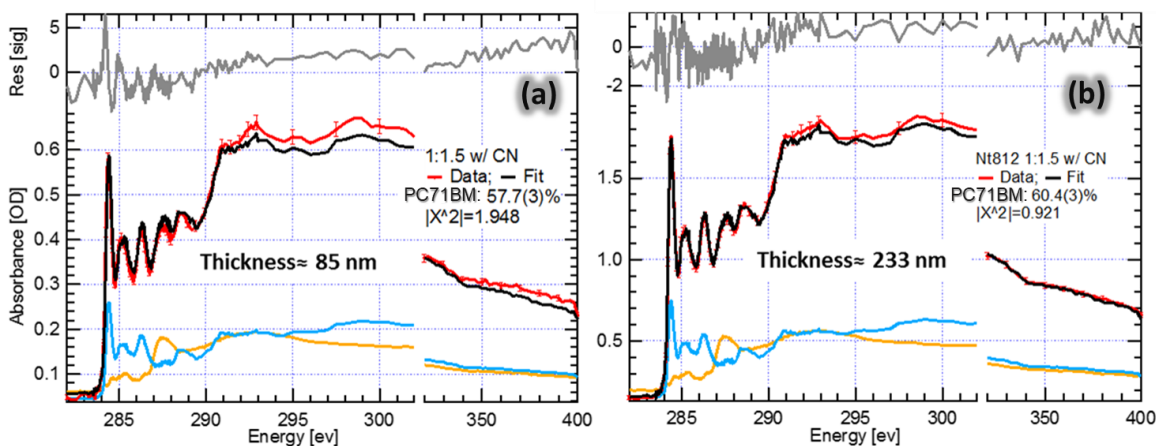


Figure S1- 11: NEXAFS for NT812: PC71BM (1:1.5) blends (red) with CN, but different thicknesses. Linear fits (black) of the NEXAFS spectra of the blend films (red) with reference NEXAFS spectra for neat materials, NT812 (orange) and PC71BM (blue). The fitting of NEXAFS spectra for blend films enables quantitative determination of average chemical composition. The film thickness also calculated from beer-lambert law. The fit residuals shown on top (gray). Results show that the average composition of both blends ~ 60% PC71BM, which agree with the blending weight ratio (1:1.5). a) for a thin NT812:PC71BM (1:1.5) blend with CN. b) for a thick NT812:PC71BM (1:1.5) blend with CN

Scanning Transmission X-ray Microscopy (STXM) for Composition Mapping

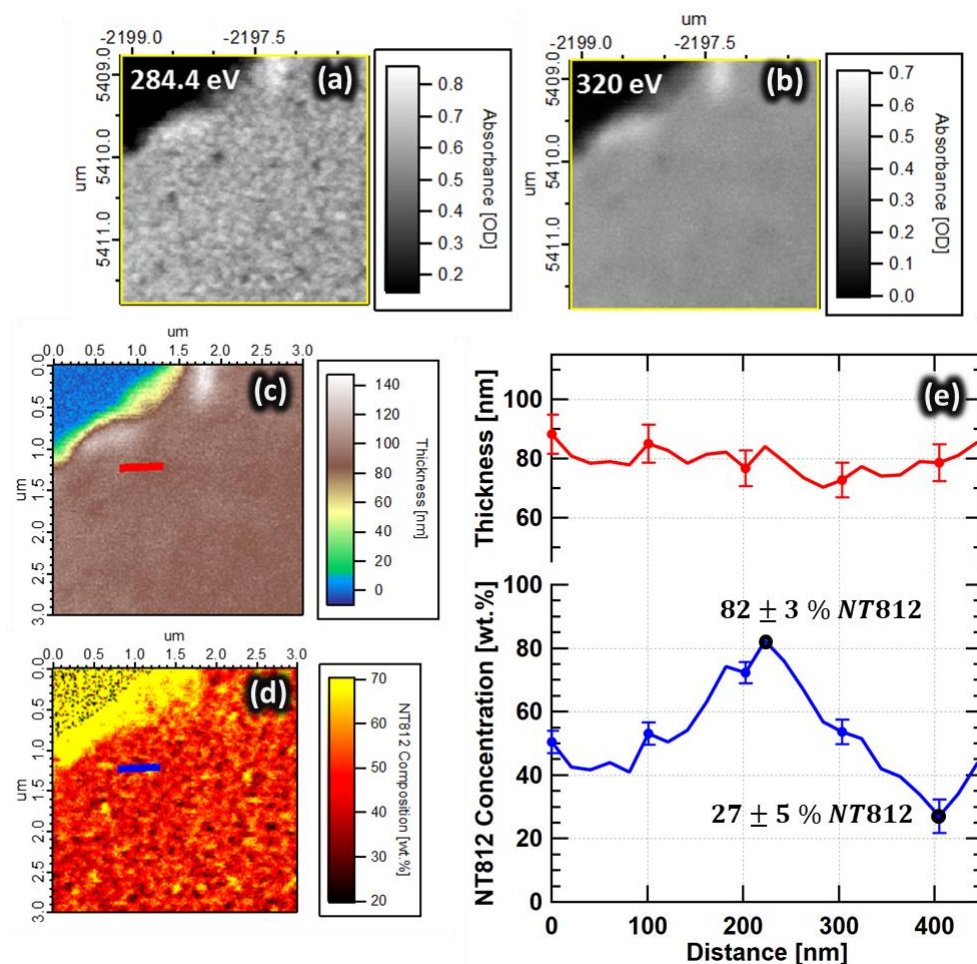


Figure S1- 12: Composition mapping analysis for a thin NT812: PC71BM (1:1.5) blend with CN. a) A STXM image was taking at fullerene resonant energy (284.4 eV) and the image in (b) was taken at a non-resonant energy (320 eV). By combining those STXM images with NEXAFS spectra for neat materials, a thickness map (c) as well as a composition map (d) were generated. e) Line profiles show variation in thickness (Red) and composition (blue) across a region of the blend film as presented in colored lines in c and d. From (e) the average thickness is about 85 nm. Also, the polymer concentration in the polymer-rich domain is 82 ± 3 wt. % and 27 ± 5 wt. % in the fullerene rich domain. The deconvolution of the X-ray beam tails suggests pure domains (see Figure S1- 13-Figure S1- 15 for the deconvolution analysis).

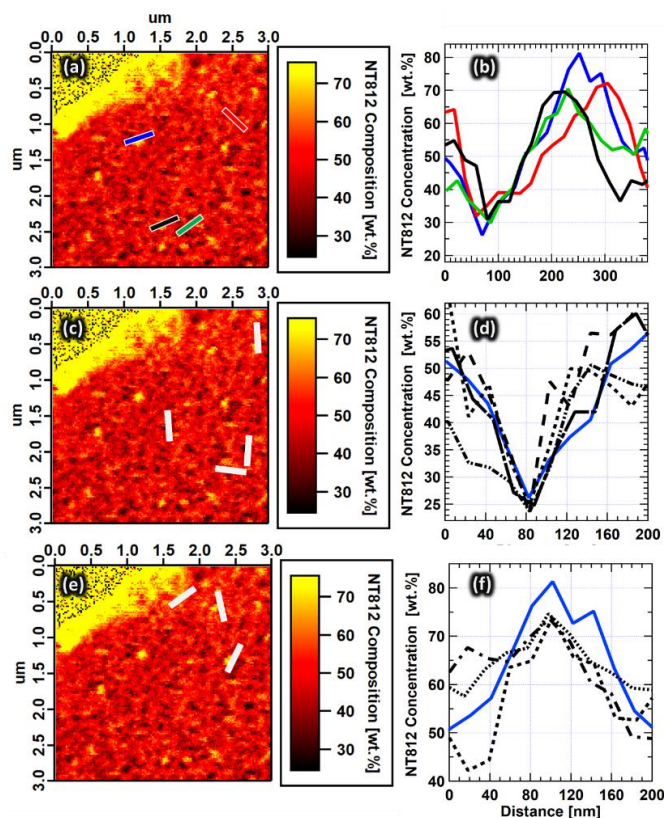


Figure S1- 13: The composition images on the left, a, c and e are the same composition image as in Figure S1- 12 d with bars that correspond to the spots where the 1D line profiles in b, d and f were extracted from. b). Shows 1D concentration profiles that were extracted from different spots as indicated with colored lines in (a). The general trends of feature size and compositional fluctuation are consistent across the film. d). The profiles were extracted from fullerene-rich spots, as indicated with white bars in (c), to show that the polymer concentration gets as low as 25% or less. f). Concentration 1D profiles extracted from (e) as indicated by white bars to show that the polymer concentration can get above 75%. The blue traces in d and f are the same as the blue one in b. In general, the polymer concentration fluctuation, high and low, can be found in several spots of the film. It was impossible to get 100% or 0% polymer concentration profiles from the raw compositional maps due to the x-ray beam convolution with the relatively small domain sizes in those NT812:PC71BM systems. Therefore, 1D and 2D deconvolution analyses were conducted to retrieve the real molecular concentration in the polymer and fullerene domains.

After considering the convolution of the x-ray beam tails with film domains, the results suggest the presence of pure polymer and fullerene domains. The deconvolution analysis of the line profiles is similar to our previously published calculation.²⁴ We have also conducted 2D deconvolution analysis as shown in Figure S1- 14 and Figure S1- 15. Our 2D deconvolution results also suggest the existence of pure polymer and fullerene domains.

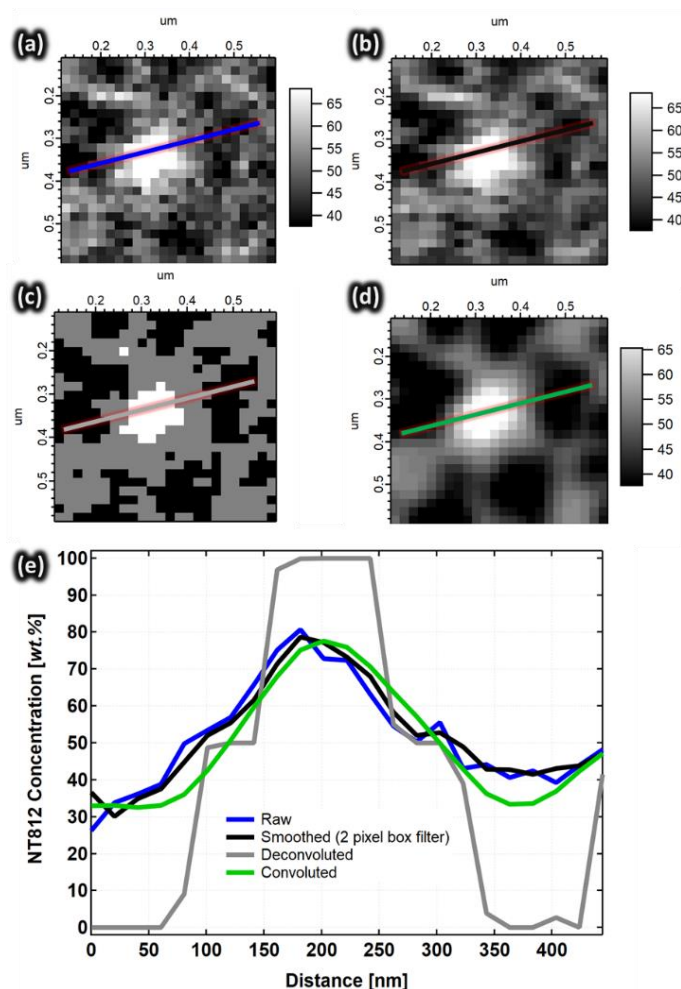


Figure S1- 14: a). This is the same image as the raw composition map in Figure S1- 12d but zoomed in on the spot where the blue line is, also in a grays color scale instead. b). A smoothed version of the image in (a), smoothed with a 2-pixel box filter to reduce the noise effects. c). A deconvoluted image that shows better representation of the real film. Where black is 100% fullerene, gray is 50% and white is 100% polymer. The gray regions, i.e., 50% concentration, indicate film spots where there are vertical overlaps between pure polymer and fullerene domains. d). A result of convolving (c) with the X-ray beam profile in Figure S1- 15. e). 1D line profiles to compare compositional variation across different domains in the 2D images, a, b, c and d (as indicated by colored lines in the images).

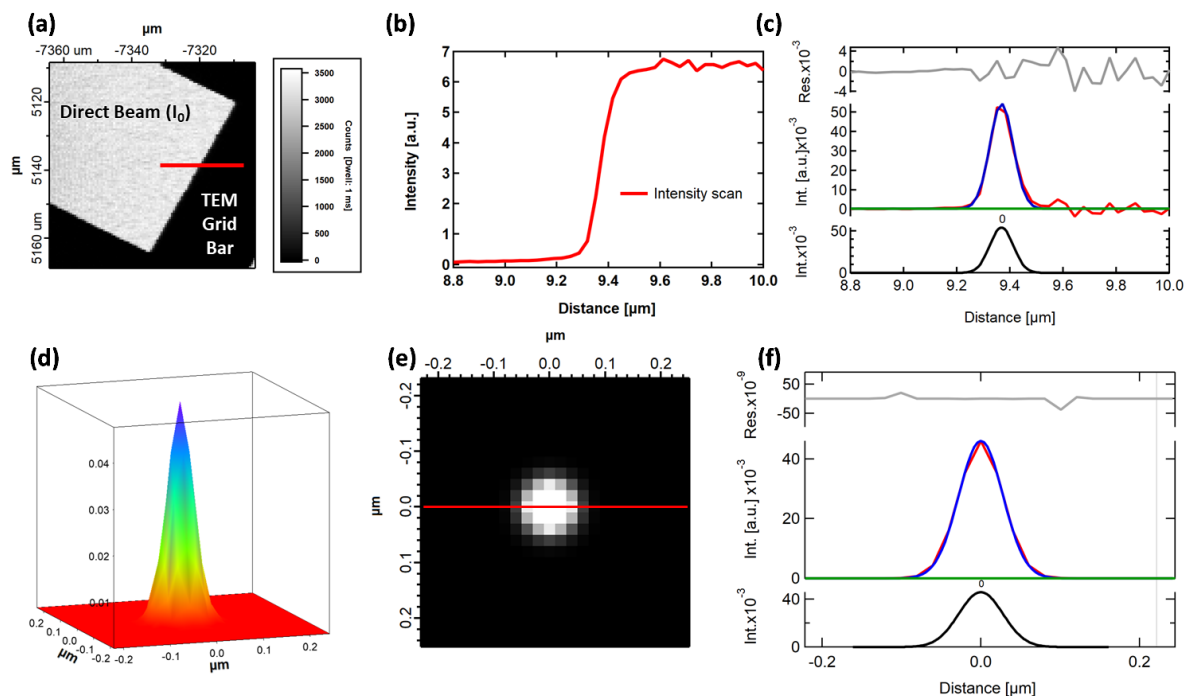


Figure S1- 15: Constructing a 3D representation of the X-ray beam profile. A scan across a TEM grid bar “a knife-edge scan” was taken as shown in (a). The dark regions show the grid bars where the beam is totally blocked. The bright region is the direct beam through a mesh hole. b) An intensity scan across a knife edge of the TEM grid bar as indicated by a red line in (a). The total intensity changes from zero “dark”, where the beam is totally blocked, to direct beam (I_0). The intensity line scan was taken at $E = 320$ eV. c) A gaussian peak fitting of the derivative (red) of the intensity line scan in b. The FWHM is ~ 100 nm, which should be the maximum beam FWHM because the beam was not 100% focused. d) An approximate 3D representation of the X-ray beam, assuming a gaussian symmetric beam. e) A 2D representation of (d). f) A peak fitting for a line profile that was extracted from (e), as indicated with a red line. The fitting results suggest a gaussian beam profile with FWHM ~ 65 nm.

The knife-edge measurement of the STXM X-ray beam is simple, yet useful to get a good approximation of the beam width and its upper limit. Our calculation of beam profile width (FWHM ~ 100 nm) shows similar or even sharper beam than previous calculations (FWHM >100 nm).⁵⁴

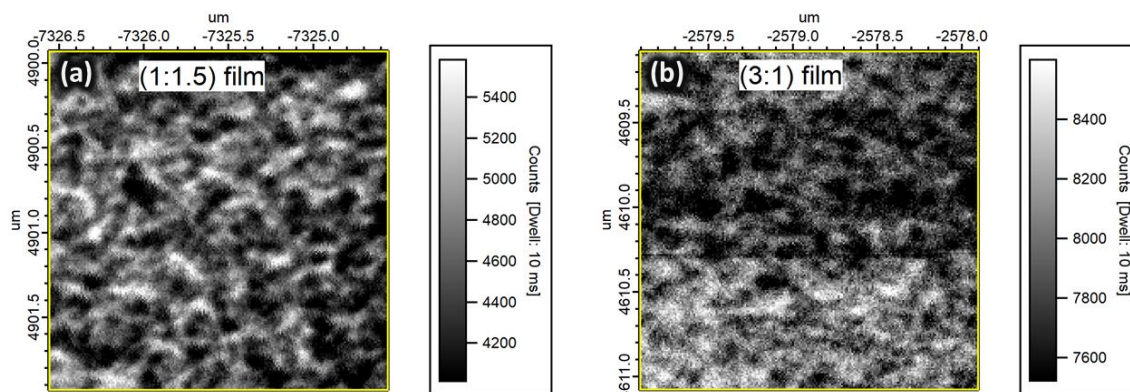


Figure S1- 16: STXM composition scans were taken on ~ 200 nm films at 284.4 eV, which is fullerene absorption peak, i.e., a fullerene resonant energy. PC71BM (dark regions) and NT812 (white fibrils). The images are for a 1:1.5 blend without CN% (a) and a 3:1 blend with 0.5 CN% (b). The overall shapes of PC71BM domains and polymer fibrils in the thick (1:1.5) film is similar to the thin film (see Figure 2- 3b in the main text).

Materials Contrast: X-ray Scattering Energy Selection

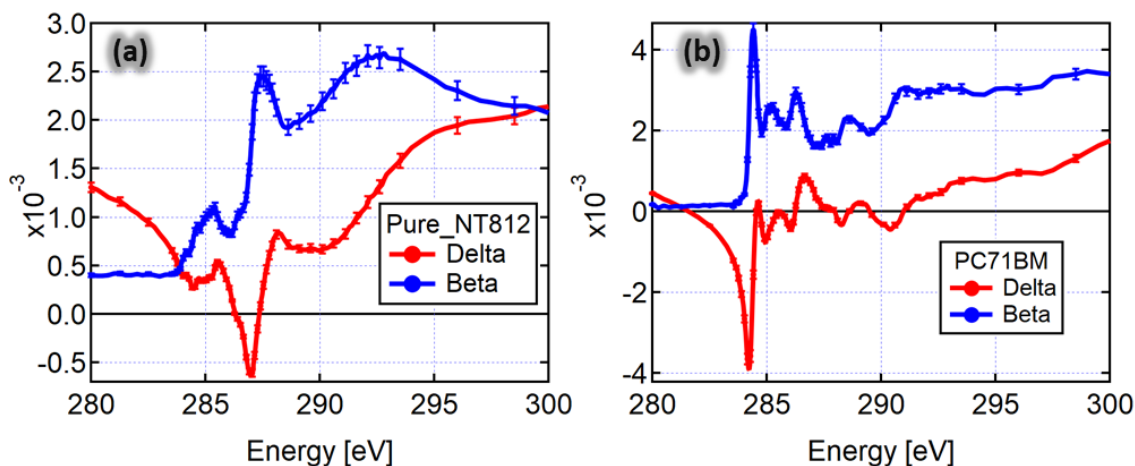


Figure S1- 17: Scattering intensity (I) is proportional to the contrast function, $I(E) \propto |\Delta \mathbf{n}|^2$, where (n) is index of refraction $\mathbf{n} = \mathbf{1} - \delta + i\beta$. The imaginary part (beta) is related to absorbance, calculated from NEXAFS measurements, and the real part (delta) is calculated from the Kramers Kronig transform. The graphs show the real (red) and imaginary (blue) parts of indices of refraction for neat polymer (a) and neat fullerene (b).

Details of the Kramers Kronig Transform can be found elsewhere.⁵⁵ See previous work for more details on this transformation and calculation of index of refraction and contrast function.⁴⁵

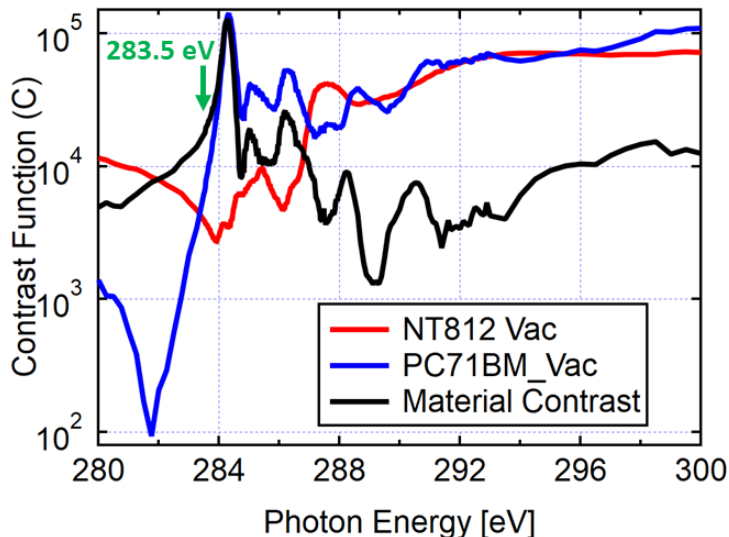


Figure S1- 18: Materials and vacuum contrast functions based on the material indices of refraction, where contrast function is $C = E^2 |\Delta \mathbf{n}|^2$.

RSoXS: Film Thickness Calculation via NEXAFS Absorbance Profiles

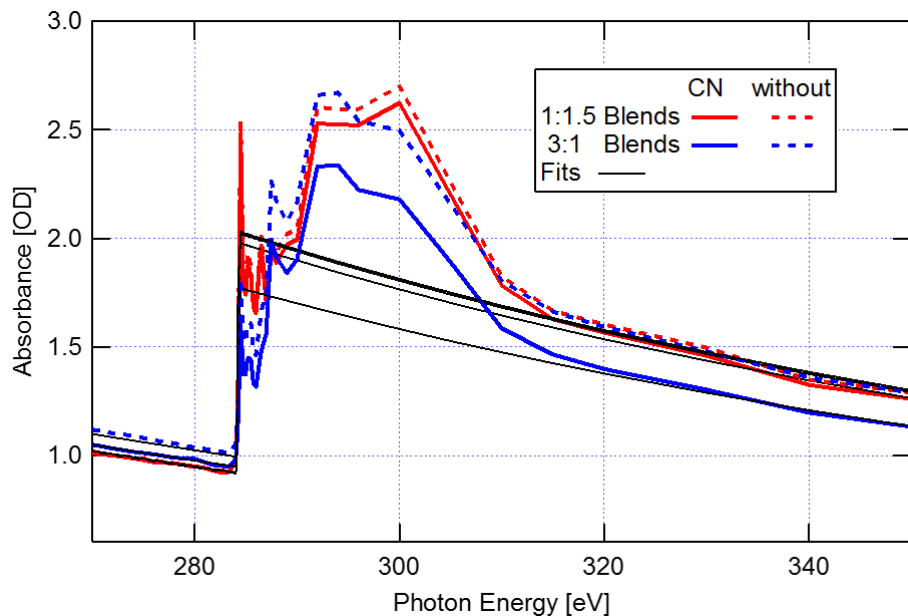


Figure S1- 19: NEXAFS measurements for all blends to determine film thickness at the same spots where RSoXS data was taken on each film. NEXAFS profiles were scaled to the mass absorbance coefficient (black fits) of the bare atoms. Film thickness calculated via Beer-lambert's law then used to normalize RSoXS data. Where the film thickness $= \frac{1}{\mu(E) \times \rho} \ln \left(\frac{I_0(E)}{I(E)} \right)$, here $I_0(E)$ is the intensity of the direct incident beam, $I(E)$ is intensity of the transmitted beam through the film, $\mu(E)$ is the mass absorption coefficient, and ρ is the film density.

RSoXS: Composition Variation and Characteristic Length

Refer to our previous work, for more details about the two domain modeling and calculation of composition fluctuation.²⁴

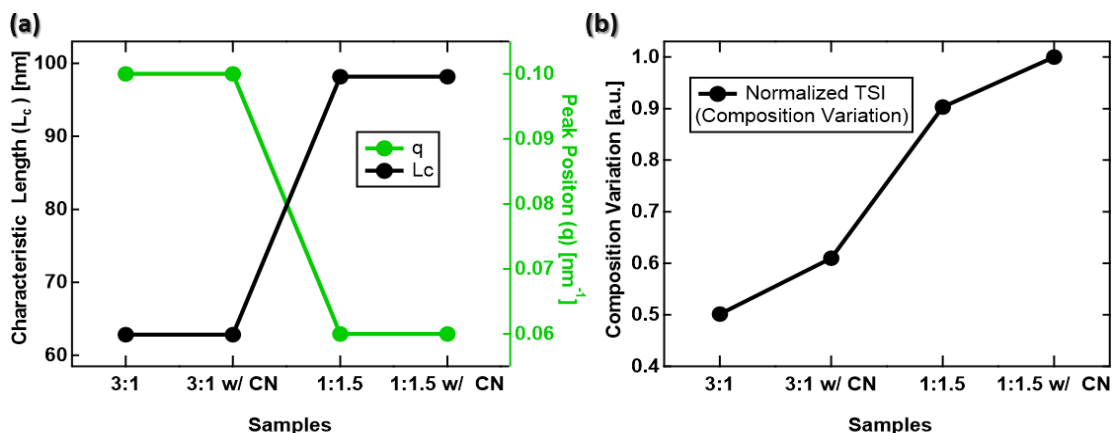


Figure S1- 20: Calculations based on RSoXS results in the main text (Figure 2- 4a). a) Characteristic length (L_c) of the corresponding features (black) for each film was calculated as $L_c = 2\pi/q$ where q is the peak position (green). b) The composition variation in each blend was calculated by normalizing the total scattering intensity (TSI) values for each blend to TSI for 1:1.5 with CN, which shows the highest scattering intensity. The TSI \sim integral of the RSoXS scattering profiles in Figure 2- 4a of the main text.

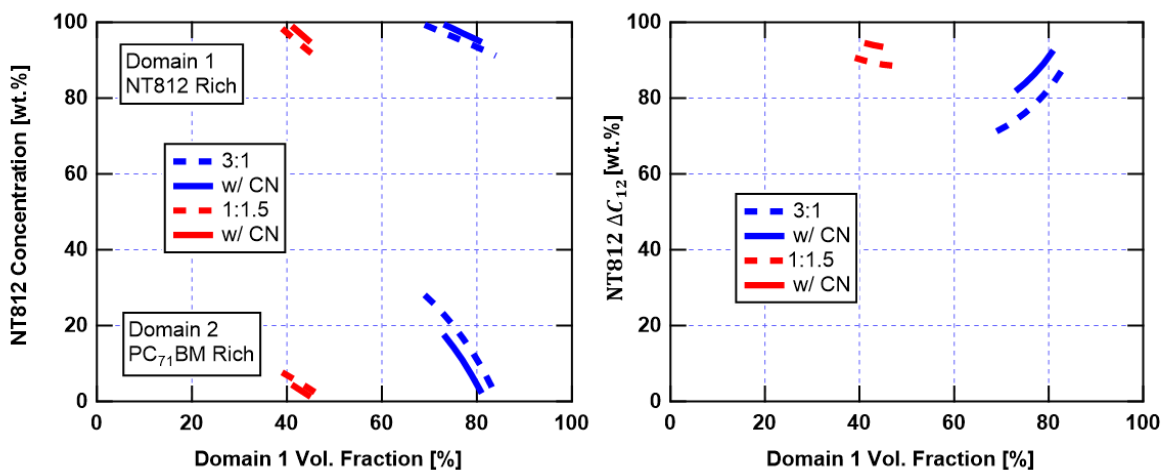


Figure S1- 21: a) Concentration variation of the polymer as a function of its volume fraction, based on two domains model. b) Composition fluctuation of the polymer between the two domains ($\Delta C_{12} = C_1 - C_2$) which indicates the lateral RMS of the polymer concentration in a film.

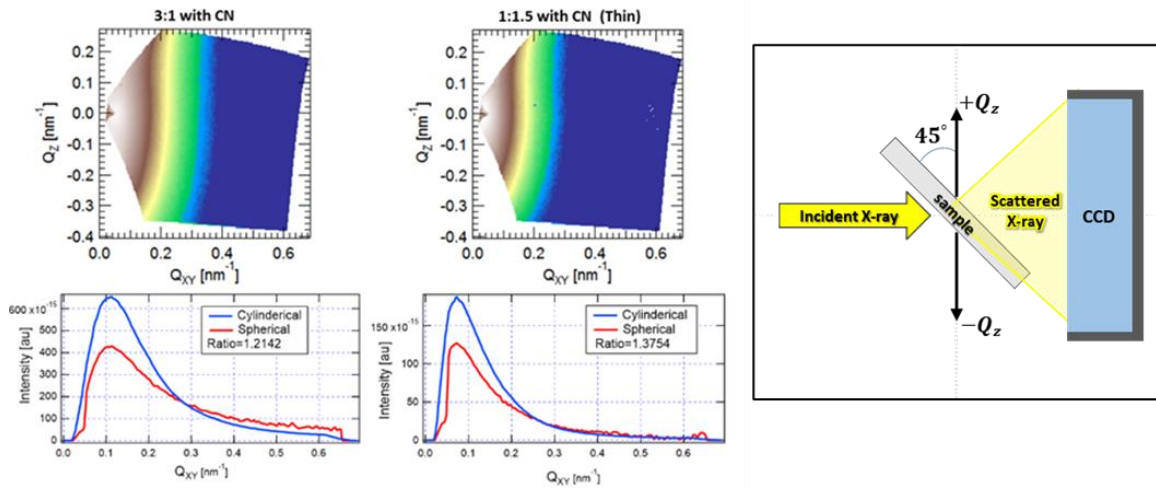


Figure S1- 22: RSoXS results at 45-degrees sample tilt plotted to explore the q_z component. Data examples shown here are for the 3:1 (200 nm) film with CN and 1:1.5 (100 nm) film with CN. 2D RSoXS data shown in Q_z vs Q_{xy} (top) and extracted average 1D profiles (bottom). The intensity decreases in direction of $-Q_z$ due to higher absorption of photons that travel longer paths through the sample as shown in the 45-degee RSoXS geometry diagram on the right side.

The 2D data indicates that there are no features in the z -direction, i.e., no vertical stratification. The 1D profiles show features with peak positions that agree with RSoXS data at normal incidence (refer to Figure 2- 4a). For more details on the transmission scattering geometry at 45-degrees of sample tilt, refer to our previous work.⁸⁷

Donor-Acceptor Interfacial Width Calculation

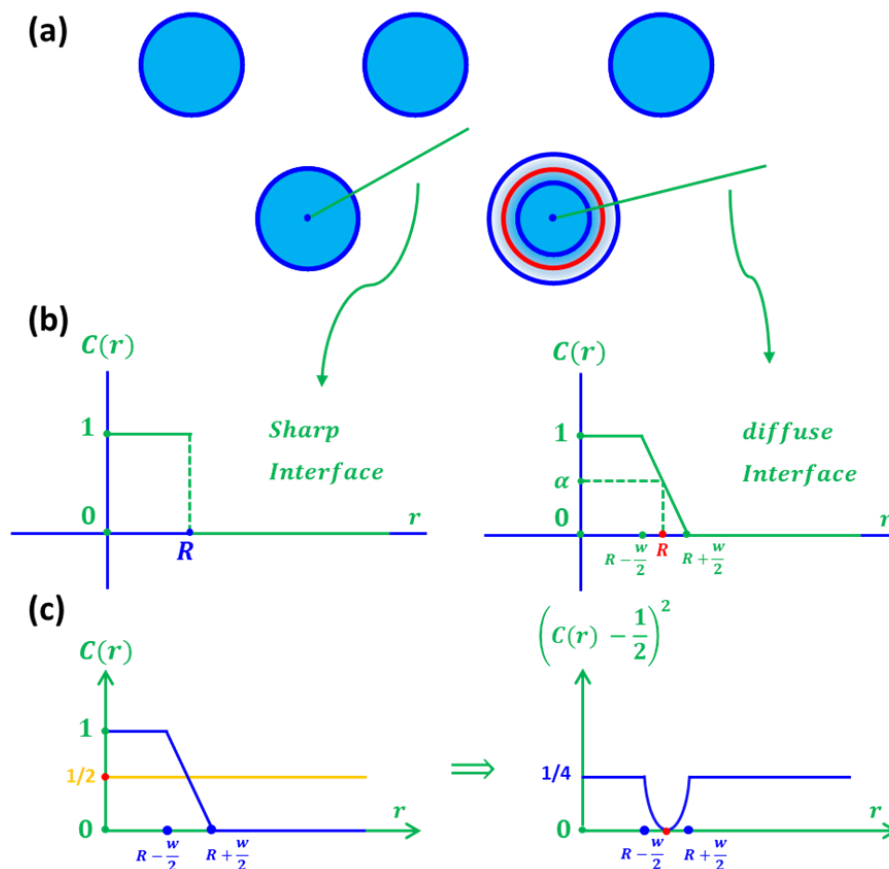


Figure S1- 23: Model to calculate interfacial width. a) Schematic of fibril cross-sections. b & c) composition profiles extracted from the green lines in (a).

RMS Composition Fluctuation Between Pure Domains Converted to Interfacial Width

To calculate the effects of molecular mixing between domains, we combine our measurement of the RMS composition fluctuation ΔC_{RMS} , and characteristic length L_C both from RSoXS analysis, and the known average polymer concentration in the blend $\alpha = \frac{m_p}{m_p + m_f}$. For the purposes of the calculation, we start with the assumption of a hexagonal lattice of pure cylindrical polymer fibrils in a matrix composed of pure fullerene (Figure S1- 23a). However, later we show how we can relax the assumption of a lattice or regular fibril radii R . We assume

that $L_C = d$ the domain spacing and can calculate the fibril radii using basic geometry of the hexagonal lattice $R = d\sqrt{\frac{\sqrt{3}\alpha}{2\pi}}$. Taking the origin to be at the center of a cylindrically symmetric fibril, we can characterize the composition as a function of radius r in the sample $C(r)$ in the case of sharp interfaces and in the case of a linearly varying concentration over a region w as shown in Figure S1- 23b. We can connect this model with our measurement ΔC_{RMS} with the following integral over the sample volume:

$$\Delta C_{RMS}^2 = \frac{1}{V} \int [C(r) - \alpha]^2 dV$$

We can use the coarea formula to solve this equation for the interfacial width w . While the case we apply — a simple linear transition — invokes only a very familiar case used in physics calculations, this method will work for a wide range of bounded curvature “cylinders”. In the calculation below, ΔC_{RMS}^2 is called the fractional reduction in RMS.

Coarea Formula

While anybody who has taken multivariable calculus has seen Fubini's theorem,¹⁵⁶ in action — we almost always do multivariable integrals one coordinate at a time — usually that deep generalization of this theorem called the coarea (pronounced co-area) formula is not well known outside of geometric analysis.

Recalling Fubini

Recalling Fubini's theorem for the case that

$$\Omega = [a_1, b_1] \times [a_2, b_2] \times [a_3, b_3] \cdots [a_n, b_n] \subset \mathbb{R}^n$$

We have:

$$\int_{\Omega \subset \mathbb{R}^n} g(\vec{x}) d\vec{x} = \int_{a_1}^{b_1} \left(\int_{a_2}^{b_2} \left(\int_{a_3}^{b_3} \cdots \left(\int_{a_n}^{b_n} g(x) dx_n \right) \cdots dx_3 \right) dx_2 \right) \cdots dx_1$$

Which, in the case of 2 dimensions becomes:

$$\int_{\Omega \subset \mathbb{R}^2} g(\vec{x}) d\vec{x} = \int_{a_1}^{b_1} \left(\int_{a_2}^{b_2} g(x_1, x_2) dx_2 \right) dx_1$$

Fiddling with Representations

Now will do something that might seem a bit overly complicated, but will help us move to the generalization. We define $F(x_1, x_2) = x_1$. We notice that the length of the gradient vector of this map is the constant 1 and note that this is $\sqrt{\det(\nabla F \cdot \nabla F^*)}$ which we call JF . (In general, for $F: E \subset \mathbb{R}^n \rightarrow \mathbb{R}^k$ where $k \leq n$, $\sqrt{\det(DF \cdot DF^*)}$ where DF is the $k \times n$ dimensional matrix

of partial derivatives of F and DF is its transpose.) We also notice that the first (innermost) iterated integral is the integral over level sets of F — i.e. we are integrating over subsets of the domain where the value of F (i.e. x_1) is fixed. So far, there is nothing new—we are simply changing representations. Finally, we will write μ to represent the usual area measure on \mathbb{R}^2 and \mathcal{H}^1 to represent the 1-dimensional length measure on 1-dimensional sets (this is the 1-dimensional Hausdorff measure).

Using our Fiddle to get to the Punchline

Let's rewrite the last integral using these representations:

$$\int_{\Omega \subset \mathbb{R}^2} g(x) J F(x) d\mu = \int_{a_1}^{b_1} \left(\int_{F^{-1}(x_1) \cap \Omega} g(x_1, x_2) d\mathcal{H}^1 \right) dx_1$$

At this point, it is very important for you to convince yourself that every piece of this makes sense to you for the simple reason that once you have the steps up to the coarea formula is much easier.

Why? *Because*: the coarea formula in our case is given by:

$$\int_E g(x) J F d\mu = \int_{\mathbb{R}} \int_{F^{-1}(y) \cap E} g(x) d\mathcal{H}^1(x) dy$$

Where $J F$ is the Jacobian of $F: \mathbb{R}^2 \rightarrow \mathbb{R}$, \mathcal{H}^1 is the 1-dimensional Hausdorff measure, and μ is the area measure on \mathbb{R}^2 .

Now, the slick thing: $F: \mathbb{R}^2 \rightarrow \mathbb{R}$, \mathcal{H}^1 can be any Lipschitz continuous mapping.

(Recall that a function is Lipschitz continuous if there is a positive constant $K < \infty$ such that $|F(x) - f(y)| \leq K |x - y|$ for every x, y , in the domain of F .)

The picture is that instead of integrating over level sets of F being the planes defined by the equation $F(x_1, x_2) = x_1$ for some fixed x_1 , we can integrate over level sets of any Lipschitz function. In our case, we are integrating over the level sets of the distance function to the set = {center of the disk} which coincide with a choice of F = the distance function to the disks of higher density. See Figure S1- 24.

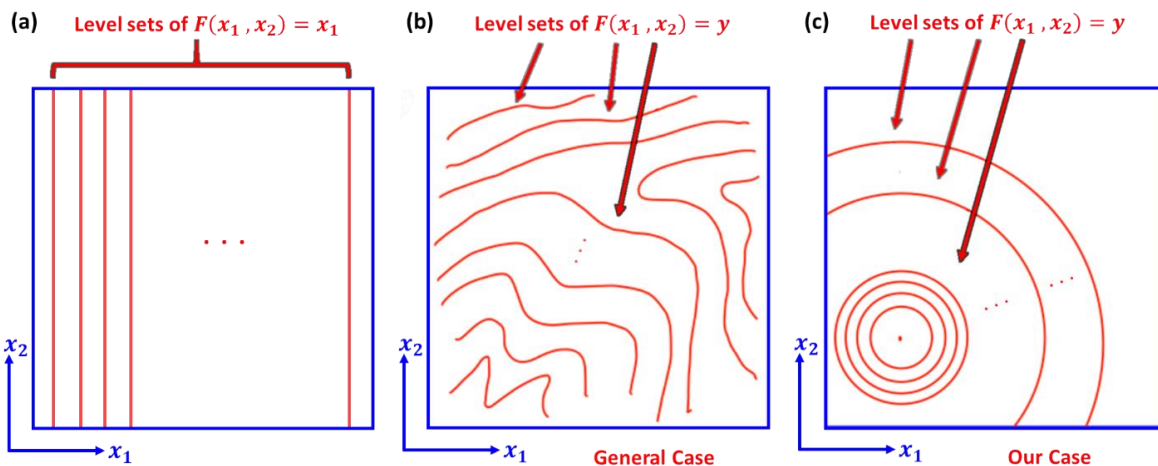


Figure S1- 24: a) The usual case of Fubini's Theorem. b) The coarea formula is a deep generalization. It applies to wild sets of mappings F that are merely Lipschitz continuous. c) Our case—a common one in physics problems with symmetries—is the case in which the level sets are spheres of some dimension.

The Co-area Formula in our Case

Because $JF = \sqrt{\det(\nabla F \cdot \nabla F^*)} = 1$ except for a set of measure 0 when F is a distance function, the above formula reduces to:

$$\int_E g(x) d\mu = \int_{\mathbb{R}} \int_{F^{-1}(y) \cap E} g(x) d\mathcal{H}^1(x) dy$$

and because we will choose transition functions $g(x)$ which are constant on the level sets of F , we can further simplify to:

$$\int_E g(x) d\mu = \int_{\mathbb{R}} g(F^{-1}(y)) \mathcal{H}^1(F^{-1}(y) \cap E) dy$$

where μ now is the area measure on E

Two Cases

We now compare the cases in which $g(x) = (C(r) - \alpha)^2$ is either a sharp transition between regions of constant density and the case in which it is a linear transition (See Figure S1-23b and c).

As a result, we can see that:

$$\int_E \left(C(r) - \frac{1}{2}\right)^2 d\mu = \begin{cases} \frac{1}{4} \mu(E) & \text{sharp transition} \\ < \frac{1}{4} \mu(E) & \text{non - sharp transition} \end{cases}$$

Assuming a hexagonal arrangement, we get that each equilateral triangle contains $\frac{1}{2}$ disk.

So, as long as E is some union of these equilateral triangles (see Figure S1-25), we get that

$$\int_E \left(C(r) - \frac{1}{2}\right)^2 d\mu = \frac{1}{4} \mu(E) - N_E \left(\frac{1}{4} \frac{\pi}{2} \left(\left(R + \frac{w}{2}\right)^2 - \left(R - \frac{w}{2}\right)^2 \right) - \int_{R - \frac{w}{2}}^{R + \frac{w}{2}} \pi r \left(C(r) - \frac{1}{2}\right)^2 dr \right)$$

where the part we have used the coarea formula for is the integral on the right side of the above equation and where $N_E =$ numbers of equilateral triangles in E

and where:

$$\left(C(r) - \frac{1}{2}\right)^2 = \left(\frac{R-r}{w}\right)^2$$

Now, if we define d to be the distance between centers, i.e. the characteristic length L_C (See Figure S1- 25b), the area A of one equilateral triangle is

$$A = \frac{\sqrt{3}d^2}{4}$$

$$\alpha = \frac{A_p}{A} = \frac{2\pi R^2}{\sqrt{3}d^2}$$

$$R = d \sqrt{\frac{\sqrt{3}\alpha}{2\pi}}$$

Where A_p is the polymer area inside the equilateral triangle in Figure S1- 25b, i.e., the area of $\frac{1}{2}$ disk.

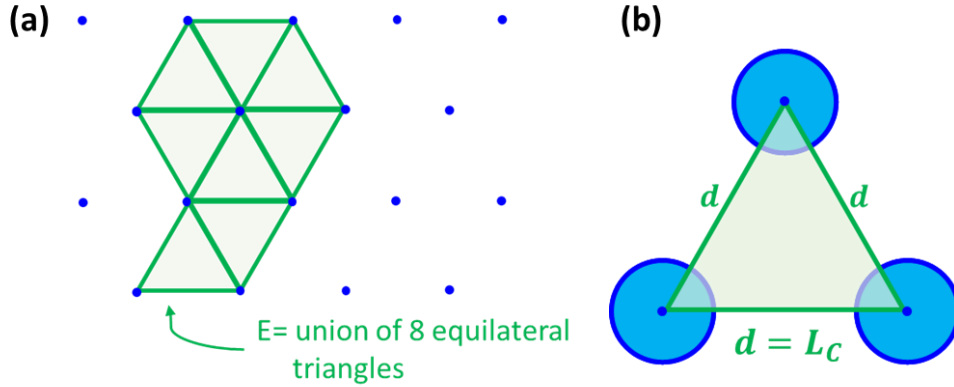


Figure S1- 25: a) Example of a set E , a union of eight equilateral triangles. b) Basic equilateral formed by centers, where the center-to-center spacing d equals the characteristic length L_C that was measured from RSoXS.

And we conclude:

$$\int_E \left(C(r) - \frac{1}{2}\right)^2 d\mu = \frac{N_E}{4} \left(\frac{\sqrt{3}d^2}{4} - \pi R w + 4\pi \int_{R-\frac{w}{2}}^{R+\frac{w}{2}} r \left(\frac{R-r}{w}\right)^2 dr \right)$$

Evaluation of the integral is:

$$4\pi \int_{R-\frac{w}{2}}^{R+\frac{w}{2}} r \left(\frac{R-r}{w} \right)^2 dr = \frac{1}{3}\pi w R$$

So, continuing:

$$\int_E \left(C(r) - \frac{1}{2} \right)^2 d\mu = \frac{N_E}{4} \left(\frac{\sqrt{3}d^2}{4} - \frac{2}{3}\pi R w \right)$$

and the fractional reduction in RMS compared to the sharp transition is:

$$\Delta C_{RMS}^2 = \frac{\frac{N_E}{4} \left(\frac{\sqrt{3}d^2}{4} - \frac{2}{3}\pi R w \right)}{\frac{N_E}{4} \frac{\sqrt{3}d^2}{4}}$$

$$\Rightarrow \Delta C_{RMS}^2 = 1 - \frac{8\pi R w}{3\sqrt{3}d^2}$$

Thus, the interfacial width becomes:

$$w = \frac{3\sqrt{3}d^2}{8\pi R} (1 - \Delta C_{RMS}^2)$$

Uneven Fractions

Suppose that you are actually interested in

$$\int_E (C(r) - \alpha)^2 d\mu$$

where $0 < \alpha < 1$ and $\alpha \neq \frac{1}{2}$.

Then, assuming that C inside the disks is 1 and outside is 0 and that $\alpha = \langle C \rangle$ we notice

that:

$$\int_E (C(r) - \alpha)^2 d\mu = \int_E \left(\left(C(r) - \frac{1}{2} \right) - \left(\alpha - \frac{1}{2} \right) \right)^2 d\mu$$

$$= \int_E \left(C(r) - \frac{1}{2} \right)^2 d\mu - \mu(E) \left(\alpha - \frac{1}{2} \right)^2$$

Thus, the adjustment yields

$$\Delta C_{RMS}^2 = \frac{1 - 4 \left(\alpha - \frac{1}{2} \right)^2 - \frac{8\pi R w}{3\sqrt{3}d^2}}{1 - 4 \left(\alpha - \frac{1}{2} \right)^2}$$

$$\Delta C_{RMS}^2 = 1 - \left(\frac{\left(\frac{8\pi R w}{3\sqrt{3}d^2} \right)}{\left(1 - 4 \left(\alpha - \frac{1}{2} \right)^2 \right)} \right)$$

and the interfacial width is

$$w = \frac{3\sqrt{3}d^2}{8\pi R} \left(1 - 4 \left(\alpha - \frac{1}{2} \right)^2 \right) (1 - \Delta C_{RMS}^2)$$

Remarks

1. It is not hard to change the calculation to accommodate arbitrary transition functions instead of the affine (piecewise linear) transition used here, as long as we stick to transitions that are constant on level sets of the distance function to the disks.
2. While the profile of the rods are disks, we can generalize this to any cylinder over a 2-dimensional figure with bounded curvature. (The curvature bound sets limits on how big $\frac{w}{2}$ can be — we would restrict $\frac{w}{2} < \frac{1}{\kappa}$ where κ is the bound on the curvature, then we can use Steiner type formulas to get the areas of the level sets that we need to use the coarea formula.)
3. As long as the $\frac{w}{2}$ -neighborhoods of the rods or generalized cylinders don't intersect we can get a similar result for a distribution of different sizes of disks or cylinders, as outlined

below.

A region E with some union of these equilateral triangles contains $\left(\frac{\mathcal{H}^2(E)}{\frac{\sqrt{3}}{2}d^2}\right)$ hexagonal lattice points, where $\mathcal{H}^2(E)$ is the 2-dimensional Hausdorff measure of E (the area of E).

If there are N disks in region E , and the hexagonal close packed lattice can accommodate all the disks (whatever their radii are) such that none of $R + \frac{w}{2}$ disks intersect, then

$$d_N \equiv \left(\frac{\mathcal{H}^2(E)}{N} \frac{2}{\sqrt{3}}\right)^{\frac{1}{2}}$$

Defining $n(R)$ to be the number of disks of radius R , we get that the fractional reduction is

$$\begin{aligned} \int_E \frac{n(R)}{N} \left(1 - \frac{8\pi R w}{3\sqrt{3}d_N}\right) dR &= \frac{1}{\mathcal{H}^2(E)} \int_E \left(C(r) - \frac{1}{2}\right)^2 d\mu \\ &= \int_E \frac{n(R)}{N} dR - \frac{8\pi w}{3\sqrt{3}d_N} \int_E \frac{n(R)}{N} \frac{R}{d_N} dR \\ &= 1 - \frac{8\pi w}{3\sqrt{3}d_N} \int_E \frac{n(R)}{N} \frac{R}{d_N} dR \end{aligned}$$

The first term reduced to 1 implies that $\frac{n(R)}{N}$ is a probability density function. The integral in the second term implies continuous convex of combination of $\frac{R}{d_N}$ over support of $n(R)$.

Recall that “support” of a function is the set on which it is not zero (more precisely, it is the closure of the set on which it is non-zero).

Now, define $\bar{R} \equiv$ mean of R under the distribution $\frac{n(R)}{N}$, that means:

$$\bar{R} \equiv \int_E \frac{n(R)}{N} R dR$$

Then the fractional reduction becomes

$$\Delta C_{RMS}^2 = 1 - \frac{8\pi \bar{R} w}{3\sqrt{3} d_N d_N}$$

Thus, the interfacial width becomes:

$$w = \frac{3\sqrt{3} d_N d_N}{8 \pi \bar{R}} (1 - \Delta C_{RMS}^2)$$

For the case where $0 < \alpha < 1$ and $\alpha \neq \frac{1}{2}$

$$\Delta C_{RMS}^2 = \frac{1 - 4 \left(\alpha - \frac{1}{2} \right)^2 - \frac{8\pi w \bar{R}}{3\sqrt{3} d_N d_N}}{1 - 4 \left(\alpha - \frac{1}{2} \right)^2}$$

$$\Delta C_{RMS}^2 = 1 - \left(\frac{\left(\frac{8\pi w \bar{R}}{3\sqrt{3} d_N d_N} \right)}{\left(1 - 4 \left(\alpha - \frac{1}{2} \right)^2 \right)} \right)$$

and the interfacial width is

$$w = \left(\frac{3\sqrt{3} d_N d_N}{8 \pi \bar{R}} \right) \left(1 - 4 \left(\alpha - \frac{1}{2} \right)^2 \right) (1 - \Delta C_{RMS}^2)$$

Thus, we conclude that even if the radii are not all the same, we can—under the conditions set out above— simply replace R with \bar{R} in the final equation of “fractional reduction” in the constant disk size case.

Blend (NT812:PC71BM)	NT812 (Volume Fraction)	PC71BM (Volume Fraction)	Lc = d [nm]	Equilateral Triangle Area (A) [nm ²]	NT812 Disk Area [nm ²]	NT812 Disk Radius (R) [nm]	D-A Interfacial Width (w) [nm]
(3:1)	0.77	0.23	62.8	1709.5	2632.6	29.0	7.5 ± 0.9
(3:1) w/CN	0.77	0.23	62.8	1709.5	2632.6	29.0	4.9 ± 0.6
(1:1.5)	0.43	0.57	98.2	4173.5	3589.2	33.8	12 ± 0.3
(1:1.5) w/CN	0.43	0.57	98.2	4173.5	3589.2	33.8	6.7 ± 0.2

Table S1- 3: Summary of the calculated variables via the donor-acceptor interfacial width calculation. The volume fraction values and characteristic length L_C are from RSoXS analysis.

RSoXS and GIWAXS: Thickness Comparison

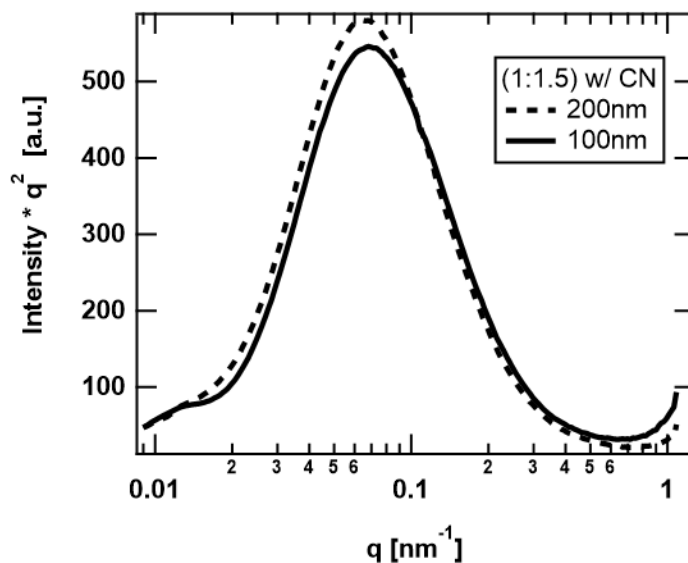


Figure S1- 26: RSoXS profiles for 1:1.5 blends with CN. The solid profile is for a 100 nm thick blend and dashed for a 200 nm thick film. The results are very similar, suggesting that the composition variation and characteristic length are almost thickness independent.

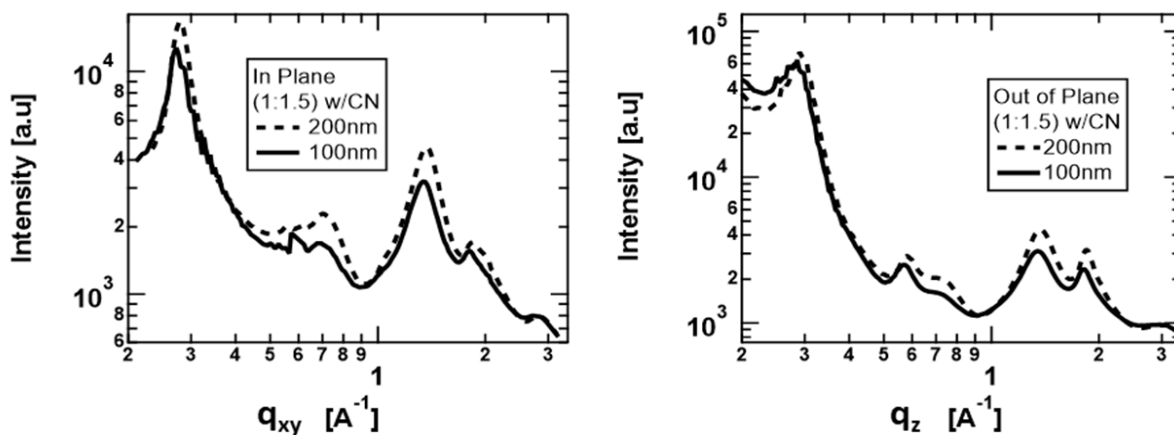


Figure S1- 27: 1D GIWAXS profiles for 1:1.5 with CN blends with different thickness: 100 nm (solid) and 200 nm (dashed). In plane (left) and out of plane (right). The thinner sample shows lower peak intensities as expected. Otherwise, the results are similar, indicating similar packing and crystallinity in those blends.

APPENDIX B: SUPPORTING INFORMATION FOR CHAPTER 4: HIGH SENSITIVITY OF
NON-FULLERENE ORGANIC SOLAR CELLS MORPHOLOGY AND PERFORMANCE TO
A PROCESSING ADDITIVE

Device performance

The EQE results follow similar trends to the J-V results. The EQE profiles show that; a peak ~ 500 - 600 nm for electron donor, peak ~ 700 - 900 nm for the electron acceptor, and an overlap ~ 650 nm. Maximum EQE in both systems was noticed in the blends with 1% CN, which

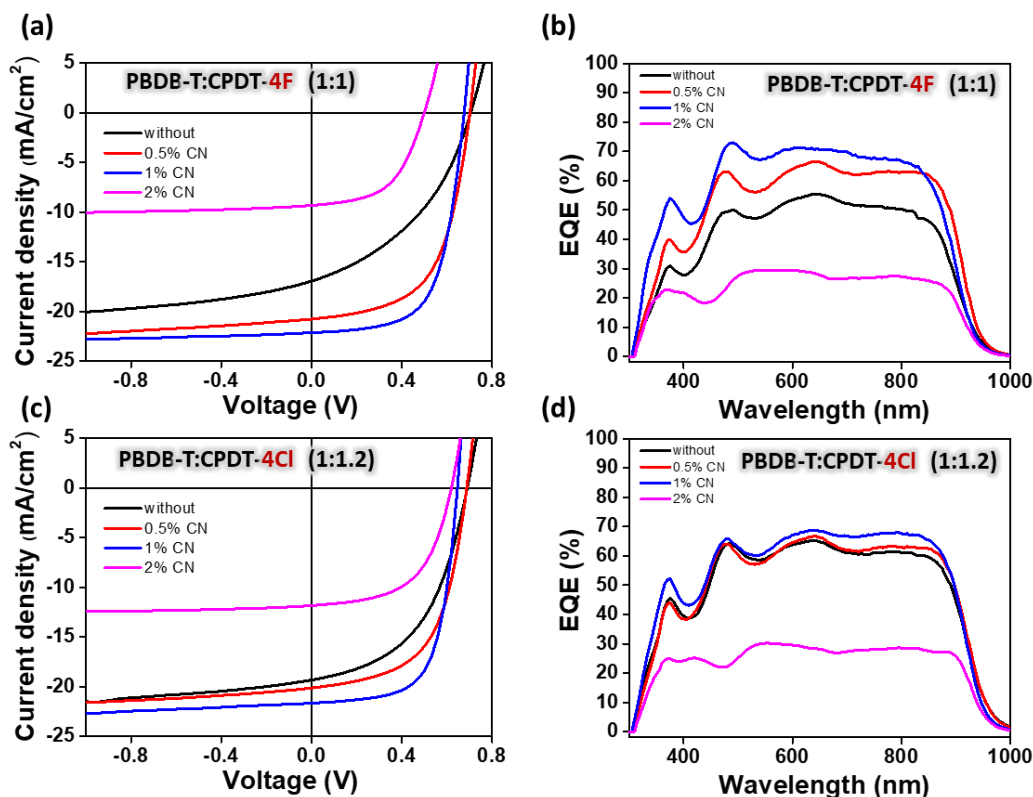


Figure S2- 1: J-V characteristics and EQE profiles for PBDB-T:CPDT-4F blends are presented in (a) and (b), respectively. For PBDB-T:CPDT-4Cl, (d) and (e) show J-V curves and EQE, respectively. The data is for junction blends processed from CB with 0, 0.5, 1, and 2% CN solvent additive (as indicated by the different colors and legends). See the summary tables of device performance below.

is about 70%. The EQE traces of the blends show similar peak positions to the UV-Vis absorbance peaks that were seen previously.³⁵

Fluorinated blends (PBDB-T: CPDT-4F)

PBDB-T:CPDT-4F	Condition	V _{oc} [V]	J _{sc} [mA/cm ²]	FF [%]	PCE (max) [%]
1:1	without	0.70(±0.01)	16.44(±0.39)	39.88(±1.06)	4.58(4.86)
1:1	0.5%CN	0.68(±0.00)	20.40(±0.33)	59.88(±0.55)	8.26(8.47)
1:1	1%CN	0.66(±0.02)	22.33(±0.20)	63.49(±0.10)	9.28(9.51)
1:1	2%CN	0.47(±0.13)	9.16(±0.14)	54.20(±3.82)	2.39(2.81)

Table S2- 1: summary of device performance parameters for PBDB-T:CPDT-4F blends. The device performance parameters are the mean of 10 cells± standard deviation.

Chlorinated blends (PBDB-T: CPDT-4Cl)

PBDB-T:CPDT-4Cl	Condition	V _{oc} [V]	J _{sc} [mA/cm ²]	FF [%]	PCE (max) [%]
1:1.2	without	0.68 (±0.00)	19.16(±0.11)	47.09 (±3.34)	6.10 (6.57)
1:1.2	0.5%CN	0.68 (±0.00)	20.21 (±0.12)	56.01 (±2.73)	7.65 (7.98)
1:1.2	1%CN	0.62 (±0.00)	21.53 (±0.11)	66.42 (±2.28)	8.92 (9.20)
1:1.2	2%CN	0.55 (±0.07)	11.31 (±0.51)	53.30 (±2.64)	3.03(4.09)

Table S2- 2: summary of device performance parameters for PBDB-T:CPDT-4Cl blends. The device performance parameters are the mean of 10 cells± standard deviation.

GIWAXS analysis and results

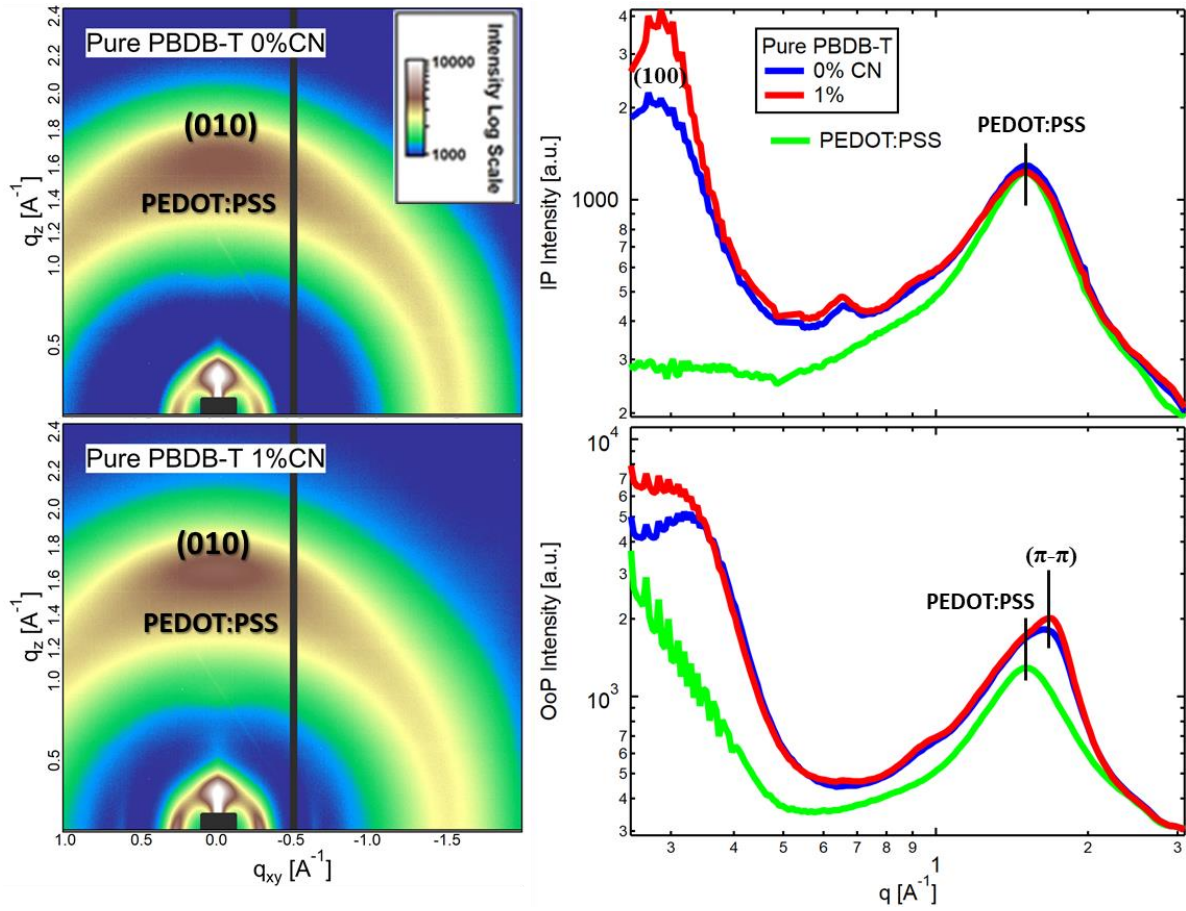


Figure S2- 2: GIWAXS data for pure polymer (PBDB-T) without CN (top) and with 1% CN (bottom). 2D GIWAXS images (left) and 1D GIWAXS profiles (right) with background profiles of PEDOT:PSS.

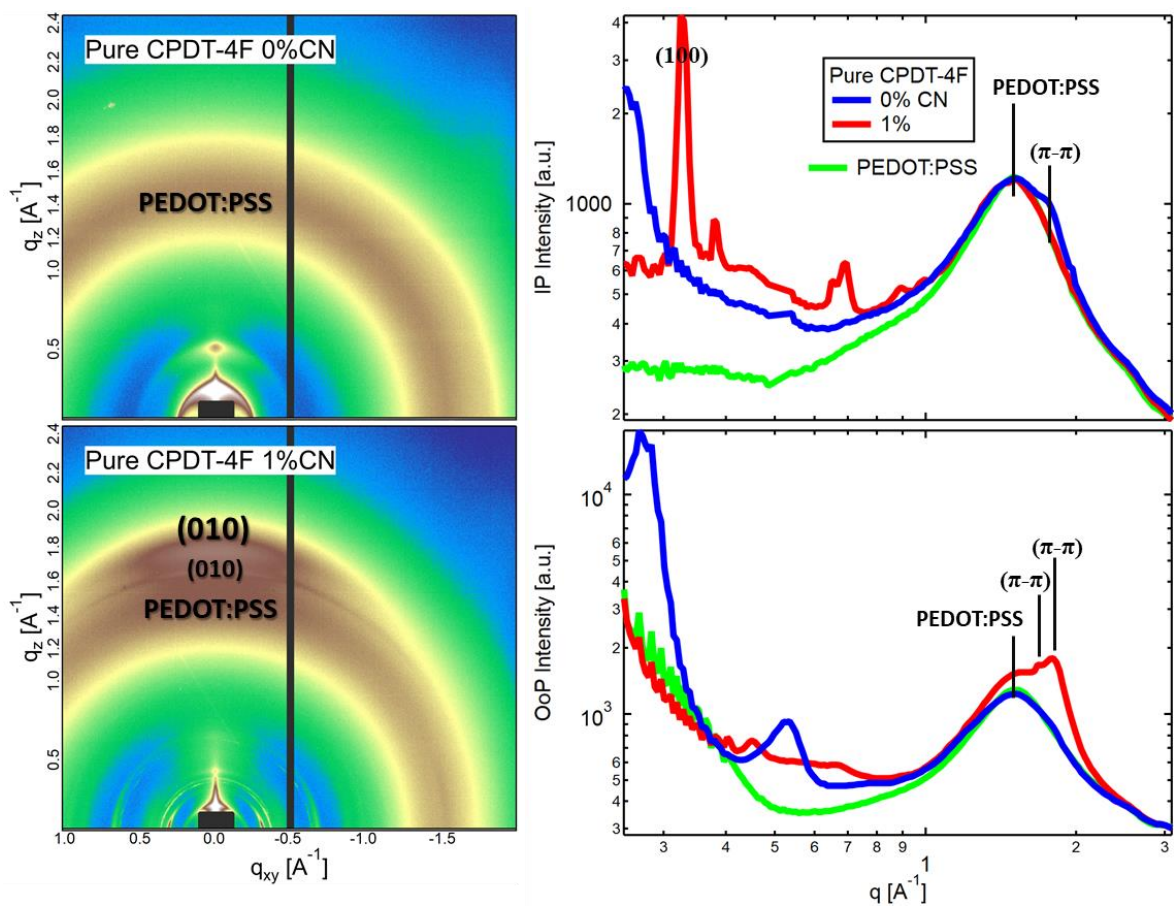


Figure S2- 3: GIWAXS data for pure small molecule (CPDT-4F) without CN (top) and with 1% CN (bottom). 2D GIWAXS images (left) and 1D GIWAXS profiles (right) with background profiles of PEDOT:PSS.

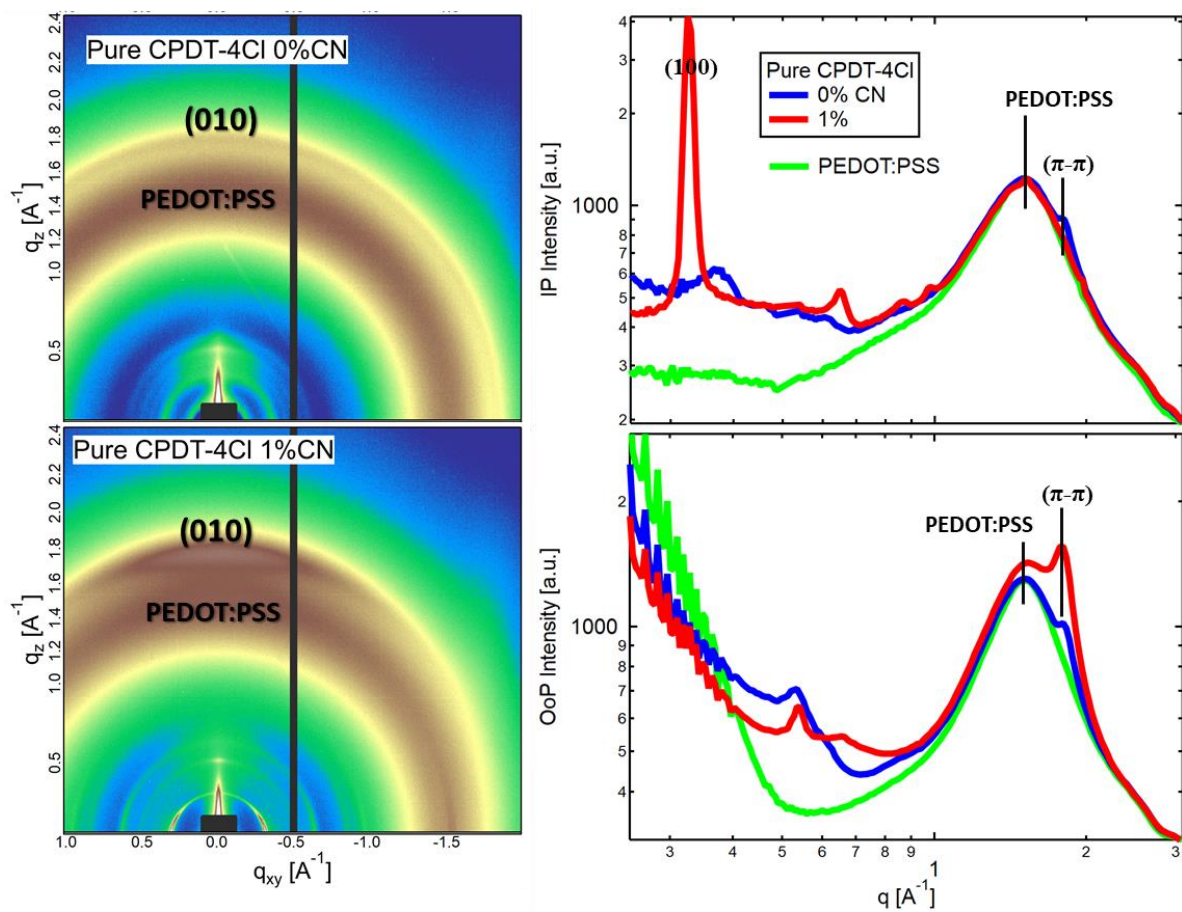


Figure S2- 4: GIWAXS data for pure small molecule (CPDT-4Cl) without CN (top) and with 1% CN (bottom). 2D GIWAXS images (left) and 1D GIWAXS profiles (right) with background profiles of PEDOT:PSS.

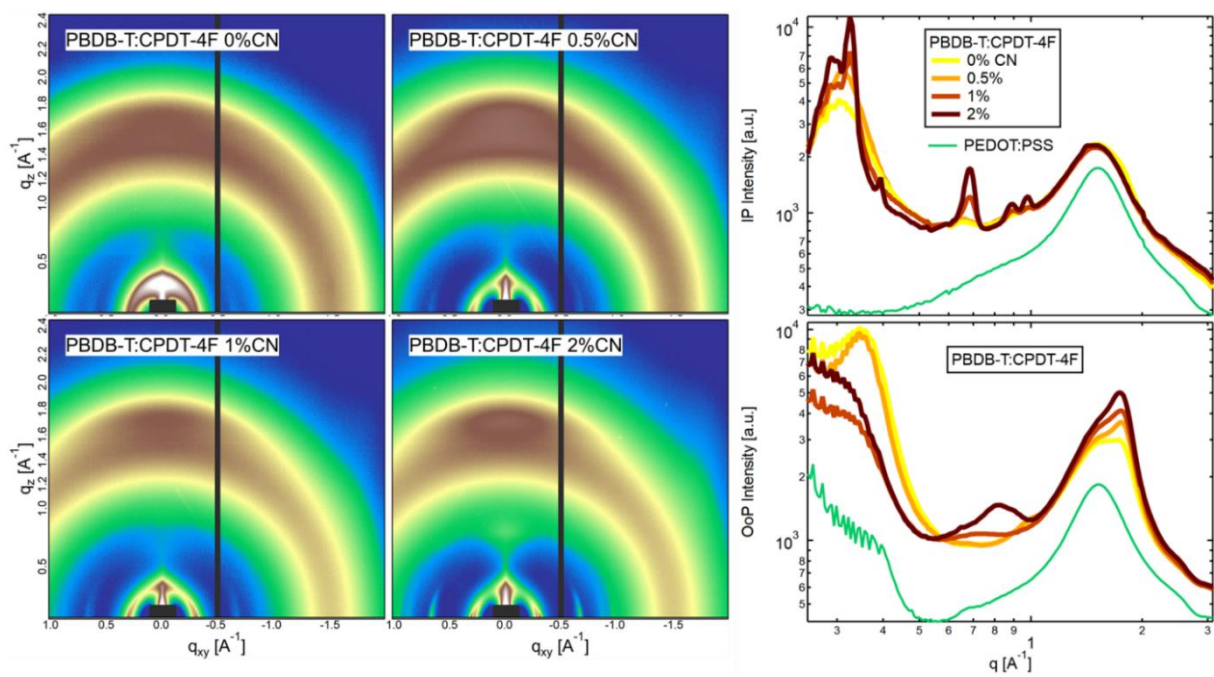


Figure S2- 5: GIWAXS data for PBDB-T:CPDT-4F with different CN concentration as indicated in the legends. 2D GIWAXS images (left and middle). 1D GIWAXS profiles (right) for IP and OoP sectors as indicated by y-axis labels. The background profiles of PEDOT:PSS were appended to the 1D profile graphs for reference (shown in green).

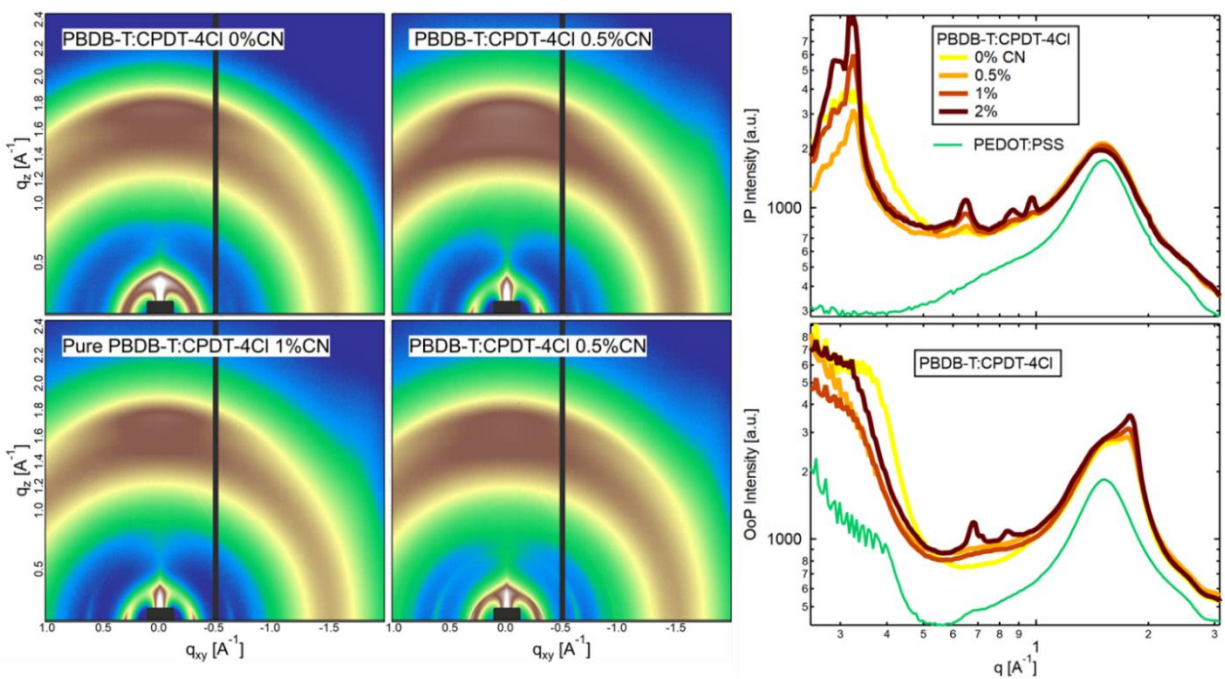


Figure S2- 6: GIWAXS data for PBDB-T:CPDT-4Cl with different CN concentration as indicated in the legends. 2D GIWAXS images (left and middle). 1D GIWAXS profiles (right) for IP and OoP sectors as indicated by y-axis labels. The background profiles of PEDOT:PSS were appended to the 1D profile graphs for reference (shown in green).

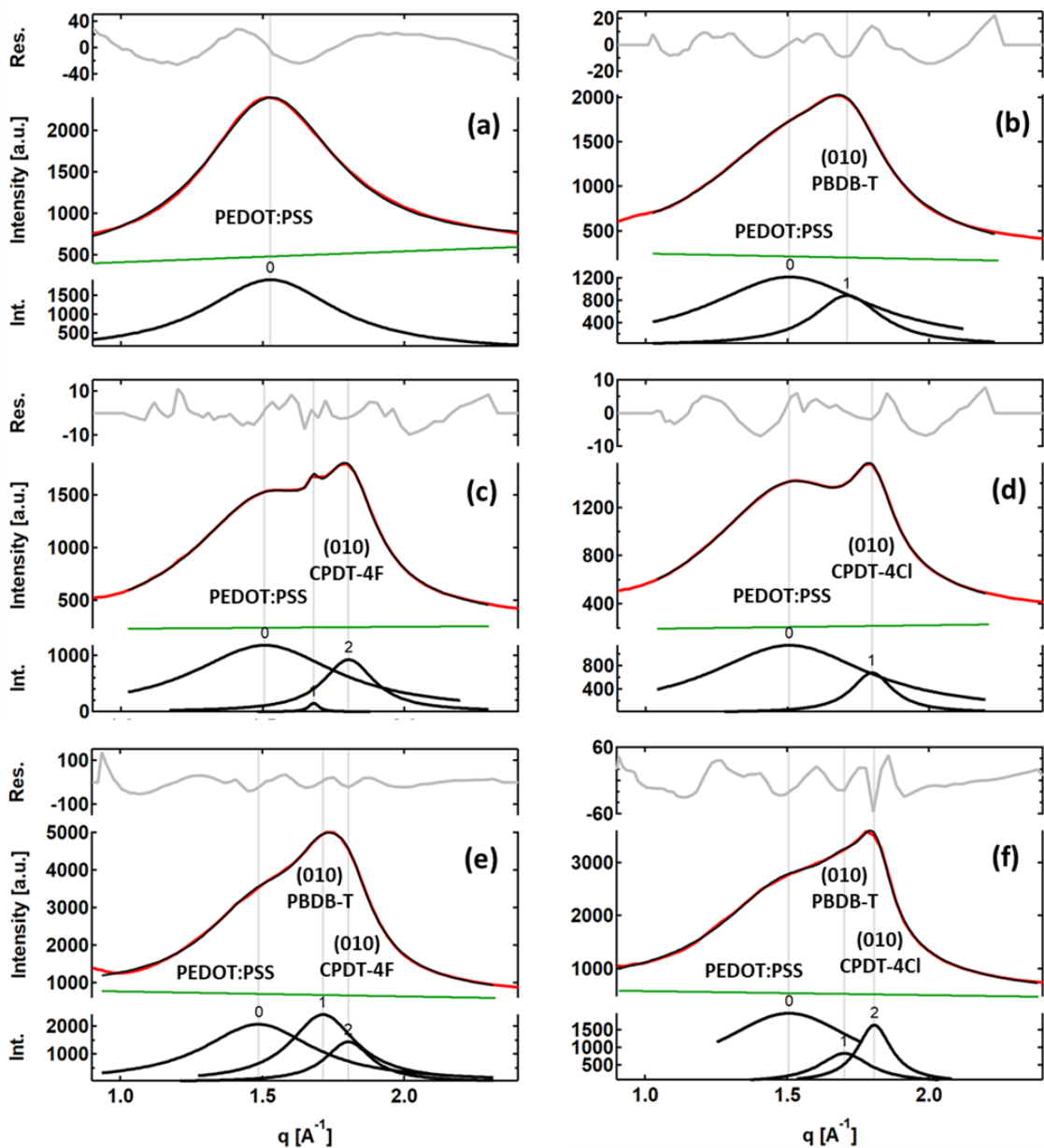


Figure S2- 7: A few examples of peaking fitting of GIWAXS scattering profiles in OoP direction: a) PEDOT:PSS, b) PBDB-T 1% CN, c) CPDT-4F with 1% CN, d) CPDT-4Cl with 1% CN, e) a PBDB-T:CPDT-4F blend with 2% CN, and f) for a PBDB-T:CPDT-4Cl with 2% CN. The GIWAXS profiles are shown in (red), Lorentzian fits (black) with linear background (green). The fit residuals are shown in gray. When fitting a blend profile, only the peak positions are held at the same q values as for the pure materials until a good fit is achieved. After that, the constrains are left so peak positions can freely adjust to get an optimal fit.

Sample	CN vol. [vol. %]	Out of Plane π - π stacking		In Plane lamellar stacking	
		face-on (010)		(100)	
		Peak Position [\AA^{-1}]	d-spacing [\AA]	Peak Position [\AA^{-1}]	d-spacing [\AA]
PBDB-T	0	1.71	3.67	0.28	22.44
	1	1.71	3.67	0.29	21.67
CPDT-4F	0	1.79	3.51	-	-
	1	1.80	3.45	0.33	19.04
CPDT-4Cl	0	1.82	3.44	-	-
	1	1.80	3.49	0.33	19.04
PBDB-T:CPDT-4F	0	1.74 (polymer) & 1.82 (NFA)	3.61 (polymer) & 3.44 (NFA)	-	-
	0.5	1.75 & 1.82	3.60 & 3.45	0.31 (polymer) & 0.33 (NFA)	20.50 (polymer) & 18.92 (NFA)
	1	1.73 & 1.81	3.63 & 3.48	0.29 & 0.33	21.67 & 19.26
	2	1.71 & 1.80	3.67 & 3.49	0.29 & 0.33	21.67 & 19.28
PBDB-T:CPDT-4Cl	0	1.71 (polymer) & 1.80 (NFA)	3.67 (polymer) & 3.49 (NFA)	0.30 (polymer) & 0.34 (NFA)	20.08 (polymer) & 18.68 (NFA)
	0.5	1.68 & 1.79	3.74 & 3.51	0.29 & 0.33	21.65 & 19.28
	1	1.68 & 1.79	3.74 & 3.51	0.29 & 0.32	21.80 & 19.35
	2	1.70 & 1.80	3.70 & 3.49	0.29 & 0.32	21.70 & 19.44

Table S2- 3: Peak position and d-spacing results extracted from multi-peak fitting of the GIWAXS 1D scattering profiles for in-plane lamellar and out-of-plane pi stacking. Where $d = 2\pi/(\text{peak position})$. In parenthesis meaning: (polymer) means values for polymer peaks in blends and (SM) means values for small molecule peaks in blends.

X-ray spectroscopy (NEXAFS) and material contrasts

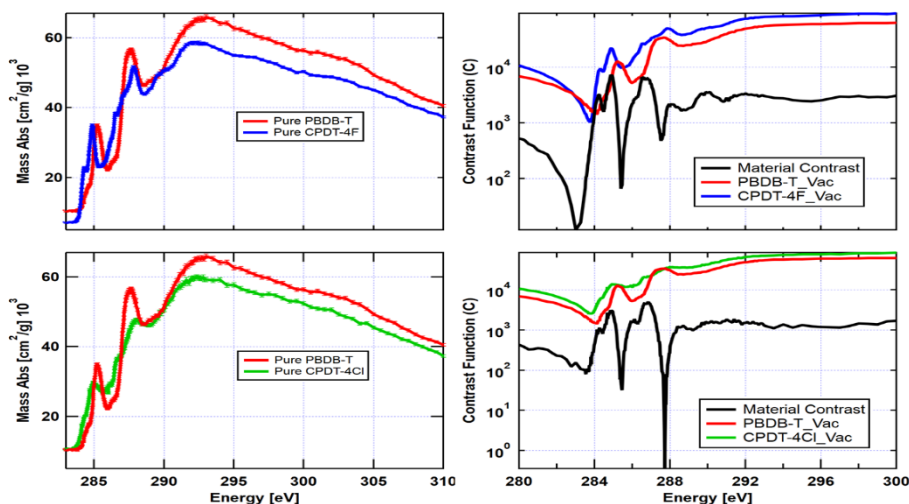


Figure S2- 8: NEXAFS spectra for neat materials (left). Right: contrast functions of material-vacuum and material-material calculated based on the material indices of refraction $n=1-\delta+i\beta$, where the imaginary part is the mass absorbance, and the real part was calculated via the Kramers Kronig transform. The contrast function is $C=E^4 \times |\Delta n|^2$, where E is the X-ray energy.

For more details about the Kramers Kronig relations, refer to the previous work by Yan et al.⁵⁵

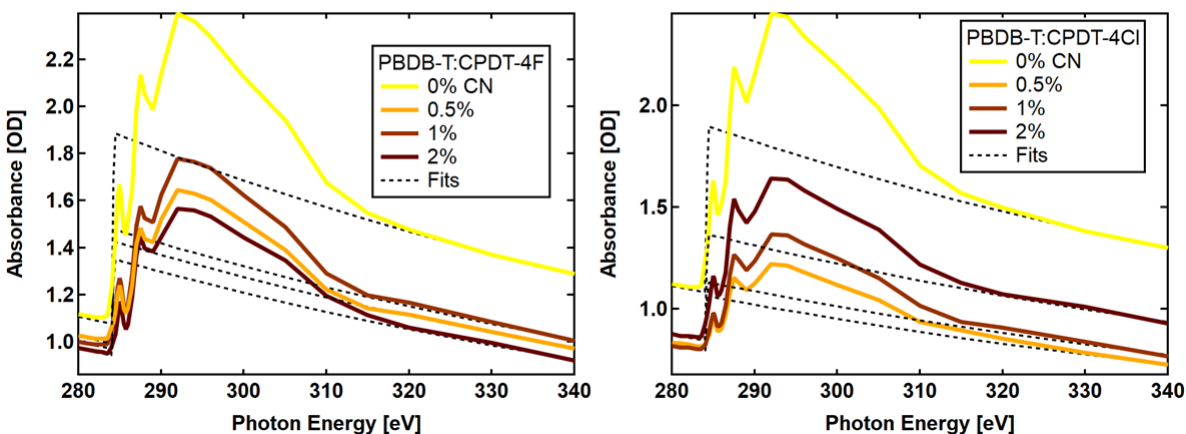


Figure S2- 9: Quick NEXAFS absorbance spectra taking for each blend on the same spots where the X-ray scattering (RSoXS) data was taken then scaled to bare atom absorbance fits (black dotted) to extract the exact film thickness at that spot. The left graph is for fluorinated blends and the right one is for the chlorinated blends. The extracted thickness values were used to normalize RSoXS scattering profiles. (RSoXS data and results shown below).

X-ray micro-spectroscopy (NEXAFS and STXM)

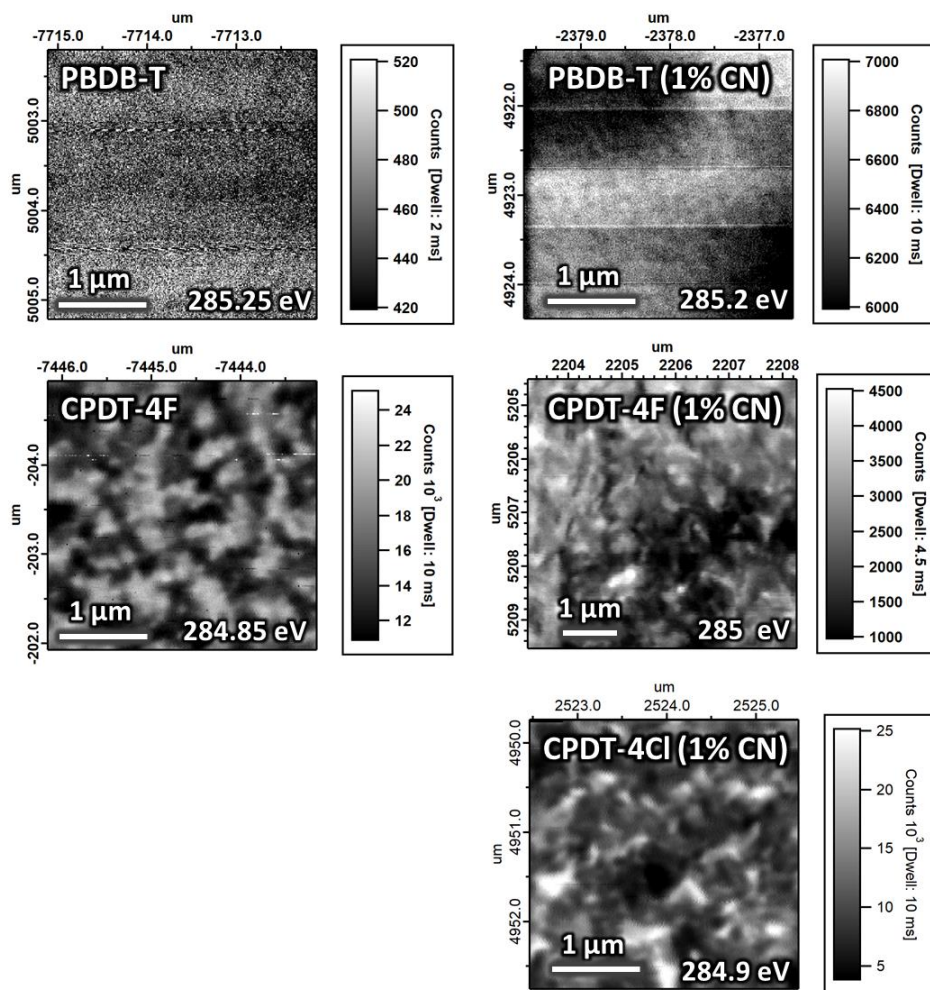


Figure S2- 10: STXM images of neat films without (left) and with 1% CN solvent additive (right).

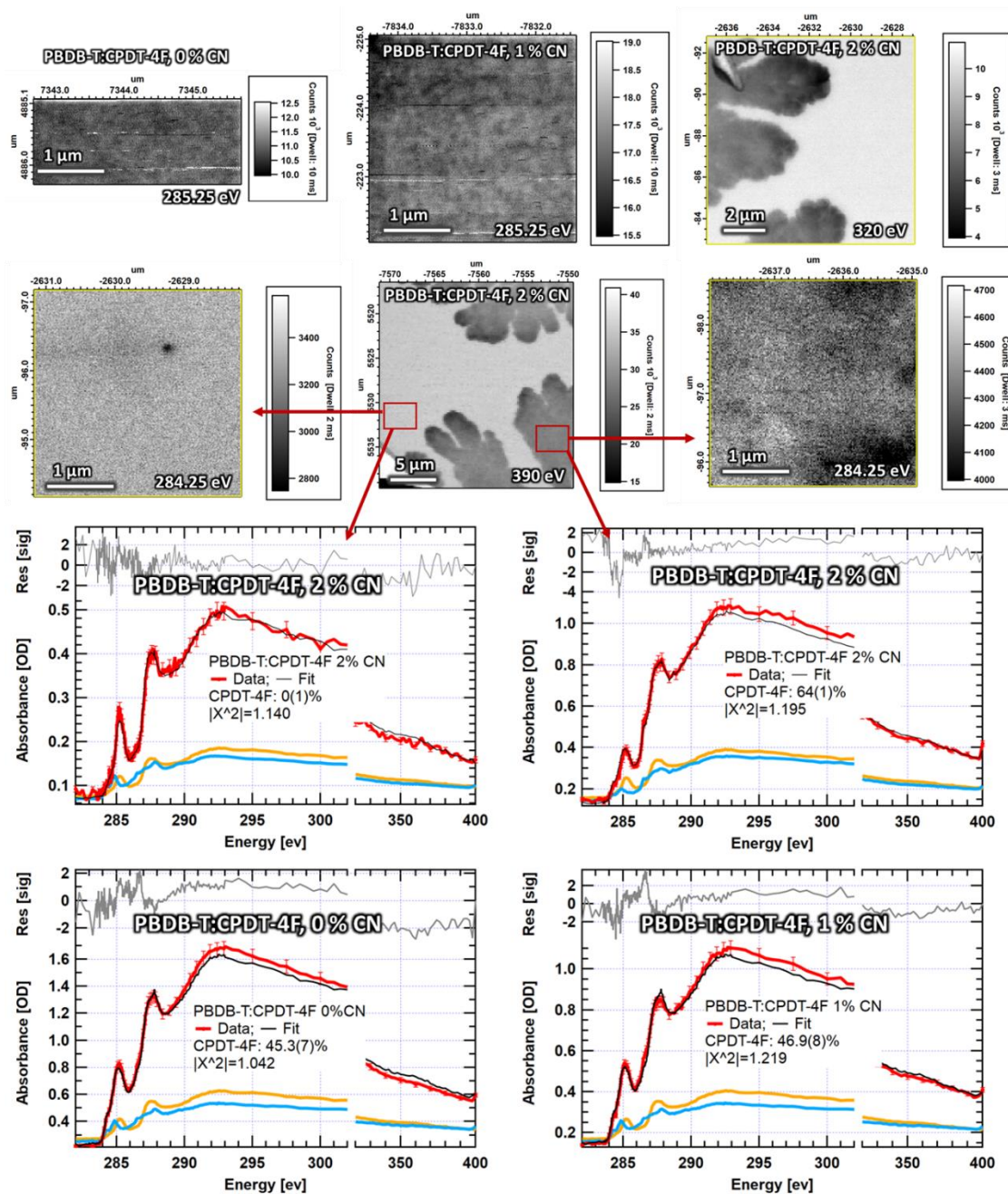


Figure S2- 11: STXM images and NEXAFS spectra of the fluorinated blends (PBDB-T: CPDT-4F). Top row shows STXM scans for blends with different CN amounts (left to right: 0, 1, and 2% CN). The second-row shows zoomed out and in scans of the blend with 2 % CN on different regions “domains” as indicated with the red squares. No features or textures were detected within those largely separates domains in 2% CN blend. NEXAFS spectra taken across those large domains in the 2% CN blends are shown in the third row. When the spectra were fitted to reference spectra of neat materials, results suggest pure polymer domains and a vertical average of 64% small molecules in the other domains. The bottom row show NEXAFS spectra taken across 0% CN blend (left) and 1% CN blend (right). Their peak fitting results confirm the weight ratio of the small molecules in those blends (i.e., ~50 wt.%)

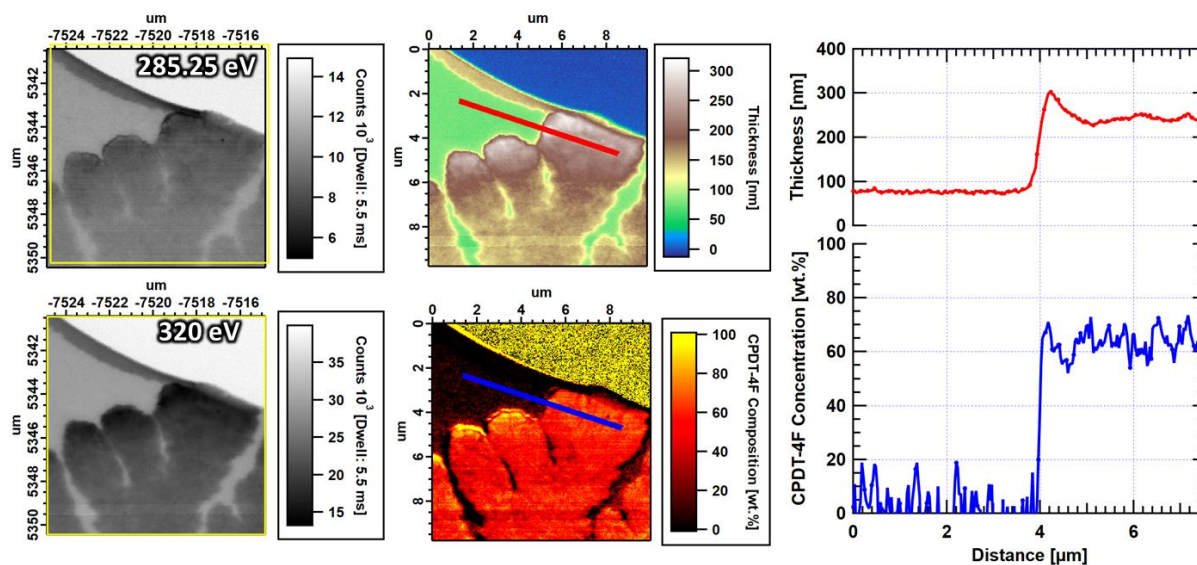


Figure S2- 12: STXM compositional analysis of the fluorinated blend (PBDB-T: CPDT-4F) with 2% CN. Images were taken a polymer resonant energy (285.25 eV) and a non-resonant energy for both the small molecule and polymer (320 eV). Composition analysis was performed to extract compositional and thickness maps (shown in the middle). Then 1D profiles of thickness and composition (presented on the right side) were extracted from those maps across different domains as indicated by the red and blue lines on the maps.

The STXM and NEXAFS analyses provided in this section follow similar methods as in our previous work.^{45,46}

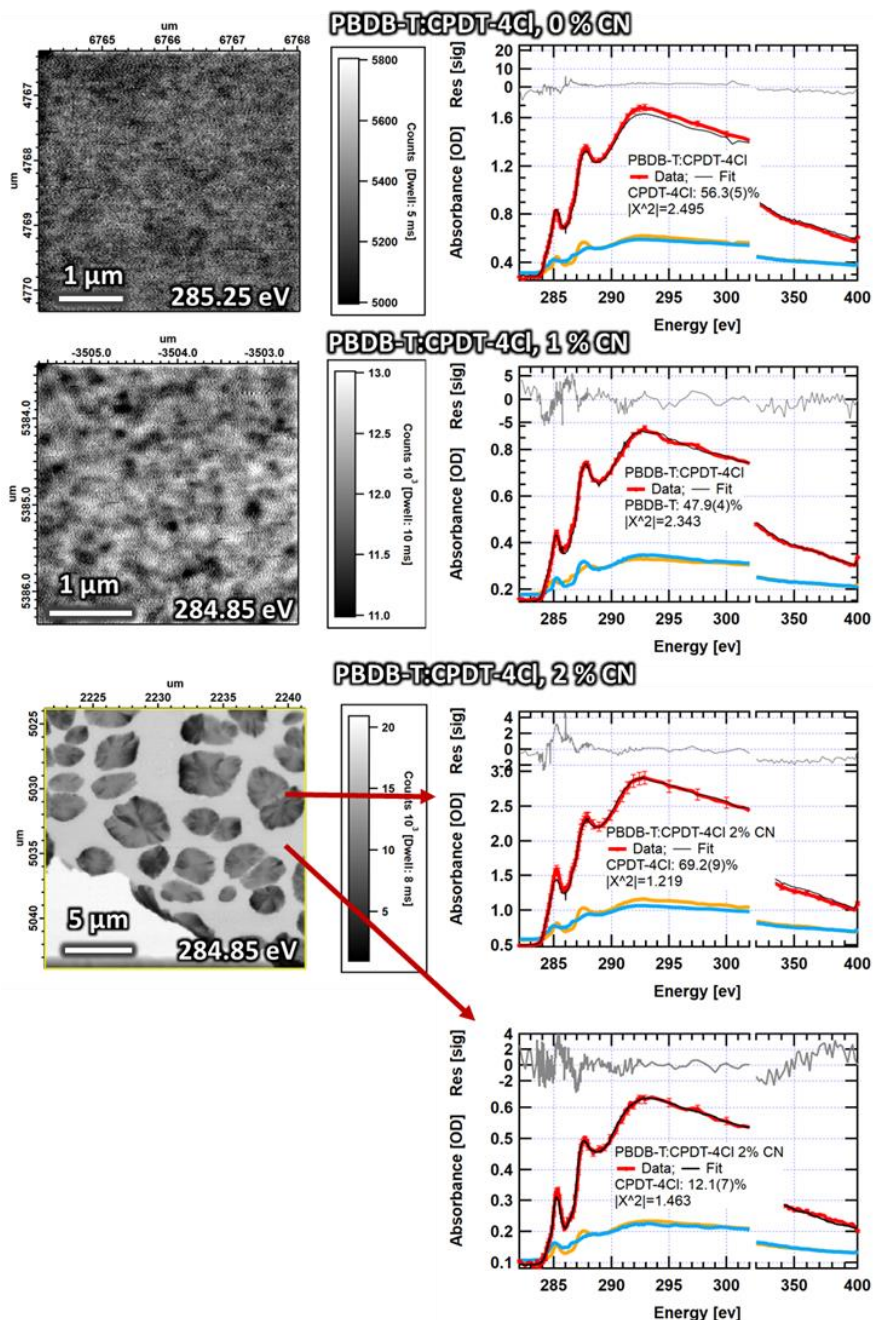


Figure S2- 13: STXM images and NEXAFS spectra of chlorinated blends (PBDB-T: CPDT-4Cl). Top row shows a STXM scan and NEXAFS spectrum for the blend without CN. Domains are within the STXM resolution and are not big enough to conduct compositional analysis. NEXAFS fitting results confirm the weight ratio (i.e., ~ 55 wt.% small molecule). The second row shows a STXM scan and NEXAFS spectrum for the 1% CN blend. The domains were big enough to perform composition analysis on this film (see Figure 3- 6 in the main text). The results of fitting the NEXAFS scan also confirms the weight ratio in this blend. Finally, data of the film with 2% CN is presented at the bottom of this graph. The STXM image show strong phase separation, with the dark domains being mostly small molecule and the bright regions being mostly polymer—as confirmed by fitting NEXAFS scans that were taken across those different domains (as indicated by the red arrows).

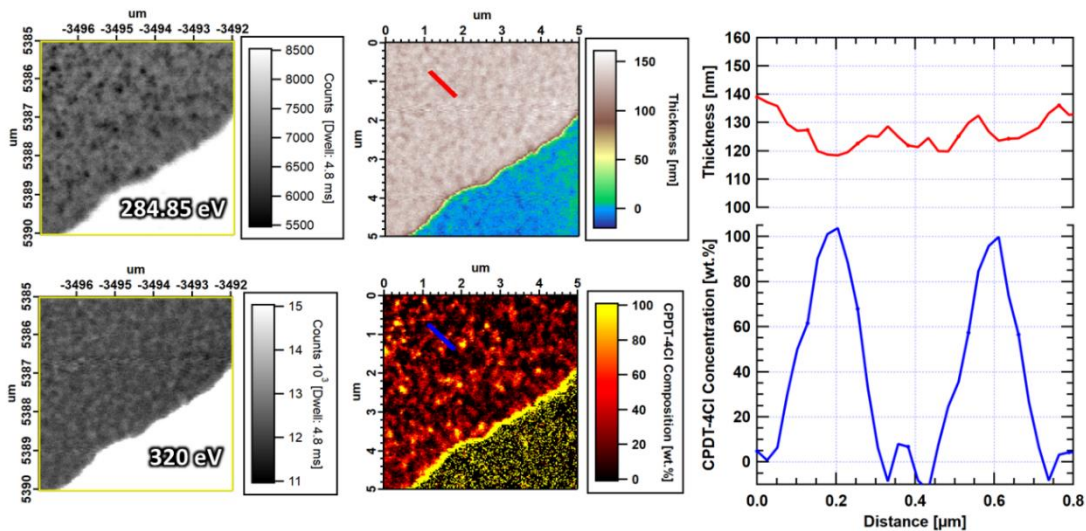


Figure S2- 14: STXM compositional analysis of the chlorinated blend (PBDB-T: CPDT-4Cl) with 1% CN. Images were taken a small molecule resonant energy (284.85 eV) and a non-resonant energy for both the small molecule and polymer (320 eV). Composition analysis was performed to extract compositional and thickness maps (shown in the middle). Then 1D profiles of thickness and composition (presented on the right side) were extracted from those maps across different domains as indicated by the red and blue lines on the maps

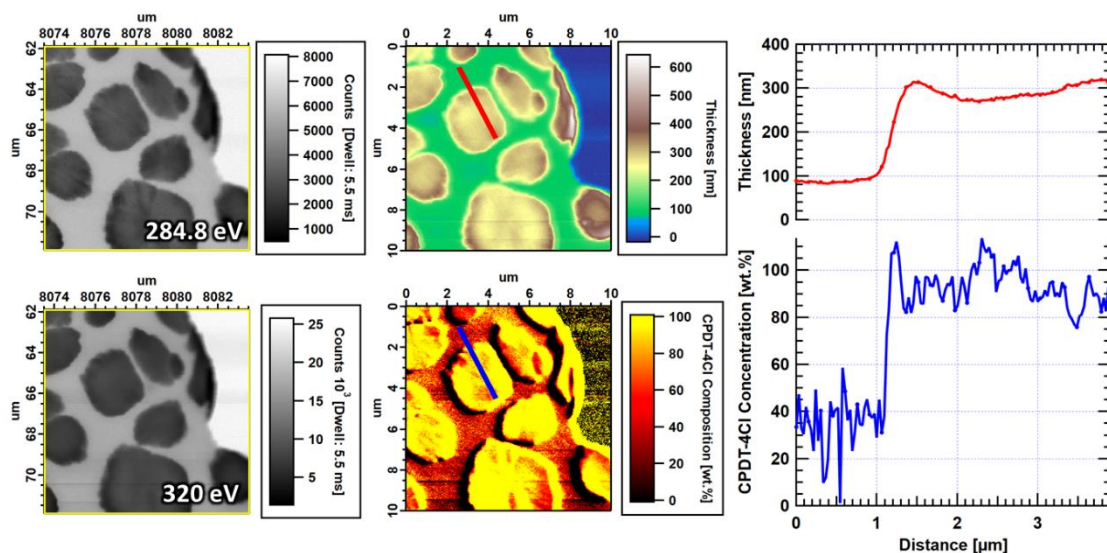


Figure S2- 15: STXM compositional analysis of the chlorinated blend (PBDB-T: CPDT-4Cl) with 2% CN. Images were taken a small molecule resonant energy (284.8 eV) and a non-resonant energy for both the small molecule and polymer (320 eV). Composition analysis was performed to extract compositional and thickness maps (shown in the middle). Then 1D profiles of thickness and composition (presented on the right side) were extracted from those maps across different domains as indicated by the red and blue lines on the maps.

Resonant soft X-ray scattering (RSoXS)

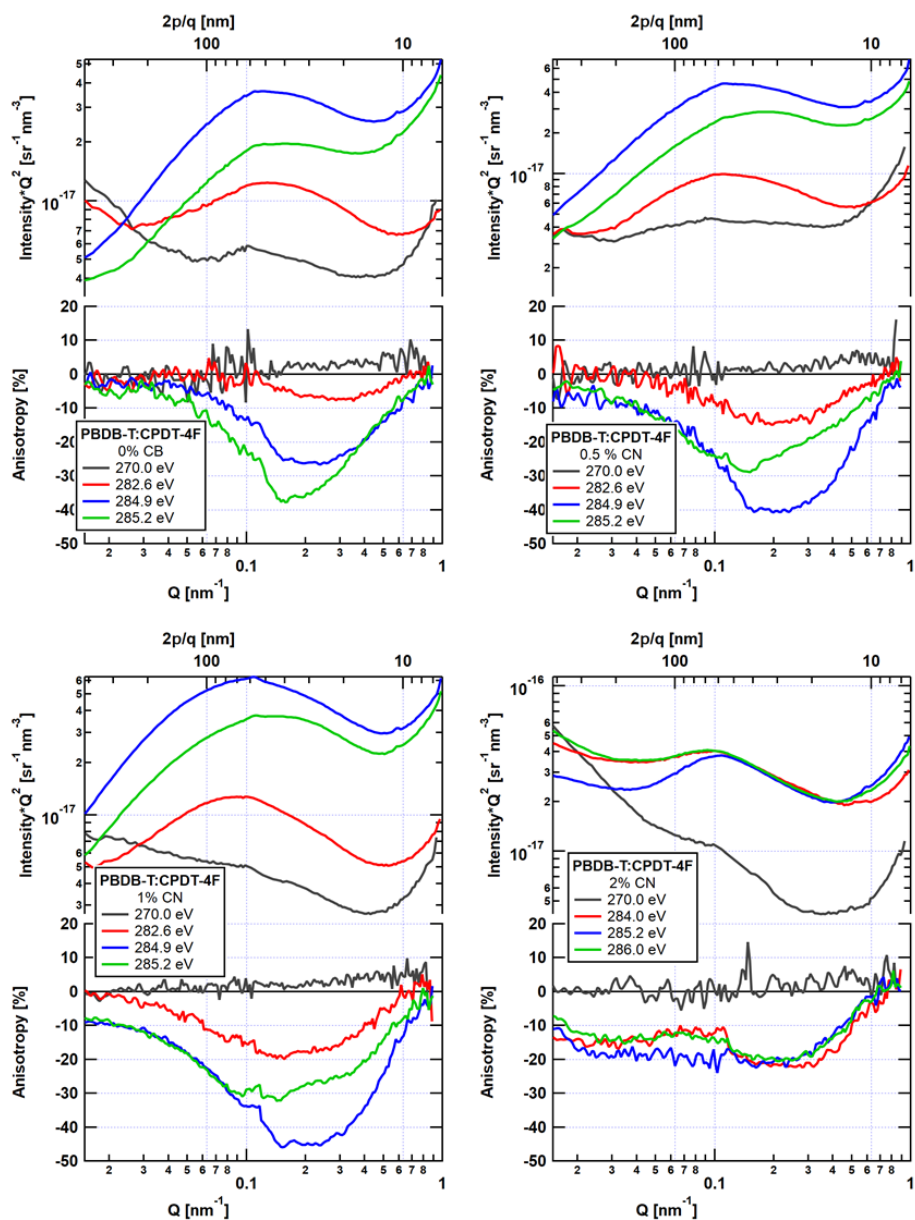


Figure S2- 16: 1D Lorentz-corrected scattering profiles of the fluorinated blends (PBDB-T:CPDT-4F) where I^*Q^2 vs Q (top) and anisotropy vs Q (bottom). The anisotropy is calculated as the difference between scattering in the vertical direction and horizontal direction over their sum. RSoXS was conducted at different X-ray energies as indicated in the graph legends.

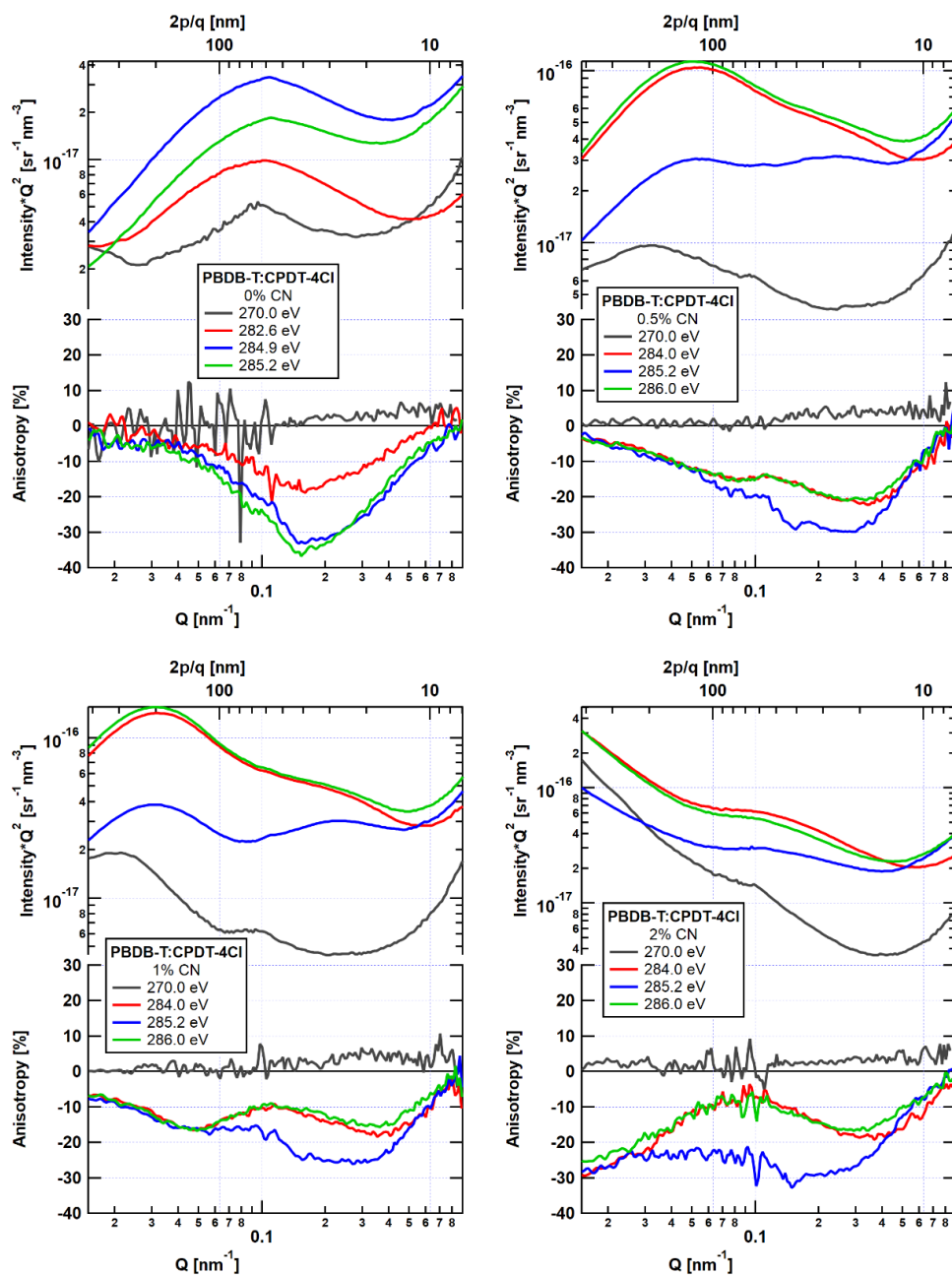


Figure S2- 17: 1D Lorentz-corrected scattering profiles of the chlorinated blends (PBDB-T: CPDT-4Cl), where $I \cdot Q^2$ vs Q (top) and anisotropy vs Q (bottom). The anisotropy is calculated as the difference between scattering in the vertical direction and horizontal direction over their sum. RSoXS was conducted at different X-ray energies as indicated in the graph legends.

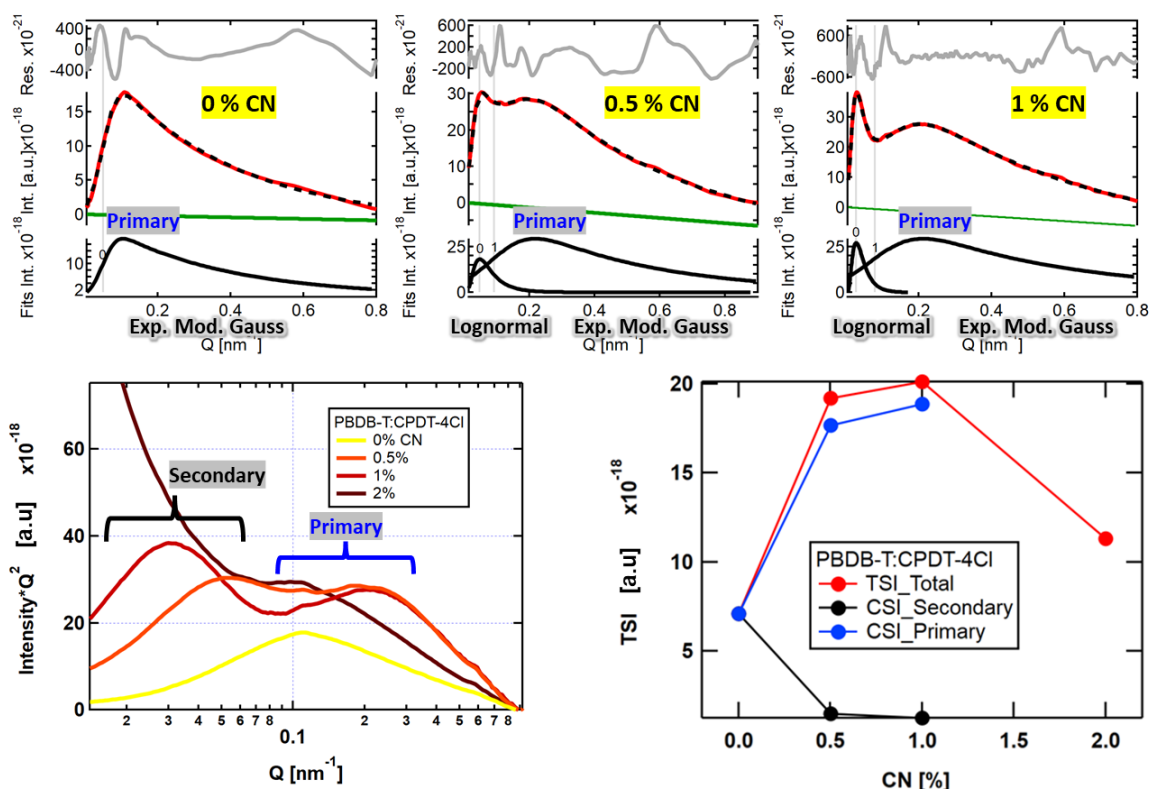


Figure S2- 18: Shown (top) are peak fitting of the scattering profiles of the chlorinated blends (PBDB-T: CPDT-4Cl) to calculate the component scattering intensity (CSI) of the primary peaks and secondary peaks (the secondary peaks emerge with solvent additive CN). Where data (red), fits (black), and fit residuals (gray). The results suggest that the dominate scattering feature that contribute to the total scattering intensity (TSI) is the one at high Q , i.e., CSI of the primary feature. Thus, CSI of the primary feature follows a similar trend as TSI of the entire scattering profiles (see red and blue traces in the bottom right graph). Whereas the CSI of the secondary features is negligible. This RSoXS data was taken at X-ray energy of 285.2 eV.

Lognormal and gaussian peaks often work well for fitting RSoXS data with multi-scale scattering features like in this case of the chlorinated blends with solvent additive.¹²⁷

TSI is calculated as the area under the entire RSoXS curve and CSI is the area an individual peak.^{127,129}

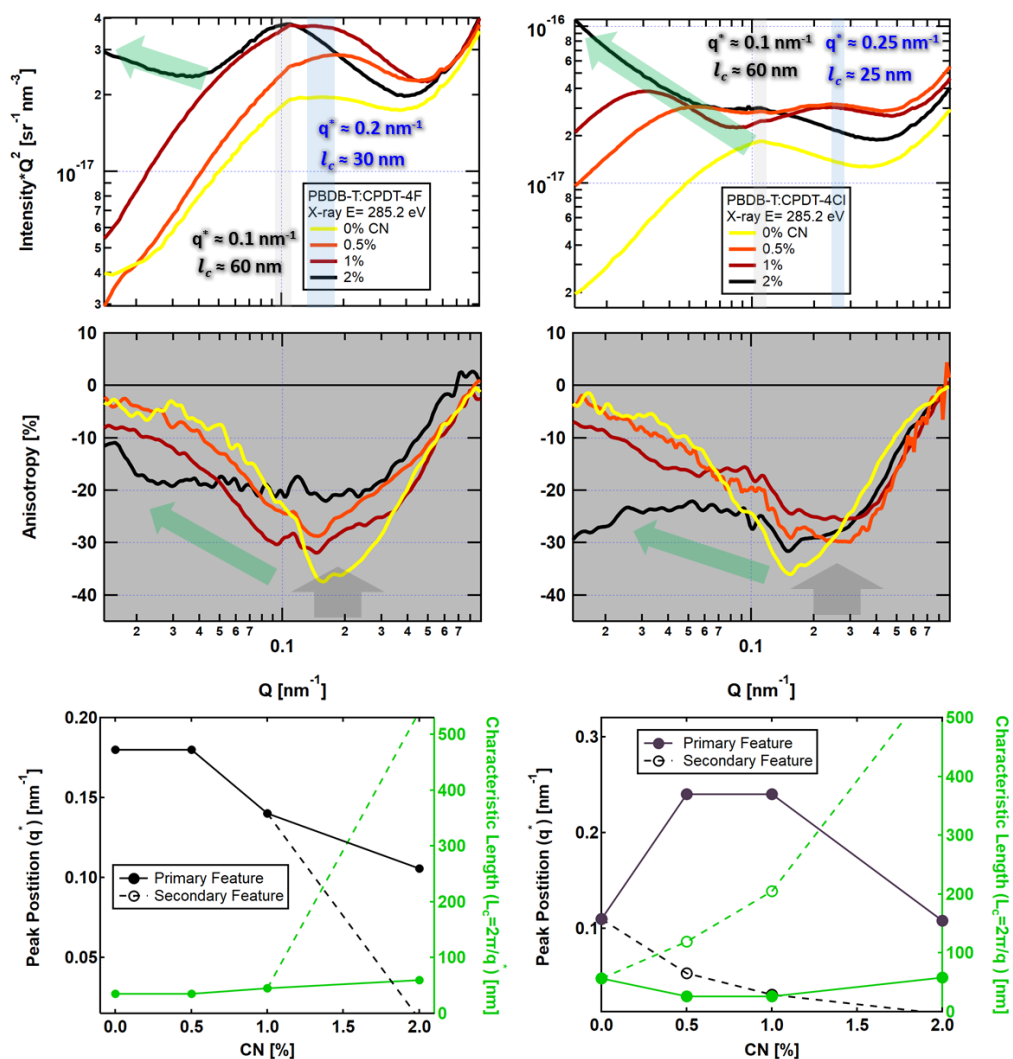


Figure S2- 19: Summary of the 1D Lorentz-corrected scattering data and peak fitting analysis of the fluorinated blends (left) and chlorinated blends (right): where I^*Q^2 vs Q (top), anisotropy vs Q (middle), and peak fitting results of peak positions and characteristic lengths (bottom). The anisotropy is calculated as the difference between scattering intensities in the vertical direction and horizontal direction over their sum. RSoXS was acquired at an X-ray energy of 285.2 eV. The onset L_c values are for the best performing devices, those are the blends with 1% CN.

Flipping of molecular orientations with different sample processing conditions often affect the polarized scattering patterns which result in changes in the sign of anisotropy.²⁸ Here, the anisotropy trends follow closely the scattering peak positions and intensities without any change signs. That suggests there are no significant changes of molecular orientations in the investigated films.

Surface roughness: atomic force microscopy (AFM)

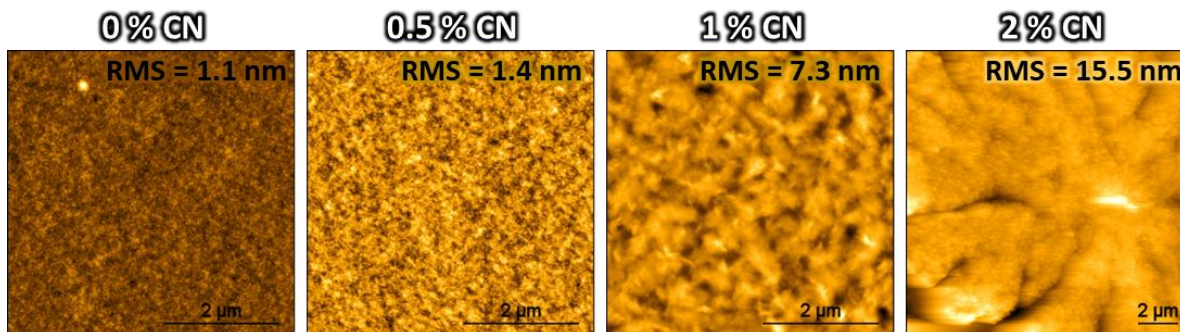


Figure S2- 20: AFM height scans of the fluorinated blends (PBDB-T: CPDT-4F) with different amount of solvent additive (0, 0.5, 1, and 2 % CN from left to right, respectively). Sale bars of 2 μm .

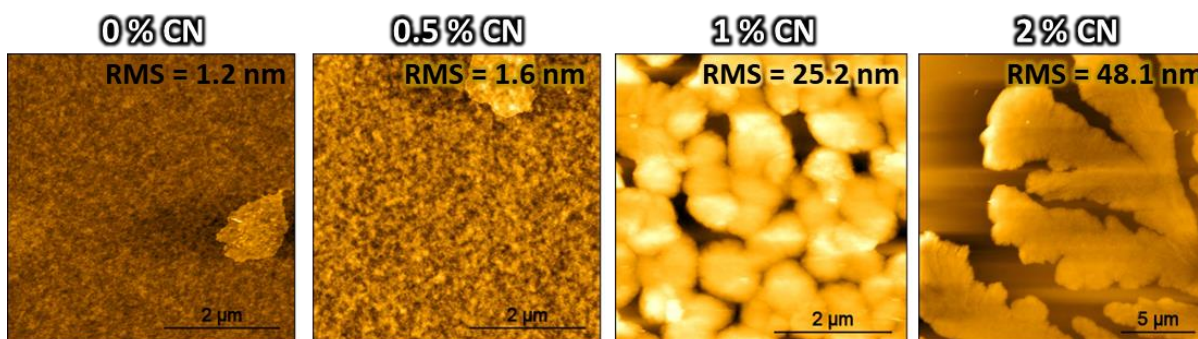


Figure S2- 21: AFM height scans of the Chlorinated blends (PBDB-T: CPDT-4Cl) with different amount of solvent additive (0, 0.5, 1, and 2 % CN from left to right, respectively).

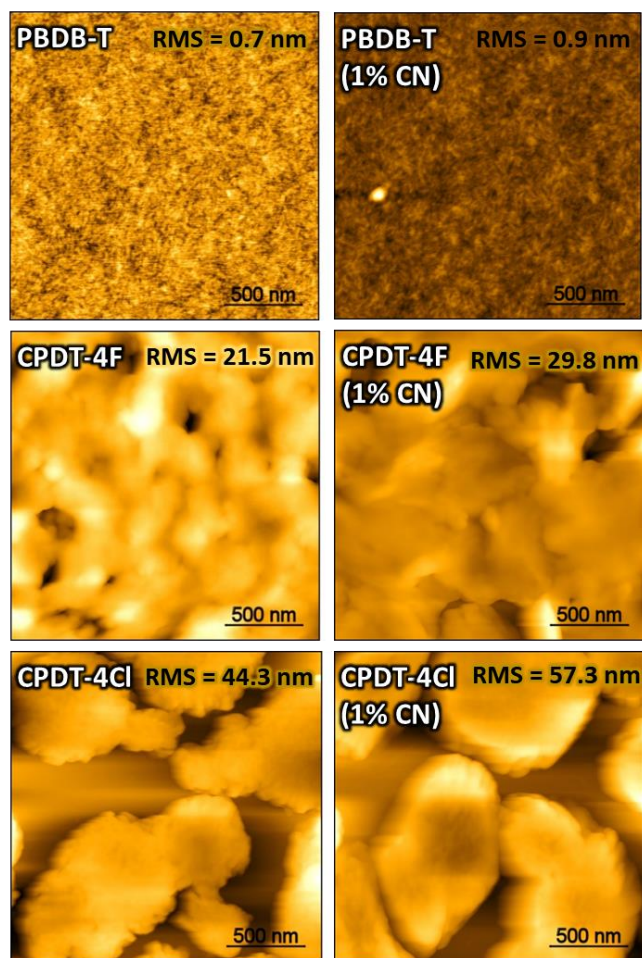


Figure S2- 22: AFM height scans for pure materials; processed from CB without solvent additive (left) and with 1% CN (right). Scale bars of 500 nm.

Blends with 2% CN: optical microscopy images

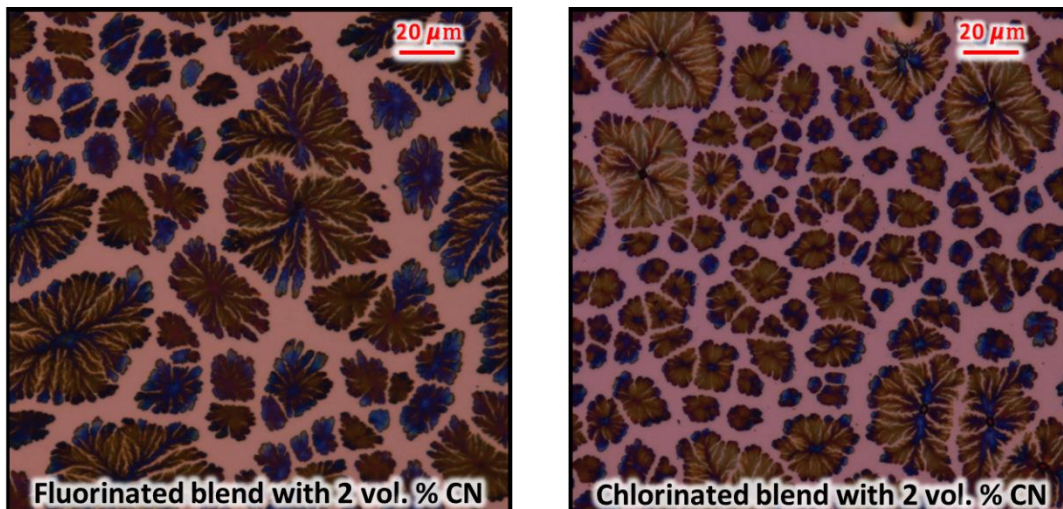


Figure S2- 23: Visible optical microscope images were obtained via IA Nikon Eclipse LV100 at 10X magnification. The small molecule domains are so large due to the dramatic phase segregation in both fluorinated and chlorinated blends with 2% CN additive.

Blends with 2% CN: scanning electron microscopy (SEM) images

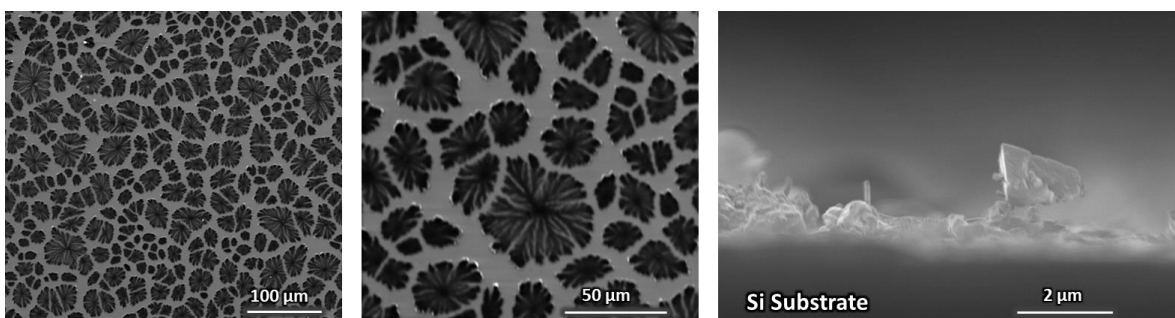


Figure S2- 24: SEM scans of the fluorinated blend (PBDB-T: CPDT-4F) with 2% CN additive. SEM surface scans (left and center) and a SEM cross-section (right).

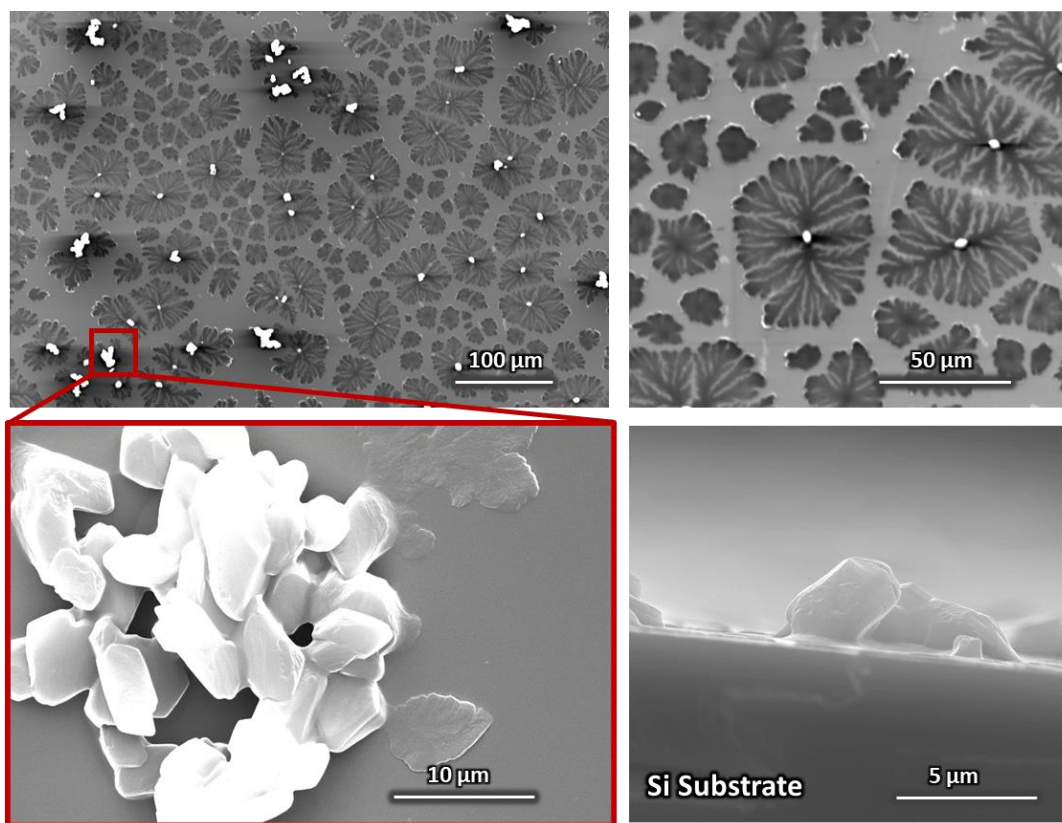


Figure S2- 25: SEM scans of the chlorinated blend (PBDB-T: CPDT-4Cl) with 2% CN additive. SEM surface scans (top). The bottom left is a zoomed in SEM surface scan on a bright mountain-like region as indicated with the red square. A SEM cross-section scan shown on the bottom right.

Transmission electron microscopy (TEM) images

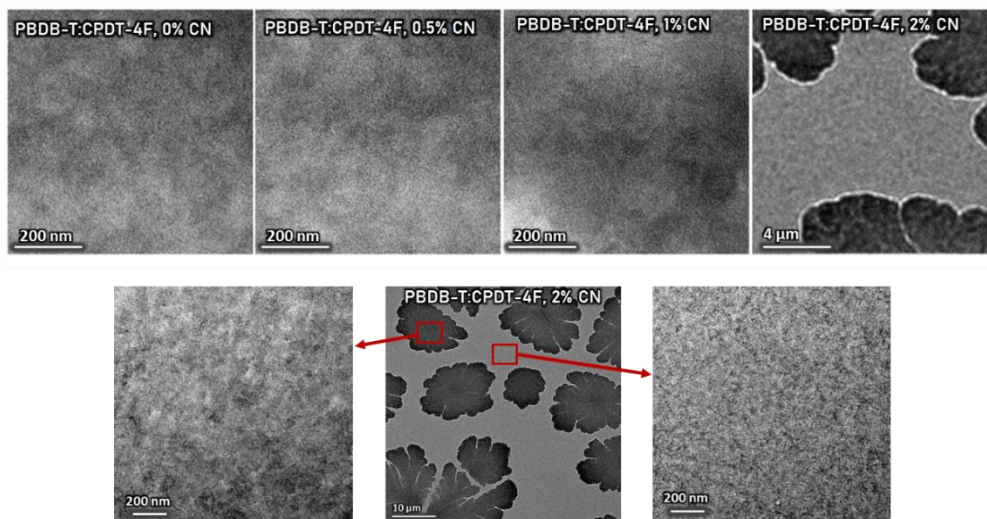


Figure S2- 26: TEM bright-field scans of the fluorinated blends (PBDB-T: CPDT-4F) with different amount of solvent additive. Top from left to right: 0, 0.5, 1, and 2 % CN, respectively. The bottom images are zoomed out and in scans of the blend with 2 % CN on different regions “domains” as indicated with the red squares.

Zoomed in scans on different domains in blends with 2% CN do not reveal obvious features.

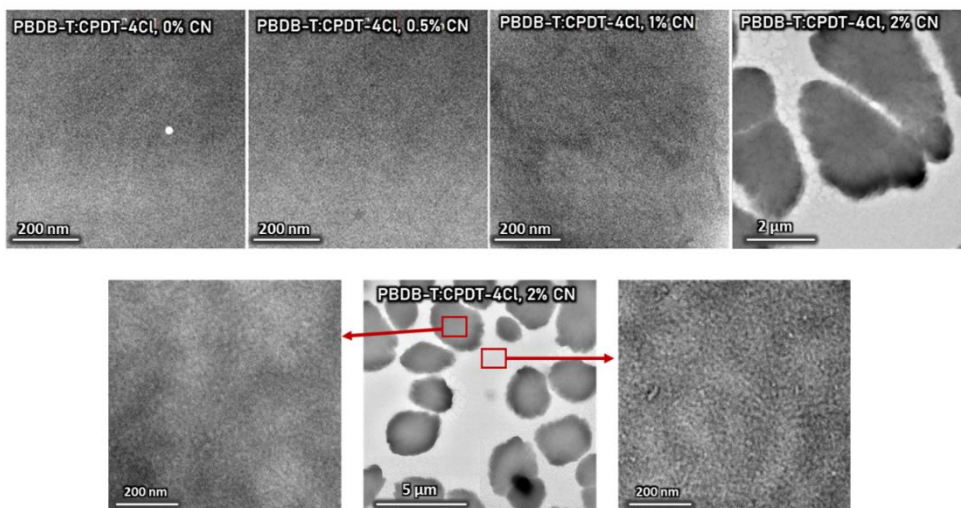


Figure S2- 27: TEM bright-field scans of the chlorinated blends (PBDB-T: CPDT-4Cl) with different amount of solvent additive. Top from left to right: 0, 0.5, 1, and 2 % CN, respectively. The bottom images are zoomed out and in scans of the blend with 2 % CN on different regions “domains” as indicated with the red squares.

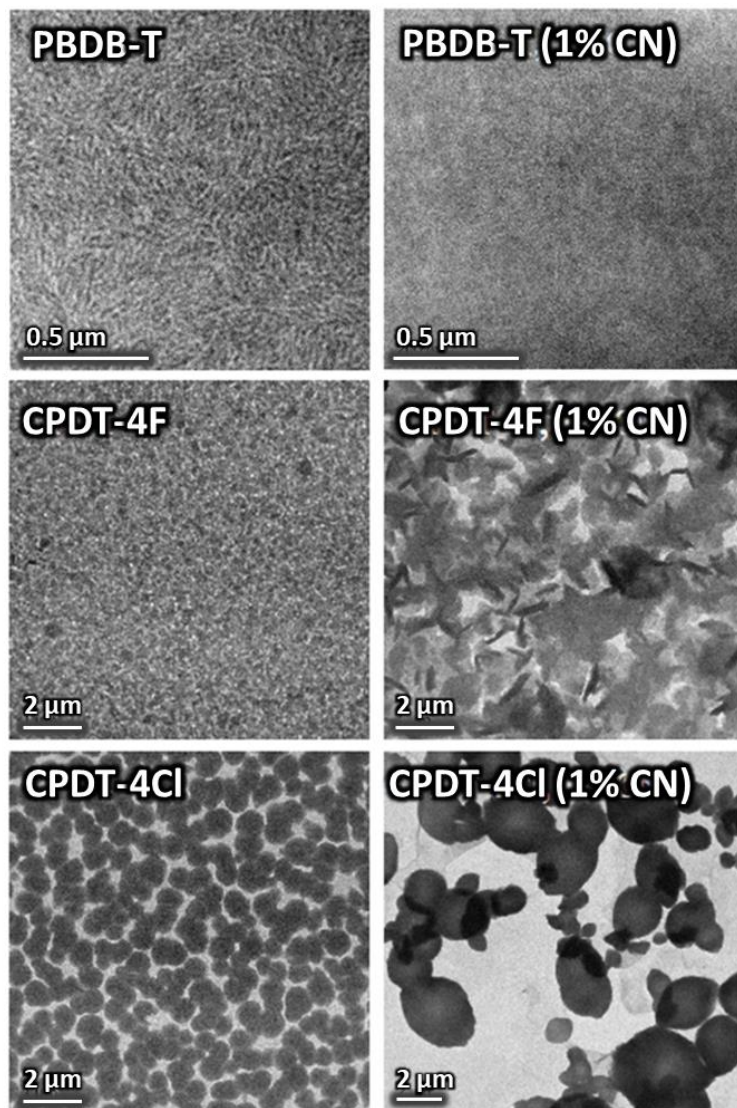


Figure S2- 28: TEM bright-field scans of pure materials: without solvent additive (left) and with 1% CN (right).

Microscopic results of PM6:Y6 blends

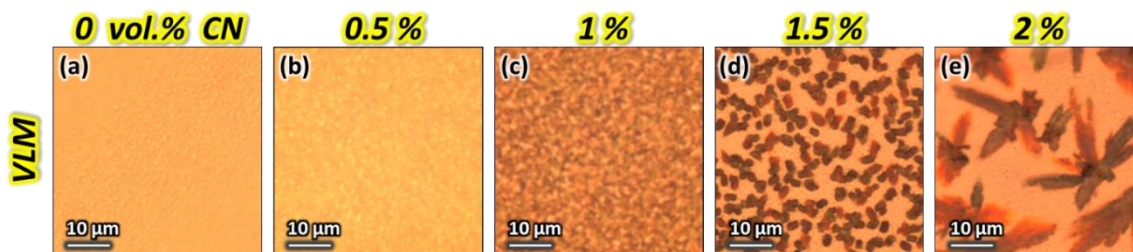


Figure S2- 29: Visible light microscope (VLM) images of PM6:Y6 blends processed from chloroform with different concentrations of CN [vol.%]. a-e) 0, 0.5, 1, 1.5, and 2 vol. % CN, respectively. Scale bar of 10 μm .

PM6:Y6 (1:1.2) blends were processed from chloroform (CF) with different concentrations of solvent additive (CN): 0, 0.5, 1, 1.5, and 2 vol. %. The blends were processed by following previous procedures from the literature.^{32,34} The PM6 and Y6 materials were purchased from 1-Material Inc. and the solvents, both CF and CN, were purchased from Sigma-Aldrich. The VLM scans were acquired via IA Nikon Eclipse LV100.

APPENDIX C: SUPPORTING INFORMATION FOR CHAPTER 5: FIELD-
INDEPENDENT GEMINATE RECOMBINATION LIMITS CHARGE SEPARATION IN
PM6:Y6 ORGANIC SOLAR CELLS: DRIVEN BY MOLECULAR ORDERING OF Y6

Device performance

PN Concentration [vol. %]	V_{oc} [V]	J_{sc} [mA/cm ²]	FF [%]	PCE (max) [%]
0.0	0.82	24.95 ± 0.14	64.49 ± 0.42	13.10 ± 0.07 (13.71)
0.2	0.80	26.14 ± 0.44	66.21 ± 0.20	13.90 ± 0.30 (14.32)
0.5	0.78	26.12 ± 0.24	68.77 ± 0.10	14.06 ± 0.13 (14.55)
2.0	0.77	25.25 ± 0.28	67.17 ± 0.15	13.05 ± 0.18 (13.82)
5.0	0.78	24.95 ± 0.49	66.16 ± 0.15	12.83 ± 0.29 (13.52)

Table S3- 1: Summary of the J-V parameters for PM6:Y6 OSCs with different concentrations of the solvent additive (PN). Uncertainties are the standard errors.

The overall lower device performance of the investigated PM6:Y6 OSCs in this study, compared to previous literature,¹⁸ can be attributed to the higher ITO surface resistivity (~ 45 ohms/sq, 145 nm thickness) vs. those of the literature (~ 15 ohms/sq, 185 nm thickness). See J-V comparisons in Figure S3- 1.

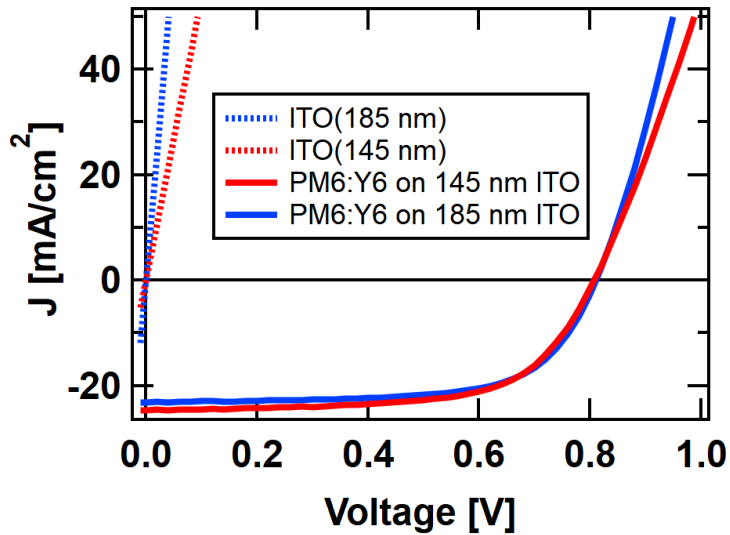


Figure S3- 1: J-V results to compare 145 nm (~ 45 ohms/sq) vs. 185 nm (~ 15 ohms/sq). Also, J-V curves of PM6:Y6 active layers on the different ITO substrates are plotted here for comparing.

UV-VIS spectroscopy

Measurements of UV-VIS spectroscopy were performed on films cast on glass substrates using an Ocean Optics QEPro spectrometer.

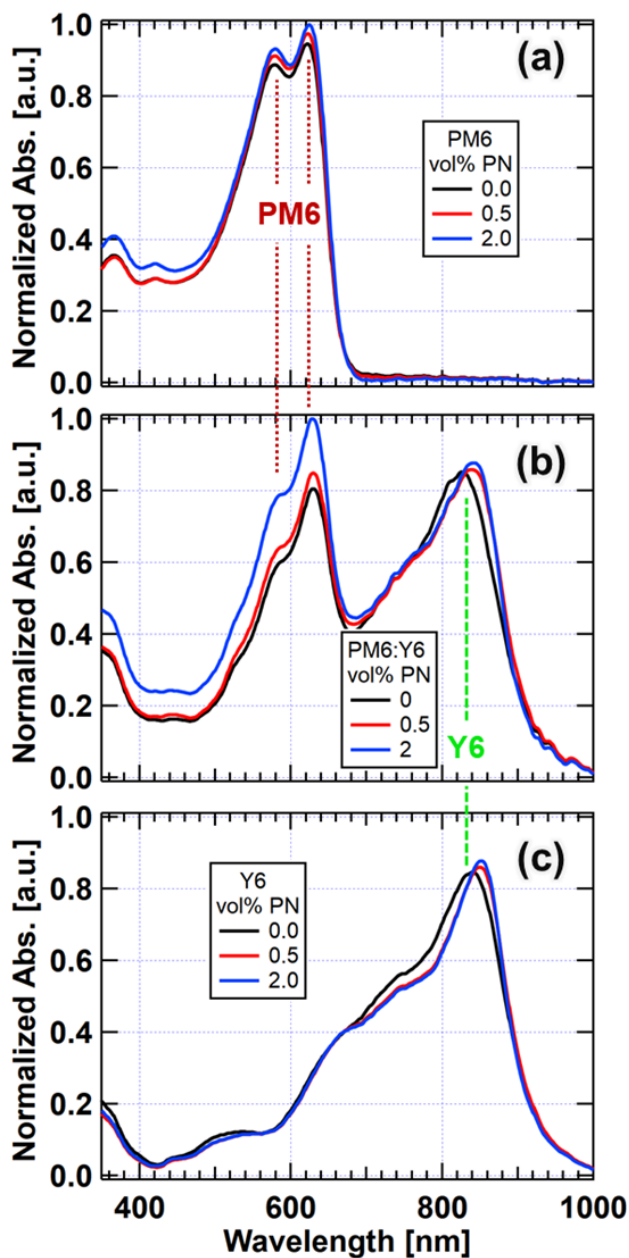


Figure S3- 2: UV-VIS Spectra of films processed with different concentrations of solvent additive PN. a) Pure PM6 films. b) PM6:Y6 blends. c) Pure Y6 films

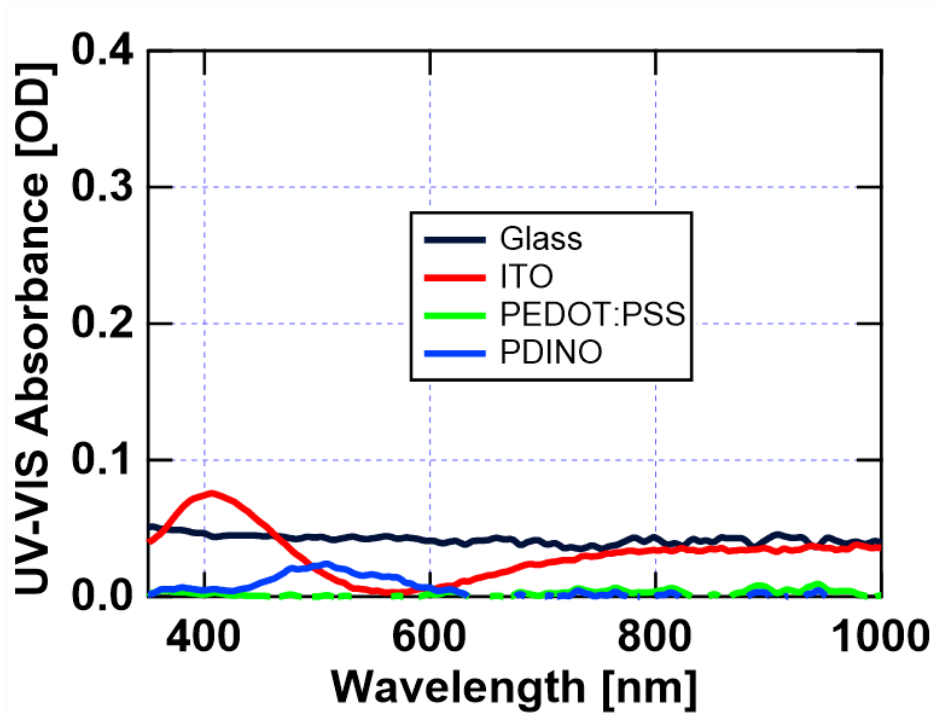


Figure S3- 3: UV-VIS spectra of the different layers used in the examined OSCs: Glass, ITO, PEDOT: PSS, and PDINO.

Variable angle spectroscopic ellipsometry (VASE)

Film thicknesses and material optical constants were measured by an alpha-SE ellipsometer (J. A. Woollam) at three angles of incidence: 65°, 70°, and 75°. All the organic films were prepared according to the device fabrication procedure while cast on Si substrates.

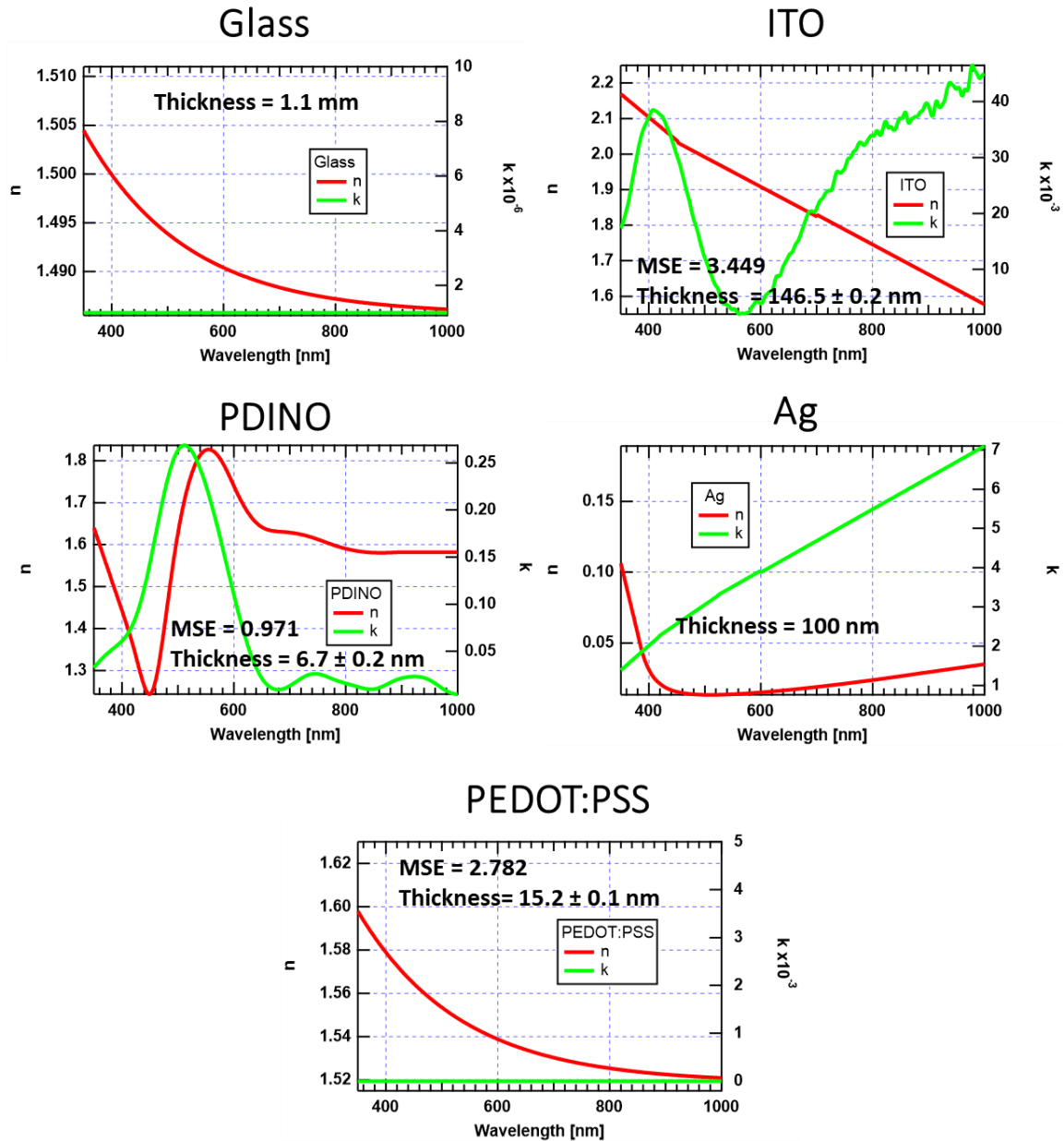


Figure S3- 4: Optical constants (k and n) of glass, ITO, PDINO, Ag, and PEDOT:PSS.

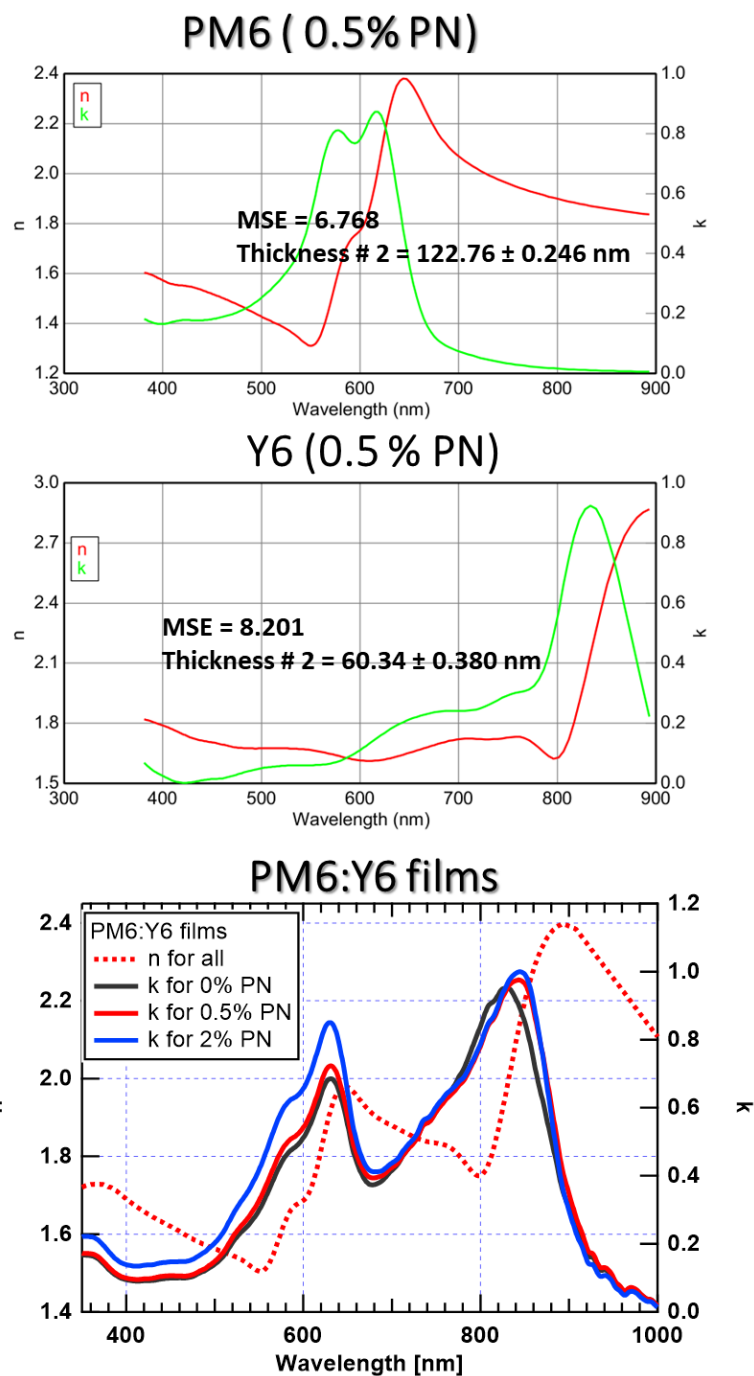


Figure S3- 5: Optical constants (n and k) of a pure PM6 film, a pure Y6 film, and blends of M6:Y6. The k profiles of the blends were converted from the UV-VIS absorbance of the blends and compared to the literature. n is measured from VASE. The film thicknesses of the blends are about 92 nm.

Absorption and maximum current density calculation

To calculate the absorption efficiency of the investigated PM6:Y6 active layers, we utilized the transfer matrix model developed by the McGehee group,⁴⁹ using film thicknesses and optical constants obtained via VASE. The simulated device structure is ITO (146 nm)/PEDOT:PSS (15nm)/active layer (92nm)/PDINO (7nm)/Ag (100nm). The modeling results of absorbance current density (J_{abs}) of the PM6:Y6 active layers are 27.5524, 27.8929, and 28.5845 mA/cm² for the blends with 0, 0.5, and 2% PN, respectively.

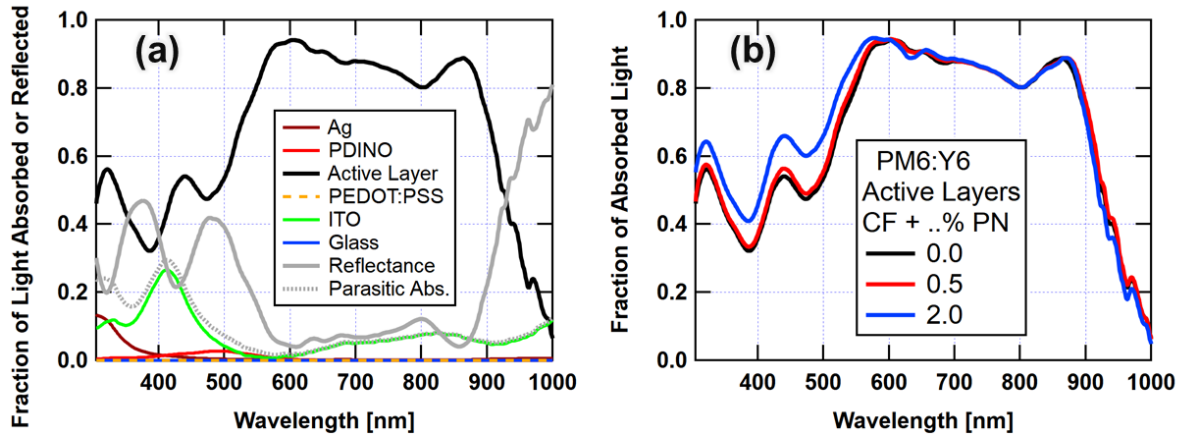


Figure S3- 6: Transfer matrix modeling results. a) Fraction of light absorbed or reflected by all device layers. b) Fraction of absorbed light of PM6:Y6 active layers with different amounts of PN.

The maximum current that can be given to an OSC device assuming 100% photo-electric conversion, can be calculated by integrating the total number of incidental photons from our solar simulator photon irradiance in the absorption spectrum range of 350-1000 nm. Then multiplying that by the electron charge can yield the maximum current density (J_{\max}). The calculated J_{\max} is 38.72 mA/cm².

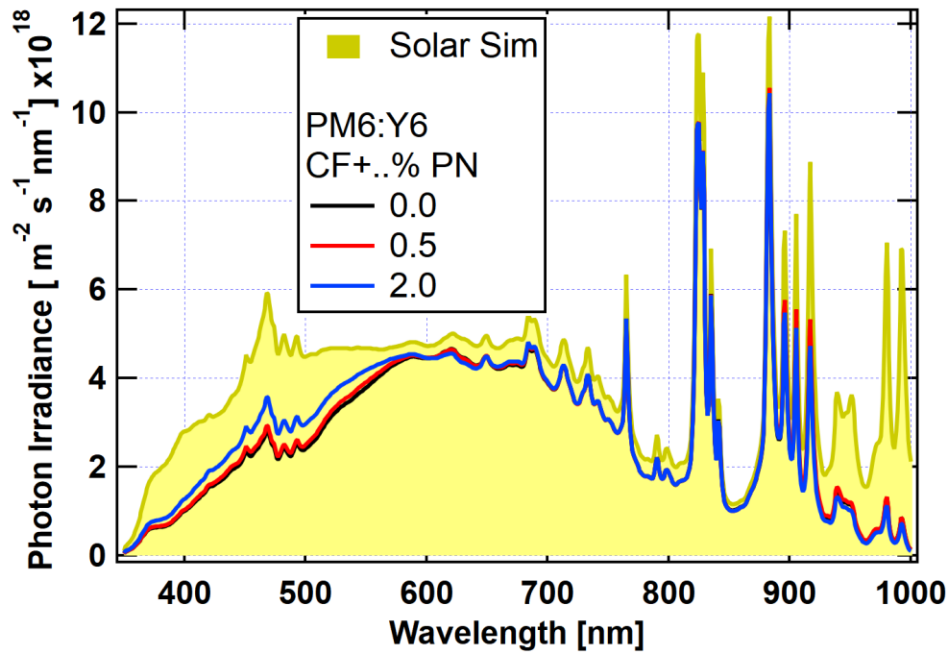


Figure S3- 7: The yellow curve is the photon irradiance of the used solar simulator to test the investigated OSCs. The blue, red and blue curves show the photon irradiance scaled to the fraction of absorbed light by the PM6:Y6 blends with 0, 0.5 and 2% PN.

Quantum efficiencies and losses: calculations and results

PM6:Y6 blend PN Conc. [%]	J_{\max} [mA/cm ²]	J_{abs} [mA/cm ²]	J_{sat} [mA/cm ²]	J_{gen} [mA/cm ²]	J_{mpp} [mA/cm ²]
0.0	38.72	27.55	26.44	25.57	21.4
0.5		27.89	26.87	26.4	22.76
2		28.58	25.75	25.2	21.96

Table S3- 2: A summary of the current densities as calculated and extracted for PM6:Y6 blends with 0, 0.5, and 2 % PN solvent additive. J_{\max} is calculated from the photon irradiance. J_{abs} is calculated from the transfer matrix modeling. J_{sat} is the current density of each blend at voltage of -3 V. J_{gen} is the current density that was generated via TDCF at maximum power point voltage (V_{mpp}). J_{mpp} is the current density at maximum power point.

PM6:Y6 blend with..	0.0 % PN	0.5 % PN	2.0 %PN
Abs. loss [%] = $(J_{\max} - J_{\text{abs}})/J_{\max}$	28.85	27.97	26.19
FI Geminate recomb. [%] = $(J_{\text{abs}} - J_{\text{sat}})/J_{\max}$	2.87	2.63	7.31
FD Geminate recomb. [%] = $(J_{\text{sat}} - J_{\text{gen}})/J_{\max}$	2.25	1.21	1.42
Bimolecular recomb. [%] = $(J_{\text{gen}} - J_{\text{mpp}})/J_{\max}$	10.77	9.40	8.37
Charged extracted [%] = J_{mpp}/J_{\max}	55.27	58.78	56.71

Table S3- 3: A summary of charge losses at each step of the charge generation process in relation to the maximum current density J_{\max} in PM6:Y6 devices with 0, 0.5, and 2% PN. The first column shows how each loss is calculated. FI stands for field-independent, and FD stands for field-dependent.

PM6:Y6 blend with..	0.0 % PN	0.5 % PN	2.0 %PN
Abs. efficiency [%] = J_{abs}/J_{\max}	71.15	72.03	73.81
Separation efficiency [%] = $J_{\text{gen}}/J_{\text{abs}}$	92.81	94.66	88.17
Extraction efficiency [%] = $J_{\text{mpp}}/J_{\text{gen}}$	83.69	86.21	87.14

Table S3- 4: Quantum efficiencies of light absorption, charge separation, and charge extraction in PM6:Y6 devices with 0, 0.5, and 2 % PN.

Photoluminescence spectroscopy

The photoluminescence spectroscopy was conducted using a laser light (Ekspla NT232) with an excitation wavelength of 600 nm and an Ocean Optics QEPro spectrometer. The samples were cast on PEDOT: PSS/glass substrates. A light background of a PEDOT:PSS/glass substrate was subtracted from the PL intensity of the samples. The PL spectrum of each sample was normalized to its thickness.

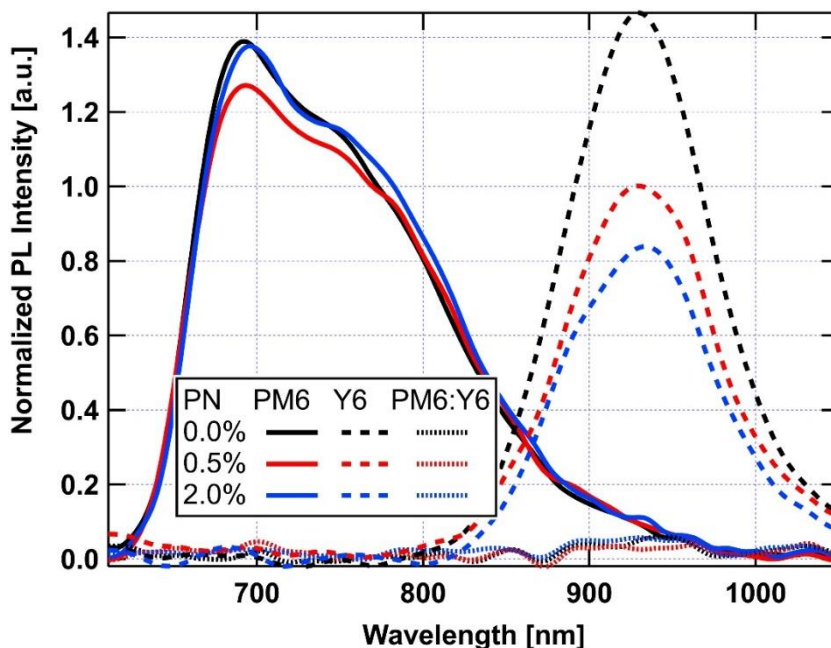


Figure S3- 8: Photoluminescence spectra of pure PM6, pure Y6, and blend PM6:Y6 films with different amounts of solvent additive (PN).

Atomic force microscopy scans

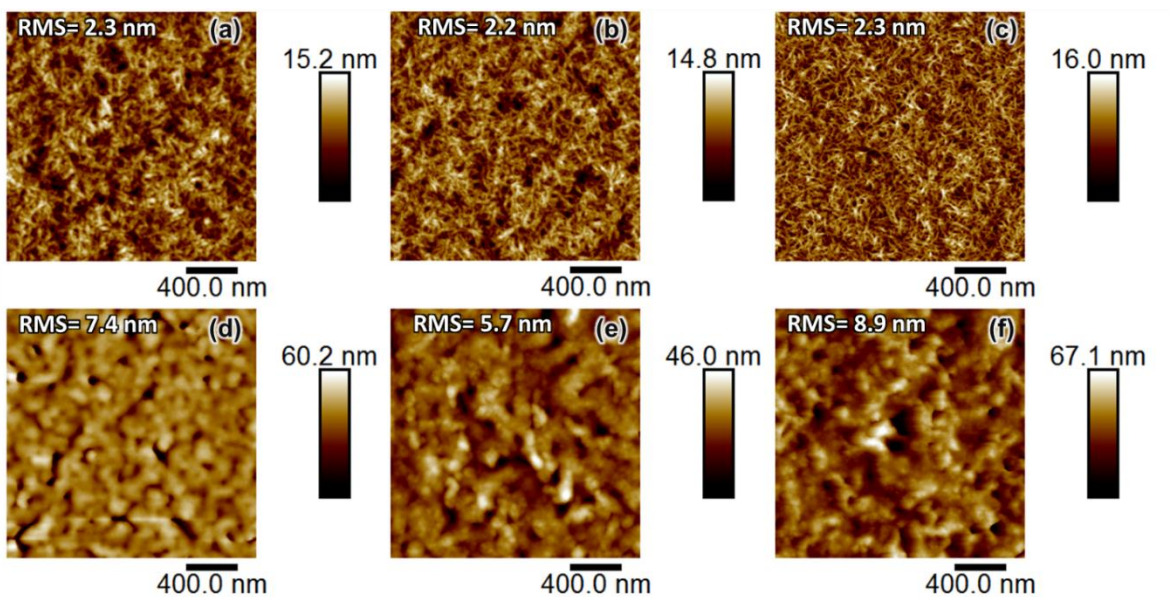


Figure S3- 10: AFM height scans of pure films with different amounts of PN. a-c) For pure PM films with 0%, 0.5%, and 2% PN, respectively. d-f) For pure Y6 films of Y6 with 0%, 0.5%, and 2% PN, respectively.

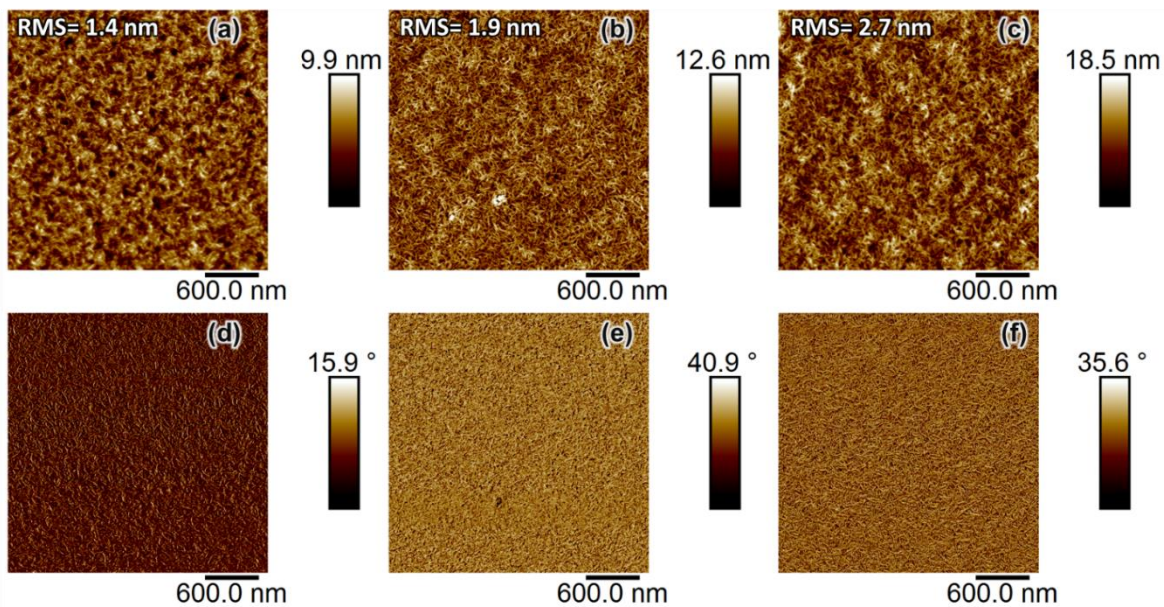


Figure S3- 9: a-c) AFM height scans of PM6:Y6 blends with 0%, 0.5%, and 2% PN, respectively. d-f) Phase scans of the blends with 0%, 0.5%, and 2% PN, respectively.

NEXAFS spectroscopy and contrast function

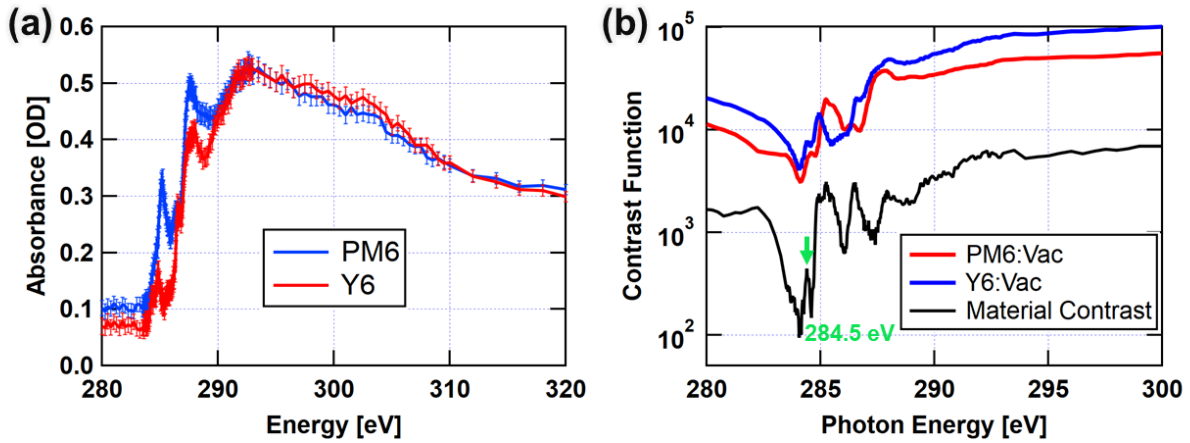


Figure S3- 11: a) NEXAFS spectra of neat films of PM6 and Y6. The π^* resonant energy of Y6 is about 285.15 eV. The π^* resonant energy of PM6 is about 285.15 eV. b) Contrast functions of materials-vacuum and material-material. The green arrow points are X-ray energy of 284.5 eV which was used to conduct the RSoXS measurement.

The contrast function (C) is calculated as $(C=E^4 \times |\Delta n|^2)$ where E is the X-ray energy and n is the material complex index of refraction ($n=1- \delta + i\beta$). Beta is the imaginary part of the index of refraction, which is the mass absorption and can be obtained from the NEXAFS spectroscopy. Delta is the real part of the index of refraction and can be calculated from beta using the Kramers-Kronig transform.⁵⁵

Grazing incidence wide-angle x-ray scattering (GIWAXS)

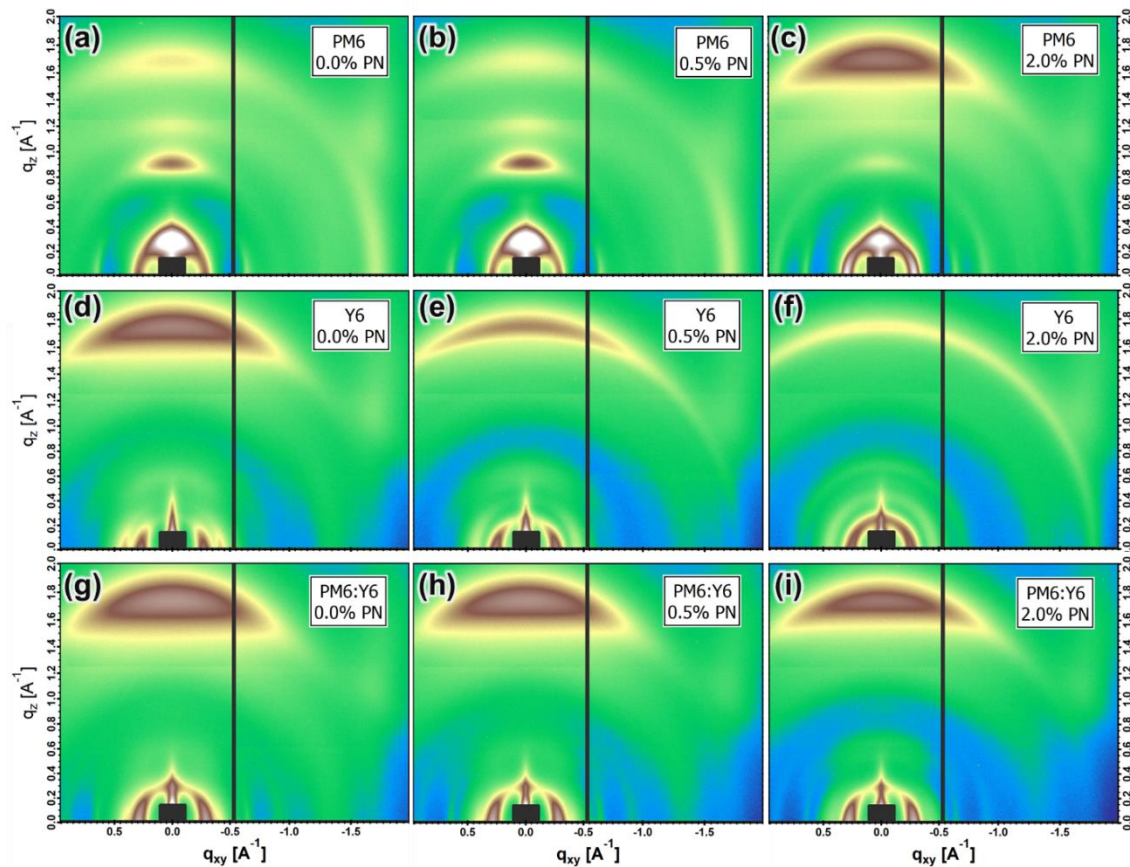


Figure S3- 12: 2D GIWAXS scans of pure PM6 films (a-c), pure Y6 films (d-f) and PM6:Y6 blends (g-i) with different amounts of PN as indicated on each scan.

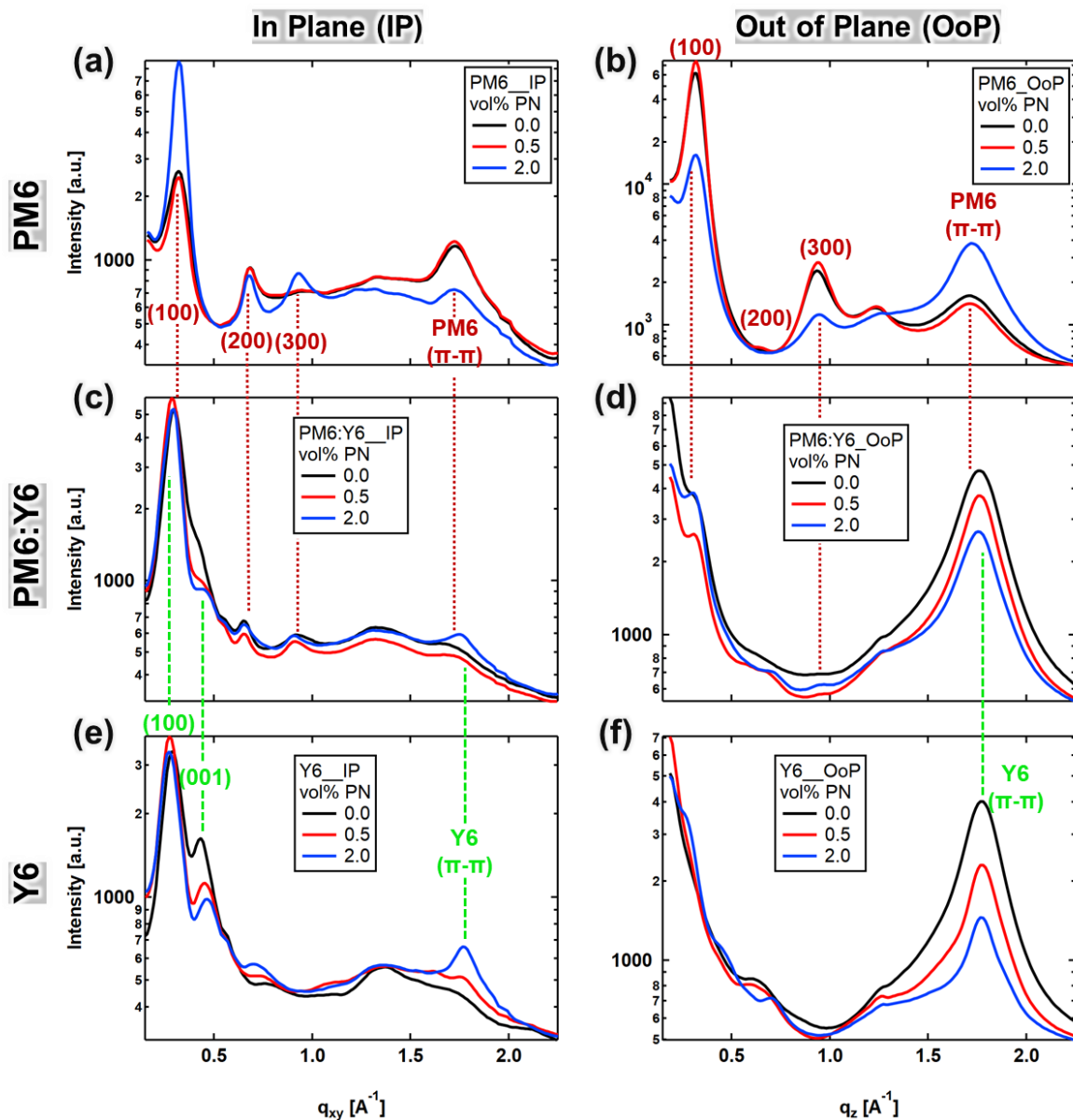


Figure S3- 13: In plane (IP) and out of plane (OoP) 1D GIWAXS profiles of pure PM6 films (a and b), PM6:Y6 films (c and d), and pure Y6 films (e and f). The films were processed with different amounts of PN as indicated in the figure legends. The diffraction patterns of pure PM6 and Y6 films were used to peak assign those of the blends.

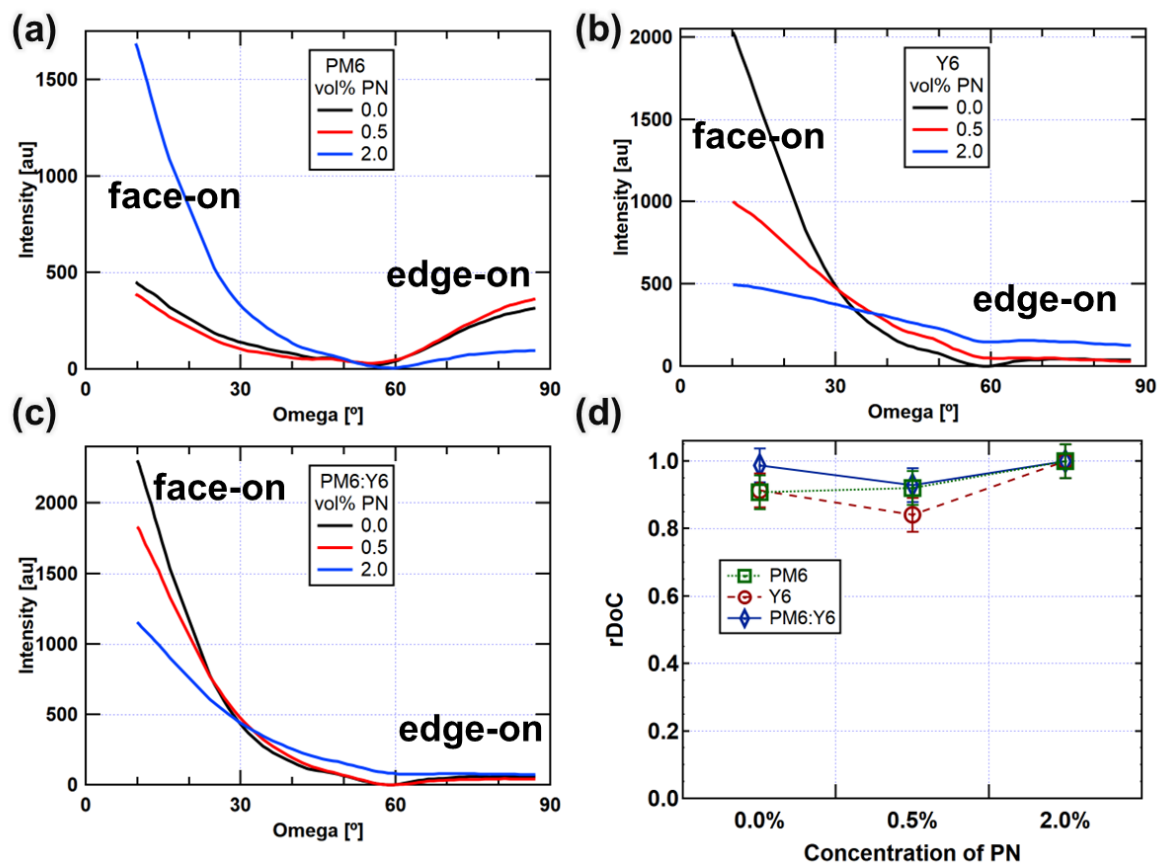


Figure S3- 14: Pole figures of the pi-pi stacking for: a) PM6 films, (b) Y6 films, and (c) PM6:Y6 blends. The films were processed with different amounts of PN as indicated in the figure legends. d) The relative degree of crystallinity (rDoC) of pi-pi stacking in pure and blend films.

More details regarding pole figures can be found elsewhere.¹⁰²

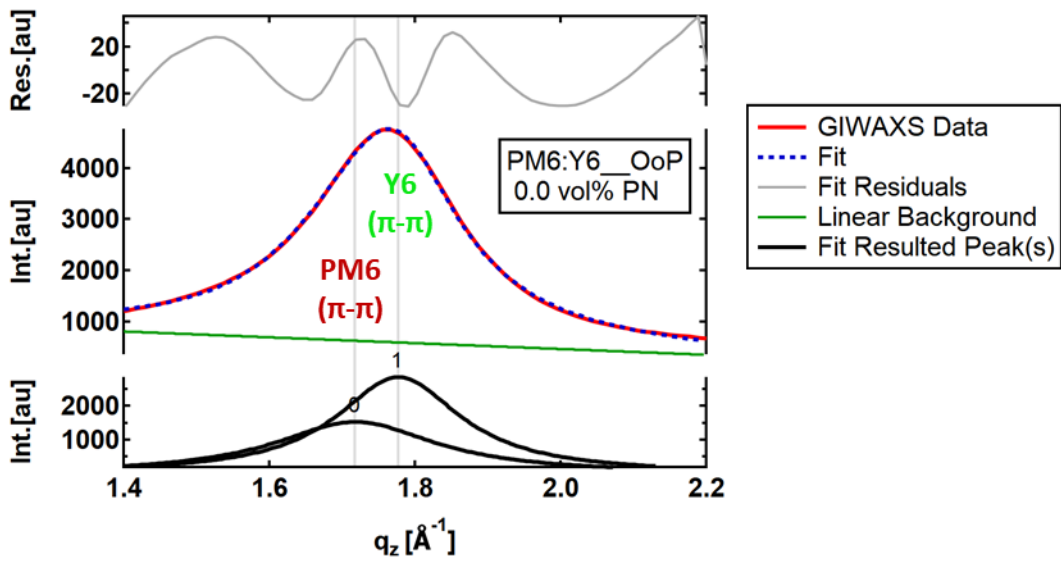


Figure S3- 15: A multipeak fitting (MPF) example of fitting the pi-pi stacking of PM6 and Y6 in the out of plane direction in the PM6:Y6 blend without PN. Similar fitting method was used to extract peak positions and areas which then used to calculated d-spacings and crystal coherence length (CCL) values of peaks of interest. CCL were calculated using Scherrer analysis. Where $CCL \sim 2 \cdot \pi / FWHM$.

Out-of-plane (010) π-π stacking			
Materials	Peak Position [\AA^{-1}]	d-spacing [nm]	CCL [nm]
PM6 (0.0% PN)	1.72	0.37	2.11(3)
PM6 (0.5% PN)	1.72	0.37	2.32(3)
PM6 (2.0% PN)	1.73	0.36	2.65(2)
Y6 (0.0% PN)	1.77	0.35	2.63(3)
Y6 (0.5% PN)	1.78	0.35	2.95(6)
Y6 (2.0% PN)	1.77	0.35	3.08(8)
PM6:Y6 (0.0% PN)	PM6	1.72	0.37
	Y6	1.78	0.35
PM6:Y6 (0.5% PN)	PM6	1.73	0.36
	Y6	1.77	0.35
PM6:Y6 (2.0% PN)	PM6	1.73	0.36
	Y6	1.77	0.35

Table S3- 5: A summary of peak position, d-spacing, and CCL values as extracted from MPF for the OoP π - π stackings in pure PM6, pure Y6 and PM6:Y6 blend films with different amounts of PN. (d -spacing= $2*\pi$ /peak position).

In-plane (100) lamellar stacking			
Materials	Peak Position [\AA^{-1}]	d-spacing [nm]	CCL [nm]
PM6 (0.0% PN)	0.32	1.97	6.22(7)
PM6 (0.5% PN)	0.32	1.96	7.27(8)
PM6 (2.0% PN)	0.32	1.96	8.92(1)
Y6 (0.0% PN)	0.29	2.18	5.96(4)
Y6 (0.5% PN)	0.28	2.28	6.56(6)
Y6 (2.0% PN)	0.27	2.29	6.33(7)

Table S3- 6: A summary of peak position, d-spacing, and CCL values as extracted from MPF for the IP lamellar stackings in pure PM6 and pure Y6 films with different amounts of PN.

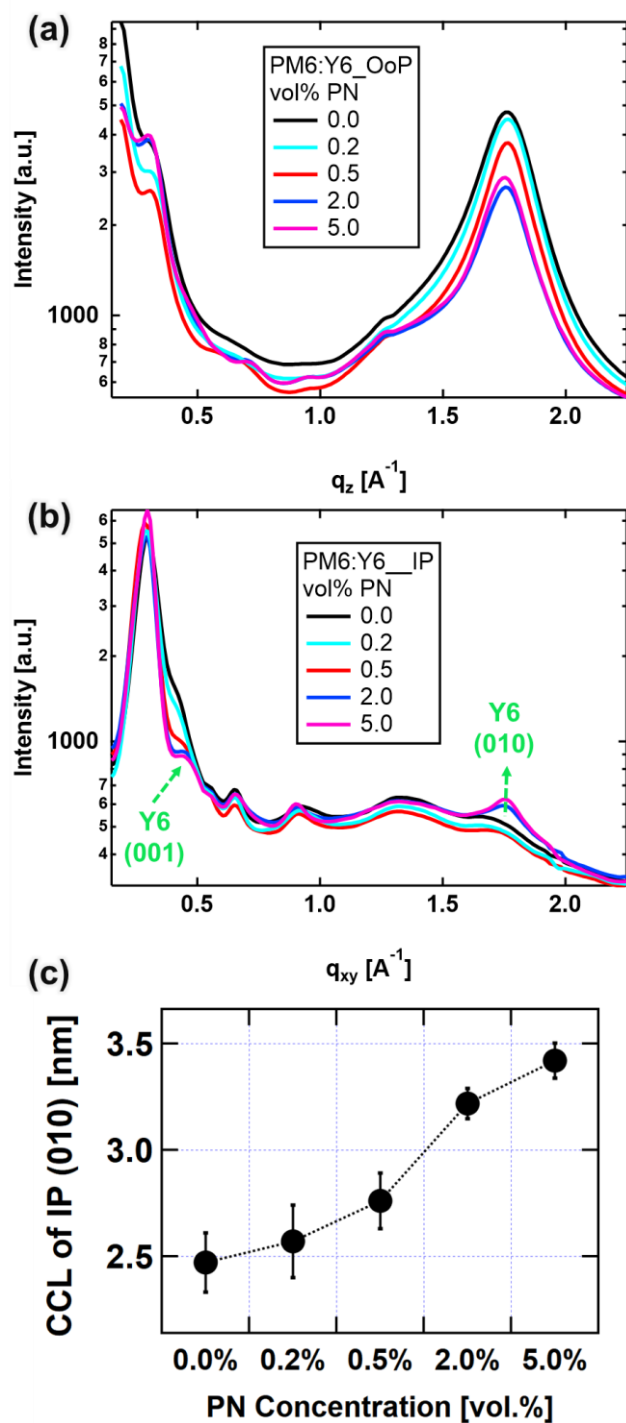


Figure S3- 16: a) 1D GIWAXS profiles of PM6:Y6 blends with 0, 0.2, 0.5, 2, and 5 % PN additive. a) GIWAXS intensity profiles in the OoP direction. b) Profiles in the IP direction. c) CCL values of the IP pi-pi (010) stacking.